The Pennsylvania State University

The Graduate School

Department of Mechanical and Nuclear Engineering

GEOMETRIC EFFECTS OF FLOW RESTRICTIONS AND CONFIGURATIONS ON INTERFACIAL STRUCTURES IN TWO-PHASE FLOW

A Thesis in

Mechanical Engineering

by

Mohan Singh Yadav

Submitted in Partial Fulfillment
of the Requirements
for the Degree of

Master of Science

December 2009

The thesis of Mohan Singh Yadav was reviewed and approved* by the following:

Seungjin Kim
Assistant Professor of Mechanical and Nuclear Engineering
Thesis Advisor

Laura L. Pauley
Arthur L. Glenn Professor of Engineering Education
Professor of Mechanical Engineering

Karen Thole
Professor
Head of the Department of Mechanical and Nuclear Engineering

*Signatures are on file in the Graduate School

ABSTRACT

This study investigates the geometric effects of flow restrictions and flow configurations on two-phase flow parameters. Experiments are conducted in two distinct experimental setups employing different flow configurations and flow restrictions. In the first experiment, comparison of the effects of 90-degree and 45-degree elbows on interfacial structures and their transport characteristics in horizontal two-phase bubbly flow is investigated. The setup is made out of 50.3 mm inner diameter glass tubes and a double-sensor conductivity probe is used to collect time averaged local data. Experimental results show that both elbows have significant effect on the development of interfacial structures as well as the bubble interaction mechanisms. Furthermore, there are characteristic similarities and differences between the effects of two elbows. While the effect of the 45-degree elbow is evident immediately after the elbow, the 90-degree elbow effect is propagated further downstream of the elbow. Moreover, it is shown that both the elbows induce oscillations in the interfacial structures and two-phase flow parameters, but the degree and the nature of oscillation differ. Comparison of the elbow effect on the axial transport of two-phase flow parameters is also investigated.

The second set of experiments is performed in combinatorial two-phase flow facility to study the effects of 90-degree vertical elbow and geometric configuration on two-phase bubbly flow. The elbow has a significant effect on two-phase flow regime transition boundaries at measurement locations downstream of the elbow. Modified two-phase flow regime maps based on the extensive flow visualization studies are suggested for both vertical and horizontal test sections. A four-sensor conductivity probe is employed to measure time averaged two-phase local parameters as the flow develops along vertical upward to horizontal section across the 90-degree vertical elbow. The elbow causes the bubbles to align along the horizontal radius of the pipe cross-section, creating a bi-peaked profile in void fraction and interfacial area concentration.

One dimensional transport of area averaged two-phase flow parameters shows that the elbow promotes bubble interaction mechanism.

TABLE OF CONTENTS

LIST OF FIGURES

LIST OF TABLES

ACKNOWLEDGEMENTS

The author would like to express gratitude to his advisor, Professor Seungjin Kim for his continuous guidance, encouragement and support. Prof. Kim not only imparted indispensable technical knowledge but also continuous motivation. Sincere thanks to Justin Talley, who worked closely during author's period of research.

The author would like to acknowledge Dr. Laura Pauley for reviewing this work. The data presented on horizontal two-phase flow is based on the experiment performed by University of Wisconsin, Milwaukee under the direction of late Professor Gunol Kojasoy as a part of Task 4-5 of Thermal Hydraulic Task (RS-RES-03-0408) supported by the US NRC Office of Nuclear Regulatory Research. Research in Combinatorial Channels is supported by U S Department of Energy, NEER Program.

Finally, the author would like to express deep appreciation to his family members for their continued support and encouragement. Sincere gratefulness is extended to the author's grandparents and parents, to whom this thesis is dedicated.

Chapter 1

Introduction

Many energy systems including the nuclear reactors have coolant channels in various sizes, orientations and interconnected via various junctions and flow restrictions such as elbows, tees, valves etc. These flow restrictions induce significant changes in the interfacial structures, their transport characteristics and flow regime transition. Interfacial area concentration and void fraction are the most important geometrical parameters of two-phase flow governing the mass, momentum and energy transfer of a system. Hence, experimental study is crucial in improving the understanding of the effects of flow restrictions on the two-phase flow parameters and development of dynamic modeling of interfacial area. There is not only a lack of database that account for the geometric effects, but also the mechanisms that govern two-phase flow transport via geometric restrictions are not well understood. Such limitations present serious shortcomings in the thermal-hydraulic reactor system safety analysis. Most thermal-hydraulic system analysis codes depend on the flow regimes to analyze the effect of interfacial structures which do not dynamically represent the change in the interfacial structure. This leads to instantaneous changes in flow regime, which can not only induce non-physical oscillations in the system but can limit the code accuracy (Ishii et al., 2000).

In order to understand and analyze the thermal-hydraulics of two-phase flow it is expressed in terms of macroscopic field equations and constitutive relations using a continuous formulation. Various formulations such as the homogeneous flow model, drift flux model (Zuber and Findley, 1965), two-fluid model (Ishii, 1975) have been developed. Two-fluid model is considered most accurate because of its detailed treatment of the phase interaction term. Two-fluid model is formulated by considering each phase separately in terms of two sets of equations

governing the balance of mass, momentum and energy. These balance equations are obtained through proper averaging and represent the macroscopic field of each phase. Since the macroscopic fields of each phase are not independent of the other phase, the phase interaction terms which couple the transport of mass, momentum and energy of each phase appear in the field equations. These interaction terms can be expressed as a function of interfacial area concentration, a_i, and the driving force. Ishii (1975) obtained a three dimensional two-fluid model by using temporal and statistical averaging. For practical purposes this model can be simplified as (Ishii, 1975):

Continuity equation:

$$\frac{\partial \alpha_k \rho_k}{\partial t} + \nabla.(\alpha_k \rho_k v_k) = \Gamma_k \tag{1-1}$$

Momentum equation:

$$\frac{\partial \alpha_k \rho_k v_k}{\partial t} + \nabla.(\alpha_k \rho_k v_k v_k) = -\alpha_k \nabla p_k + \nabla.\alpha_k(\bar{\bar{\tau}}_k + \tau'_k) + \alpha_k \rho_k g + v_{ki}\tau_k + M_{ik} - \nabla\alpha_k.\tau_i \tag{1-2}$$

Enthalpy energy equation:

$$\frac{\partial \alpha_k \rho_k H_k}{\partial t} + \nabla.(\alpha_k \rho_k H_k v_k) = -\nabla.\alpha_k(\bar{\bar{q}}_k + q'_k) + \alpha_k \frac{\mathrm{D_k}}{\mathrm{Dt}} p_k + H_{ki}\Gamma_k + \frac{q''_{ki}}{L_s} + \Phi_k \tag{1-3}$$

Here Γ_k, M_{ik}, τ_i, q''_{ki}, Φ_k are the mass generation, generalized interfacial drag, interfacial shear stress, interfacial heat flux, and dissipation, respectively. The subscript *k* denotes the *k* phase and *i* stands for the value at the interface. α_k, ρ_k, v_k, p_k and H_k denote the void fraction, density, velocity, pressure and enthalpy of the k phase, whereas τ_k, τ^i_k, q_k, q^i_k, and g stand for average viscous stress, turbulent stress, mean conduction heat flux, turbulent heat flux and acceleration due to gravity. L_s denotes the length scale at the interface, and thus $1/L_s$ has the physical meaning of the interfacial area per unit volume a_i, (Ishii, 1975), thus

$1/L_s = a_i$ = Interfacial area/Mixture Volume

The above field equations show that several interfacial terms appear on the right hand sides of the equations. Since these interfacial terms should also obey the balance laws at the interface, interfacial transfer conditions could be obtained from an average of the local jump conditions given by (Ishii, 1975) as:

$$\sum_k \Gamma_k = 0$$

$$\sum_k M_{ik} = 0$$

$$\sum_k \left(H_{ki}\Gamma_k + \frac{q''_{ki}}{L_s} \right) = 0$$

Therefore constitutive equations for M_{ik}, q''_{Gi}/L_s and q''_{Li}/L_s are necessary for the interfacial terms. The enthalpy interfacial transfer condition indicates that specifying heat flux for both the phases at the interface is equivalent to the constitutive relation for Γ_k if the mechanical energy transfer term can be neglected (Ishii, 1975). This aspect greatly simplifies the development of the constitutive relations for interfacial transfer terms.

By introducing the mean mass transfer term per unit area, m_k, defined by

$$\Gamma_k = a_i m_k \tag{1-4}$$

The interfacial transfer term in [3] can be rewritten as

$$H_{ki}\Gamma_k + \frac{q''_{ki}}{L_s} = a_i\left(m_k H_{ki} + q''_{ki}\right) \tag{1-5}$$

The heat flux at the interface should be modeled using the driving force or the potential for an energy transfer. Thus,

$$q''_{ki} = h_{ki}(T_i - T_k) \tag{1-6}$$

Where T_i and T_k are the interfacial and bulk temperatures based on the mean enthalpy and h_{ki} is the interfacial heat transfer coefficient. A similar treatment of the interfacial momentum transfer term is also possible (Ishii and Mishima, 1980). In view of the above, the importance of the interfacial area a_i, in developing the constitutive relation for this term is evident. The interfacial transfer terms are now expressed as a product of interfacial area and the driving force. It is essential to make a conceptual distinction between the effects of these two parameters.

Thus, in general, the interfacial transfer terms are given in terms of the interfacial area concentration a_i and driving force (Ishii, 1975)

(Interfacial transfer term) ~ a_i X (Driving force) (1-7)

The interfacial area concentration defined as the interfacial area per unit volume of the mixture characterizes the first-order geometrical effects; therefore, it must be related to the structure of the two-phase flow field. On the other hand the driving forces for the interfacial transport characterize the local transport mechanisms such as the turbulent and molecular diffusions.

In nuclear reactor systems, under the postulated reactor accident conditions, two-phase flow may develop and undergo significant changes in interfacial structure, which results in drastic transitions in flow regime and hence the transport phenomena. There is a lack of experimental data and knowledge of the mechanisms that govern two-phase flow through flow restrictions. Such limitations present shortcomings in the thermal-hydraulic analysis of nuclear reactor systems. Experimental studies are crucial to improve the understanding of the effects of flow restrictions on two-phase flow and development of the correlations for the terms in the two-fluid model, including the interfacial area concentration.

1.2 Literature Review

The following chapters deal with the effect of flow restrictions on the two-phase flow. 45-degree and 90-degree elbows are employed in different flow orientations, i.e. horizontal and vertical. A comprehensive comparison of the 90-degree and 45-degree elbows in horizontal two-phase flow is presented. Furthermore, a detailed study is presented on the effect of 90-degree vertical elbow using flow visualization and local four-sensor conductivity probe (Kim et al., 2000). The local four –sensor conductivity probe is capable of obtaining local time-averaged two-phase flow parameters in view of building an experimental database for the effect of flow restrictions two-phase flow. The literature review presented in this chapter brings out the previous work on two-phase flow regimes, models, measurement techniques and the effect of the flow restrictions on two-phase flow parameters.

There is only a small database available on the local conditions for horizontal two-phase flow configuration, whereas most of the studies have been carried out in vertical configuration. Studies by Salcudean et al. (1983, 1988) and Wang et al. (2004) shows that the flow restrictions induce significant changes in the interfacial structures, their transport characteristics and flow regime transition. Among the limited studies available for horizontal two phase flow, Kocamustafaogullari et al. (1994), Sharma et al. (1998), Iskandrani and Kojasoy (2001) and Lewis et al. (2002) worked on the analysis of local two-phase flow parameters in horizontal flows. Kocamustafaogullari et al. (1994) and Franca and Lahey (1992) performed drift flux analysis for the data acquired in various flow regimes in a horizontal channel. The present study seeks to continue and complete the work done by Kim et al. (2007) and Talley et al. (2009) and focuses on the comparison of local interfacial structures around 45-degree and 90-degree elbows for horizontal bubbly flow.

Among the limited studies available on the effect of flow restrictions in horizontal two-phase flows, important contribution have been made by Kim et al. (2007, 2008) and Talley et al. (2009).Their work demonstrates that the elbows have a significant effect on the interfacial structures and bubble interaction mechanisms. Some of the important results from above studies are discussed in this section:

The experimental facility in Kim et al. (2007, 2008) is made out of 50.3 mm inner diameter glass pipes with a 90 degree and a 45-degree elbow installed. The detailed description of the setup is discussed in Chapter-2. The detailed local two-phase flow parameters are acquired by the double sensor conductivity probe. The effect of a 90-degree elbow is found to be evident in the development of interfacial structures. The elbow effects are highlighted by (1) significant peaking phenomena in the profiles of local two-phase flow parameters and (2) flow oscillations in both vertical and horizontal directions across the pipe cross-sections. It is also found that the degree and the position of peaking are dependent on gas and liquid flow rates. Characteristic geometric effects are seen in development of one-dimensional interfacial area concentration and void fraction. The elbow effect is often found to be prominent further downstream than in the immediate vicinity of the elbow. The elbow promotes bubble interaction resulting in significant changes in interfacial area concentration.

Talley et al (2009) investigated the effect of a 45-degree on the development of local two-phase flow parameters and their distribution in horizontal two-phase flows. Fig. 1-1, 1-2 and 1-3 show the effect of 90-degree and 45-degree elbow on one-dimensional transport of area averaged void fraction, $\langle \alpha \rangle$, area averaged interfacial area concentration, $\langle a_i \rangle$ and void weighted bubble velocity. Since, all these parameters are dependent on the gas flow rates they have been plotted for two characteristic flow conditions. At lower gas flow rates, for both the elbows, there is a decline in $\langle a_i \rangle$ for increasing $\langle \alpha \rangle$. This indicates that both the elbows promote bubble

coalescence. However, at higher gas flow rates, the 45-degree elbow promotes bubble disintegration as shown by steep rise in $<a_i>$.

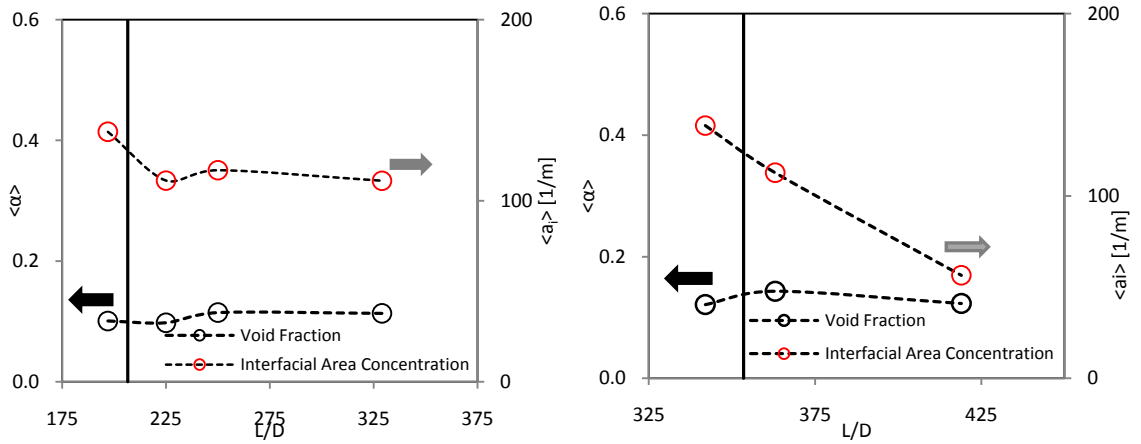

(a) 90-degree elbow; $j_{g,atm}$ = 0.67 m/s (b) 45-degree elbow; $j_{g,atm}$ = 0.76 m/s

Figure **1-1**: Axial development of area averaged void fraction and interfacial area concentration for 90-degree and 45-degree elbow at lower gas flow rate and constant liquid flow rate; j_f = 4.3 m/s, Talley et al. (2009)

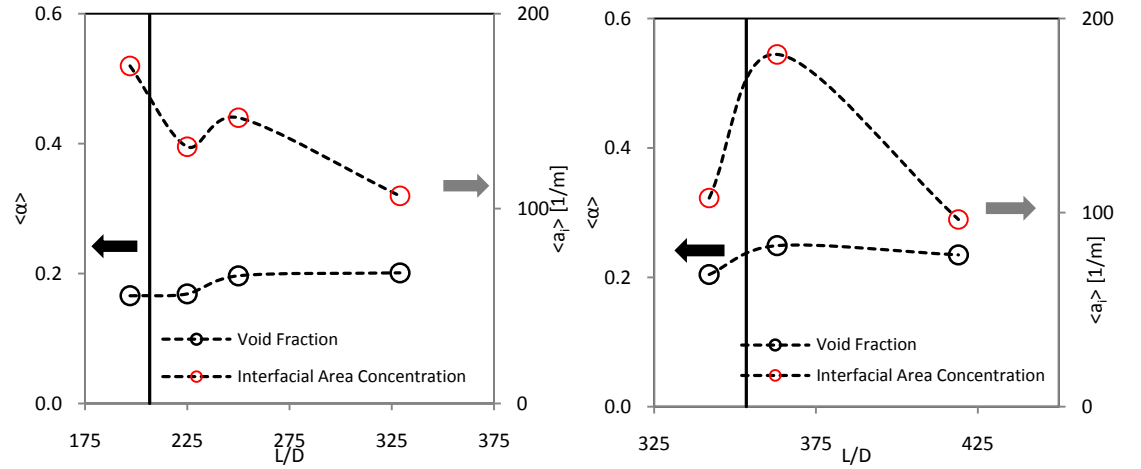

(a) 90-degree elbow; $j_{g,atm}$ = 1.4 m/s (b) 45-degree elbow; $j_{g,atm}$ = 1.6 m/s

Figure **1-2**: Axial development of area averaged void fraction and interfacial area concentration for 90-degree and 45-degree elbow at higher gas flow rate and constant liquid flow rate; j_f = 4.3 m/s, Talley et al. (2009)

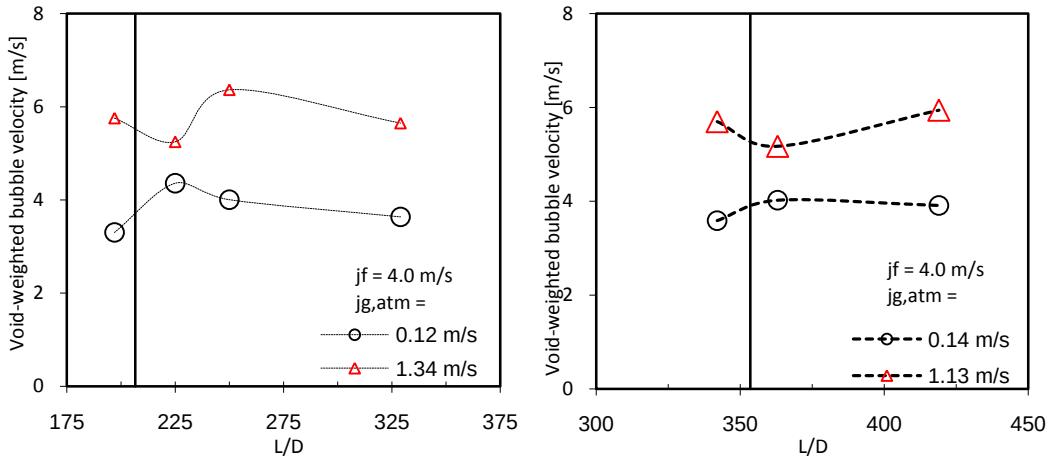

(a) 90-degree elbow (b) 45-degree elbow

Figure **1-3**: Axial development of one dimensional void weighted bubble velocity in two characteristic flow conditions, Talley et al. (2009)

Studies by Talley et al. (2009) emphasized the effect of 45-degree on the local interfacial structures and their one-dimensional transport. They also developed an interfacial area transport equation applicable to an air-water horizontal bubbly flow along which two types of horizontal elbows are installed as flow restrictions. The characteristic effects due to the 45-degree are clearly shown the distribution of local two-phase flow parameters and development of one-dimensional two phase flow parameters. A one-dimensional one-group interfacial area transport equation is developed for horizontal bubbly flow with a 90-degree or 45-degree elbow based on the existing model for vertical air-water flow. Additional pressure drop due to the minor loss of the elbows is taken into account through a newly developed correlation for two-phase minor loss in an elbow. The simple correlation developed by Kim et al. (2007) is analogous to that of Lockhart and Martinelli to account for the minor losses. It is shown that the pressure loss around the elbows can be predicted within ±2% difference (Kim et al., 2007).

In horizontal two-phase flow, the distribution of local two-phase flow parameters across the pipe cross-section is highly non-uniform due to gravity, moreover characteristic oscillations in both vertical and horizontal axis of pipe cross-section downstream of the elbow are also observed.

A distribution parameter used in process of area-averaging to account for the distribution effects is defined as:

$$COV\langle AB\rangle = \frac{\langle AB\rangle}{\langle A\rangle\langle B\rangle} \tag{1-7}$$

Such that Eq. 1-7 reflects the degree of peaking in the process of averaging two-phase flow parameters.

The mechanistic models for random collision (RC) and turbulent impact (TI) applied in this study are same as that employed in vertical two-phase flow. The wake entrainment (WE) term has not been included since, no model exists for WE in horizontal flows and the relative velocity between the bubbles is negligent. The RC and TI coefficients in the current model are determined based in the data by carefully selecting flow conditions and identifying the dominant mechanism. Fig. 1-4 shows the model evaluation results for the 90-degree and 45-degree elbow.

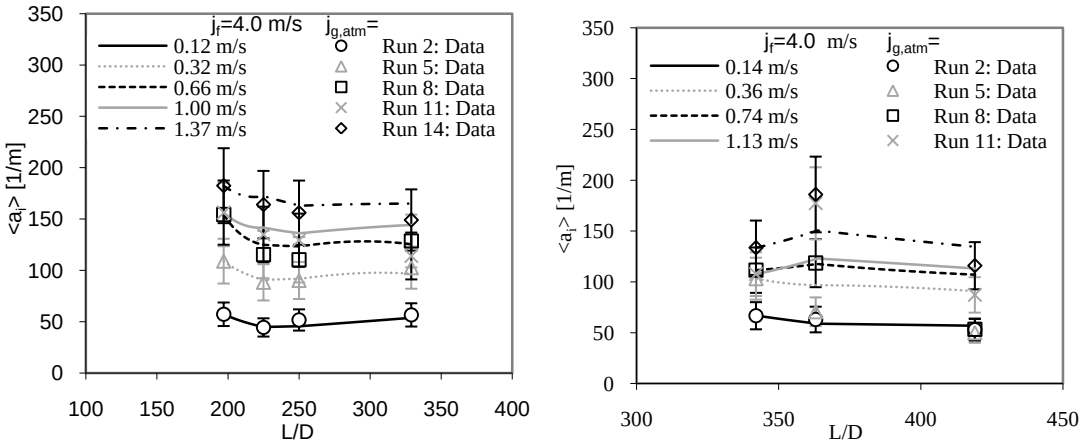

a. 90-degree experiment b. 45-degree experiment

Figure **1-4**: 90-degree and 45-degree model evaluation results. Error bars shown: ±20%, Talley et al. (2009)

It is found that the velocity gradient (VG), RC and pressure drop (PD) are the dominant mechanisms in lower void fraction conditions. At higher void fraction conditions, for the 90-degree experiment, the TI, PD and RC becomes dominant, while for the 45-degree experiment the

TI and PD mechanisms are alone dominant. The model is benchmarked against 105 data points acquired by a double-sensor conductivity probe in 15 different flow conditions for each experiment. Overall, the model predicts the data well with an average error of ±20%.

1.3 Two-phase pressure drop correlation across the elbow

Two-phase pressure drop is one of the most fundamental design parameters closely related to the performance of two-phase flow systems. The two-phase pressure drop through the straight pipes of any configuration (vertical or horizontal) can be predicted using the conventional Lockhart –Martinelli approach. There have been a number of studies on pressure drop in various two-phase flow configurations (Kim et al., 2007; Salcudean et al., 1982 & 1988; Spedding et al., 2007). Chenoweth and Martin (1955) showed that the two-phase pressure drop across the bends is higher than for the single phase flow, but it can be correlated using the Lockhart-Martinelli model, originally developed for the straight pipes. Spedding and Benard (2004) reported the pressure data for two-phase flow through a 90-degree vertical elbow connecting a vertical to horizontal pipe. They presented a general correlation for the elbow pressure drop in terms of total Reynolds number and used Lockhart-Martinelli model to predict the data. Kim et al. (2008) presented the two- phase flow data for air-water flow through a 90-degree and 45-degree horizontal elbow. They developed a general correlation for the pressure drop across the flow restriction based on the conventional Lockhart-Martinelli model by addition of an extra term to account for the frictional pressure drop for the elbow as explained below:

For a straight pipe the two-phase frictional pressure drop can be expressed by the pressure drop caused by each phase and its combination as:

$$\left(\frac{dp}{dz}\right)_F^{2\emptyset} = \left(\frac{dp}{dz}\right)_F^{g} + \left(\frac{dp}{dz}\right)_F^{f} + C\left[\left(\frac{dp}{dz}\right)_F^{g}\left(\frac{dp}{dz}\right)_F^{f}\right]^{1/2} \quad (1\text{-}8)$$

Lockhart and Martinelli (1949) expressed the above correlation as:

$$\emptyset_f^2 = 1 + \frac{C}{X} + \frac{1}{X^2} \tag{1-9}$$

Where,

$$\emptyset_f^2 \equiv \frac{(\frac{dp}{dz})_F^{2\emptyset}}{(\frac{dp}{dz})_F^f} \quad \text{and} \quad X^2 \equiv \frac{(\frac{dp}{dz})_F^f}{(\frac{dp}{dz})_F^g} \tag{1-10}$$

In the above equations, superscripts f, g and 2Ø are the phase indices for liquid, gas and two-phase mixture, respectively, and the subscript F indicates the frictional loss,

The pressure drop due to the k^{th} phase can be obtained via the following correlation using the friction factor *f*:

$$\left(\frac{dp}{dz}\right)_F^k = \frac{2f}{D}\rho_k j_k^2 \tag{1-11}$$

where, k = f or g

The friction factor used in the above equation can be obtained from the Blasius [ ]

$$f = m\,Re^{-n} \text{ , where } Re = \frac{\rho_k j_k D}{\mu_k} \tag{1-12}$$

The above correlation can only be used for a straight pipe flow without the flow restriction. To account for the minor losses in the pressure due to the flow restriction, Kim et al. (2008) developed a new correlation analogous to that of Lockhart and Martinelli as:

$$\emptyset_f^2 = \left[1 + \frac{1}{X_M^2}\right] + \left[1 + \frac{1}{X_M^2}\right]^{1/2} \frac{C}{X} + \frac{1}{X^2} \tag{1-13}$$

where, $\quad X_M^2 \equiv \frac{(\frac{dp}{dz})_F^f}{(\frac{dp}{dz})_{FM}^g}$

The new parameter X_M^2 represents the losses occurring due to the flow restriction and the minor loss factor k can be obtained by rewriting the new parameter X_M^2 in Eq. (1-13) as:

$$X_M^2 = 4\left(\frac{f}{k}\right)\left(\frac{L}{D}\right)_{Restriction} \quad (1\text{-}14)$$

Where $\left(\frac{L}{D}\right)_{Restriction}$ and f are specified by the restriction geometry and Eq. (1-12), respectively. This newly developed correlation matches well with the experimental data with C=65 and the k factors of k=0.58 and k=0.35, for the 90 and 45-degree elbows, respectively. The significantly higher value of C=65 compared to the conventional value of C=20 signifies the geometric effects of elbows on the two-phase frictional pressure loss. This present correlation predicts the data very well for both the 90 and 45-degree elbow cases with average percent difference of ±2.1% and ±1.3%, respectively.

1.4 Classification of flow patterns

To analyze the two-phase flow at a basic level, it is necessary to classify different patterns of phase distribution that are specifically similar for different pipe sizes and fluid properties. Traditionally different flow patterns or the regimes have been described based on the experimental observations. The objective of the flow pattern classification is to characterize the flow conditions or situations where the phase distribution are spatially similar, so that one can calculate where the phases are located as functions of space and/or time. Based on the review of the research results on two-phase flow pattern classification provided by Rouhani and Sohal (1982), following section describes the simplest set of flow patterns.

1.4.1 Vertical Upward Two-Phase Flow

Fig 1-5 shows the different flow patterns or flow regimes observed in vertical upward two-phase flow.

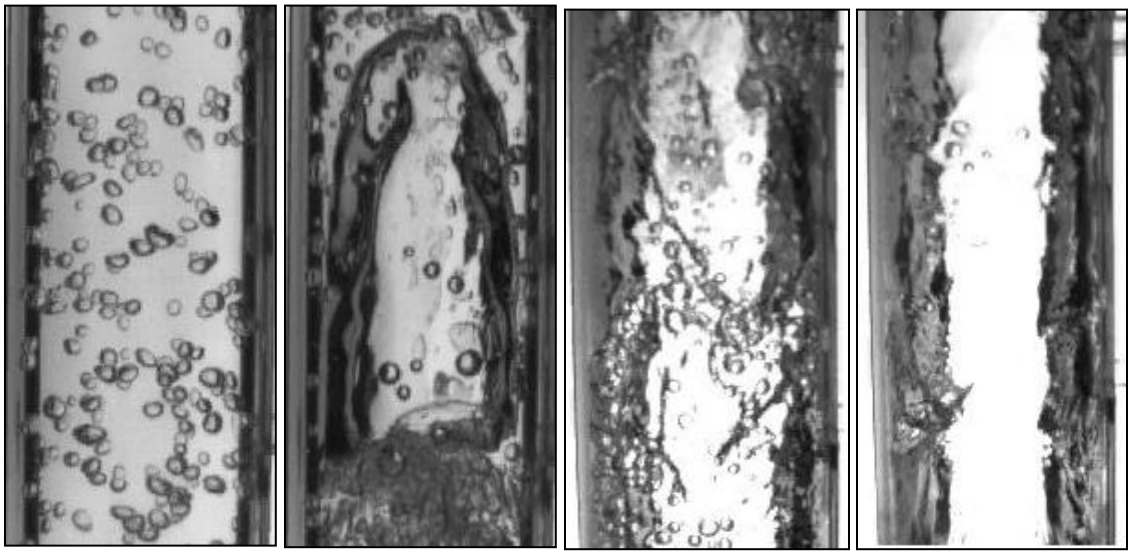

Bubbly Slug Churn Turbulent Annular

Figure **1-5**: Different flow regimes observed in a vertical upward two-phase flow

Bubbly Flow

In the bubbly flow the gas phase is distributed more or less uniformly in form of discrete bubbles in a continuous liquid phase. The bubbles are generally close to spherical shape, but it also includes the distorted bubbles and small cap bubbles. Bubbly flow usually occurs at low void fraction conditions ranging upto 30% (Ishii and Mishima, 1980).

Slug flow

As the gas flow rate is increased keeping the liquid flow rate constant slug flow is encountered. In the slug flow pattern, the gas flows largely in form of "Taylor bubbles" which have diameter equal to the pipe diameter and can vary in length from the pipe diameter to over a hundred diameters. Successive Taylor bubbles are separated by slugs of continuous liquid which

bridge the pipe and contain dispersed gas bubbles. Between the Taylor bubble and the pipe wall, the liquid flows in the form of a thin falling film.

Churn turbulent flow

Increasing the gas flow rate further, keeping the liquid flow constant leads the transition from slug to churn. Churn flow is similar to the slug flow; however it is much more chaotic, frothy and disordered. The Taylor bubble becomes narrow and its shape is distorted. The liquid slug between the successive Taylor bubbles is continuously destroyed by the high local gas concentration (which is highly turbulent). As this happens the liquid from the slug falls, it accumulates again to form a bridge, and is again lifted by the gas. Typical churn flow is oscillatory or alternating direction of motion of a liquid.

Annular/annular mist flow

Annular flow is achieved by increasing the gas flow rate further. Annular flow is characterized by the continuity of the gas phase in the core. Liquid flows upward, both as a thin film and as droplets dispersed in the gas. Except at the highest flow rates, the liquid appears to flow as large fast moving lumps that are intermittent in nature- either large roll waves traveling over the film or a high local concentration of droplets.

1.4.2 Horizontal Two-Phase Flow

Fig 1-6 shows the different flow patterns or flow regimes observed in vertical upward two-phase flow.

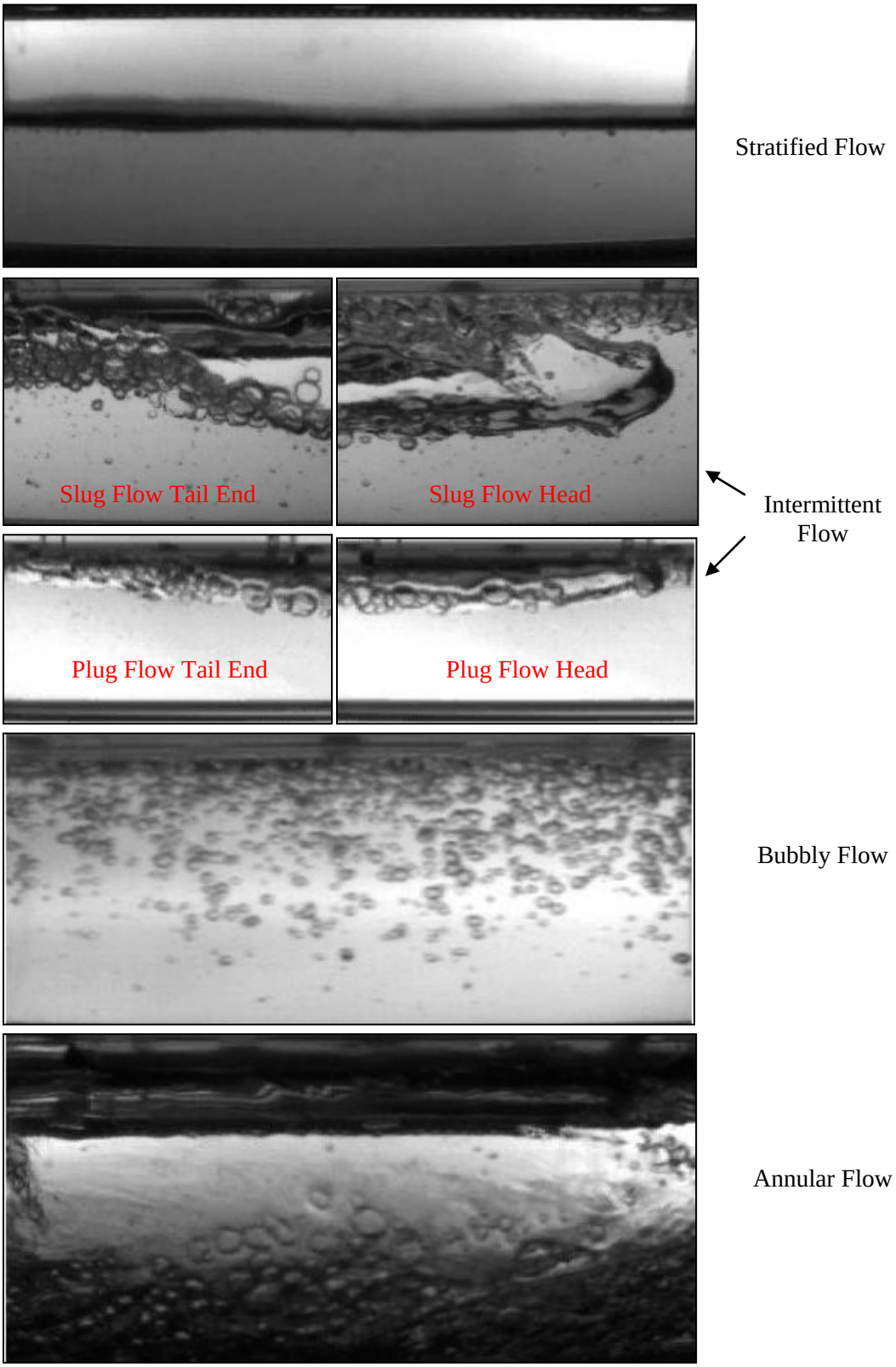

Figure **1-6**: Different flow regimes observed in concurrent horizontal two-phase flow

Stratified flow

In stratified flow, the liquid flows along the bottom of the pipe with the gas flowing on top. Both the phases are continuous in the axial direction. Two sub-patterns are defined as: stratified smooth and stratified wavy.

Intermittent flow

In the intermittent flow pattern, the liquid in the pipe is distributed non-uniformly in the axial direction. Plugs or slugs of liquid, which fill the pipe, are separated by gas zones that overlay a stratified liquid layer flowing along the bottom of the pipe. In the slug flow, the liquid is aerated with small bubbles that are concentrated towards the front of the liquid slug and top of the pipe. The intermittent pattern is subdivided into slug or plug (elongated bubble). Elongated bubbly is the flow pattern when the liquid slug is free of the dispersed bubbles. The flow at any cross-section is highly intermittent. As the liquid slug passes, there exists a high liquid rate and a low gas flow rate. However when the gas bubble passes, there is a high gas flow rate and low liquid rate.

Annular flow

With an increase in the gas flow rate alone and keeping constant low liquid flow rate the annular flow condition is achieved. In this case the gas flows in the core of the pipe occupying the maximum region and the liquid flows as a thin layer in the annular region and as dispersed droplets in the gas core. In some cases the liquid film may also entrain some small bubbles.

Dispersed bubbly flow

Dispersed bubbly flow occurs at relatively high liquid flow rates and small gas flow rates. In this condition the liquid phase is continuous and the gas phase is dispersed in form of scattered bubbles.

1.5 Identification of flow patterns

The problem of flow regime identification, or determining which pattern actually exists, is complicated by two facts (a) certain flow pattern descriptions contain arbitrary elements and (b) transition between some flow-pattern pairs is a gradual process, and there is difficulty in defining the boundary. Thus by the very nature of the problem, there is a little point in attempting to make fine distinctions. With this reservation, however, it is possible to describe a variety of methods that have proven useful. Most are based in one way or another in observing the time, amplitude and positional variation of voids.

Visual methods

Visual method is the simplest method for detecting the flow pattern. At flow rates low enough to make an observation possible, it is done by focusing on an element of liquid or gas and allowing the line of sight to move with the velocity of the element and then scanning the length of the pipe. This is usually performed for the transparent liquid flowing in the transparent test section. At high flow rates photographic methods are useful, as demonstrated by Raissan (1965), Hsu and Graham (1963), Bergles and Suo (1966), and Hewitt and Roberts (1969). Most photographic methods are limited by the size of the field of view, usually no more than several diameters long, so that only instantaneous local behavior can be observed. This restricts the

observation of the axial voids, which are important to the characterization. However, with the advancements in the photographic techniques, high speed movie cameras have been successful in characterization of the high flow rate conditions. A high speed movie is captured at different axial locations and is analyzed either visually or using an image analysis software. This method not only proves to be highly useful in flow pattern characterization but also in revealing the structure of the flow in detail and modeling the transition conditions.

Methods based on pressure measurements

Flow pattern maps based on visual observations have been suggested by many researchers. Since, the visual observations are subjective to each observer there is an inconsistency among these maps. Methods based on the pressure measurement are an objective way to classify and construct flow regime maps. This technique involves statistical analysis of the pressure fluctuations to obtain different flow regimes. Early attempts in this direction were made by Hubbard and Dukler (1966) by using the power spectral density analysis of their recorded measurements of wall pressure fluctuations, for various flow regimes in horizontal two-phase flow and showed that there is a clear relationship between the observed flow patterns and normalized power spectral density (PSD) distribution as a function of frequency. Wiesman et al. (1979) attempted to extend this method by extending the amplitude analysis into the characterization. They suggested specific number criteria on amplitude and frequency to characterize all the patterns, but this could not be generalized to all the systems and the specific number depends on the specific system being used in the experiment.

However, further elaboration on the use of PSD, reported by Albrecht et al. (1982), shows that this is a powerful means for indicating flow regime transition. Tutu (1982) developed a method for the vertical two-phase flow. Two pressure transducers attached on the wall and are

axially separated by a distance equal to pipe radius. The time variation of the pressure gradient is analyzed for probability density distribution. In vertical flows the average pressure drop is mostly gravitational, that is, for bubbly flow, the pressure gradient will fluctuate about $\rho_L(1-\alpha)g$, while for annular flow it will fluctuate about $\rho_G g$. Hence, for two fluids of highly different densities this method can be applied to characterize different flow regimes.

.

Methods based on photon attenuation

This method is has applications in providing direct measurement and view of flow pattern inside metallic channels. Jones and Zuber (1975) used a fast response linearized X-ray void measurement system in a rectangular channel with vertical configuration. The time-varying signal was subjected to probability density analysis, and characteristic PDF curves were shown to exist for bubbly, annular and slug flow patterns. For the horizontal flow, the method can be applied by positioning the beam vertically. Then the slug flow could be characterized by a bimodal density distribution, annular-dispersed flow by a broad single peak with its maximum at low voids, and the stratified pattern by the narrow peaks at intermediate voids. The existence of smooth stratified flow can be detected by the degree of spread of the PDF around its peak value. The limitation of the method is largely based on its high cost and need for careful installation and operation to ensure the safety of the personal.

Methods based on electrical conductivity

Measurement of change in conductivity is one of the ways to discern flow patterns in electrically conductive liquids. A conductance probe technique was applied by Solomon (1962),

and Griffith (1964) using a single sensor conductivity probe. Fiori and Bergles (1966) and Bergles et al. (1976) used a central single sensor conductivity probe to detect differences among bubbly, slug and annular flows. Barnea et al. (1980) suggested an improved conductivity probe technique using multiple probe modification that appears to be able to discriminate in a more diagnostic way between the various patterns.

The basic design and arrangement of the probes for application to horizontal and inclined flows where asymmetries are expected consists of three set of probes to detect different flow patterns. Probe A consists of two sensors flush mounted on the opposite walls and helps in detection of thin film as in an annular flow. Probe B consists of a sensor which is insulated throughout except for the very tip, which is conductive. This helps in the detection of bubbles by interpretation of the voltage reading across the resistor R_B. Probe C consists of a pair of sensors of which one sensor is an uninsulated needle while the other is a flush mounted electrode. This probe detects the condition for stratified flow.

Measurement techniques

Void fraction and interfacial area concentration are among the most important geometric parameters in two-phase flow systems. Void fraction represents the distribution of the gas phase in a two-phase mixture and is important in view of hydrodynamics and heat transfer. The interfacial area concentration is directly related to the interfacial transport of mass, momentum and energy. Various techniques have been employed for measurement of these parameters. Among these, the popular measurement techniques are – chemical absorption technique, optical methods such as light attenuation method and photographic method and local conductivity probe technique.

The chemical absorption method has been one of the widely used techniques in measuring the interfacial area and void fraction in industrial gas-liquid systems and chemical engineering field. The chemical methods are based on the study of a reaction of known kinetics in which the absorption rate is a function of the interfacial gas-liquid area. It uses pseudo-first order chemical reaction in conjunction with surface renewal theory in terms of chemical combinations and geometry of the system. The chemical methods are highly dependent on certain specific gas-liquid systems and knowledge of certain physicochemical properties. Moreover, the application of these methods is limited by the steady state flow without any phase change. It is also time consuming and a detailed local parameter cannot be obtained.

The light attenuation method and photography method are two of the popular optical methods for measurement of void fraction and interfacial area concentration. The light attenuation method can be used to acquire the area averaged parameters from the information on intensity of scattered light. These methods face the problem of reflection and refraction on the interface boundaries and hence are flow regime dependent. For the technique to be valid, multiple and forward light scattering should be negligibly small and the fraction of light scattered should be higher than 0.1 %.

The photographic method calculates the interfacial area by obtaining the mean particle diameter and void fraction of the dispersed phase. It involves the analysis of the image obtained from the two-phase mixtures. Similar to the light attenuation method, it requires flat and transparent flow duct and is only applicable to flows with low void fraction conditions. Moreover, this technique cannot be used to obtain detailed local information of the desired parameters.

The conductivity probe is used for the local measurement of void fraction and interfacial area concentration. Working of the conductivity probe is based on the differences in conductivity of air and water. There is a characteristic rise/fall of the impedance signals between the sensors

and the common ground as the bubbles pass through the exposed tips of the sensors. The most important feature of the conductivity probe is its ability to measure local interfacial velocity of the bubbles which helps in calculating the local time averaged interfacial area concentration.

Conductivity probe

The conductivity probe is one of the popular instrumentation for measuring local parameters. Working of the conductivity probe is based on the characteristic rise/fall in the signal when it is in a two phase mixture. Depending on whether the tip is in contact with gas or liquid, the circuit is open or closed, yielding a two-stage signal. Neal and Bankoff (1963) were the first ones to apply conductivity probe to two-phase flows, based on the fundamental differences in the conductivity between water and air. Local time averaged void fraction can be easily obtained by dividing the total time of residence of bubbles by the total time. The bubble interface velocity in a projected direction can be obtained by placing the sensors in particular direction. Furthermore, its capability to measure the interfacial area concentration makes it a widely used measurement technique in recent experimental studies Kataoka et al. (1986). Applications of the conductivity probe to measure local interfacial area concentration were made possible by the theoretical formulation by Kataoka et al. (1986). Wu and Ishii (1999) recently improved the two-sensor formulation through detailed analytical verification and numerical simulations. Currently, two types of conductivity probes are used based on the application range. The double sensor conductivity probe is used for the bubbly flow regime where the bubbles are assumed to be spherical in shape, and the four-sensor conductivity probe is used for the group-II bubbles which fall under distorted, cap, slug and churn-turbulent flow regimes.

Measurement principle

The measurement principle for local time-averaged interfacial area concentration, a_i, by multi-sensor conductivity probe is based on the definition given by Ishii (1975), where the local time-averaged $\bar{a}_i^t$ is defined by:

$$\bar{a}_i^t = \frac{1}{\Delta T}\sum_j \left(\frac{1}{|v_i . n_i|}\right)_j \tag{1-15}$$

where, j denotes the j^{th} interface which passes a local point during the time interval, ΔT. In the above formulation v_i and n_i are the bubble interfacial velocity and unit surface normal vector of the j^{th} interface, respectively. Eq. (1-15) implies that local interfacial area concentration can be obtained if the bubble interfacial velocity is known. Fig. 1-6 shows the general method to obtain velocity information from the signals obtained by sensors of a conductivity probe. In view of the Eq. (1-15), Kataoka et al. (1985) derived a mathematical method to determine the local time-averaged a_i for both double sensor and four sensor probes.

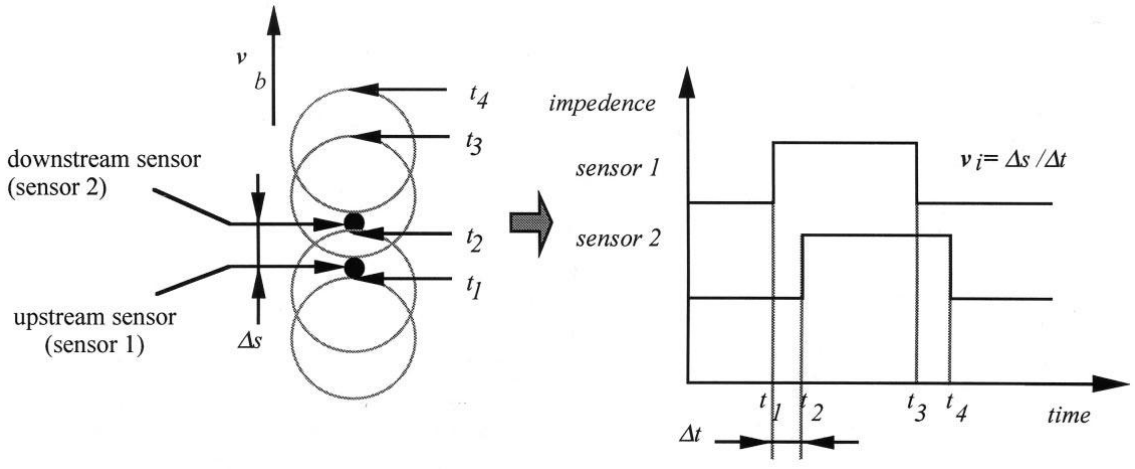

Figure **1-7**: Signals obtained by the sensors of a conductivity probe (Kim et al., 2000)

In practical two-phase flow systems involving flow patterns such as slug and churn-turbulent, the bubble interface is highly distorted and far from spherical. The application of four-

sensor conductivity probe becomes important in these flow conditions. The four-sensor conductivity probe can accurately determine the interfacial structure from three independent velocity components of the bubble interface without the limitation imposed by the bubble shape. Three independent downstream sensors of the four-sensor conductivity probe can be paired individually with the upstream sensor to form three pairs of double sensor probe, which then are used to obtain the three components of interfacial velocity. The equation for time-averaged $\bar{a}_i^t$ can then be simplified as:

$$\bar{a}_i^t = \frac{1}{\Delta T}\sum_j \left[\left(\frac{1}{v_{s1\,j}}\right)^2 + \left(\frac{1}{v_{s1\,j}}\right)^2 + \left(\frac{1}{v_{s1\,j}}\right)^2\right]^{1/2} \tag{1-16}$$

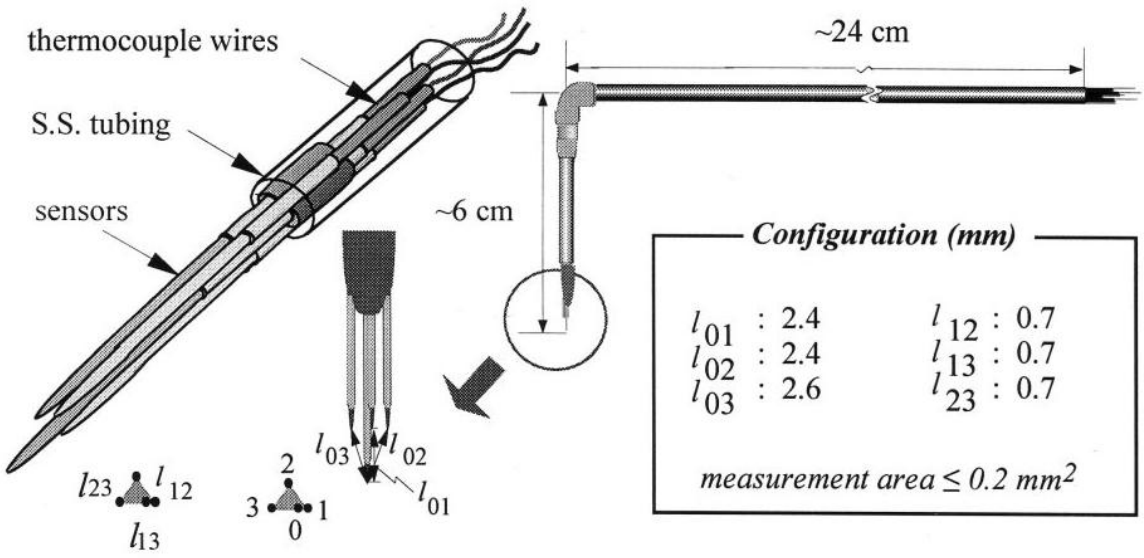

Figure **1-8**: A simple schematic of the four-sensor conductivity probe (Kim et al., 2000)

The following section provides brief description of the miniaturized four-sensor conductivity probe developed by Kim et al. (2000). This design is an improvement over the conventional four-sensor probe and addresses the limitations and shortcomings of the conventional design. The probe consists of four sensors made out of the stainless steel acupuncture needles. The needles are coated throughout with the dielectric coating except for the

tip, which is conducting. The sensors are arranged in specific configuration as shown in Fig 1-7. Since, the new design accommodates a built in double-sensor probe in a four-sensor configuration, it can be used over a wide range of two-phase flow conditions: from bubbly to churn turbulent conditions.

The signal processing scheme for this probe is structured in two-parts; namely signal conditioning and processing the signals to obtain the desired two-phase flow parameters. The signal conditioning involves moving median filtering process of the raw signals, normalization of the filtered signals, filtering noises through noise threshold, generation of step signals. After completion of the signal conditioning process, the signals are separated into spherical, distorted, cap, and Taylor bubbles based on the bubble chord information. This categorization allows one to study the transport phenomena of different types of bubbles independently. Three kinds of bubble signals are identified as signals that cannot be used to obtain local instantaneous interfacial velocity. The first kind occurs when a small spherical bubble misses one sensor of a double sensor probe. In this case only a single signal is registered and it is usually called '*missed*' or '*missing*' bubble signal. In bubbles with highly distorted surfaces, the signals due to the rear interfaces of the bubble registered by the common sensor may not precede the downstream sensors. With these kinds of signals, it is not possible to estimate the interfacial velocity and are called '*non-effective*' signals. The third kind occurs due to the very steep interface of the Taylor bubble near the wall. In such a case it is possible for one of the sensors to miss the interface. The signal processing scheme takes into account adequate measures based on the previous studies to account for all the three kinds of missing signals. Fig. 1-8 shows the three different kinds of signals which cannot be used to obtain local instantaneous interfacial velocity.

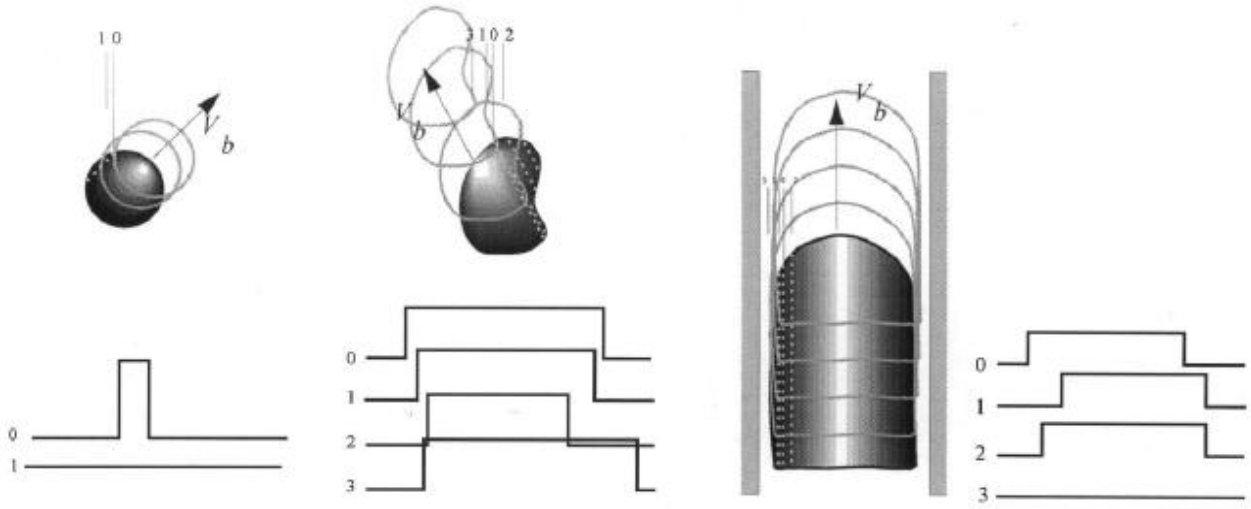

a) Missing Signals (Spherical Bubbles)

b) Non-effective Signals (Distorted Bubbles)

c) Missing Signals due to Steep Interface (Slug Bubbles)

Figure **1-9**: Examples of missing signals (Kim et al., 2000)

Chapter 2

Two-Phase Flow through 45 and 90-Degree Horizontal Elbows

2.1 Experimental Setup

A simplified schematic of the top view of the horizontal two-phase flow facility is shown in Fig.2-1. The experimental test facility is made out of 50.3 mm inner diameter glass pipes with the 90-degree and 45-degree elbows installed. Two separate experiments are conducted. The first experiment is performed with the 90-degree elbow only, and five measurement ports (P_{ref}, P1, P2 and P3) are used to acquire the data. A 45-degree elbow is then added to the existing facility and four measurement ports (P1, P5, P6 and P7) are used to acquire the data. The 90-degree and 45-degree elbows are located at the development lengths of 206.6 and 353.5 respectively from the inlet. The 90-degree elbow has a radius of curvature of 89 mm with L/D_{elbow} of approximately 6, while the 45-degree elbow has L/D_{elbow} of 4. The inset of Fig.2-1 shows the detailed dimensions of the elbows. In total, eight pressure taps are installed in the instrumentation ports along the test section, including one directly after the two-phase mixing chamber (P_{ref}), and are denoted in the figure as P1 through P7. The first measurement port, P1 (9.5 diameter upstream of the 90-degree elbow) is located at development length of 197 from P_{ref}, and the ports P2, P3, and P4 (ports downstream of the 90-degree elbow) are located at development lengths of 225, 250, and 329 from P_{ref}, respectively. The port P5 (10.5 diameter upstream of the 45-degree elbow) is located at development length of 342 from P_{ref}, and ports P6, and P7 (ports downstream of the 45-degree elbow) are located at development lengths of 363 and 419 from P_{ref}, respectively.

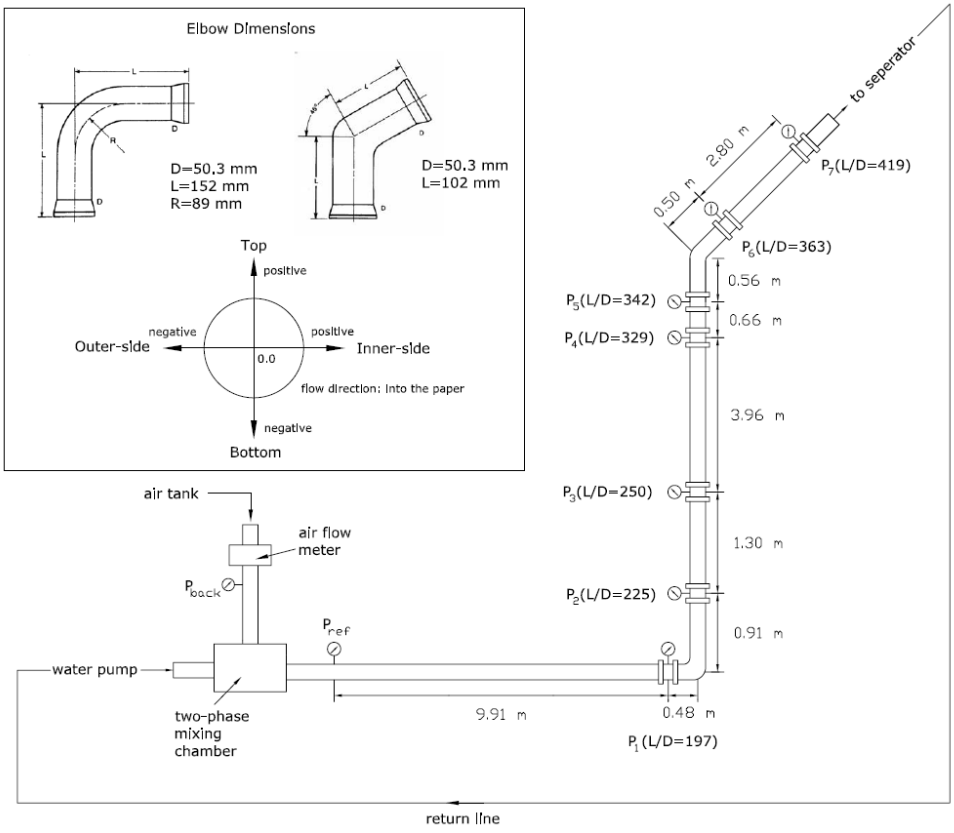

Figure **2-1**: A simple schematic of top view of the horizontal two-phase flow facility, Kim et al., 2008.

At each instrumentation port, local two-phase flow parameters are acquired by traversing the double-sensor conductivity probe. The measurement port is designed such that probe can be traversed and rotated in the radial and azimuthal directions of the pipe cross-section. The local parameters acquired by the probe include bubble frequency (f_b), bubble velocity (v_g), void fraction (α) and interfacial area concentration (a_i).

Accounting for the asymmetric distribution of bubbles in the horizontal two-phase flow, the local measurements are made across the entire pipe diameter. In the 90-degree experiment, at ports P1 and P4, a local probe is traversed only in the vertical direction along the pipe cross-section diameter (r/R_V), assuming the bubble distribution to be symmetric across the vertical axis.

At ports P2 and P3, on the other hand, the probe is traversed along both vertical and horizontal direction to capture the elbow effects caused by the 90-degree elbow. Similarly, for the 45-degree experiment, the local probe is traversed only in the vertical direction at ports P5 and P7, while at port P6 the probe is traversed along both the vertical and horizontal axis of the pipe cross-section. The inset of Fig.2-1 shows the measurement coordinate system used in the experiment. To identify the inner and outer sections (or curvatures) of the elbow, r/R=0 is chosen to be at the center of pipe cross-section. Then, a positive r/R denotes the inner or upper half of the horizontal and vertical pipe diameters, respectively. Similarly, a negative r/R indicates the outer or lower half of the horizontal and vertical pipe diameters, respectively.

A total of 15 different combinations of j_g and j_f are selected as test conditions for each elbow type, all within or near the bubbly flow regime according to the horizontal two-phase flow regime map suggested by Taitel and Dukler (1977). The flow conditions are denoted by runs 1-15 in the Table 2-1 and Table 2-2. Since the superficial gas velocity is a function of pressure, the gas flow rates to denote each run are calculated based on the atmospheric pressure condition.

Table **2-1**: Summary of the 15 different flow conditions for 90-degree elbow; $j_{g,atm}$ denotes the superficial gas velocity under atmospheric pressure condition.

	Run 1	Run 2	Run 3	Run 4	Run 5
$j_{g,atm}$ [m/s]	0.116	0.124	0.127	0.312	0.320
j_f [m/s]	3.762	4.051	4.335	3.765	4.047
	Run 6	Run 7	Run 8	Run 9	Run 10
$j_{g,atm}$ [m/s]	0.329	0.644	0.659	0.673	0.985
j_f [m/s]	4.338	3.772	4.048	4.338	3.764
	Run 11	Run 12	Run 13	Run 14	Run 15
$j_{g,atm}$ [m/s]	1.004	1.031	1.336	1.372	1.406
j_f [m/s]	4.049	4.313	3.760	4.051	4.332

Table **2-2**: Summary of the 15 different flow conditions for 45-degree elbow; $j_{g,atm}$ denotes the superficial gas velocity under atmospheric pressure condition.

	Run 1	Run 2	Run 3	Run 4	Run 5
$j_{g,atm}$ [m/s]	0.135	0.140	0.145	0.348	0.355
j_f [m/s]	3.755	4.042	4.340	3.778	4.045
	Run 6	Run 7	Run 8	Run 9	Run 10
$j_{g,atm}$ [m/s]	0.368	0.707	0.736	0.760	1.090
j_f [m/s]	4.342	3.760	4.050	4.341	3.767
	Run 11	Run 12	Run 13	Run 14	Run 15
$j_{g,atm}$ [m/s]	1.134	1.176	1.504	1.577	1.630
j_f [m/s]	4.042	4.342	3.769	4.042	4.340

The local two-phase flow parameters are averaged by:

$$\langle\psi\rangle = \frac{1}{A}\int \psi dA = \frac{1}{A}\sum_{i=1}^{N} \psi_i \Delta A_i \tag{2-1}$$

where ψ, A and ΔA_i are any two-phase flow parameters of interest, total flow area and i^{th} partial area segment, respectively. Accounting for the asymmetry of the flow in horizontal pipe through the elbow junction, two different measurement meshes are employed based on the measurement position and hence, two different methods are employed in defining ΔA_i based on the measurement orientation as shown in Fig. 2-2. Hence, for the data acquired along R_V, ΔA_i is defined by:

$$\Delta A_i = \frac{R_i^2}{2}(\theta_i - \theta_{i-1}) - R\left(h_i . sin\frac{\theta_i}{2} - h_{i-1} . sin\frac{\theta_{i-1}}{2}\right) \tag{2-2}$$

And for the data acquired along both the R_V and R_H, the ΔA_i is defined as:

$$\Delta A_i = \frac{\pi}{4}\left(h_i^2 - h_{i-1}^2\right) \tag{2-3}$$

where, R_V and R_H are the vertical and horizontal radii of the elbow cross-section, respectively. Therefore, Eq.2.2 is used to calculate the area-averaged parameters from the local data acquired at P1 and P4 for the 90-degree experiment and at ports P5 and P7 for the 45-degree experiment. Similarly, Eq.2.3 is used for the data obtained at ports P2 and P3 for the 90-degree experiment and at port P6 for the 45-degree experiment.

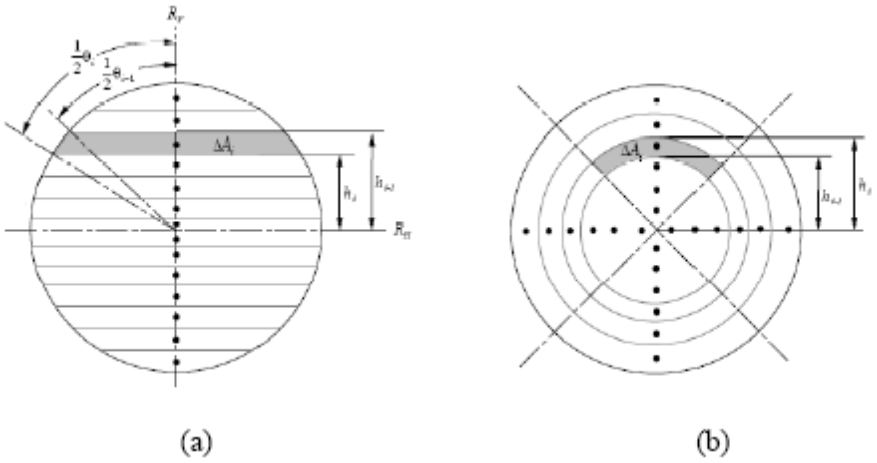

Figure **2-2**: The definition of ΔA_i in two area-averaging schemes. (a) For the data obtained along vertical radius, R_V (Ports P1, P4, P5, P7) (b) For the data obtained along both vertical, R_V and horizontal, R_H radii (Ports P2, P3 and P6).

2.1 Experimental Results and Data Analysis

In view of benchmarking the reliability of the probe measurements, the local superficial gas velocity at each measurement port measured by the flow meter along with the local gage pressure measurement is compared with that calculated based on the data acquired by the probe via:

$$\langle j_g \rangle_{loc} = \langle \alpha u_g \rangle_{loc} \tag{2.4}$$

The result is shown in Fig.2-3, and they are in relatively good agreement with each other within ±10% difference. The discrepancies at the higher flow rates can be attributed to the error

associated with the pressure measurement as well as the velocity measurement at the higher void fraction using the double-sensor conductivity probe. It is to be noted that one of the data points for the 90-degree experiment falls considerably outside the error bounds is not used for the data analysis.

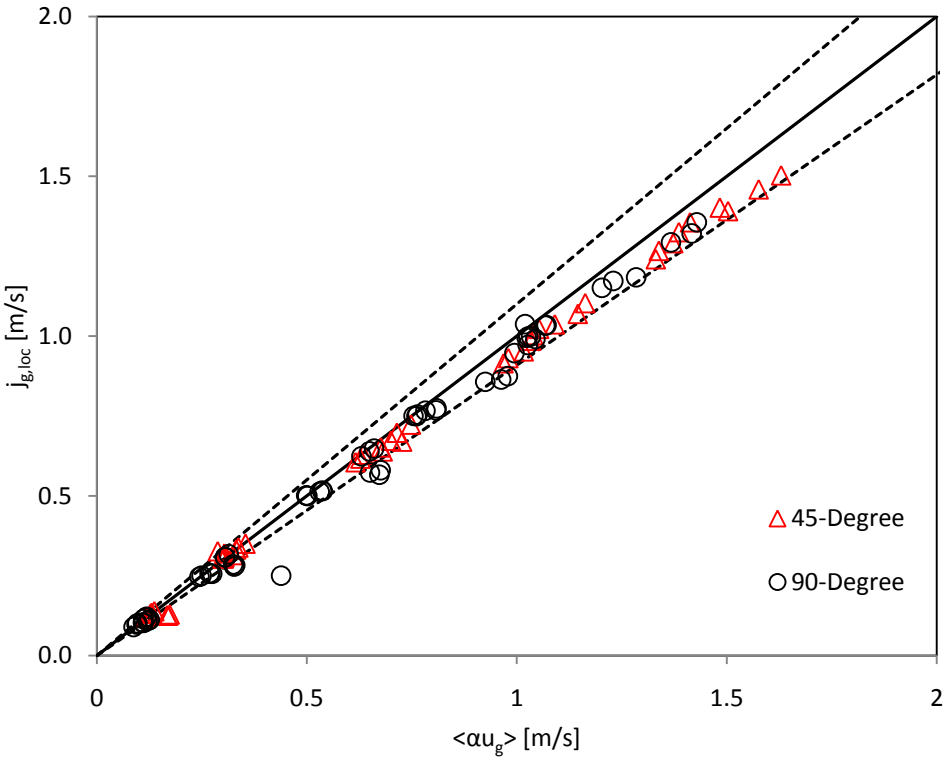

Figure **2-3**: Comparison of the local superficial gas velocity, $j_{g,loc}$, measured by the flow meter with $<\alpha u_g>$ acquired by the conductivity probe, dotted lines represent ±10%

2.2.1 Pressure drop

The local static pressure is acquired at five different axial positions for the 90-degree experiment (P_{ref}, P1, P2, P3 and P4) and four different axial positions for the 45-degree experiment (P1, P5, P6 and P7). In Fig. 2-4 the local static pressure is plotted with the

development length for both the experiments. Each Figure represents the change in pressure at a fixed liquid flow rate and varying gas flow rate. Characteristic geometric effects of the elbows on the pressure drop are clearly demonstrated in both experiments. In the 45-degree experiment effect of the elbow is characterized by an expected additional pressure drop across the elbow due to the two-phase minor loss. It is interesting to note, however, that in the 90-degree experiment there is little elbow effect seen at the measurement location immediately downstream of the elbow, i.e. L/D=225. The pressure drop due to the 90-degree elbow is more pronounced, but is observed further downstream of the elbow between L/D=225 and L/D=250. This indicates that the effect of 90-degree elbow is propagated further downstream of the elbow. It is speculated that this phenomena is due to the turbulent structures and secondary flow caused by the 90-degree elbow which is different from that of the 45-degree elbow. Kim et al. (2008) developed a new correlation to predict the two-phase pressure drop across both a 90-degree or 45-degree elbow based upon the traditional Lockhart-Martinelli formulation by including an addition term for minor loss. Their newly developed correlation matches the experimental data with coefficient, C = 65 and minor loss factors, k = 0.58 and k = 0.35 for 90-degree and 45-degree elbows, respectively. The higher value of the parameter C = 65 as compared to the conventional value C = 20 in Lockhart-Martinelli correlation signifies the geometric effect of elbows on two-phase pressure. The study of pressure drop is important with regard to the interfacial area transport equation, where the gradient of the pressure almost always occurs as one of the source terms.

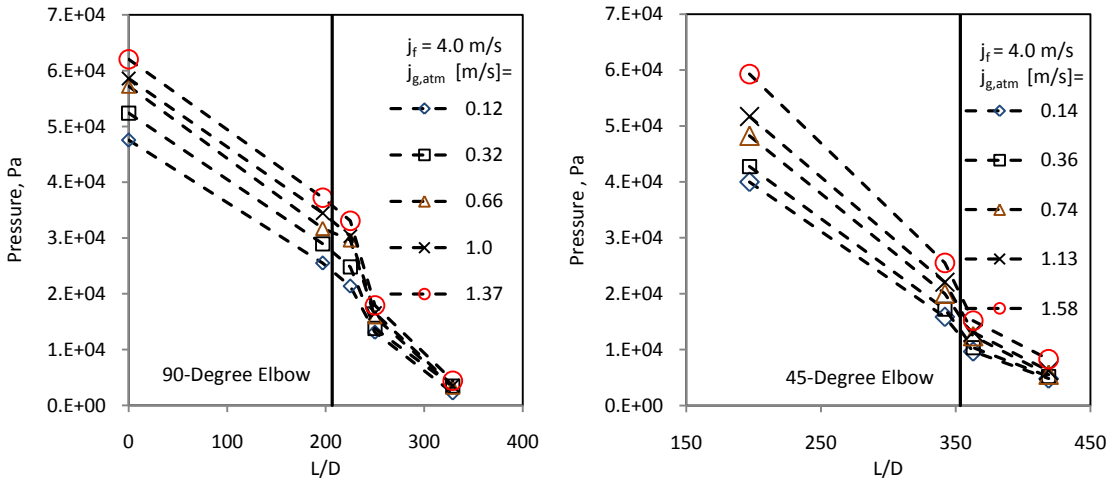

Figure **2-4**: Change in the local gage pressure measured along the axial direction of the flow (vertical line shows the position of the elbows)

2.2.2 Local interfacial structures

A comparison on the local profiles of α and a_i along the horizontal axis of the pipe cross-section for 90-degree and 45-degree elbows is presented in Fig. 2-5. As noted earlier, the local data is collected only along the vertical axis of the pipe cross-section at measurement ports P1, P4 for 90-degree experiment and ports P5 and P7 for the 45-degree experiment, assuming the bubble distribution to be symmetrical across the vertical axis. However, to capture the effect of the elbows, the local data is collected along both vertical and horizontal radii at ports P2 and P3 for the 90-degree case and at port P6 for the 45-degree case.

In Fig.2-5 local void fraction and interfacial area concentration are plotted along the horizontal axis of the pipe cross-section at measurement locations immediately downstream of the 90-degree and 45-degree elbows for $j_{g,atm}$ = 0.124 m/s and j_f = 4.3 m/s. It is important to mention here that the bubble distribution is dependent on the gas and liquid flow rates and hence, the results can only be generalized for a limited range of flow conditions. The 45-degree elbow causes the bubbles to migrate to the inner half of the pipe cross-section and hence peaking of the

void fraction profile is observed around $r/R_H = 0.5$. As seen from the figures α and a_i show similar trends. Although the 90-degree elbow shows a similar effect, the degree of peaking is significantly smaller compared to the 45-degree. This shows that the elbows cause significant oscillations in the local profiles. Furthermore, the degree and the position of peak in the local profiles are dependent on the gas and the liquid flow rate, as discussed later.

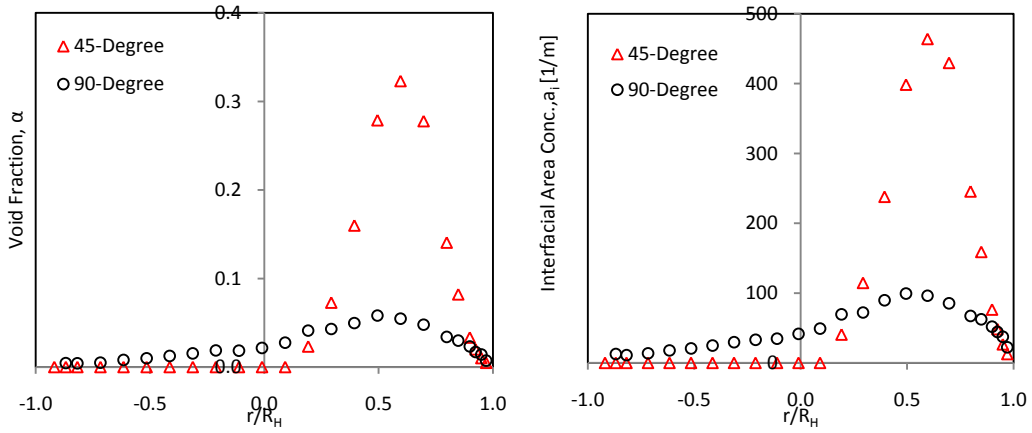

Figure **2-5**: Comparison of local horizontal α and a_i profiles for 45-degree and 90-degree elbows at $j_{g,atm}$= 0.124 m/s; j_f=4.3 m/s

Fig.2-6 shows the effect of the increasing gas flow rate on the local profiles of α and a_i along the horizontal axis of the pipe cross-section, immediately downstream of the elbows. Here, void fraction and interfacial area concentration are plotted along the horizontal radius for three different gas flow rates and a constant liquid flow rate of j_f = 4.0 m/s. In general, for both the elbows increasing the gas flow rate causes the movement of the bubbles from the inner half to the outer half of the pipe cross-section. However, there is a significant difference in the nature of oscillation and location of peak induced by the two elbows. Although, there is a movement of the gas phase to the outer half of the pipe cross-section, for the 45-degree case the peaking of the local profiles always occurs in the inner half of the pipe cross-section, except for Run-9 ($j_{g,atm}$=0.76 & j_f = 4.3 m/s) where the peak shifts to the outer half ($r/R_H \approx -0.5$). On the other hand,

for the 90-degree case the position of the peak shifts to the outer half of the pipe cross-section and as well as the degree of peaking becomes more pronounced with increasing gas flow rate.

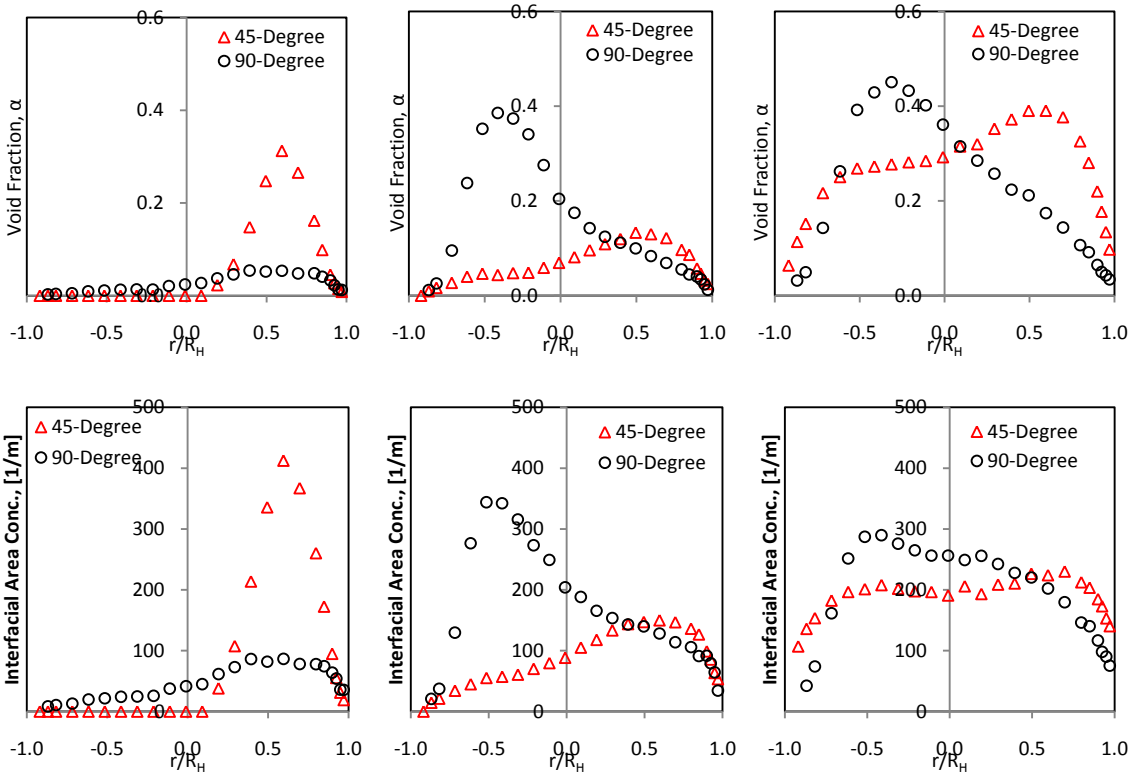

a) $j_{g,atm}$ = 0.124 m/s
Re_g = 413

b) $j_{g,atm}$ = 0.7 m/s
Re_g = 2330

c) $j_{g,atm}$ = 1.3 m/s
Re_g = 4327

Figure **2-6**: Comparison of local horizontal α and a_i profiles for 45-degree and 90-degree elbows for different gas flow rates and constant j_f=4.0 m/s

It is interesting to note that further downstream of the 90-degree elbow, at measurement port P3, L/D =250 from the inlet, the local profiles of α and a_i demonstrate behavior very similar to the profiles at measurement location immediately downstream of the 45-degree elbow. It is shown throughout in this study that this phenomenon is very characteristic of the 90-degree elbow wherein, the elbow effect is propagated and becomes more pronounced further downstream of the elbow. Fig.2-6 shows the effect of the gas flow rate at measurement port P3 (L/D=250) for the 90-degree case.

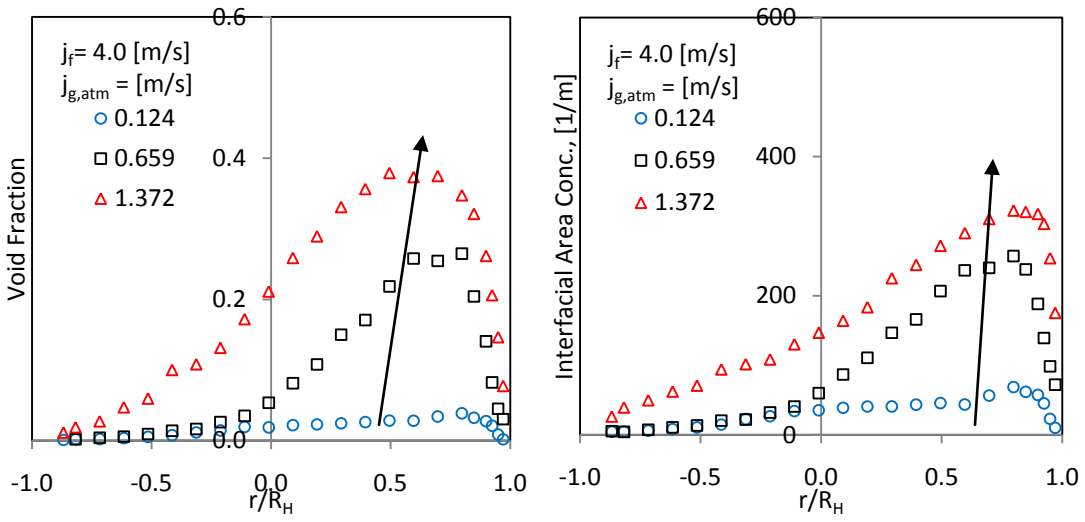

Figure **2-7**: Local horizontal α and a_i profiles for the 90-degree elbow for different gas flow rates and constant j_f=4.0 m/s at L/D=250

The liquid flow rate has a very little effect on local profiles of α and a_i for both the elbows. The position of peak remains almost unchanged however, the degree of peaking becomes more pronounced with increasing liquid flow rates. Comprehensive results for all the flow conditions can be found in appendix –A1.

A comparison of the local profiles of α and a_i along the vertical axis of the pipe cross-section for different development lengths is shown in Fig.2-8. At measurement locations upstream of the elbows, the dominant buoyancy force on the gas phase causes the bubbles to remain in the top half of the pipe cross-section and hence, the peak in α and a_i profiles is observed around $0.5<r/R_V<1$. The elbow effect is clearly observed at measurement locations immediately downstream of the elbows. As noted earlier, the elbow effect is highly dependent on the gas and liquid flow rates. It can be seen from the plots that both the elbows cause the displacement of the gas phase to the lower half of the pipe cross-section. A comparison on the similar scale shows that the 45-degree elbow causes a greater degree of peaking than the 90-degree elbow. Also, the position of the peak is lower for the 45-degree case (r/R_V= -0.5) compared to that of the 90-

degree case (r/R_V= - 0.25). A lower than expected value in the a_i profile for 45-degree case indicates that the elbow causes bubble coalescence.

As the flow develops, at the measurement locations further downstream of the elbows, L/D=250 for the 90 degree elbow and L/D=419 for the 45-degree elbow, the void fraction almost recovers its original profile. However, it can be seen that the a_i profile is not fully restored. This shows that the elbows promote bubble interaction mechanisms.

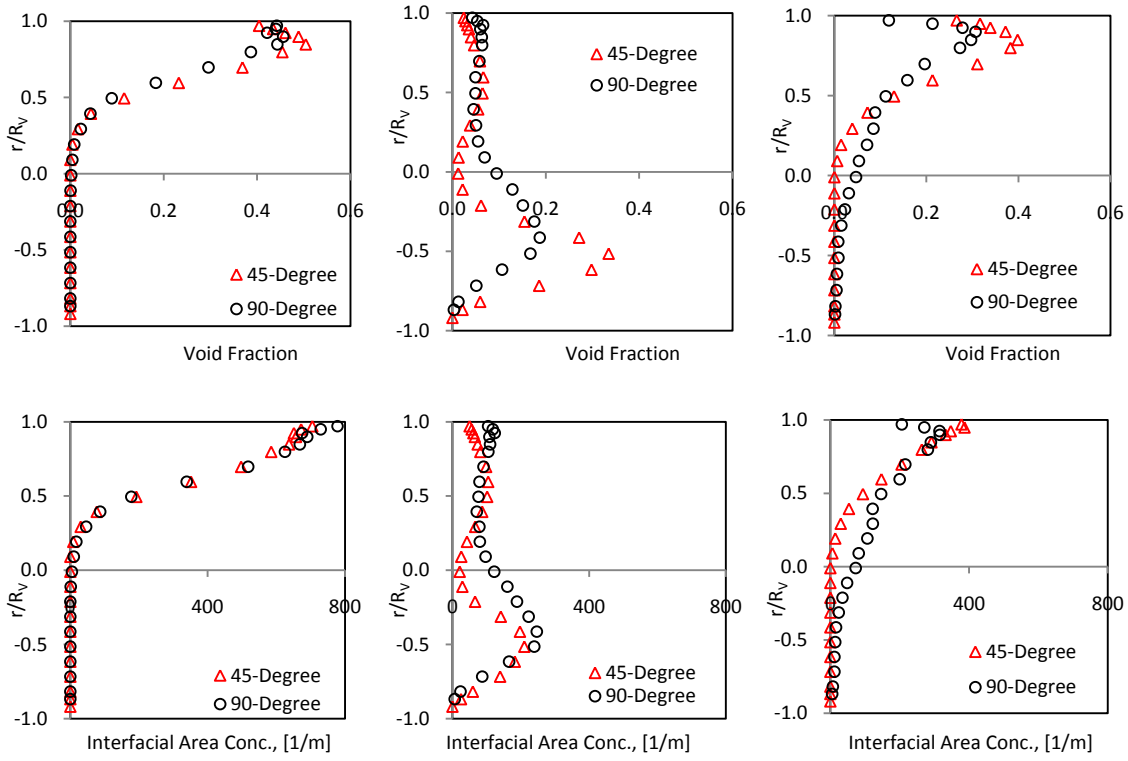

a) $L/D_{90\text{-degree}}$ = 119, $L/D_{45\text{-degree}}$ = 342

b) $L/D_{90\text{-degree}}$ = 225, $L/D_{45\text{-degree}}$ = 463

c) $L/D_{90\text{-degree}}$ = 250, $L/D_{45\text{-degree}}$ = 419

Figure **2-8**: Comparison of the local vertical α and a_i profiles for the 45-degree and 90-degree elbows at different development lengths for $j_{g,atm}$ = 0.320 m/s & j_f=4.0 m/s

Comparison of the effect of gas flow rates on the profiles of α and a_i along the vertical radius of the pipe cross-section is presented in Fig.2-8. As noted earlier, at measurement location

immediately downstream of the elbow for the 45-degree case, the elbow causes the downward movement of the bubbles. This causes a peak in the local profiles of α and a_i in the lower half of the pipe cross-section. With increase in the gas flow rates, the bubbles tend to move to the upper half of the pipe cross-section without causing much change in the position of peak.

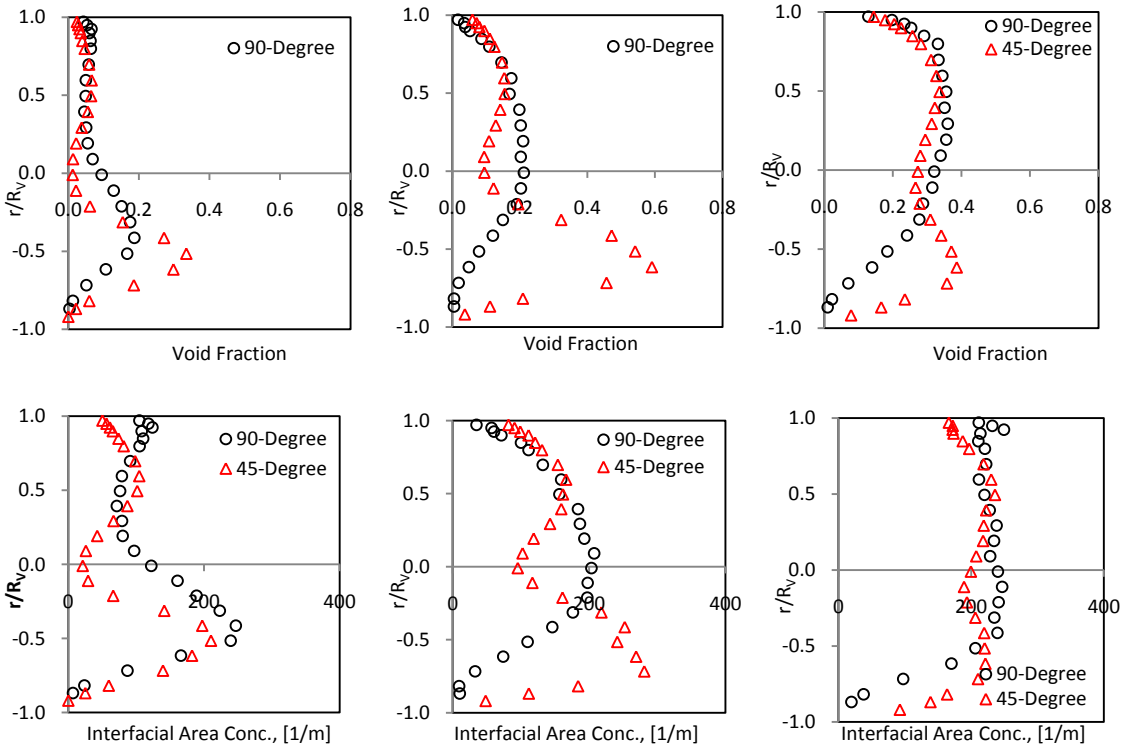

a) $j_{g,atm}$ = 0.3 m/s
Re_g = 999

b) $j_{g,atm}$ = 0.7 m/s
Re_g = 2330

c) $j_{g,atm}$ = 1.3 m/s
Re_g = 4327

Figure **2-9**: Comparison of the local vertical α and a_i profiles for the 45-degree and 90-degree elbows at different gas flow rates and constant j_f=4.0 m/s

Similar to the 45-degree case, the 90-degree elbow causes the bubbles to move to the lower half of the pipe cross-section and hence the peak in the profile occurs near the centre of the lower half (r/R_V = -0.5). However, with an increase in the gas flow rate up to $j_{g,atm}$ = 0.7 m/s, the bubbles start migrating towards the upper half of the pipe cross-section and the profile spreads out along the vertical radius causing the peak to occur around the centre of the pipe cross-section

($r/R_V = 0$). With further increase in the gas flow rate, the buoyancy force again becomes dominant, countering the elbow effect, and hence the local profiles peak in the upper half of the pipe cross-section, around $r/R_V = 0.5$.

Similar to the local profiles along horizontal axis, increase in the water flow rate has a very little effect on the local profiles along the vertical axis. Although, the general distribution of the gas phase and the position of the peak remain almost constant, the degree of peaking becomes more pronounced with an increase in water flow rate.

2.2.3 One-dimensional transport of interfacial structures

In view of comparing the one dimensional transport of interfacial structures across the two elbows, area averaged void fraction, $<\alpha>$ and area averaged interfacial area concentration, $<a_i>$ are plotted with the development length. It is found that the one-dimensional transport of interfacial structures is dependent on the gas flow rates and Fig.2-10 shows its comparison for two typical flow conditions. In order to make the comparison consistent, the measurement ports right before each elbow is been chosen as reference and all the development lengths are calculated based on the respective reference point.

At lower gas flow rates, for the 90-degree experiment, there is an overall increase in $<\alpha>$, while the overall decrease in $<a_i>$ across the elbow. Further downstream of the elbow, $<a_i>$ starts to recover while $<\alpha>$ remains almost constant. This shows that the elbow promotes the bubble coalescence but, further downstream of the elbows as the flow develops disintegration of the bubbles dominates. The one dimensional transport of $<\alpha>$ and $<a_i>$ in the 45-degree experiment is similar to the 90-degree case with an exception that the coalescence of bubbles dominates at all locations.

At higher gas flow conditions ($j_{g,atm}$ = 1.3 m/s), for the 90-degree case there is an overall increase in $<\alpha>$ and decrease in $<a_i>$ along the axial direction. This is characteristic of the coalescence phenomena, which dominates the flow for higher gas flow rates. However, the 45-degree elbow promotes bubble disintegration. The area averaged void fraction, $<\alpha>$ remains almost uniform across the elbow, while there is an increase in the area averaged interfacial area concentration, $<a_i>$. Moving further downstream of the 45-degree elbow there is a significant drop in overall $<a_i>$. This signifies that at higher gas flow rates disintegration process dominates across the elbow, but further downstream the elbow promotes coalescence.

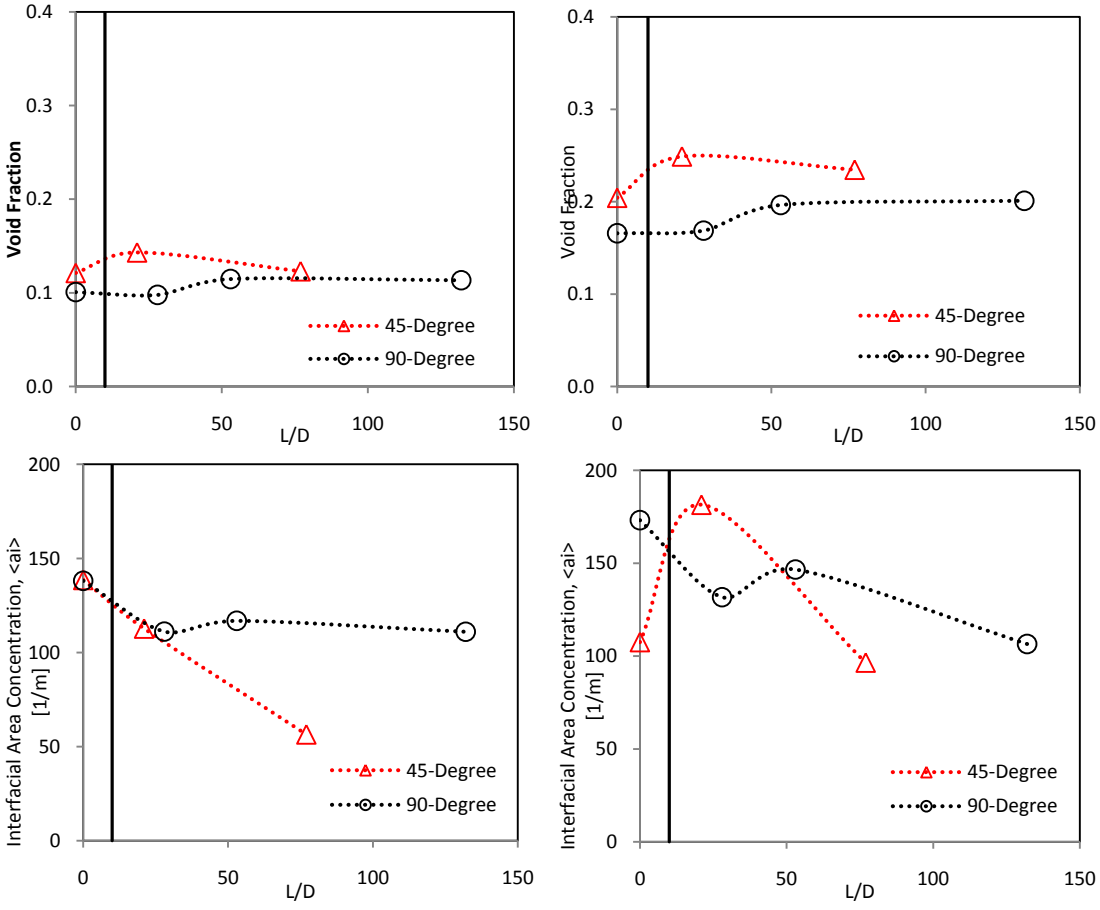

a) $j_{g,atm}$=0.7 m/s b) $j_{g,atm}$=1.3 m/s

Figure **2-10**: Comparison of the one-dimensional transport of $<\alpha>$ and $<a_i>$ across the elbows for two characteristic flow conditions with constant j_f=4.3 m/s

2.2.4 Void-weighted bubble velocity

Another characteristic effect induced by the elbows is the change in the bubble velocity along the flow direction. The bubble velocity across the elbow is dependent on the gas flow rate. The void-weighted gas velocity at two characteristic flow conditions across 90-degree and 45-degree elbows is plotted in Fig.2-11. For both the plots, liquid flow rate is kept constant while the gas flow rate is changed. The development length is defined similar to the previous section. In general both the elbows have similar effect on the bubble velocity, which is void fraction dependent as discussed below.

At the lower gas flow rates, the bubbles tend to accelerate as they move across the elbow. Moving further downstream, the elbow effect starts to dampen and the bubbles regain their original velocities. It is speculated that at lower void fraction conditions, the gas phase is entrained along with the liquid, across the elbow and hence the velocity increases due to convective acceleration.

However, at higher void fraction conditions, the bubbles tend to decelerate across the elbows. Moving further downstream, the elbow effect dampens out and bubbles regain their original velocities. At higher void fraction conditions, the gas phase gets accumulated in the elbow and hence causing a decrease in the bubble velocity. In general both the elbows induce oscillations in the void weighted bubble velocity but, the degree of oscillation is higher in the 90-degree case.

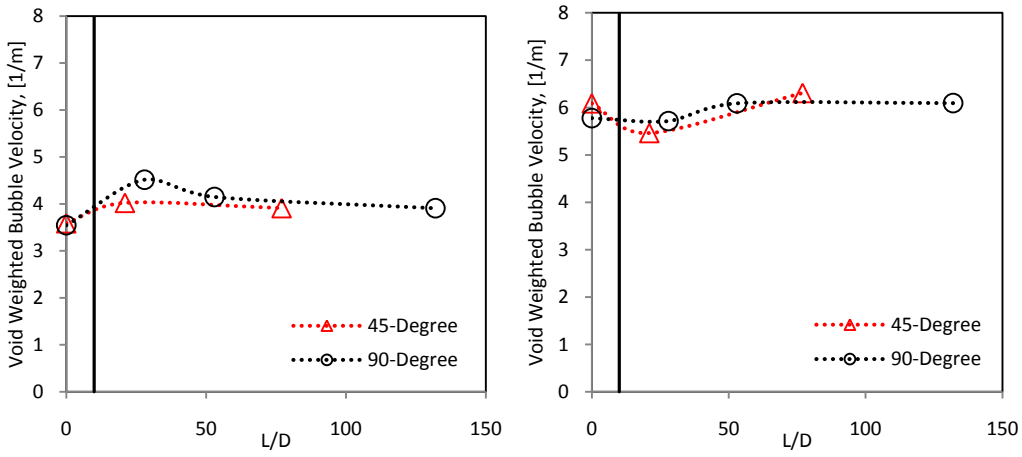

a) $j_{g,atm}$=0.13 m/s b) $j_{g,atm}$=1.3 m/s

Figure **2-11**: Axial development of one dimensional void weighted bubble velocity in two characteristic flow conditions at constant j_f=4.0 m/s

Chapter 3

Geometric Effects of a 90-degree Vertical Elbow on Two-Phase Flow Parameters

The effect of two different elbows in horizontal bubbly flow is presented in the previous chapter. Present chapter investigates the effect of a 90-dgree vertical elbow on two-phase bubbly flow transitioning from vertical upward to horizontal flow in a 50.4 mm inner diameter test section. Modified two-phase flow regime maps are constructed based on extensive flow visualization studies performed in both vertical and horizontal test sections by employing a high speed camera. Pressure measurements are taken at seven different axial locations (three upstream and four downstream of the elbow) for a range of flow conditions to characterize frictional and minor two-phase pressure loss along the test section. A four-sensor conductivity probe is used to obtain local two-phase flow parameters at different axial lengths along the test section. This study demonstrates the effect of 90-degree vertical elbow on two-phase flow regime transition, bubble interaction mechanism, transport of interfacial structures and other two-phase flow parameters.

3.1 Experimental Facility

The Combinatorial test facility is designed to simulate various air water two-phase flow conditions through channels of varying orientations. The test loop consists of horizontal and vertical sections made out of two inch inner diameter pipes, as shown in Fig. 3-1. The maximum lengths of the horizontal and vertical sections are 9.449 m and 3.353 m yielding development

lengths of 186 and 66 L/D, respectively. This test facility is capable of producing bubbly to annular flow in both the horizontal and vertical directions. In addition, through the use of two injection systems, co-current as well as counter-current flow conditions can be investigated with the present design. As shown in the layout, if the green valves are open and the orange valves are closed, the flow will travel as indicated by the green arrow. Similarly, if the orange valves are open and the green valves are closed, then the flow will travel as indicated by the orange arrow.

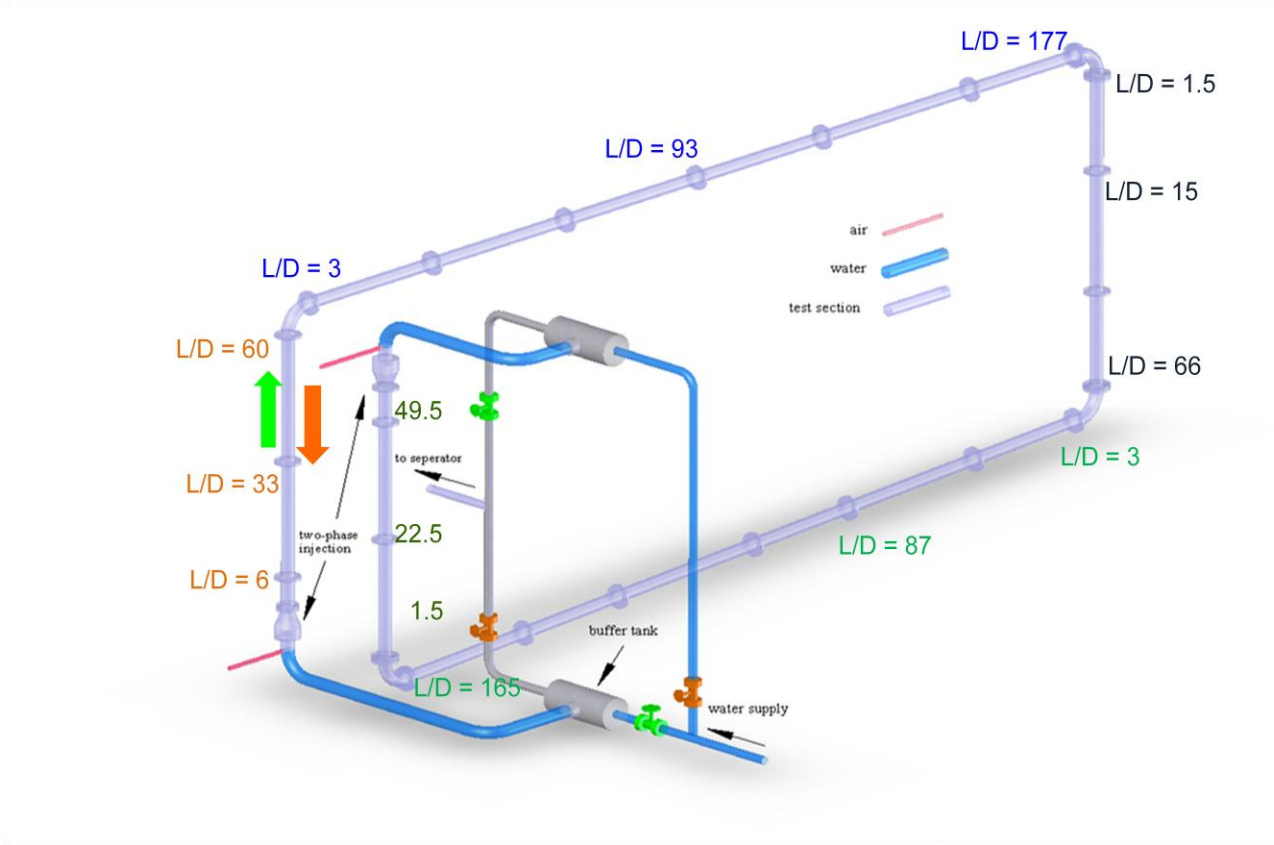

Figure **3-1**: A simple schematic of the combinatorial two-phase flow facility

3.1.1 Test sections

The test loop comprises of five legs, two horizontal and three vertical legs. Each section is made out of acrylic pipe segments of various lengths which are then connected through flanges as described below. The acrylic pipes allow for flow visualization as well as various optical methods to measure different parameters.

Horizontal Sections: the top horizontal section has three 1.219 m segments and three 1.524 m segments and the bottom section is made out of four 1.219 m segments and one 1.524 m segment.

Vertical Sections: the first vertical section with injector in the upward direction is made out of one 0.304 m and two 1.219 m segments. The second vertical section (rightmost) has one 0.762 m and two 1.219 m segments while the third vertical section (injector in downward direction) has one 0.304 m and two 1.067 m segments.

The segments are glued to the flanges on both the ends and the flanges are bolted to each other using four 5/8 inch bolt holes. All the flanges are made out of 0.152 m outer diameter acrylic sheets. The flanges used to connect the vertical pipes are 2.5 cm thick and have four 5/8 inch bolt holes. Fourteen of the vertical section flanges have grooves for 1/8 inch o-ring and the other four are without the o-ring. An important change in the design of the horizontal flanges is the thickness, which is increased to 3.8 cm. This provides more surface area for gluing, thus increasing the strength of the flange against shear stresses which will be significantly higher in horizontal test sections. Sixteen of these flanges have grooves for 1/8 inch o-ring and the rest twenty are without o-ring.

There are six horizontal measurement ports and nine vertical measurement ports. Also, as it can be seen, there are three vertical legs and two horizontal legs in the test loop. In that particular test section, the flange facing the reader has an o-ring groove while the flange in the

other end has no groove for the o-ring. The o-rings are basically used to seal the gaps to prevent leakage. The locations of flanges are chosen in such a way that the measurement ports can be moved to any flange-to-flange connection as required.

3.1.2 Injection system

The injection system consists of two injectors with both vertically upward and downward configuration installed in adjacent vertical legs. The two phase injection system utilizes a double annulus configuration and sparger as shown in the Fig. 3-2. The sparger is a 0.75 inch outer diameter pipe which is installed at the center of the auxiliary (inner) pipe. The top six inches of the sparger, denoted as the red region in the figure, is a porous tip with pore size of ten microns capable of generating 1-2 mm diameter bubbles.

Both auxiliary (inner) and the main (outer) annulus are made out of acrylic pipes. The auxiliary annulus pipe is 1.25 inches inner diameter, 0.25 inches thick and 12 inches long yielding an 11.5 L/D. A small flow rate is supplied around the sparger within the inner pipe which allows for the bubbles of uniform size to be sheared from the sparger. The flow condition in the test section can be varied via the flow rate in the main (outer) annulus which is a 3 inch ID, 0.25 inch thick and 10.5 inch long pipe having an L/D of 6. The main annulus is supplied through three 1.5 inch ID injection pipes. One header is used to buffer the flow from one inlet line (from the pump) into the three main injection lines. The three injection lines are chosen to help in reducing the non-uniformity and swirling of the flow in the main annulus. This configuration minimizes the effect of flow on the bubble diameter. The constant inlet bubble size is desirable for consistent modeling of the interfacial area transport with multiple flow conditions. The injector in turn is

connected to the main test section through a glass reducer. The area for main flow in the reducer is adjusted to minimize the formation of low and high pressure regions.

The main and auxiliary pipes are glued to a 7.5 inch OD and 1 inch thick circular flange, which in turn sets on top of a 1 sq foot and 0.25 inch thick stainless steel plate. A stainless steel elbow is welded to the bottom of the plate which supplies the auxiliary flow.

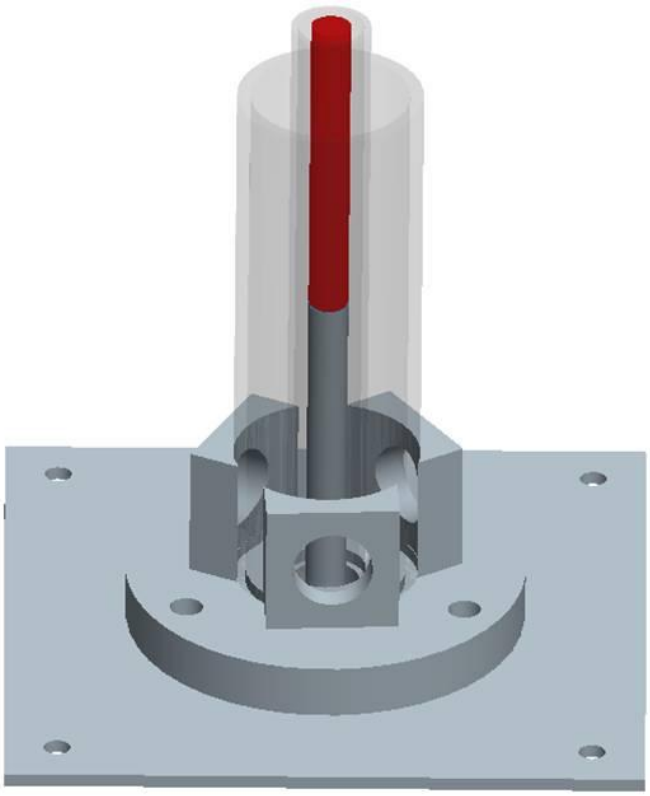

Figure **3-2**: A simple schematic of the injector assembly

3.1.3 Measurement Ports

Due to the symmetric and asymmetric distribution of the two phase flow in the vertical and horizontal sections respectively, two different measurement ports are designed. A flat face has been shaved on all the ports to facilitate the flow visualization using a high speed imaging device.

3.1.3.1 Horizontal measurement port

In horizontal pipe sections, gravity tends to make the gas phase agglomerate in the upper portion of the pipe, making the phase distribution asymmetric. Hence the horizontal port is designed to take measurements along the entire vertical radius to obtain the area averaged values. The port is made out of a 6 inch OD and 6 inch long acrylic rod. A 2 inch ID hole is bored through the port to match the test section. Two rectangular faces are shaven on the port one of which serves for visualization and the other for setting the probe port and the pressure tap. Four 5/8 inch bolt holes run along the length of the main body around its circumference. The port is connected to the test section through an additional mechanism which allows it to be rotated along the axis of the test section. This mechanism comprises a 3.875 inch long pipe nub connected on one end to a 3.5 inch OD and 7/8 inch thick flange and on the other end to a regular 6 inch OD flange. The small flange is connected the main port body and a Teflon coated o-ring is used to seal them. The regular flange is used to connect to the test section. This probe body is bolted along its length between two of these parts using two additional flanges matching the cross-section of the probe body. One of the smaller flanges has holes drilled along its circumference every 22.5 degrees which allows us to control the rotation of the horizontal probe port using a spring loaded mechanism. Fig. 3-3 shows the schematic of the horizontal measurement port.

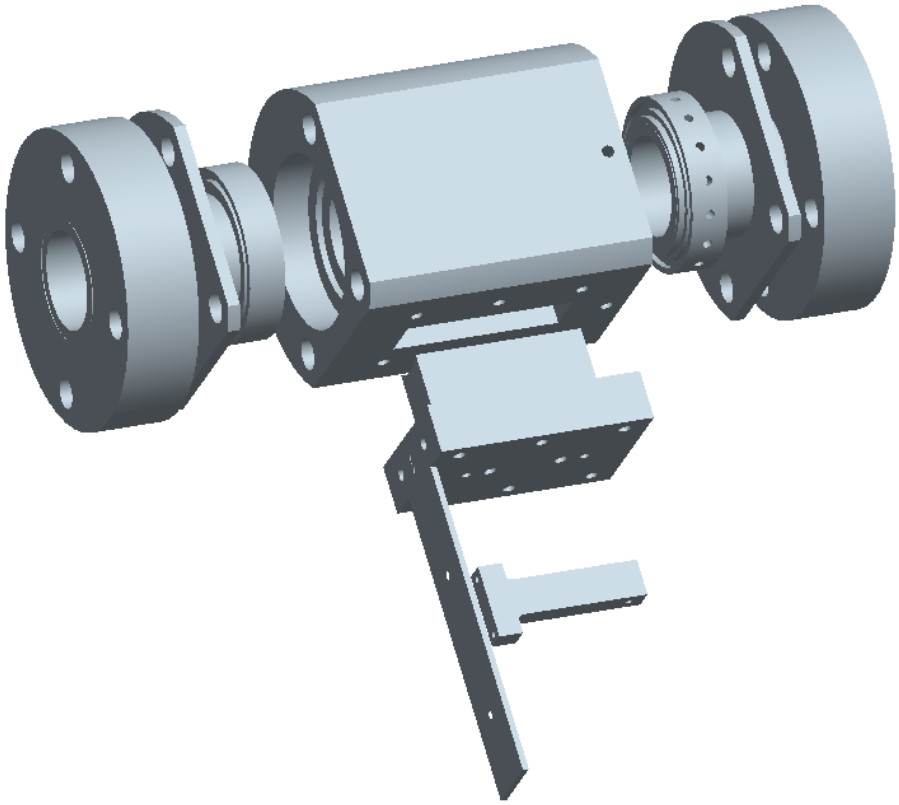

Figure **3-3**: A simple schematic of a horizontal measurement port.

3.1.3.2 Vertical measurement port

The two phase flow distribution in vertical (upward and downward) direction is nearly symmetric and hence allows for measurements in any direction along one radius to obtain area averaged values. This eliminates the need for the measurement port to be rotational. The design of the vertical port is very similar to the horizontal except that it does not include the mechanism for rotation. Fig. 3-4 shows the schematic of the vertical measurement port.

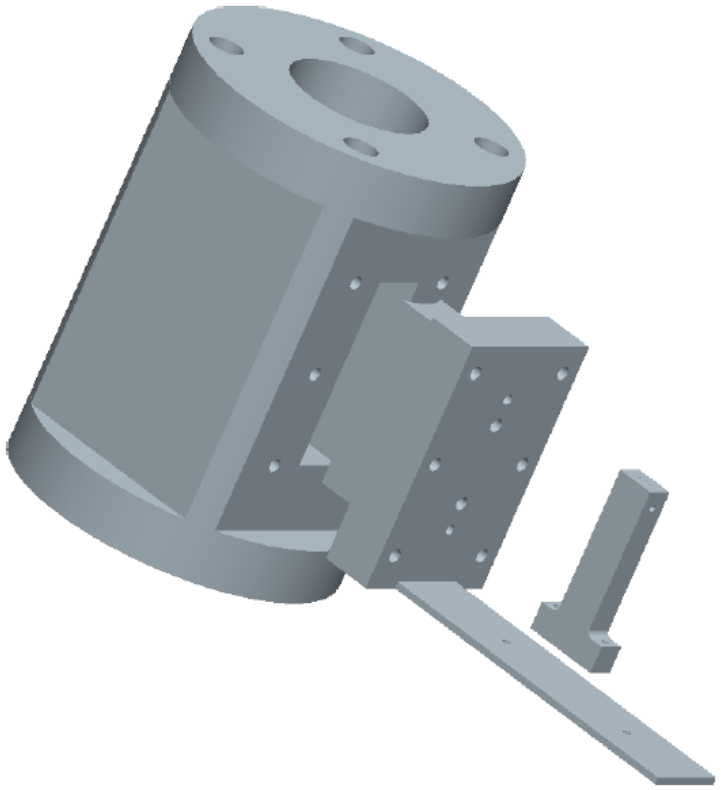

Figure **3-4**: A simple schematic of a vertical measurement port.

3.1.4 Conductivity probe, probe port cover, and traversing mechanism

The conductivity port is made out of four acupuncture needles of 0.12 mm diameter. Each of these is laser welded to 27 gauge tubing which then is Teflon coated leaving the tip of the needle and the top of the tubing as the only conducting part. All four of the pipes and needles are then glued inside a 1/8 inch pipe. Each of the needles is connected to a DC circuit via thermocouple wires. The data acquisition system reads the voltage of each needle. The needles are bent perpendicular to the flow direction and arranged in a configuration to achieve measurements in different directions.

A plug is used to hold the conductivity probe and the pressure tap, and a cover with 1/8 inches o-ring is used to seal this system. Out of 15 plugs for the measurement ports 3 are designed to carry both a conductivity probe and pressure tap and the rest of them carry just the pressure tap. The ones designed for the conductivity probe have an1/8 inches hole in addition to the 1/16 inches hole for the pressure tap. Each plug is mounted to the measurement port using two ¼ inches screws. The covers used for the plugs with conductivity probe are made 1 inch thick in comparison to the rest of them which are ½ inches thick. This is in order to support the conductivity probe.

The traversing mechanism for the conductivity probe consists of a unislide which allows for measurements accurate to 0.01 mm. The unislide used is 6 inches long and 1.5 inches. It ensures that the probe can be traversed completely across the test section. An aluminum T shaped mount is used to attach the unislide to the measurement port. The T portion of the mount is screwed to the front of the probe port cover.

3.1.5 Positioning of the measurement ports:

There are a total of 24 measurement positions possible along the test section.

Horizontal section: There are two horizontal sections (top and bottom). Each section has three horizontal measurement ports. Going clockwise along the test loop the ports are positioned at 3, 93, and 177 L/D along the top section and 3, 87, and 145 L/D along the bottom section from their respective elbows. Moving counterclockwise the positions are 3, 87, and 177 L/D along the top and 3, 81, and 145 L/D along the bottom section from their respective elbows. The test facility is capable of achieving several other L/D combinations along the horizontal section.

Vertical section: There are three vertical sections with each section having three measurement ports. Going clock wise from the leftmost vertical section the ports are positioned at 6, 33, and 60 L/D along the first section, at 3, 21, and 72 L/D along the second vertical section and at 3, 27, and 51 L/D along the third vertical section. Moving counterclockwise the positions are 3, 30, and 57 L/D along the first, at 3, 54, and 72 L/D along the second and at 6, 30, and 54 L/D along the third vertical section.

3.2 Experimental results and data analysis:

Fig. 3-5 shows the schematic of the test facility in two-dimensional plane geometry. Two-phase flow parameters are measured in the vertical upward and first horizontal section. The measurement locations are shown in the highlighted boxes.

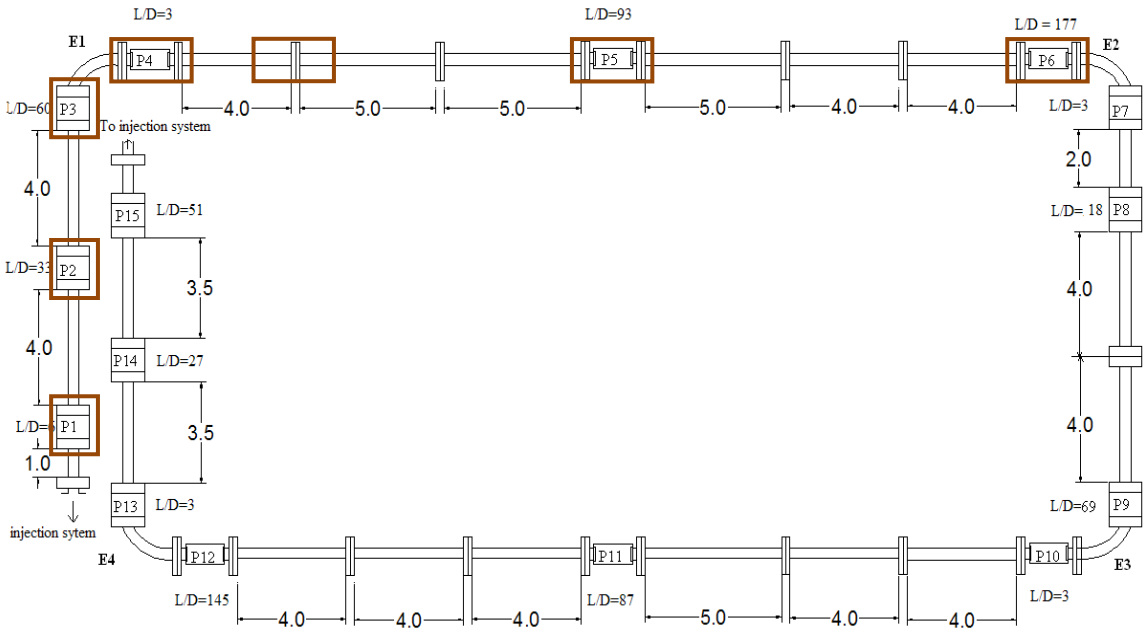

Figure **3-5**: Simple schematic of the combinatorial channels in two-dimensional plane geometry (measurement locations are highlighted)

A total of six different combinations of j_g and j_f are selected to measure two-phase flow parameters. The flow conditions are denoted by runs 1-9 in table 3-1. All the flow chosen flow conditions are within or near the bubbly flow regime in both vertical and horizontal section. Since the superficial gas velocity is a function of pressure, the gas flow rates to denote each run are calculated based on the atmospheric pressure condition.

Pressure measurements are made for all the run conditions. Local measurements using the four-sensor conductivity probe are obtained using Run 2-6 in the vertical upward section and Run 4-6 in the first horizontal section.

Table **3-1**: Summary of the 6 different flow conditions used to measure two-phase flow parameters; $j_{g,atm}$ denotes the superficial gas velocity under atmospheric pressure condition.

Run	$j_{g,atm}$ [m/s]	j_f [m/s]	Vertical Leg	Horizontal Leg	
				Port 4	Port 7
1	0.136	2.0	Bubbly	Bubbly	Bubbly
2	0.228	2.0	Bubbly	Bubbly	Bubbly
3	0.343	2.0	Bubbly	Bubbly	Plug
4	0.139	3.0	Bubbly	Bubbly	Bubbly
5	0.232	3.0	Bubbly	Bubbly	Bubbly
6	0.353	3.0	Bubbly	Bubbly	Bubbly

3.2.1 Benchmarking:

In view of benchmarking the reliability of the probe measurements, the local superficial gas velocity at each measurement port measured by the flow meter along with the local gage pressure measurement is compared with that calculated based on the data acquired by the probe using:

$$\langle j_g \rangle_{loc} = \langle \alpha u_g \rangle_{loc} \tag{3.1}$$

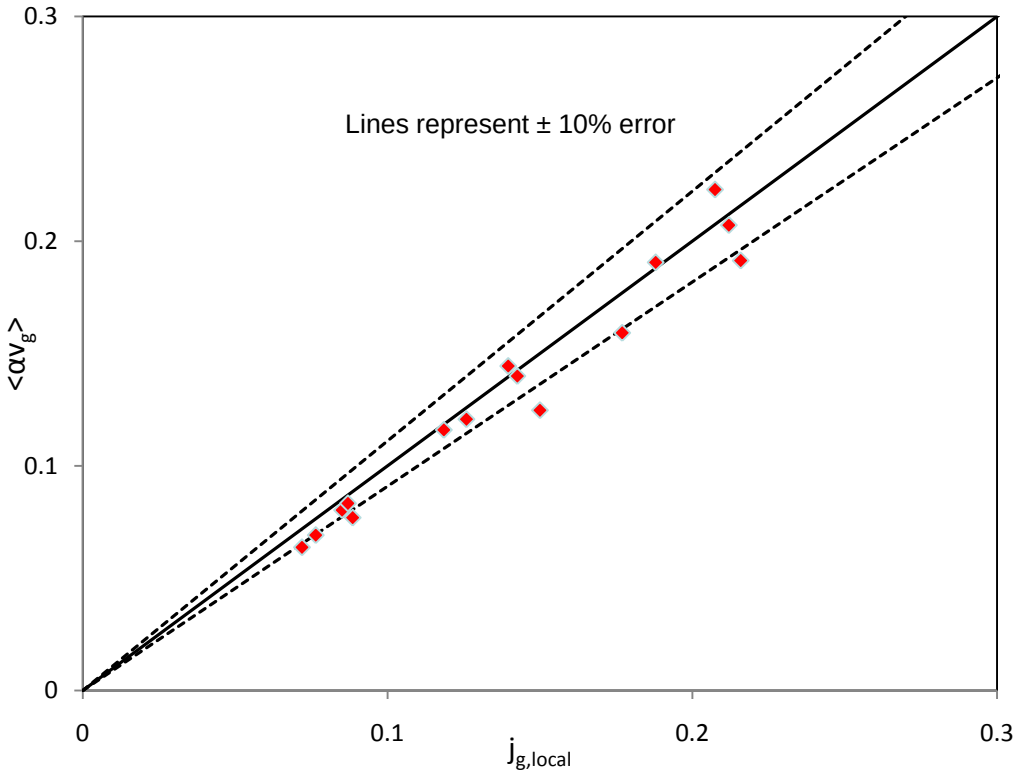

Figure **3-6**: Comparison of the local superficial gas velocity, $j_{g,loc}$, measured by the flow meter with $<\alpha u_g>$ acquired by the conductivity probe, dotted lines represent ±10%

The result is shown in Fig. 3-6, and they are in relatively good agreement with each other within ±10% difference. The discrepancies at the port P1 (L/D =6) can be attributed to the insufficient development length.

3.2.2 Flow regime identification:

All energy systems including nuclear reactors have coolant channels with varying orientation and interconnected via various flow restrictions. As shown in the previous chapters, elbows have a significant effect on the two-phase flow parameters and their transport. It has also

been shown that elbows induce bubble interaction which is dependent on the type of elbows and the flow conditions. The nuclear reactor safety codes use the conventional flow regime maps for the entire system which is valid only for the straight pipe flows. Two-phase flow structure changes in the vicinity of the flow restrictions cause deviation in the flow regime transition boundaries from the conventional boundaries. Hence, modified flow regime maps are required to accurately model the flow in these sections.

To study the geometric effects of a 90-degree vertical elbow on regime transition, flow regime identification is performed in the combinatorial round pipe test section for the two-phase flow moving from vertical upward to horizontal section, based on the flow visualization. A high speed movie camera is employed and images are collected at three instrumentation ports (one upstream and two downstream of the elbow) with development lengths 60D, 66D, and 156D respectively from the inlet. Fig 3-7 shows the high speed images for typical two-phase flow conditions. It is observed that the 90-degree vertical elbow, in general causes disintegration of the larger bubbles. The classification of the different flow regimes is based on the definitions mentioned in detail in Chapter-1. The results obtained at port P3 for vertical two-phase flow are compared with the flow regime map suggested for the vertical flow in round channels by Mishima and Ishii (1980) and results for the horizontal two-phase flow at ports, P4 and P7 are compared with the horizontal flow regime map suggested by Mandhane (1974).

The flow conditions for the experiment are selected based on the flow regime map for vertical two-phase flow suggested by Mishima and Ishii (1980), ranging from bubbly flow to transition into slug flow regime. Another criterion in selecting the flow conditions was to exclude any condition that would lead to kinematic shock (Ishii et al., 2004) or flooding in the vertical downward flow section.

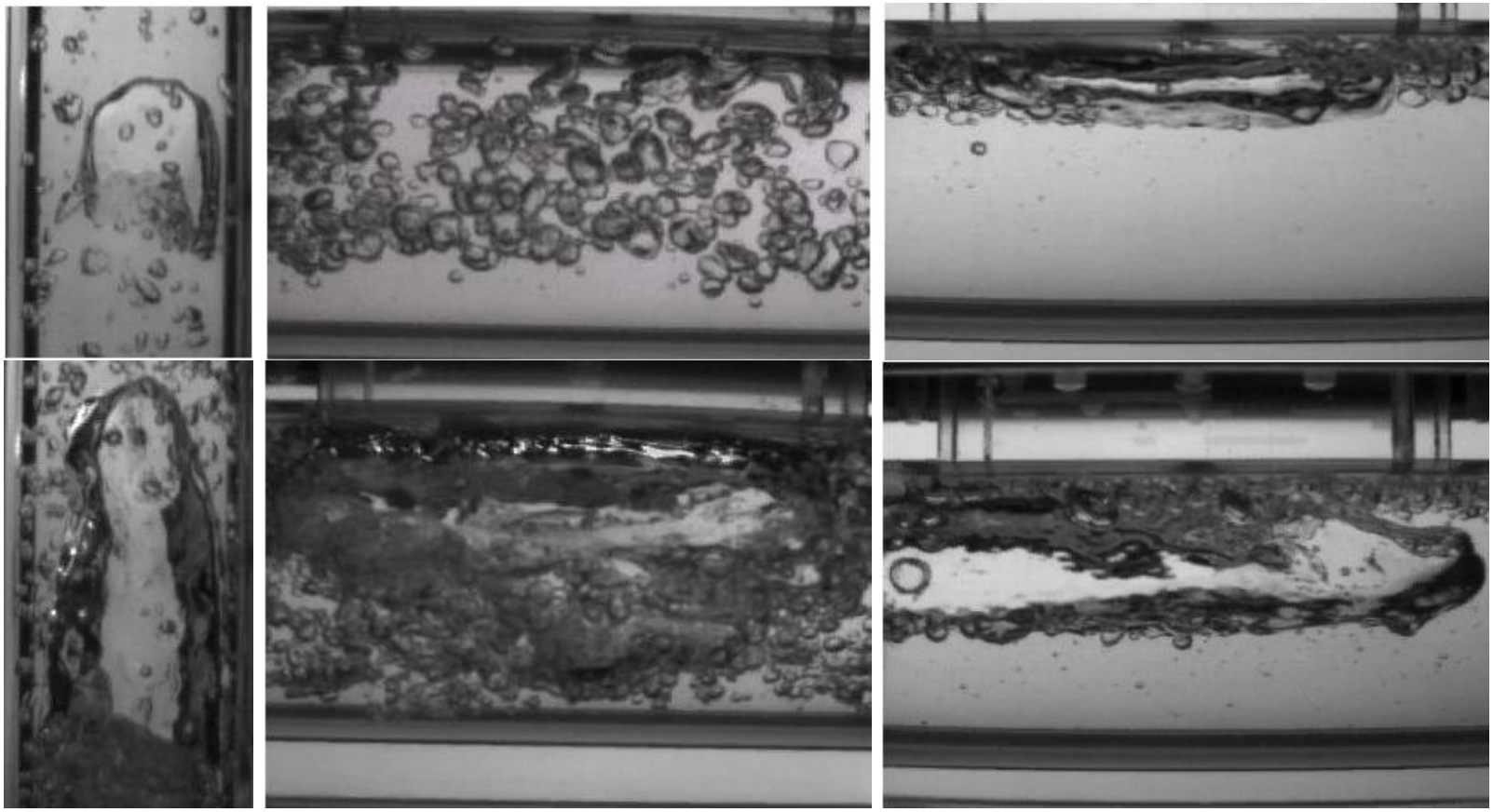

$(L/D)_V = 60$ $(L/D)_H = 3$ $(L/D)_H = 30$

Figure **3-7**: High speed images of the development of two-phase flow across the 90-degree elbow

The geometric effect of elbow and configuration is clearly observed at the measurement locations downstream of the elbow. For the vertical two-phase flow at port P3, L/D=60, the flow regime boundaries shift toward the lower void fraction conditions. The flow regime map, which is based on theoretical analysis predicts a line with area averaged void fraction, $<\alpha> = 0.3$, as the transition between bubbly and slug flow. However, since the transition is gradual, a transition region is defined, where the flow cannot be categorized as either bubbly or slug flow.

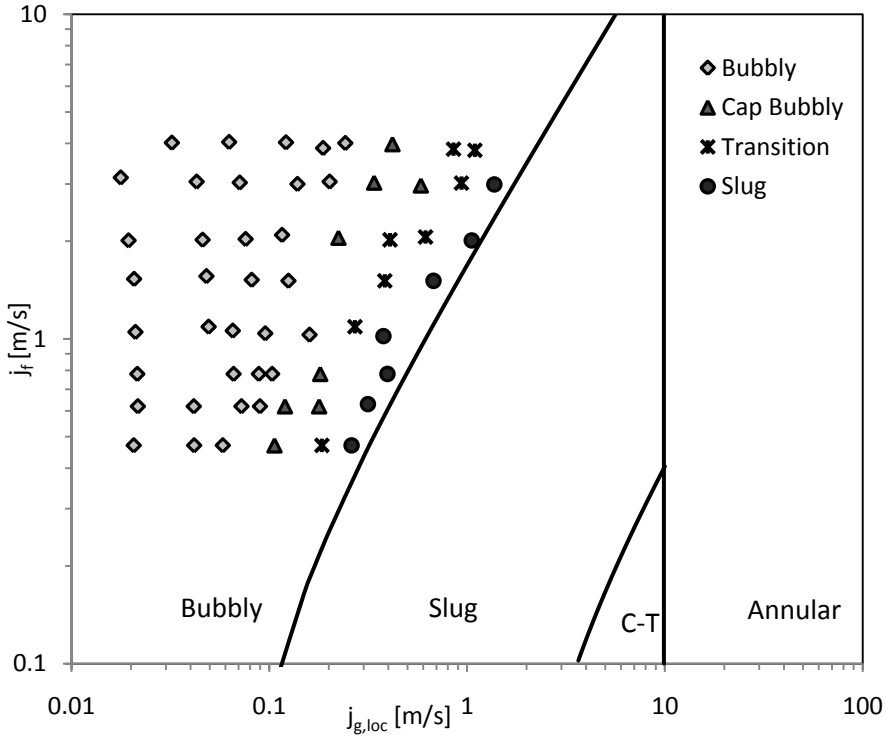

Figure **3-8**: Modified flow regime map at port P3, L/D = 60 in the first vertical channel, based on the vertical two-phase flow regime map suggested by Mishima and Ishii, (1984)

Fig. 3-0 shows comparison between the horizontal flow regime map suggested by Mandhane (1974) and the flow visualization results at port P4 located at development length of 3D from the elbow. The flow regime transition boundaries suggested by modified map significantly deviate from the conventional flow regime map. The horizontal bubbly flow occurs

even at lower liquid flow rates and extends into the conventional plug flow region. This can be attributed to secondary flow and turbulent structure generated by the 90-degree vertical elbow, which causes disintegration of plug bubbles. Furthermore, the transition from plug to slug flow regime occurs at lower void fraction conditions.

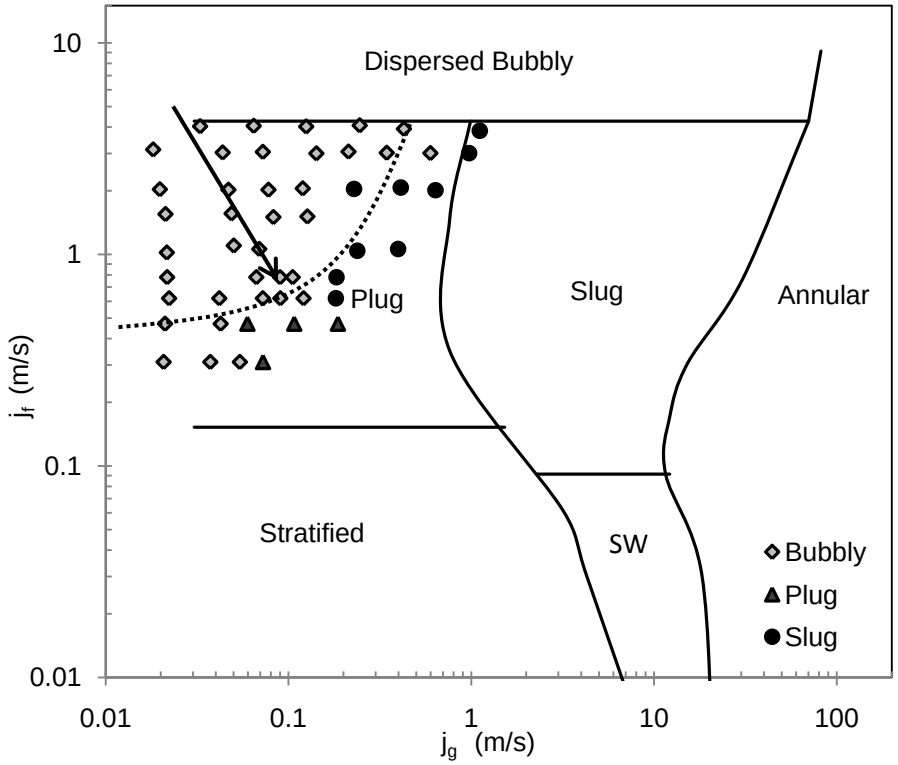

Figure **3-9**: Modified flow regime map at port P4; $L/D_{elbow} = 3$, based on the horizontal two-phase flow regime map suggested by Mandhane et al.

The effect of the development length on the flow regime transition is shown in Fig. 3-10. The flow regime boundaries are plotted for port P7 located at a development length of 90D from the elbow. As the flow develops further downstream the elbow effect starts to decay. The bubbly flow regime boundary shifts towards the boundaries suggested by the conventional regime map.

It is predicted that with sufficient development length the elbow effect will decay completely and the flow regime boundaries would match the conventional boundaries.

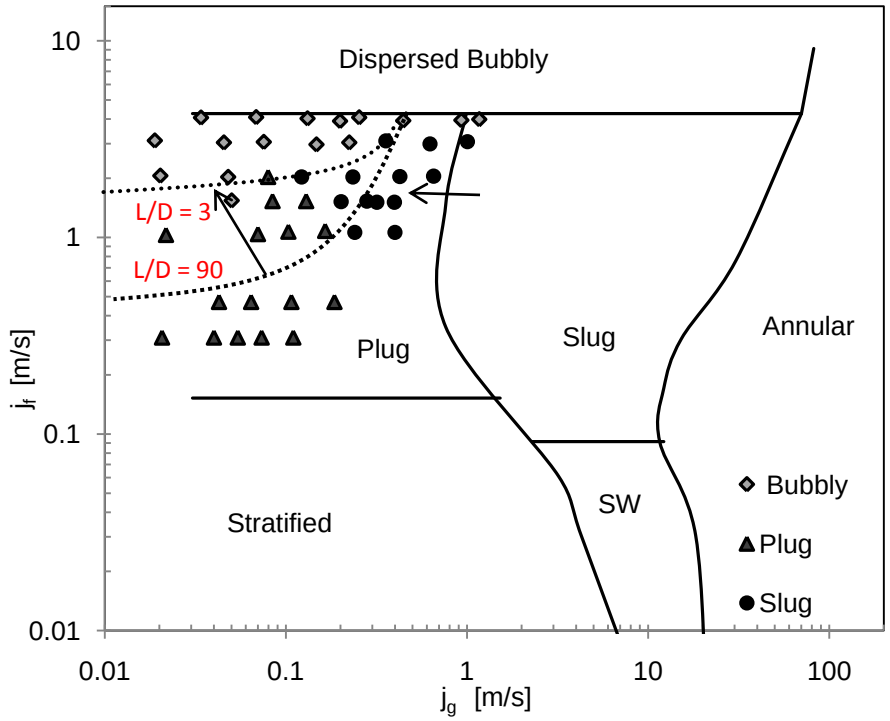

Figure **3-10**: Modified flow regime map at port P7; L/D_{elbow} = 90, based on the horizontal flow regime map suggested by Mandhane et al.

3.2.3 Pressure:

Single-phase pressure measurements are made over a wide range of flow conditions to characterize the frictional pressure drop and minor loss across the vertical elbows, as shown in Fig. 3-11 and 3-12. Local static pressure is collected at various locations along the flow direction using a differential pressure transducer. The pressure transducer is calibrated against the

hydrostatic pressure head in the first vertical leg. The accuracy of pressure transducer is ±5% of the given flow conditions.

As a reference pressure for the differential pressure measurements, the local gauge pressure at port location P1 is obtained for each flow condition. Then subsequently, the frictional pressure drop between the ports P2, P3, P4, P6, P7 and P9 are also measured. The local gauge pressure at all other port locations are obtained by using the following relation.

$$p_i = p_1 - \rho g h - \Delta p_{1i} \tag{3-1}$$

where, the subscript 'i' represents the port location and '$1i$' represents the pressure drop due to friction and/or minor loss between the first and the i^{th} port. Here the term Δp is acquired from a differential pressure measurement, or theoretically given by,

$$\Delta p = f\left(\frac{L}{D}\right)\frac{\rho v^2}{2} + \left(\sum k \frac{\rho v^2}{2}\right) \tag{3-2}$$

The friction factor is obtained from the conventional Blassius correlation for turbulent flow, Blassius (1913) given by,

$$f = 0.316 Re_d^{-1/4} \qquad 4000 < Re_d < 10^5 \tag{3-3}$$

The minor loss term in Eq. 3-2 is included when the loss due to the vertical elbow needs to be taken into account. The minor loss factor *k*, for 90º bend is correlated by curve fit formula given by Ito (1960).

$$k \approx 0.388 \propto \left(\frac{R}{d}\right)^{0.84} Re_D^{-0.17} \tag{3-4}$$

where,

$$\propto = 0.95 + 4.42\left(\frac{R}{d}\right)^{-1.96} \geq 1 \tag{3-5}$$

It is observed that all the data agree well with the prediction made by the existing correlations within ±5% difference.

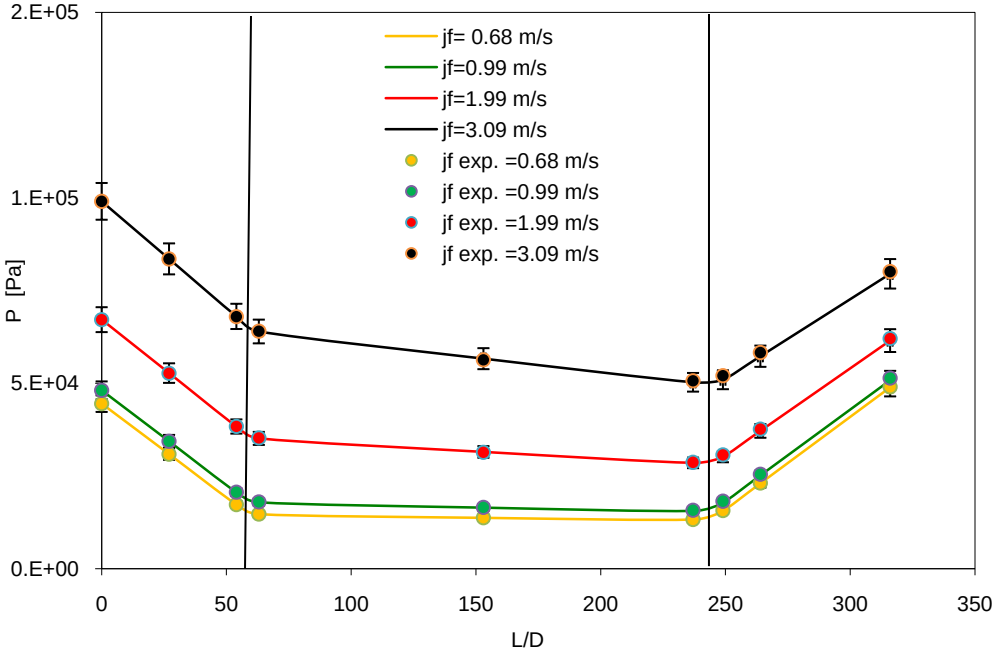

Figure **3-11**: Comparison of the measured single-phase pressure with the theoretical calculations (vertical lines show the location of the elbows)

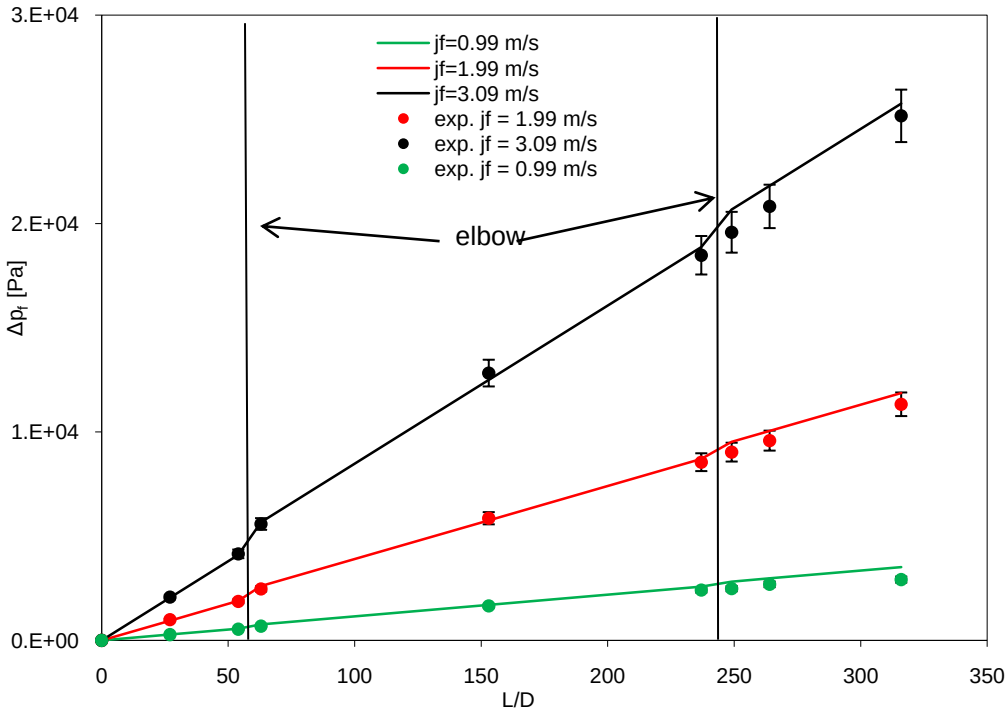

Figure **3-12**: Comparison of the measured frictional pressure drop against the prediction

Two-phase pressure is acquired across the 90-degree vertical elbow for six different run conditions as mentioned earlier. Fig 3-13 shows the plot of two-phase pressure with development length at a constant liquid flow rate of 3.0 m/s and increasing gas flow rate. The two-phase pressure drop here comprises of the hydrostatic pressure drop in the vertical section, frictional pressure drop and the minor pressure drop across the elbow. The 90-degree vertical elbow causes a significant pressure drop due to minor losses. However, this is not clearly evident in Fig. 3-12 because of a high hydrostatic pressure drop in the vertical section.

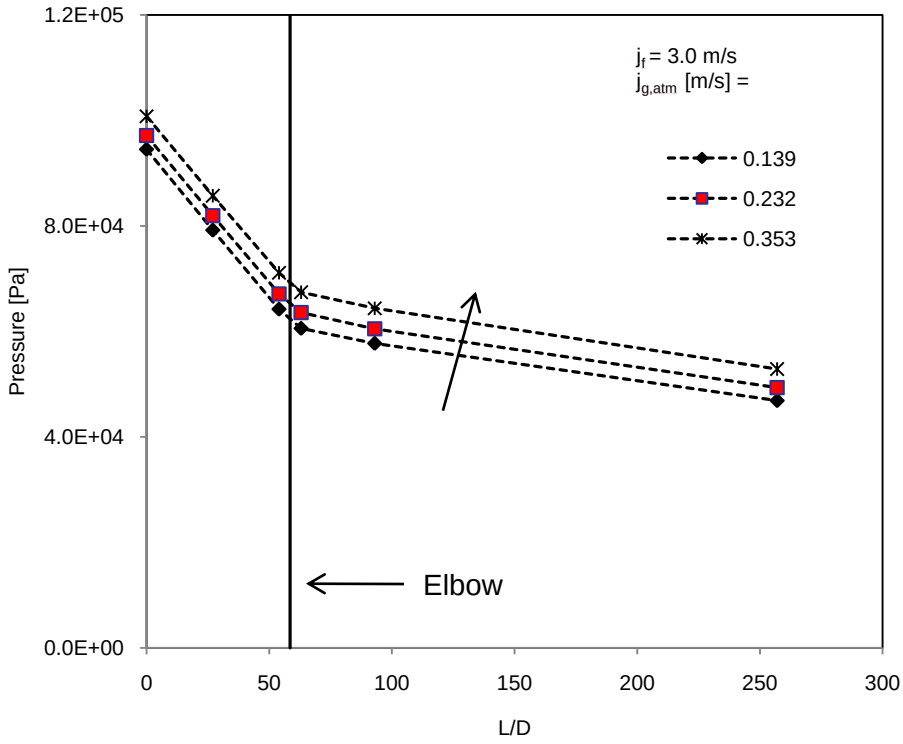

Figure **3-13**: Two-phase pressure drop across the 90-degree vertical elbow at a constant liquid flow rate, j_f = 3.0 m/s and increasing gas flow rate.

3.2.4 Local interfacial structures:

3.2.4.1 Vertical Section:

A four-sensor conductivity probe is used to obtain local data at three axial locations along the vertical section with corresponding development lengths of LD = 6, 33 and 60, respectively. Five different combinations of gas and liquid flow rates, all within bubbly flow regime, are investigated. Local data is obtained across the whole pipe cross-section for test run conditions to establish the symmetry across the axis in the direction of the flow. These results are shown in Appendix A-8. Following that, local measurements are made only across the half cross-section.

Time averaged local void fraction and interfacial area concentration along the first vertical section for j_f = 3.0 m/s and $j_{g,atm}$ = 0.139 m/s is shown in Fig. 3-13. The bubble distribution follows a parabolic profile with center peak, at port P1. The flow becomes more developed as it approaches ports P2 and P3. The bubbles start to move towards the pipe wall causing a distinct wall peak in the local profiles. The local interfacial area concentration profile is very similar to the local void fraction profile, which is a characteristic of bubbly flow regime. The plots of local data for different flow conditions are specified in Appendix A-9.

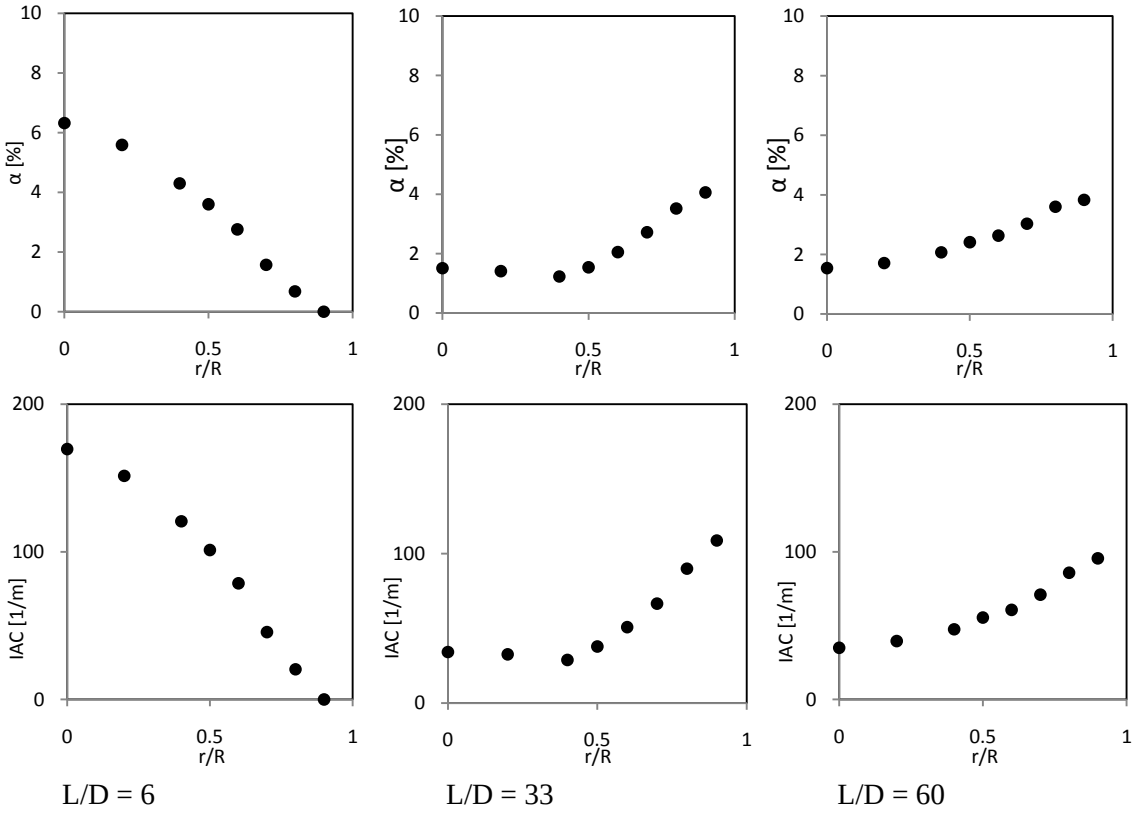

Figure **3-14**: Local void fraction and interfacial area concentration profiles in the vertical section at j_f = 3.0 m/s and $j_{g,atm}$ = 0.139 m/s

Fig. 3-15 demonstrates the effect of liquid flow rate on the local profiles of void fraction and interfacial area concentration along the vertical channel. The time averaged local profiles are plotted along half pipe cross-section for a fixed gas flow rate of $j_{g,atm}$ = 0.232 m/s and increasing liquid flow rates. In general, increasing the liquid flow rate for constant gas flow rate decreases the area averaged void fraction. At port P1, L/D = 6, the flow is relatively undeveloped and hence the bubble distribution profiles are very similar. However, as the flow develops further downstream at ports P2 and P3, there is a significant decrease in the wall peak with increasing the liquid flow rate. Moreover, the bubbles are more uniformly distributed across the pipe cross-section. It is speculated, an increase in the liquid flow rate increase turbulence in the pipe flow, which increases the degree of mixing and hence a more uniform bubble distribution profile is

observed. Bubble distribution is also a function of development length and becomes more uniformly distributed as the flow develops axially.

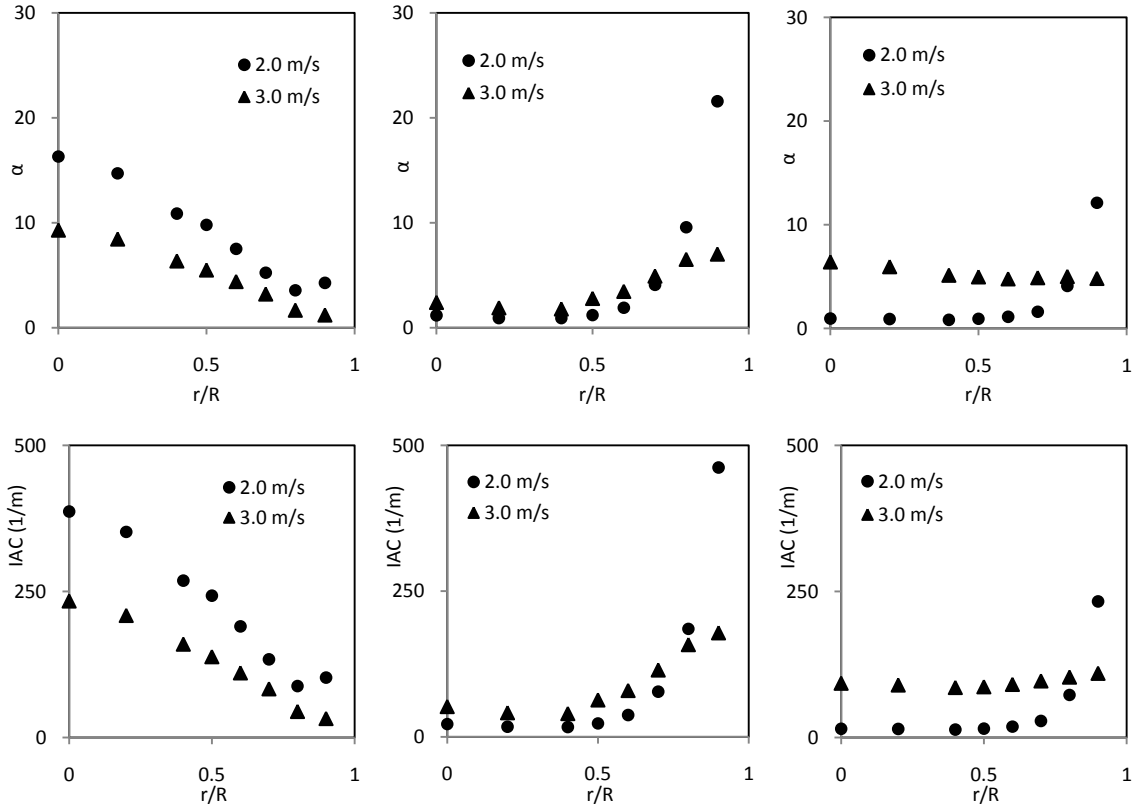

Figure **3-15**: Local void fraction and interfacial area concentration profiles in the vertical section at constant gas flow rate, $j_{g,atm}$ = 0.232 m/s and increasing liquid flow rate

3.2.4.2 Horizontal Section:

Measurements in the first horizontal section are made at ports P4, P5 and P10 which have corresponding development lengths of 3D, 90D and 177D from the 90-degree vertical elbow. Accounting for the asymmetry of the phase distribution in horizontal section caused by the elbow, measurements are made across the whole cross-section. Fig-3-16 shows the measurement

scheme used to obtain the local data. The horizontal measurement port is rotated every 22.5 degree and the conductivity probe is traversed to 15 different radial positions along each direction, leading to 120 local data points at across the whole cross-section.

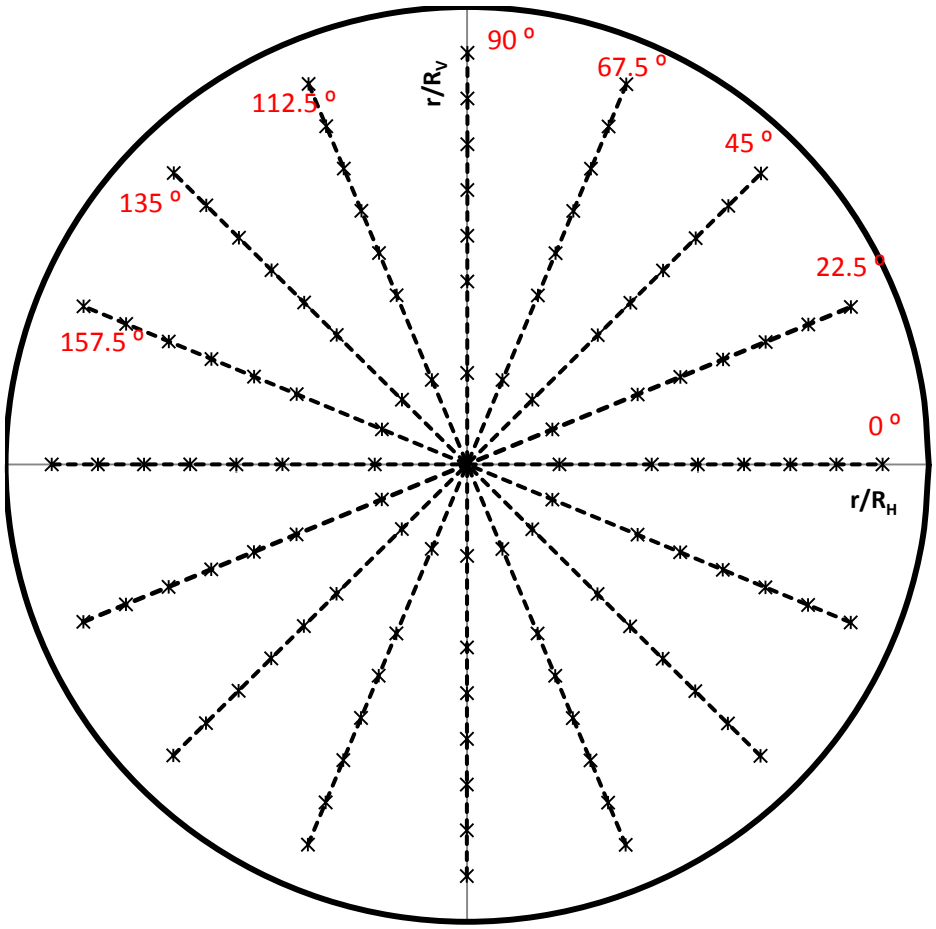

Figure **3-16**: Schematic of the pipe cross-section showing the measurement scheme employed in horizontal section (Flow direction is into the page)

Fig 3-17 shows the local profiles of void fraction along the radial direction at different azimuthal angles at port 4 (3 L/D downstream of the elbow). The value of void fraction at the center of the pipe cross-section for all the measurements falls between 3.2%– 3.6%. This demonstrates the repeatability of the conductivity probe measurements. It is interesting that the elbow causes the bubbles to be distributed along the horizontal radius of the pipe cross-section. This causes a bi-peaked distribution along the horizontal radius of the pipe cross-section. The local profile along the vertical radius indicates a higher distribution of the bubbles in top half of the pipe cross-section.

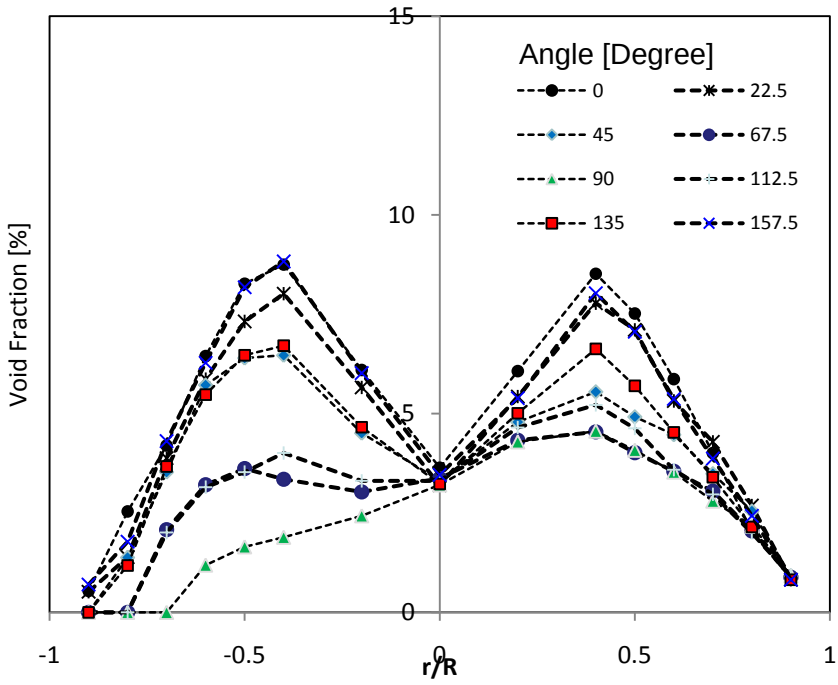

Figure **3-17**: Local profiles of void fraction measured along the radial direction at different azimuthal angles at port 4 for run 4 (j_f = 3.0 m/s, $j_{g,atm}$ = 0.139 m/s)

Fig 3-18 and 3-19 shows the local profiles of void fraction and interfacial area concentration along the radial direction for individual direction of measurement. The profiles for α and a_i are similar, which is a characteristic of the bubbly flow regime.

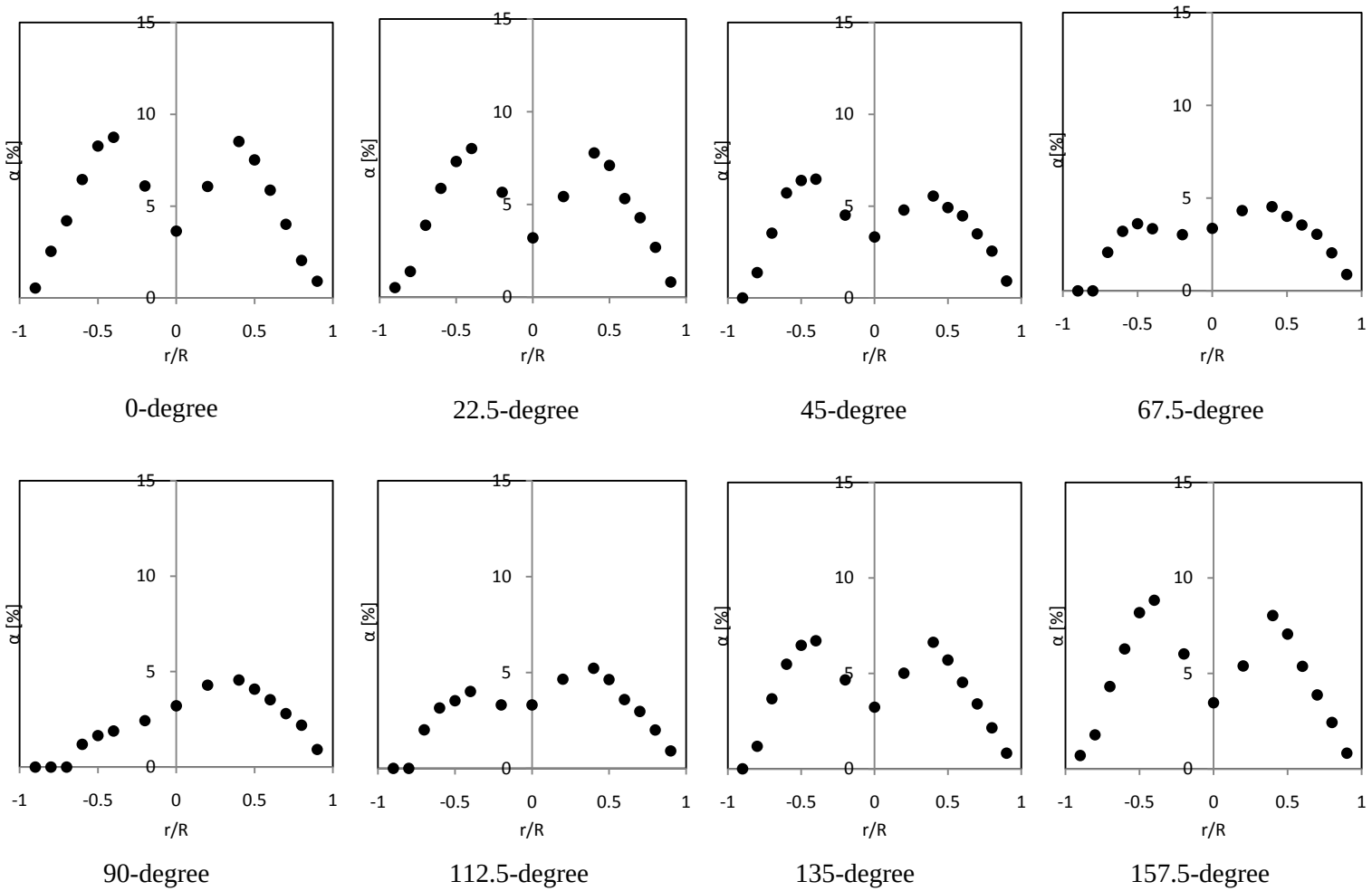

Figure **3-18**: Local profiles of void fraction at different angles of measurement at port P4, L/D = 3 from the 90-degree vertical elbow at run-4, j_f = 3.0 m/s and $j_{g,atm}$ = 0.139 m/s

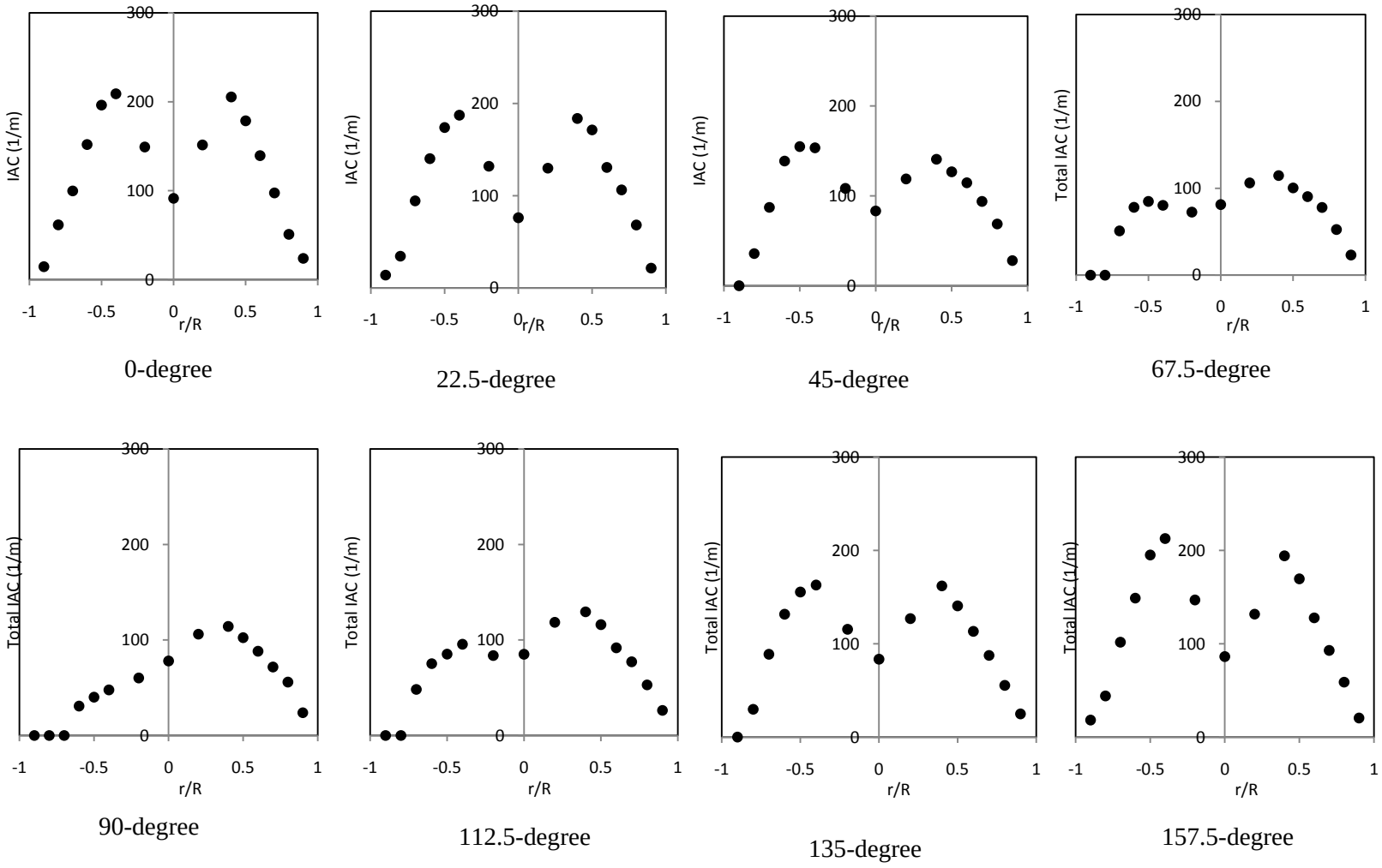

Figure **3-19:** Local profiles of interfacial area concentration at different angles of measurement at port P4, L/D = 3 from the 90-degree vertical elbow at run-4, j_f = 3.0 m/s and $j_{g,atm}$ = 0.139 m/s

The above detailed local data is used to generate three-dimensional profiles and contour plots for void fraction, interfacial area concentration and bubble velocity. Fig 3-20 shows the three dimensional profile and contour plot for local void fraction at port-4 (3 L/D downstream of the 90-degree vertical elbow) for Run-4 corresponding to liquid flow rate, j_f = 3.0 m/s and gas flow rate, $j_{g,atm}$ = 0.139 m/s. As mentioned in the previous analysis, bubbles are distributed along the horizontal axis of the pipe cross-section. This creates dual peak along the horizontal radius of the pipe cross-section in the void fraction profile. The interfacial area concentration profile is very similar to the void fraction profile, which is a characteristic of dispersed bubbly flow. It is speculated that this phenomena is due to the secondary flow created by the 90-degree vertical elbow which entrains the bubbles in two distinct streaks.

In order to confirm this phenomena flow visualization is performed by capturing high speed images from underneath the measurement port. Fig 3-21 shows two typical high speed images for Run-4 and 6 corresponding to a constant liquid flow rate, j_f = 3.0 m/s and gas flow rates, $j_{g,atm}$ = 0.139 m/s and 0.353 m/s respectively. It is clearly observed that the bubbles are distributed in two distinct streaks and hence confirms the probe measurements.

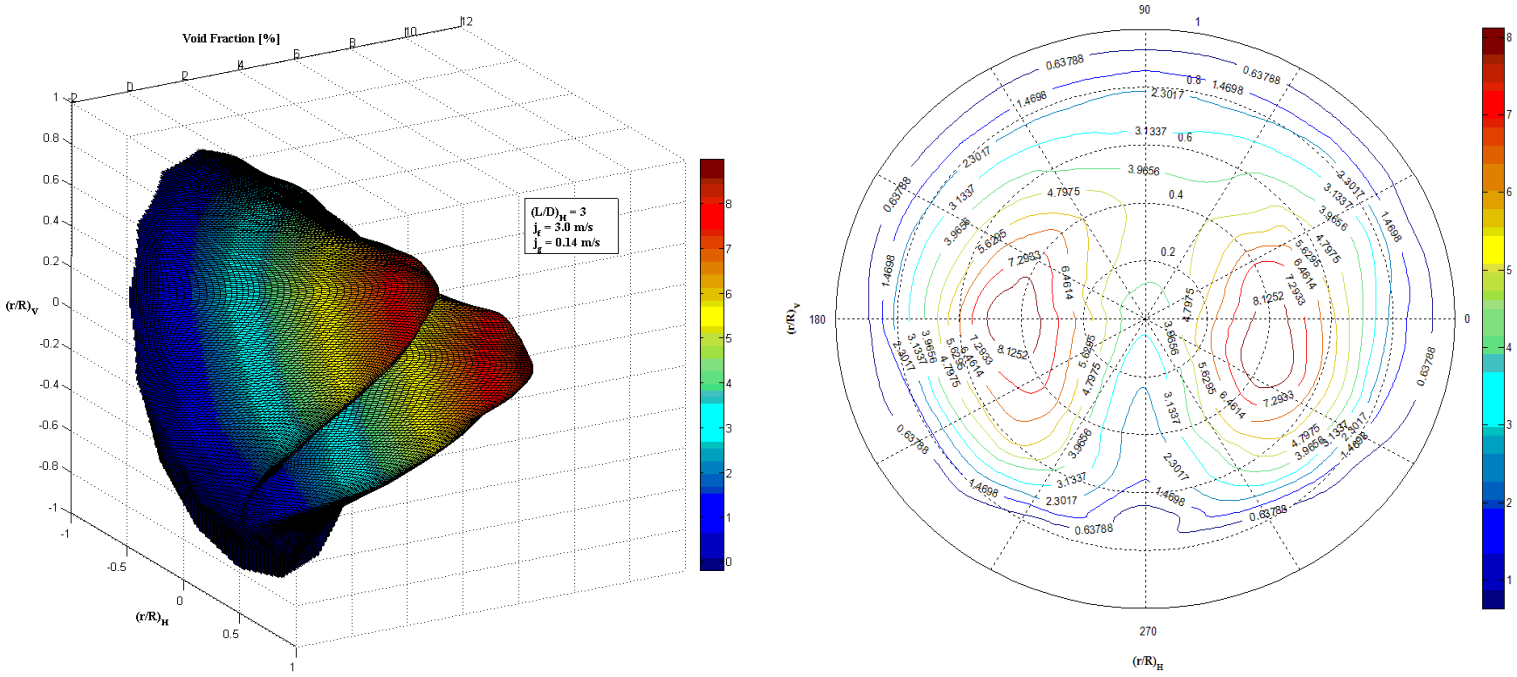

Figure **3-20**: Three-dimensional profile and contour plot of local void fraction at port P4, L/D = 3 from the 90-degree vertical elbow at run-4, j_f = 3.0 m/s and $j_{g,atm}$ = 0.139 m/s

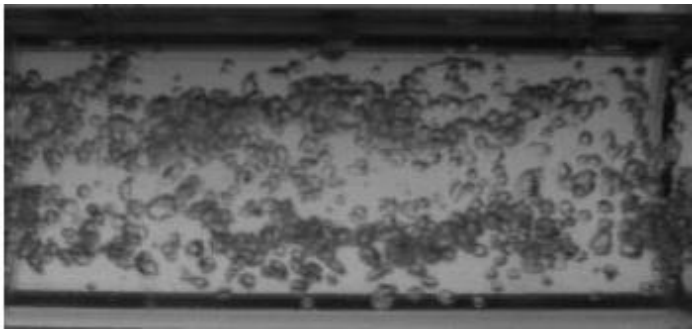

j_f = 3.0 m/s and $j_{g,atm}$ = 0.139 m/s

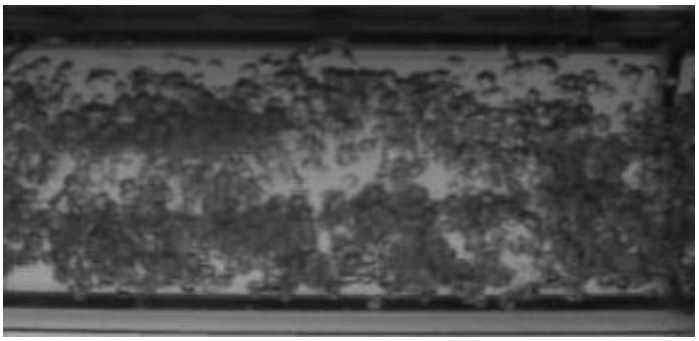

j_f = 3.0 m/s and $j_{g,atm}$ = 0.139 m/s

Figure **3-21**: High speed image at port-4; 3 L/D downstream of the 90-degree vertical elbow obtained from the bottom of the measurement port

Fig. 3-22 shows the three-dimensional profiles and contour plots for void fraction at port-5 for Run-4, corresponding to j_f = 3.0 m/s and $j_{g,atm}$ = 0.139 m/s. The elbow effect decays at measurement locations downstream of the elbow. Buoyancy force starts to dominate and bubbles start to migrate to the top half of the pipe cross-section. This causes a steep peak in the local void fraction and interfacial concentration profiles in the top half of the pipe cross-section. Comprehensive development of the interfacial structures moving from vertical to horizontal section is shown in Fig 3-23.

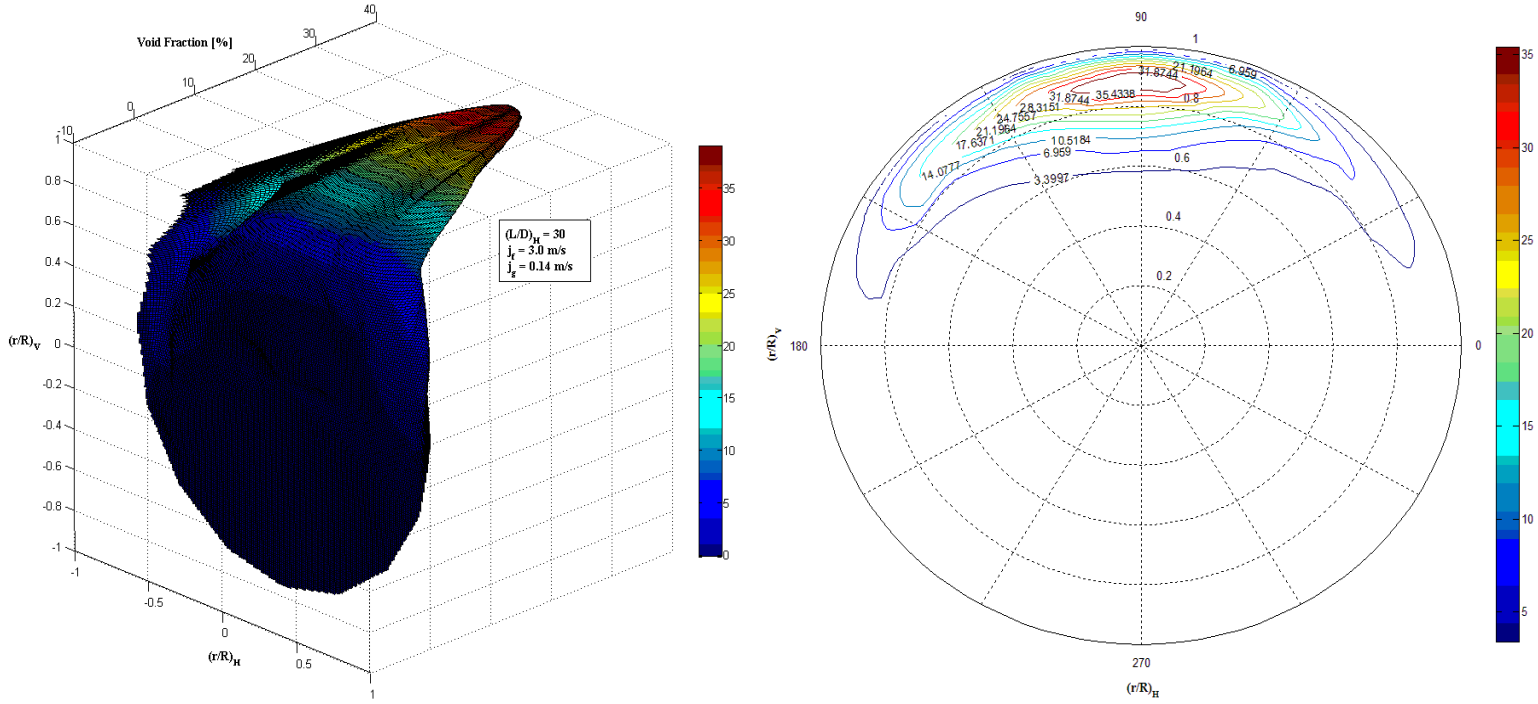

Figure **3-22**: Three-dimensional profile and contour plot of local void fraction at port-5, L/D = 30 from the 90-degree vertical elbow at run-4, j_f = 3.0 m/s and $j_{g,atm}$ = 0.139 m/s

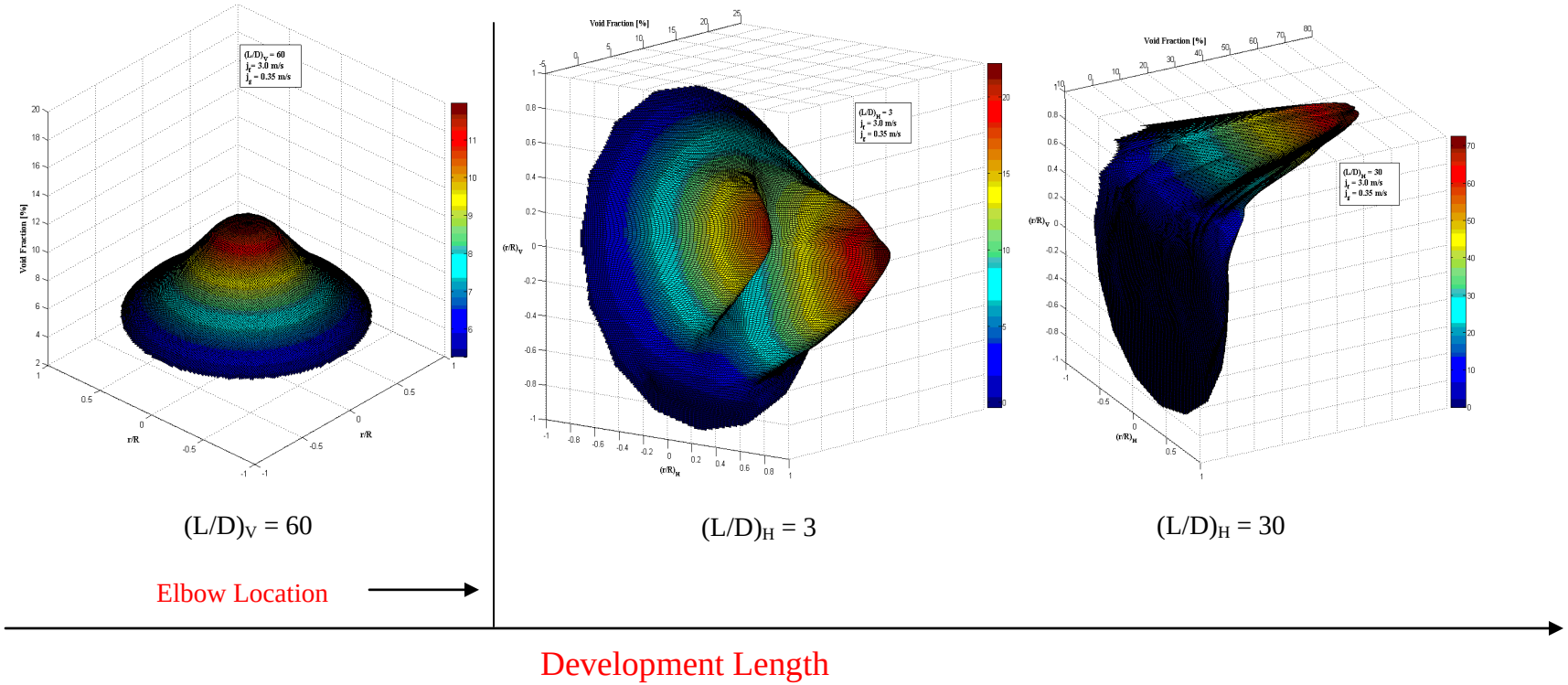

Figure **3-23**: Development of void fraction across the 90-degree vertical elbow at run-4, j_f = 3.0 m/s and $j_{g,atm}$ = 0.139 m/s

3.2.5 One-dimensional transport of interfacial structures:

One dimensional transport of area averaged void fraction and interfacial area concentration for a constant liquid flow rate, j_f = 3.0 m/s and varying gas flow rate is shown in Fig. 3-24. There is an increase in the area averaged void fraction along the axial direction. Void fraction and pressure drop are linearly related in bubbly flow regime. As shown by the pressure measurements in the previous section, pressure drop increases in the direction of flow due to both frictional and minor two-phase pressure loss across the elbow, hence causing an increase in the void fraction. In low void fraction condition, $<a_i>$ increases along the vertical section. However, as the void fraction increases, there is a decrease in $<a_i>$ along the vertical section. This happens due to the coalescence of the bubbles leading to formation of larger bubbles and hence $<a_i>$ decreases.

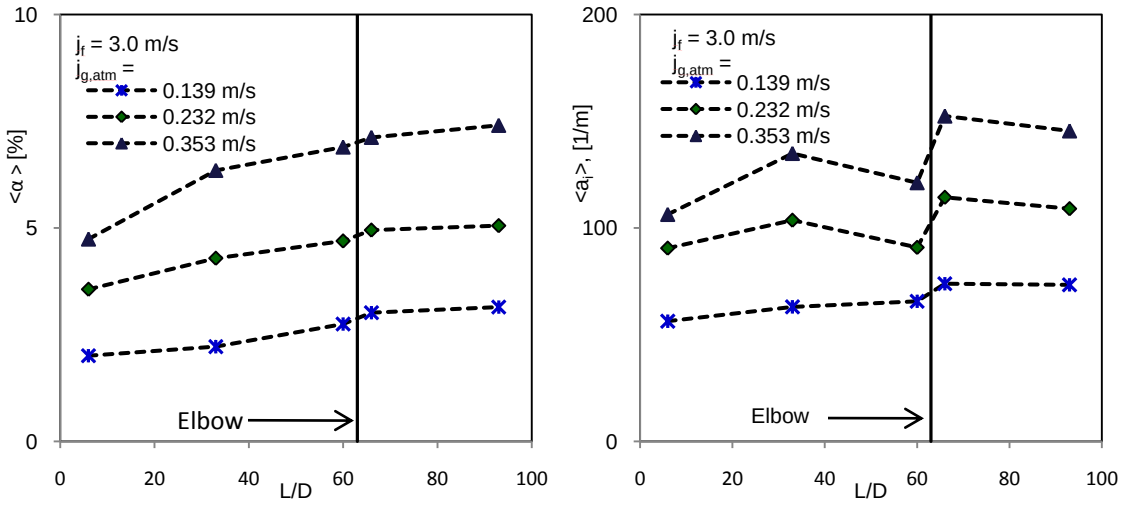

Figure **3-24**: One-dimensional transport of $<\alpha>$ and $< a_i>$ at constant liquid flow rate, j_f = 3.0 m/s and increasing gas flow rates

As the flow moves across the elbow, a steep increase in the area averaged interfacial area concentration is observed. This indicates that the 90-degree vertical elbow promotes the disintegration of the larger bubbles. This fact is also supported by the flow visualization studies as mentioned in the previous sections. This leads to the occurrence of dispersed bubbly flow in the conventional plug flow regime. In general, $<\alpha>$ and $< a_i>$ increases with increasing gas flow rate.

3.2.6 Convective acceleration:

Fig. 3-25 shows the axial development of void weighted bubble velocity. Since, the local profiles for void fraction shows wall peak in the bubble distribution in the vertical section, $<<v_g>>$ provides a better estimate of the transport of bubble velocity. The 90-degree vertical elbow causes a decrease in $<v_g>$ and $<<v_g>>$. This signifies that the bubbles are decelerated across the elbow. It is speculated that this is due to the bubbles getting stuck in the elbow and instead of getting entrained with the liquid. The gas phase creates way for the faster moving, higher momentum liquid phase. Convective deceleration acts as one of the source terms in the interfacial area transport equation. Hence, an increase in the $<a_i>$ across the elbow as shown in the previous section can also be explained based on the deceleration of the bubbles.

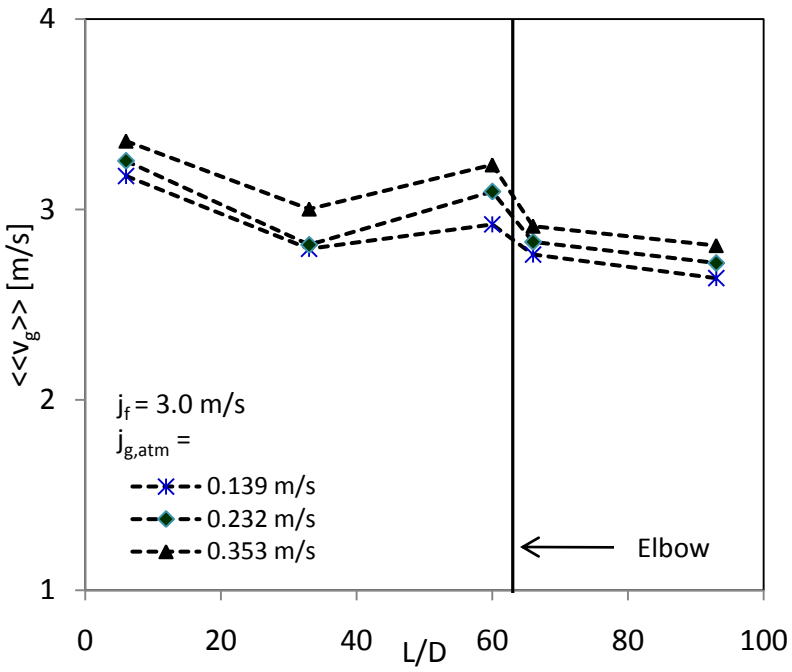

Figure **3-25**: One-dimensional transport of void weighted bubble velocity at a constant liquid flow rate, j_f = 3.0 m/s and increasing gas flow rates

Chapter 4

Summary and Future Recommendations

The geometric effects of different elbows and two-phase flow configurations on interfacial structures, their transport characteristics and other two-phase flow parameters are investigated. The experiments are performed in two separate experimental facilities and hence this study is divided in two parts based on the two-phase flow configuration.

The first set of experiments compares the effect of 90-degree and 45-degree elbows on the interfacial structures of horizontal bubbly flow. Two separate experiments are carried out using 50.3 mm inner diameter glass pipes; the first experiment being for the 90-degree elbow (L/D=206.6 from the inlet) and then a 45-degree elbow (L/D=353.5) is added for the second experiment. Local two-phase flow parameters are obtained using a double-sensor conductivity probe for 15 different flow conditions in each experiment.

In general both the elbows induce oscillations in the vertical and horizontal profiles of α and a_i. Along the vertical axis of the pipe cross-section, the elbows cause the gas phase to move toward the lower half of the cross-section, but the degree and location of the peaking position depends on the flow condition. However, in general it is found that the 45-degree elbow causes a higher degree of peaking compared to the 90-degree elbow.

Along the horizontal axis it is found that the bubbles start moving to the outer half. The peak for the 90-degree subsequently shifts from inner half to the outer half of the pipe cross-section, however, for the 45-degree experiment the peaking always occurs in the inner half of the pipe cross-section. It is interesting to note that for the 90-degree experiment, profiles of α and a_i further downstream of the elbow are very similar to the profiles immediately downstream of the 45-degree elbow. This demonstrates the characteristic difference between the two elbows, where

the elbow-effect in the 90-degree experiment is propagated and observed further downstream of the elbow.

Gas and water flow rates have a distinct effect on the horizontal and vertical profiles of interfacial structures for both the elbows. With an increase in the gas flow rate the bubble distribution immediately downstream of the elbows becomes more uniform along both axes of the pipe cross-section. Along the vertical axis, the bubbles start moving to the upper half. The peak for the 90-degree subsequently shifts from lower half to the upper half of the pipe cross-section, however, for the 45-degree experiment the peaking always occurs in the lower half of the pipe cross-section.

In nearly all flow conditions the area averaged void fraction increases across the elbow, sometimes as much as 30%. It is found that the corresponding decrease in the area averaged interfacial area concentration is as much as 45%. This shows that the elbows promote coalescence of the bubbles. Although coalescence is almost always promoted by 90-degree elbow, for 45-degree case it is dominant only for the lower gas flow rates. In contrast, at higher void fraction conditions disintegration process is dominant across the 45 degree elbow. The area averaged interfacial area concentration increases by 70%. It is found that for both the elbows, for all the run conditions the coalescence process is dominant further downstream as the flow recovers.

The behavior of void weighted bubble velocity is also void fraction dependent. For the lower void fraction conditions the bubbles accelerate across the elbow, however for the higher void fraction condition, there is a deceleration of the bubbles across the elbow. Further downstream of the elbow, gas phase tends to recover to its original velocity before the elbow. Although both the elbows have similar effect, the degree of oscillation in 90-degree elbow is greater than the 45-degree elbow.

Effect on the pressure drop is observed due to the minor losses occurring in both the elbows. In 45-degree experiment, the elbow-effect can be observed right across the elbow, however, the effect of 90-degree elbow is propagated further downstream, between L/D=225 and L/D=250. This emphasizes the characteristic difference between the 45-degree and 90-degree elbow.

In the second set of experiment, geometric effects of a 90-degree vertical elbow on interfacial structures and their transport characteristics in bubbly flow transitioning from vertical upward to horizontal in 50.4 mm inner diameter pipe sections is investigated. A high speed camera is used to capture two-phase flow movies at four different measurement locations in combinatorial channels. Modified two-phase flow regime maps are constructed in both vertical upward and first horizontal section based on extensive flow visualization studies.

Single phase liquid pressure drop is measured at nine axial locations to characterize the single-phase frictional and minor pressure loss. Analytical correlations provided by Blasius and Eto is used to estimate the frictional and minor loss. The theoretical results match experimental data within ± 5%.

Two phase pressure is measured at six axial locations across the first vertical elbow. There is a significant drop in pressure across the elbow due to the two-phase minor pressure losses. A new correlation developed by Kim et. al (2008) based on the conventional Lockhart-Martinelli approach is used to predict frictional and minor pressure loss across the elbow.

A four-sensor conductivity probe is used to measure time-averaged, local two-phase flow parameters along the test section. The local profiles for void fraction and interfacial area concentration in the vertical section are symmetric across the pipe axis in the direction of the flow. There is a strong wall peak observed in the vertical section, as the flow develops. It is also

observed that with increase in the liquid flow rate the degree of wall peaking is reduced and the bubble distribution profiles become more uniform.

As the flow moves to the horizontal section across the elbow, most of the bubbles are aligned along the horizontal axis of the pipe cross-section. This creates a dual peak or bi-peaking in the local α and a_i profiles. It is speculated that this phenomena is caused by the bubbles following the secondary flow generated by the 90-degree vertical elbow. With an increase in the gas flow rate, the peaking becomes higher towards the inner half of the pipe cross-section. Moving further downstream, the elbow-effect starts to diminish and bubbles migrate to the top half of the pipe cross-section, due to the dominant buoyancy force.

One-dimensional transport of interfacial structures shows that the elbow promotes bubble interaction mechanisms, namely causes the disintegration of the larger bubbles. This effect is consistent with the flow visualization studies, where the flow regime transition boundary from plug to dispersed bubbly moves to lower liquid flow rates caused by the breakup of the larger bubbles.

Based on the above studies, following recommendations are suggested for the future work:

- Generating comprehensive database on the effect of 90-degree elbow by including additional flow conditions to study the effect of gas and liquid flow rates
- Including the measurements at additional port locations downstream of the elbow
- Including the measurements in the vertical downward section of the combinatorial channels
- Implementing two-phase flow pressure drop correlation developed by Kim et. al (2008)
- Implementing interfacial area transport equation for vertical upward to horizontal two-phase flow

REFERENCES

Blasius, H., 1913, Das Ähnlichkeitsgesetz bei reibungsyorgängen in flüssigkeiten, *Ver. Dtsch. Ing. Forschungsh*, pp. 131.

Franca, F. and Lahey Jr., R.T., 1992, The use of drift-flux techniques for the analysis of horizontal two-phase flows, *Int. J. Multiphase Flow*, **18**(6), pp. 787-801.

Ishii, M., Kim, S. and Uhle, J., 2000, Interfacial Area Transport: Data and Models, *OECD/CSNI Workshop on Advanced Thermal-Hydraulics and Neutronics Codes: Current and Future Applications*, Barcelona, Spain

Ishii, M., Kim, S. and Uhle, J., 2000, Interfacial Area Transport: Model development and benchmark experiments, *Int. J. Heat and Mass Transfer*, 45, N.15, pp. 3111-3123.

Ishii, M., 1975, Thermo-fluid dynamic theory of two-phase flow, *Eyrolles*, Paris

Ishii, M., 1977, One-dimensional drift flux model and constitutive equations for relative motion between phases in various two-phase flow regimes, *Report ANL*, pp. 77-47

Ishii, M. and Mishima, K., 1980, Study of two-fluid model and interfacial area, *ANL-80-111, NUREG/CR-1873,* Argonne National Laboratory, Argonne, Ill

Iskandrani, A. and Kojasoy, G., 2001, Local void fraction and velocity field description in horizontal bubbly flow," *Nuclear Engineering Design*, **204**, pp. 117-128.

Ito, H., 1960, Pressure losses in smooth pipe bends, *Journal of Basic Engineering*, Vol.82, pp. 131.

Kim, S., Fu, X. Y., Wang, X. and Ishii, M., 2000, Development of the miniaturized four-sensor conductivity probe and the signal processing scheme, *Int. J. Heat and Mass Transfer*, Vol. 43, pp. 4101-4118.

Kim, S., Park, J. H., Kojasoy, G. and J. Kelly, 2007, Interfacial structures in horizontal bubbly flow with 90-degree bend, *Nuclear Engineering and Design*, **237**, pp. 2105-2113.

Kim, S., Park, J. H., Kojasoy, G. and J. Kelly, 2006, Two-phase frictional pressure loss in horizontal bubbly flow with 90-degree bend, Proceedings of *14th International Conference on Nuclear Engineering (ICONE-14)*, Miami, FL.

Kim, S., Kojasoy, G. and Guo, T., 2008, Two-phase minor loss in horizontal bubbly flow with elbows: 45º and 90º elbows, *Nuclear Engineering and Design*, NED-5167

Kocamustafaogullari, G., Huang, W. D. and Razi, J., 1994, Measurement and modeling of average void fraction, bubble size and interfacial area, *Nuclear Engineering Design*, **148**, pp. 437-453.

Lewis, S., Fu, W. L., and Kojasoy, G., 2002, Internal flow structure description of slug flow-pattern in horizontal pipe, *Int. J. Heat and Mass Transfer*, **45**, pp. 3879-3910.

Lockhart, R. W and Martinelli, R. C, 1949, Proposed correlation of data for isothermal two-phase two-component flow in pipes, *Chem. Eng. Prog.*, Vol. 45, pp. 39.

Mandhane, J. M., Gregory, G. A. and Aziz, K., 1974, A flow pattern map for gas-liquid flow in horizontal pipes, *Int. J. Multiphase Flow*, Vol.1, pp. 537.

Rouhani, S. Z. and Sohal, M. S., 1982, Two-phase flow patterns: A review of research results, *Progress in Nuclear Energy*, Vol. 11, No. 3, pp. 219-259.

Salcudean, M. E., Groeneveld, D. C. and Leung, L. K. H., 1983, Effect of flow obstruction geometry on pressure drop in horizontal air-water flow, *Int. J. Multiphase Flow*, **9**(1), pp. 73-85.

Salcudean, M. E. and Leung, L. K. H., 1988, Two-phase pressure drop through obstructions, *Nuclear Engineering Design*, **105**, pp. 349-361 (1988)

Sharma, S., Lewis, S., and Kojasoy, G., 1998, Local studies in horizontal gas-liquid slug flow, *Nuclear Engineering Design*, **184**, pp. 305-318 (1998).

Spedding, P. L. and Benard, E., 2007, Gas-liquid two-phase flow through a vertical 90º elbow bend, *Experimental Thermal and Fluid Science*, Vol. 31, pp. 761-769

Talley, J. D, Kim, S., Guo, T., Kojasoy, G., 2009, "Geometric effects of 45-degree elbow in horizontal air-water bubbly flow", *Nuclear Technology*, Vol. 167 (1), pp. 2-12

Taitel, Y. and Dukler, A. E., 1976, A Model for Predicting Flow Regime Transitions in Horizontal and Near Horizontal Gas-Liquid Flow, *AIChE Journal*, **22**(1), pp. 47-55.

Taitel, Y. and Duckler, A. E., 1976, A model for predicting flow regime transition in horizontal and near horizontal gas liquid flow, *AIChE J.*, Vol. 22, pp. 47-55

Wang, C., Chen, I. Y., Yang, Y. and Hu, R., 2004, Influence of horizontal return bend on the two-phase flow pattern in small diameter pipes, *Experimental Thermal and Fluid Sci.*, **28**, pp. 145-152.

Zuber, N. and Findlay, J. A., 1965, Average volumetric concentration in two-phase flow systems, *ASME Journal of Heat Transfer*, Vol. 87, pp. 453-468.

Appendix A1

Comparison of Pressure Drop Across the Elbows

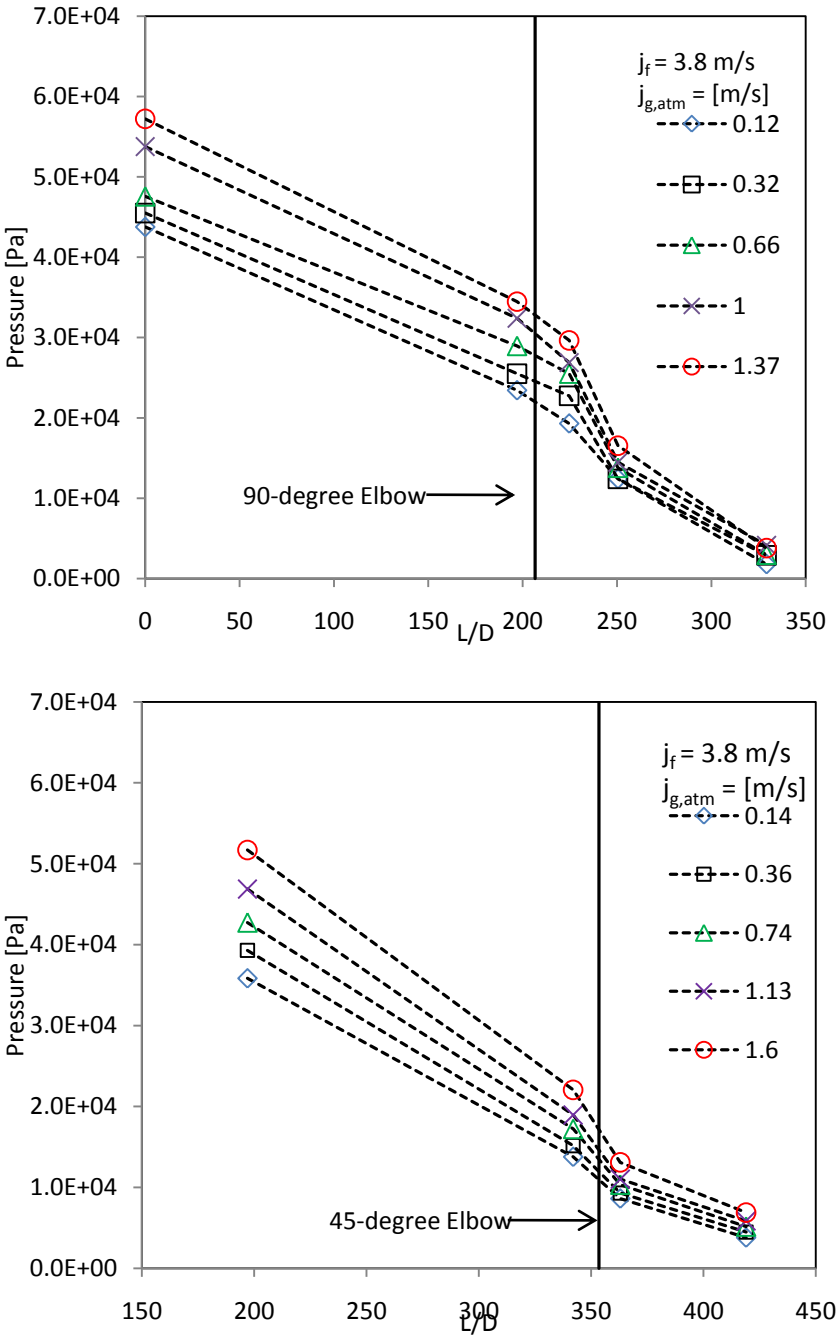

Figure **A1-1**: Change in the local gage pressure measured along the axial direction of the flow with different gas flow rates and constant liquid flow rate; j_f = 3.8 m/s (vertical line shows the position of the elbows)

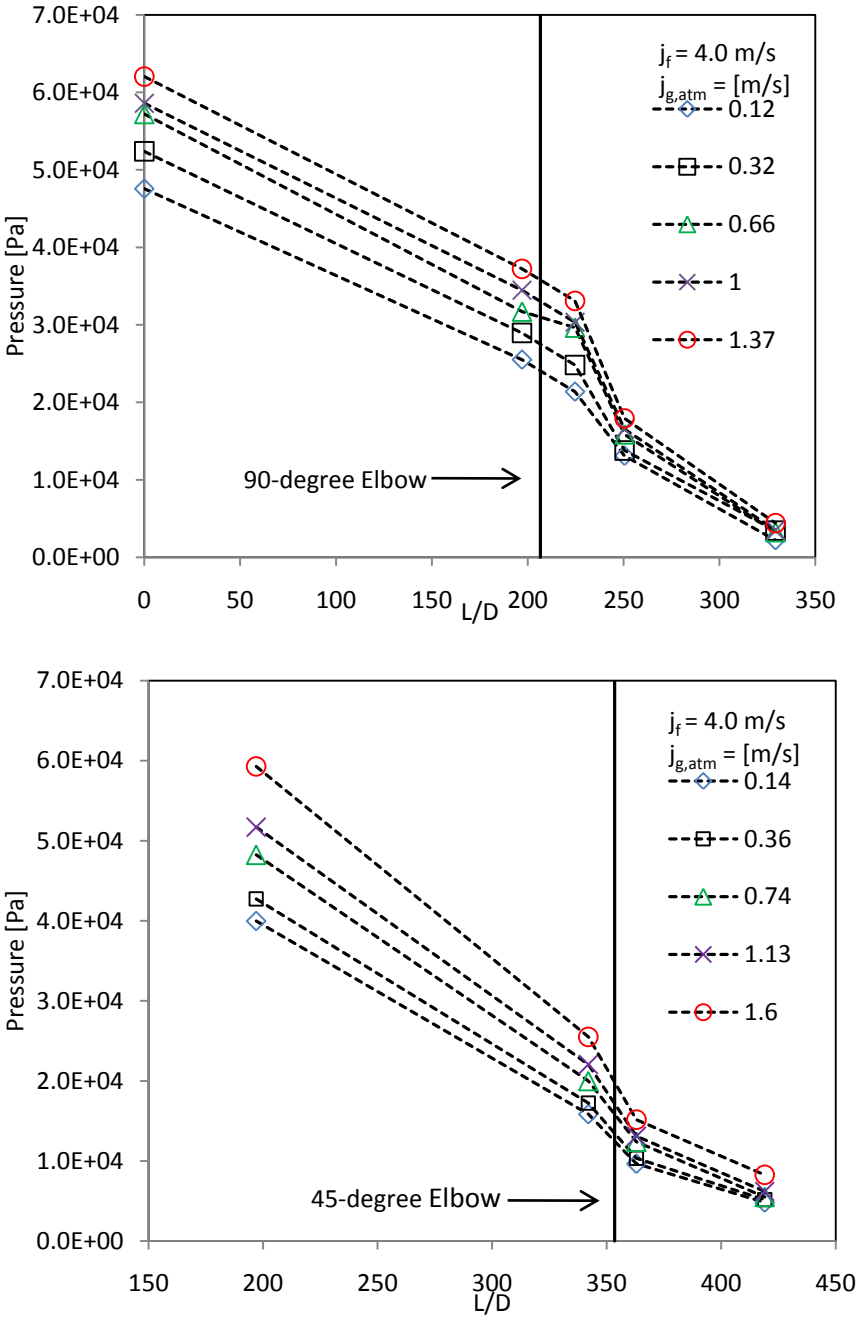

Figure **A1-2**: Change in the local gage pressure measured along the axial direction of the flow for different gas flow rates and constant liquid flow rate; j_f = 4.0 m/s (vertical line shows the position of the elbows)

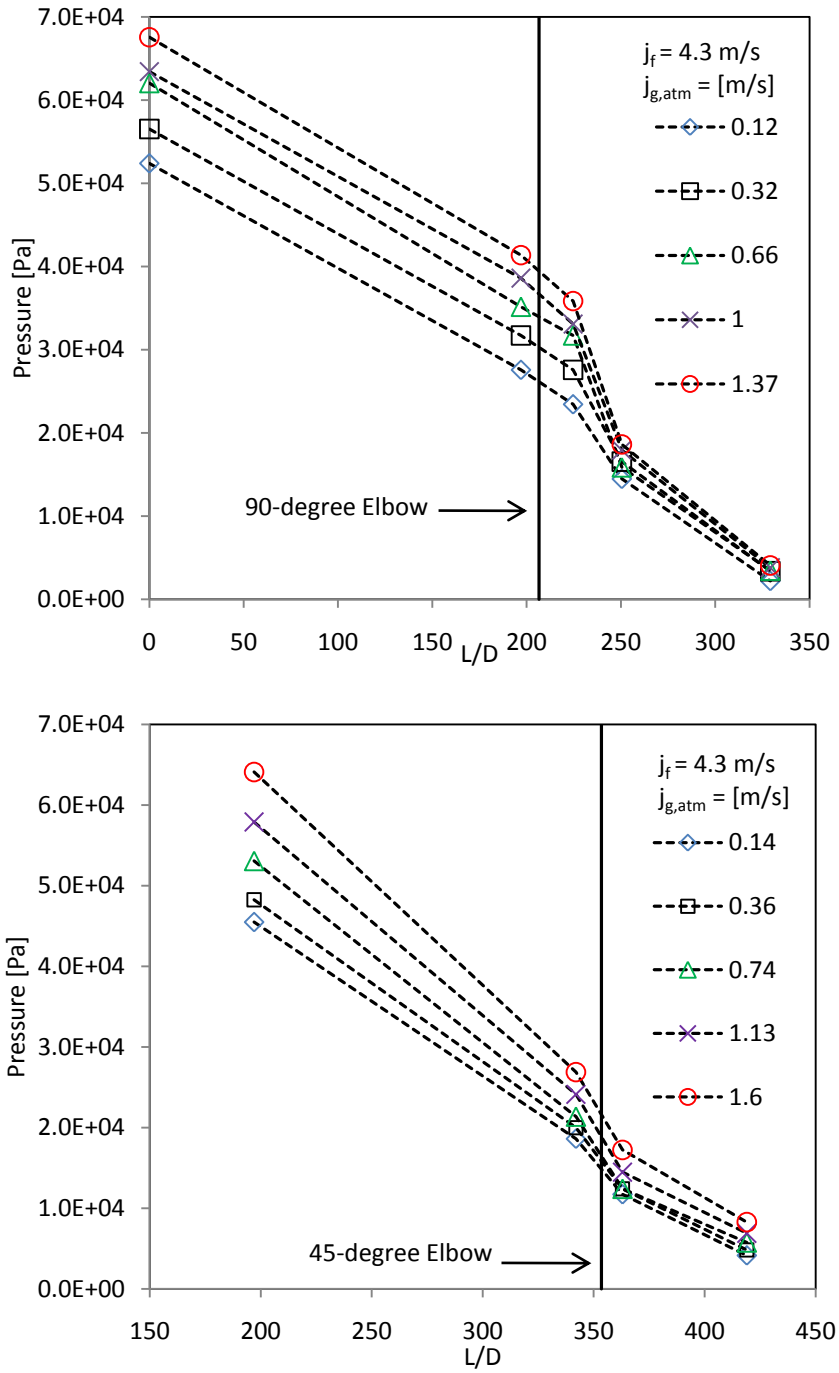

Figure **A1-3**: Change in the local gage pressure measured along the axial direction of the flow at different gas flow rates and constant liquid flow rate; j_f = 4.3 m/s (vertical line shows the position of the elbows)

Appendix A2

Comparison of Local Interfacial Structures

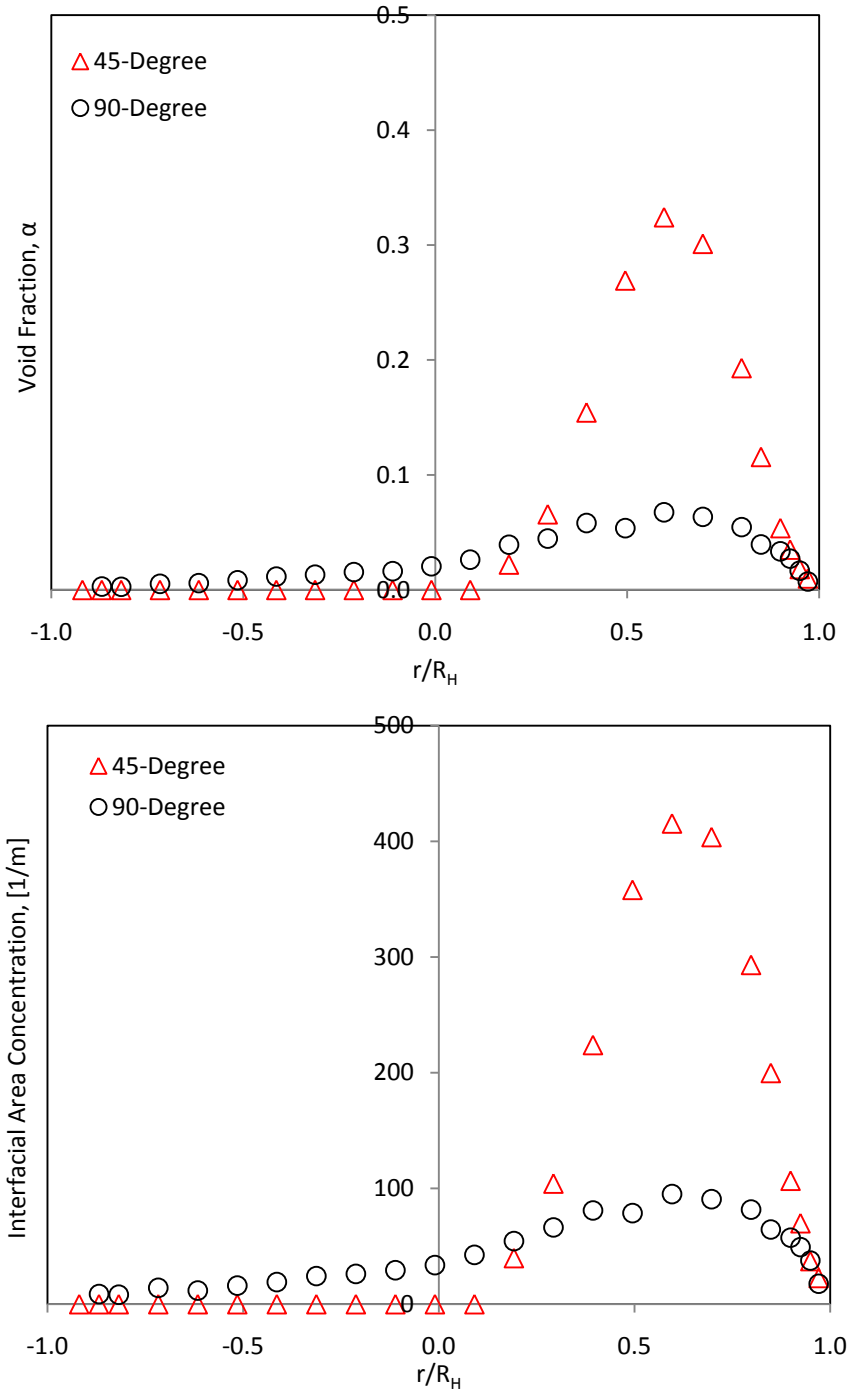

Figure **A2-1**: Comparison of local horizontal α and a_i profiles for 45-degree and 90-degree elbows at $j_{g,atm}$= 0.1 m/s; j_f=3.8 m/s

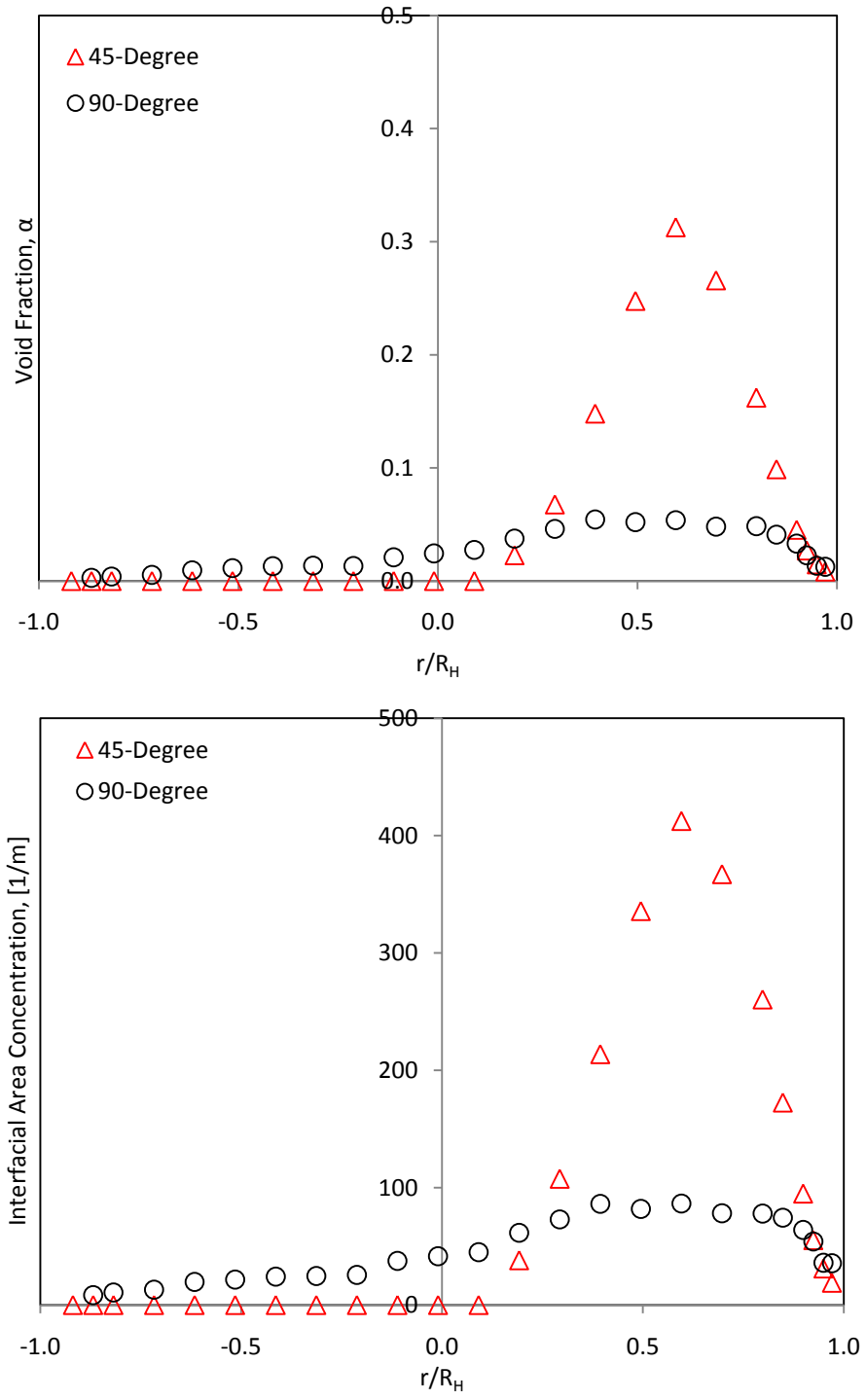

Figure **A2-2**: Comparison of local horizontal α and a_i profiles for 45-degree and 90-degree elbows at $j_{g,atm}$= 0.1 m/s; j_f=4.0 m/s

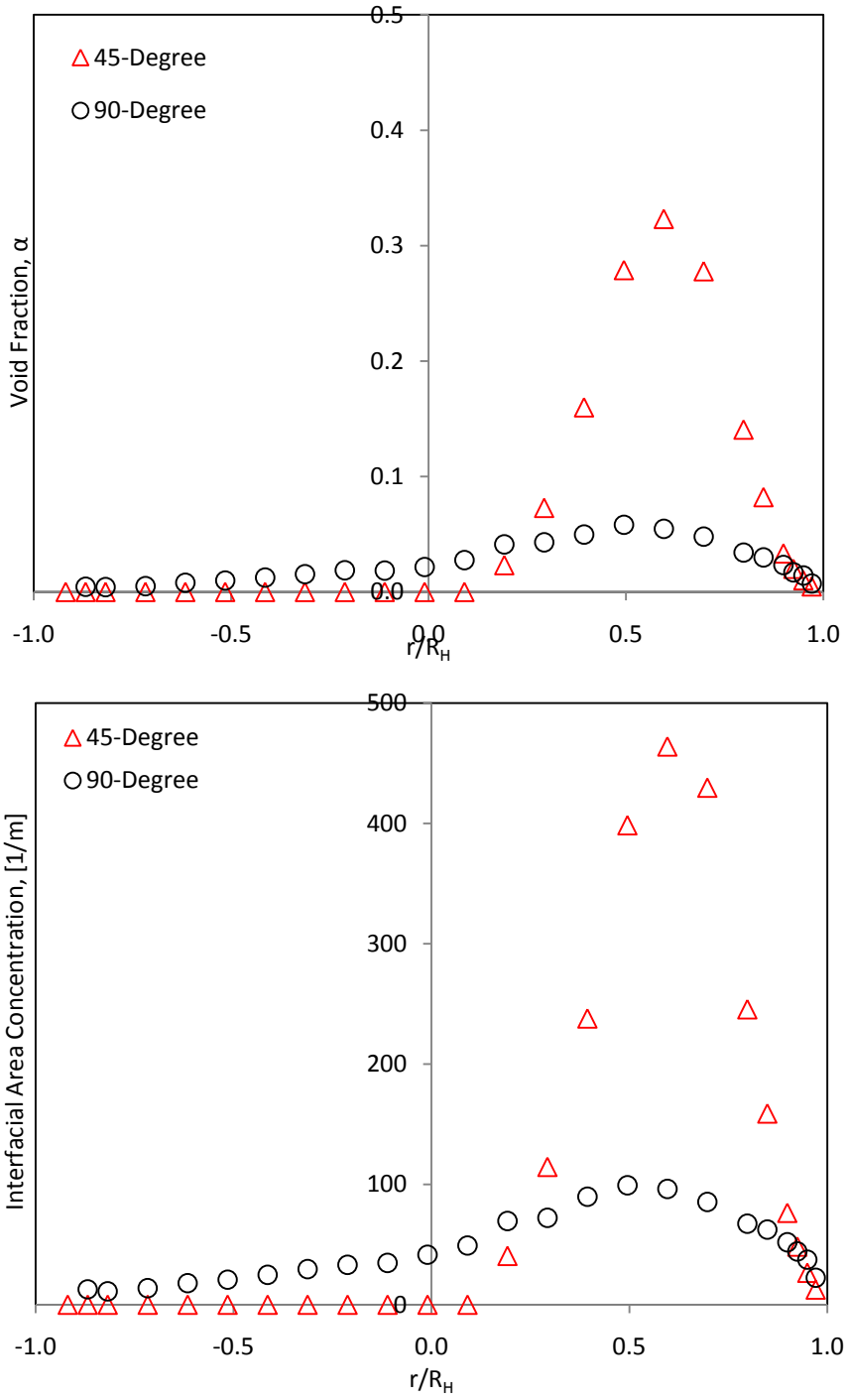

Figure **A2-3**: Comparison of local horizontal α and a_i profiles for 45-degree and 90-degree elbows at $j_{g,atm}$= 0.1 m/s; j_f=4.3 m/s

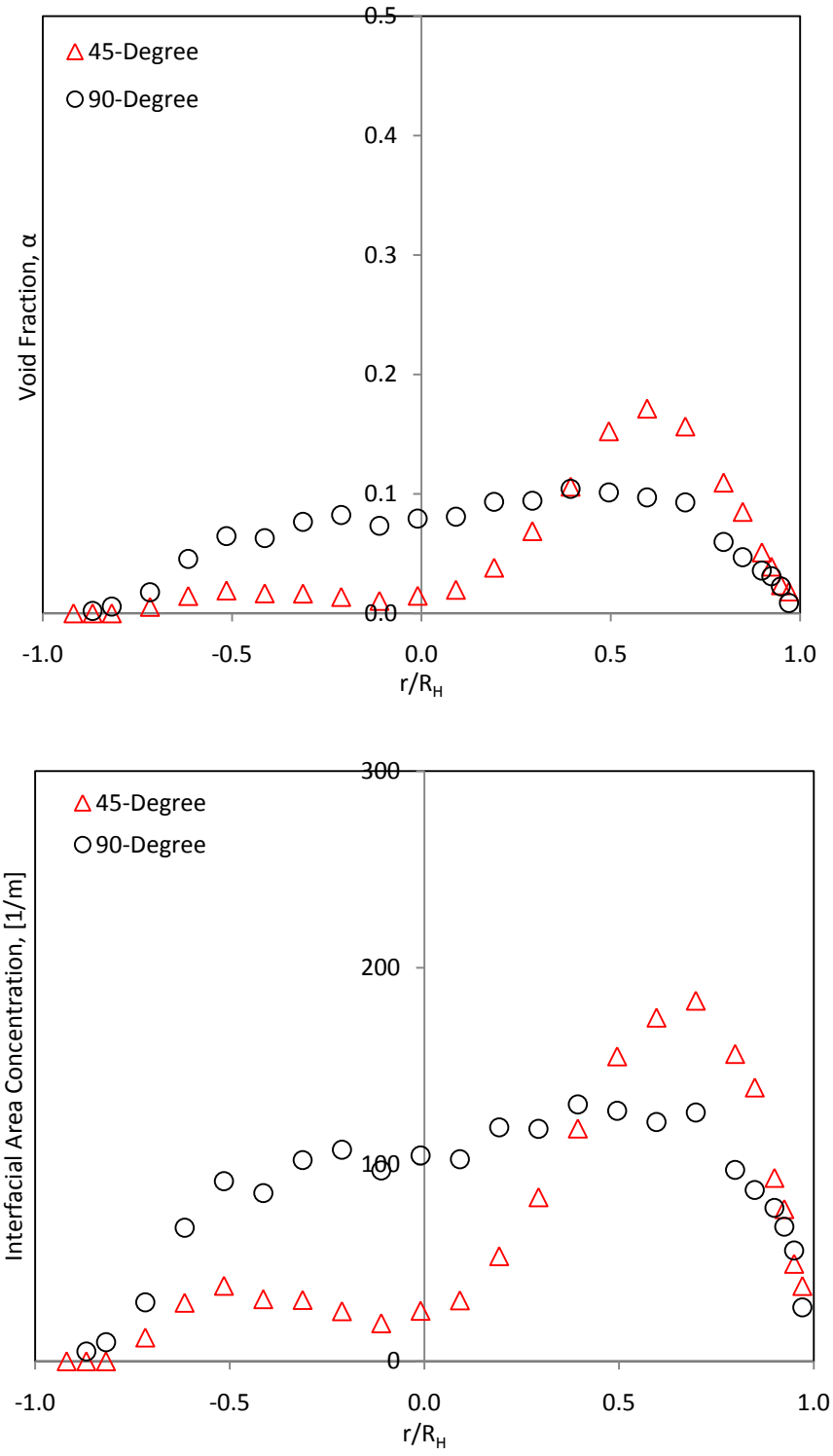

Figure **A2-4**: Comparison of local horizontal α and a_i profiles for 45-degree and 90-degree elbows at $j_{g,atm}$= 0.3 m/s; j_f=3.8 m/s

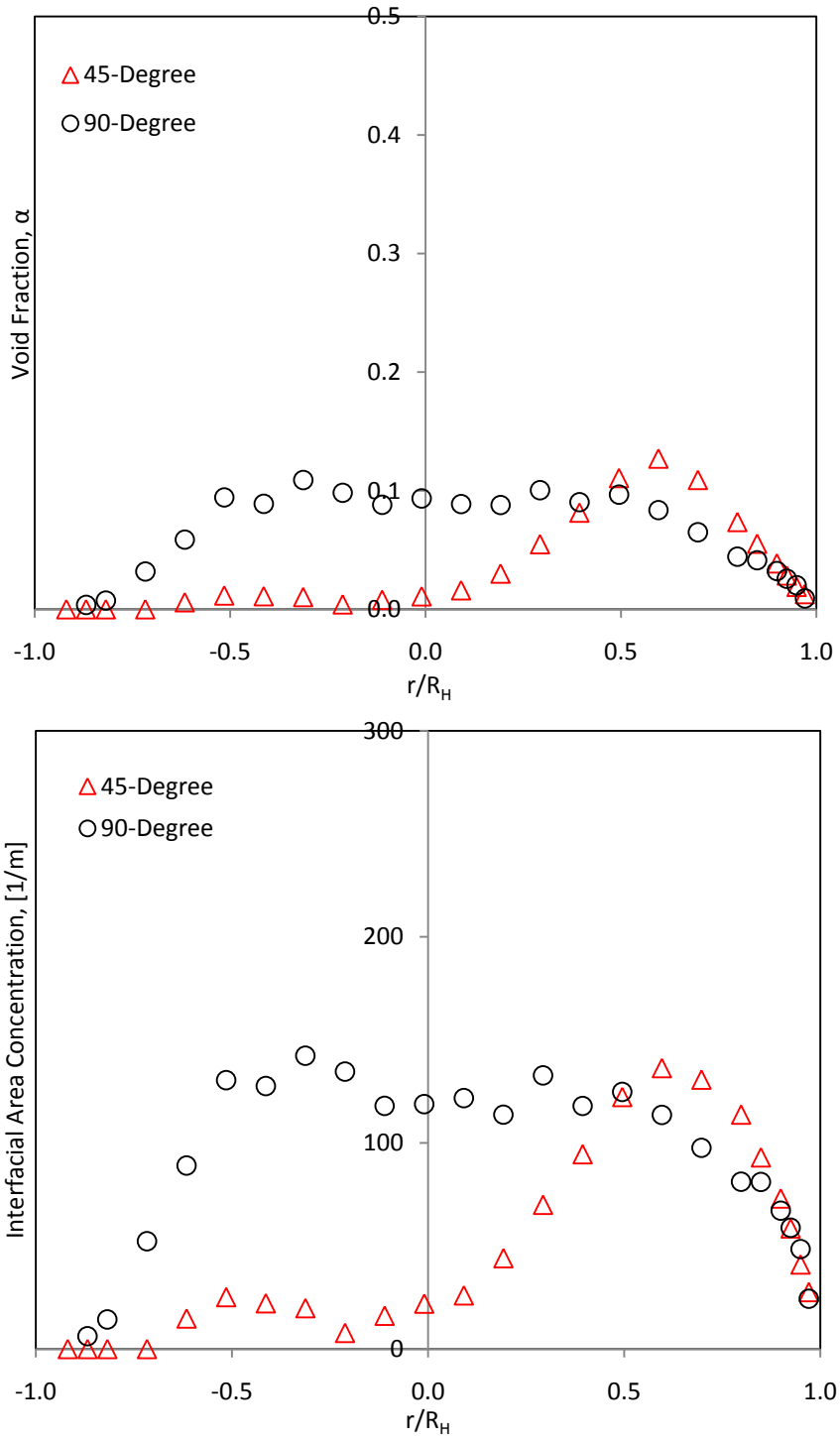

Figure **A2-5**: Comparison of local horizontal α and a_i profiles for 45-degree and 90-degree elbows at $j_{g,atm}$= 0.3 m/s; j_f=4.0 m/s

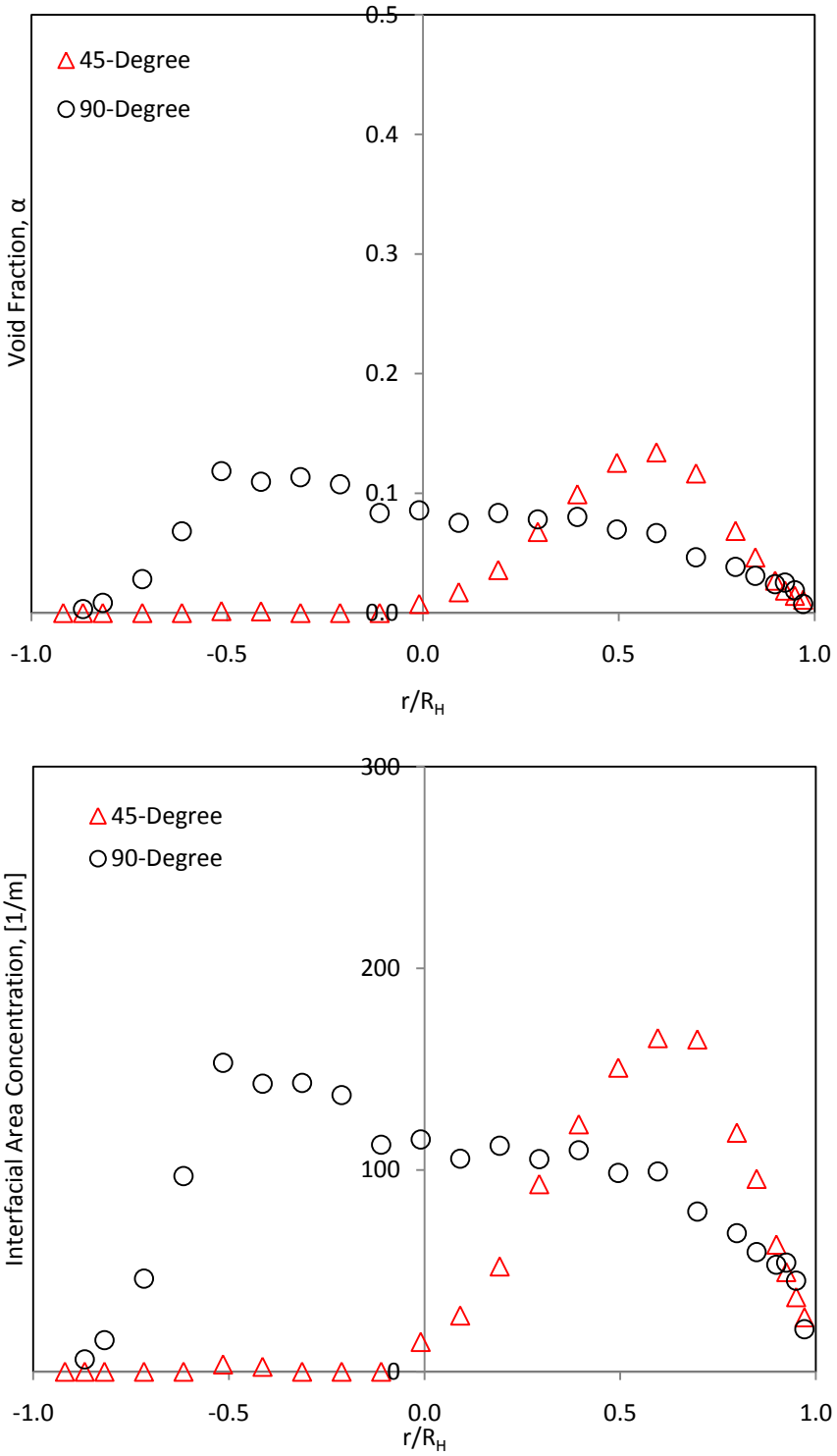

Figure **A2-6**: Comparison of local horizontal α and a_i profiles for 45-degree and 90-degree elbows at $j_{g,atm}$= 0.3 m/s; j_f=4.3 m/s

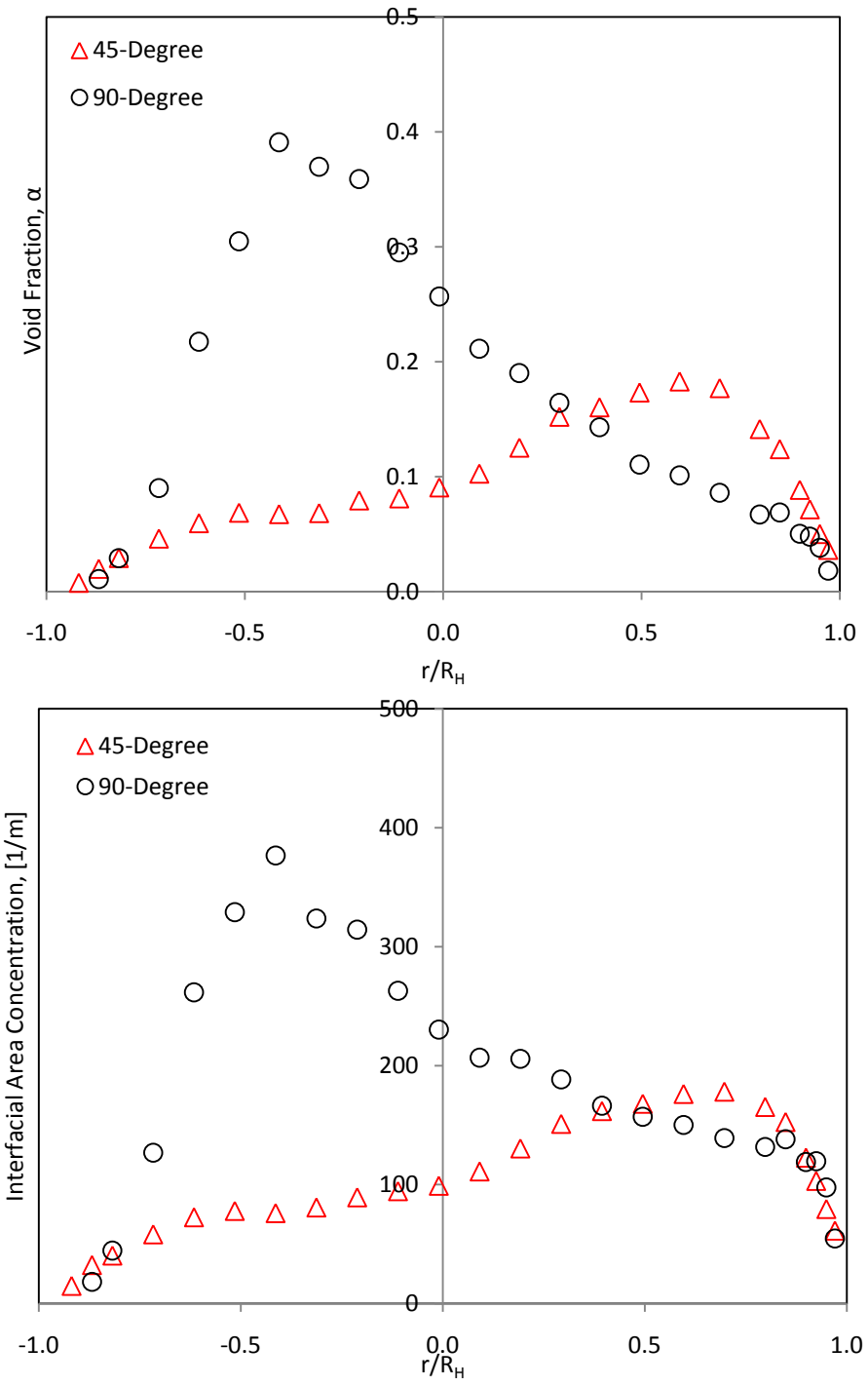

Figure **A2-7**: Comparison of local horizontal α and a_i profiles for 45-degree and 90-degree elbows at $j_{g,atm}$= 0.7 m/s; j_f=3.8 m/s

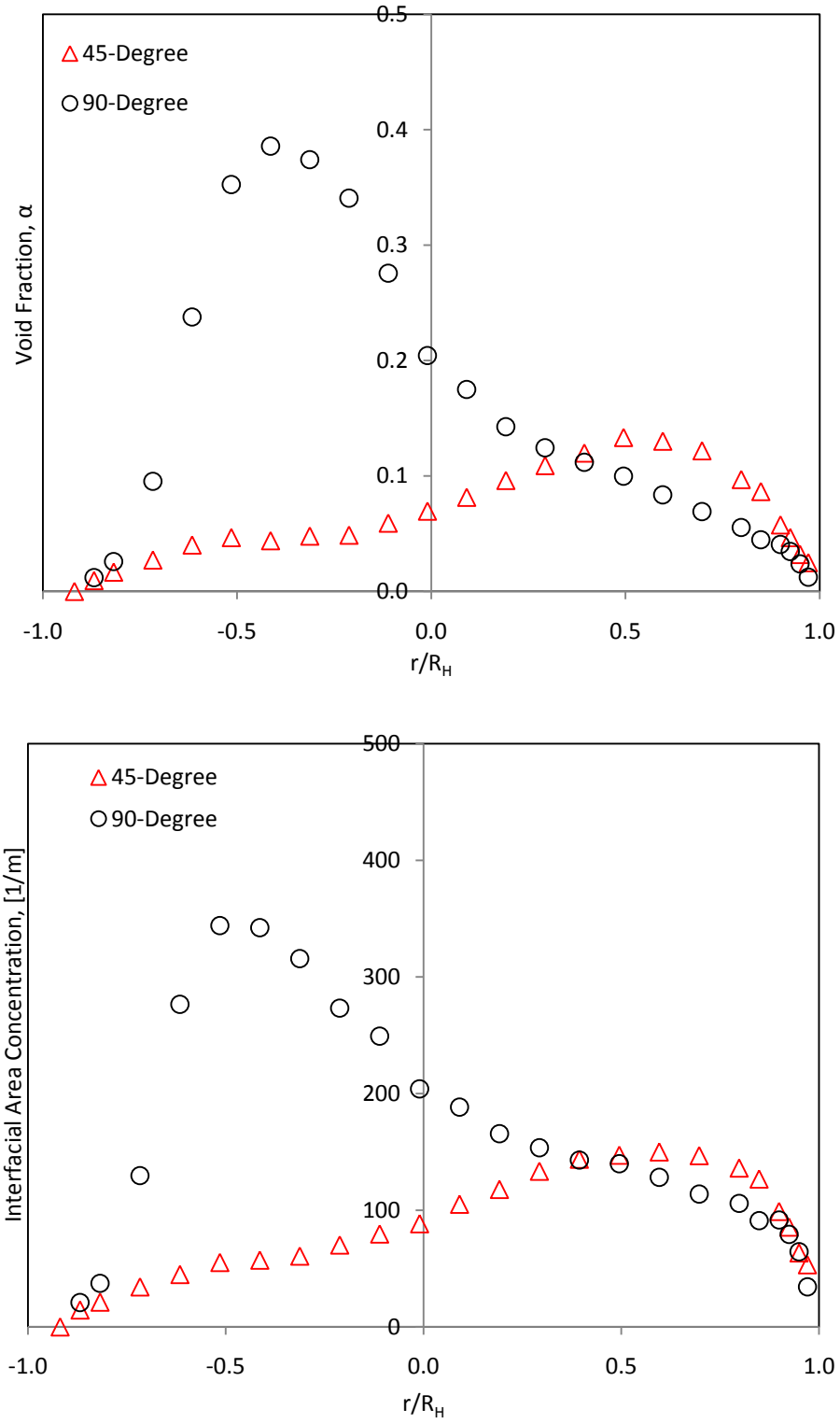

Figure **A2-8**: Comparison of local horizontal α and a_i profiles for 45-degree and 90-degree elbows at $j_{g,atm}$= 0.7 m/s; j_f=4.0 m/s

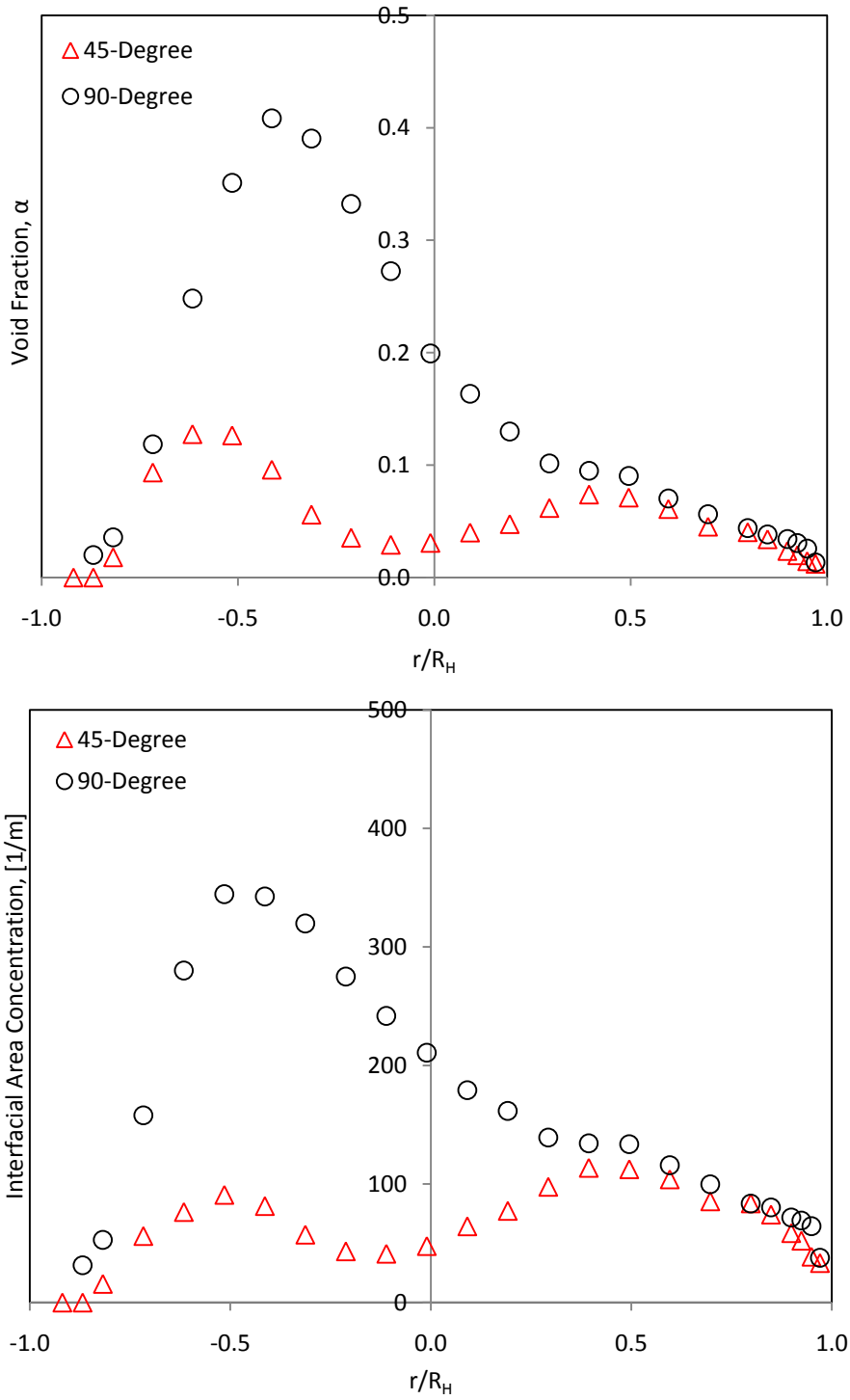

Figure **A2-9**: Comparison of local horizontal α and a_i profiles for 45-degree and 90-degree elbows at $j_{g,atm}$= 0.7 m/s; j_f=4.3 m/s

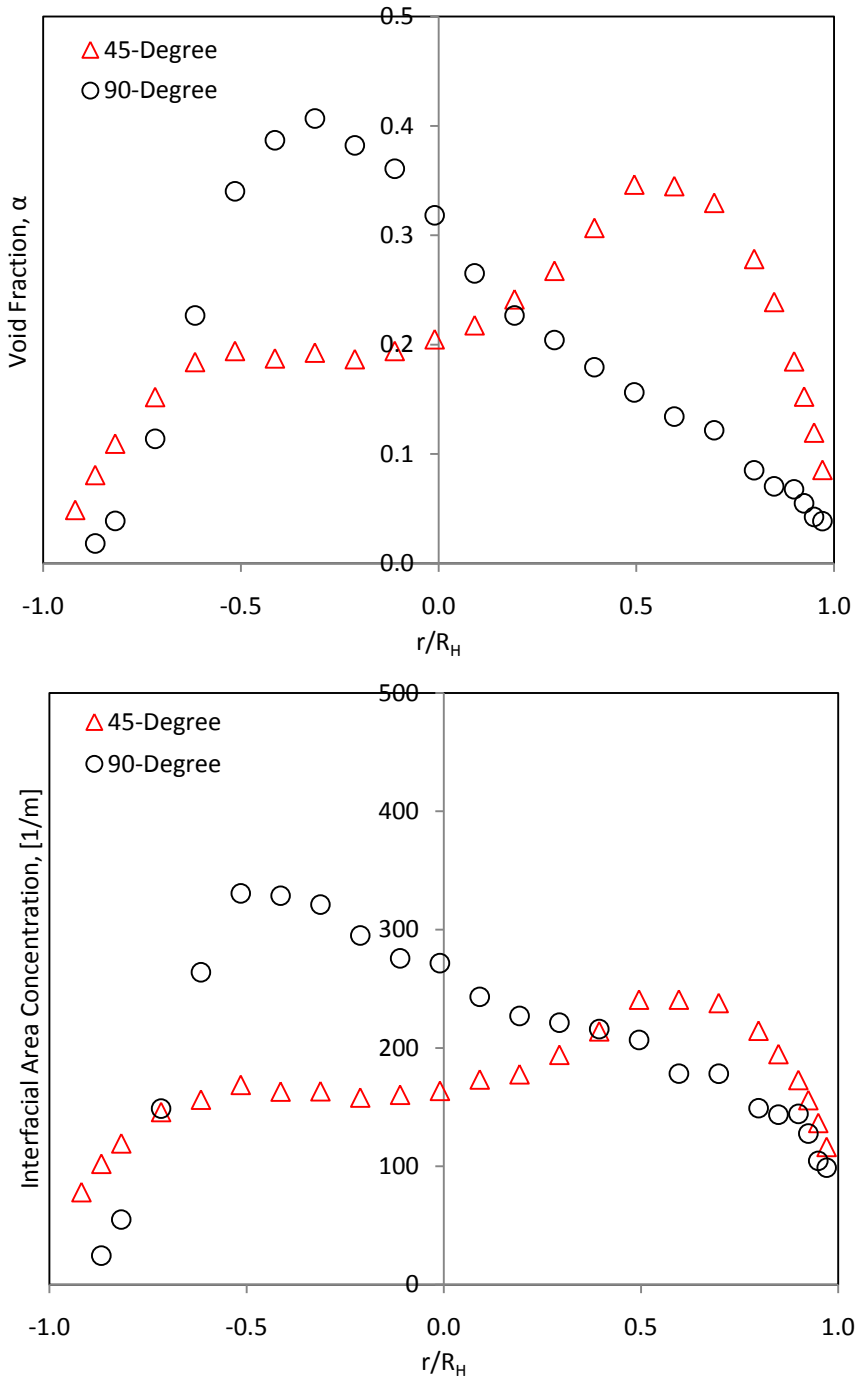

Figure **A2-10**: Comparison of local horizontal α and a_i profiles for 45-degree and 90-degree elbows at $j_{g,atm}$= 1.0 m/s; j_f=3.8 m/s

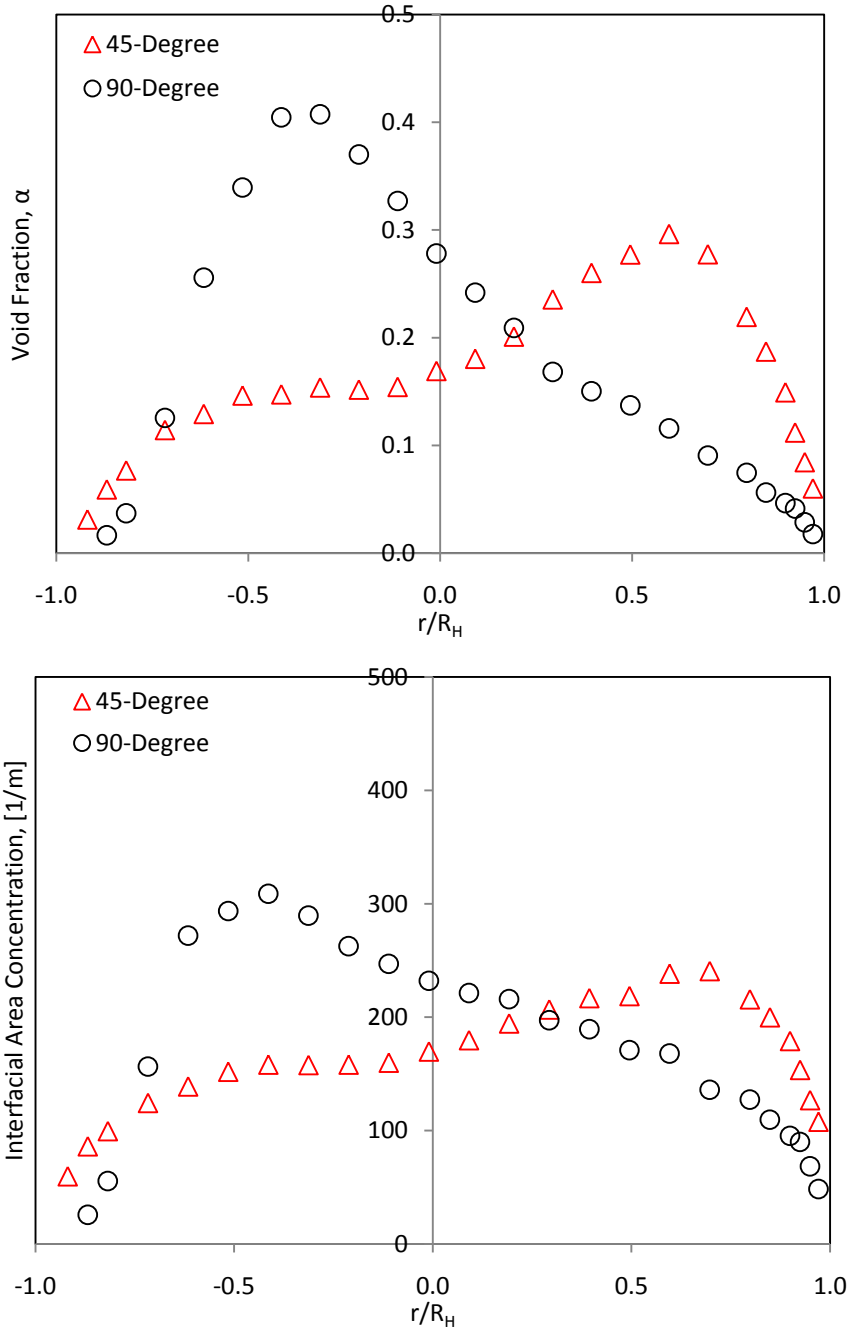

Figure **A2-11**: Comparison of local horizontal α and a_i profiles for 45-degree and 90-degree elbows at $j_{g,atm}$= 1.0 m/s; j_f=4.0 m/s

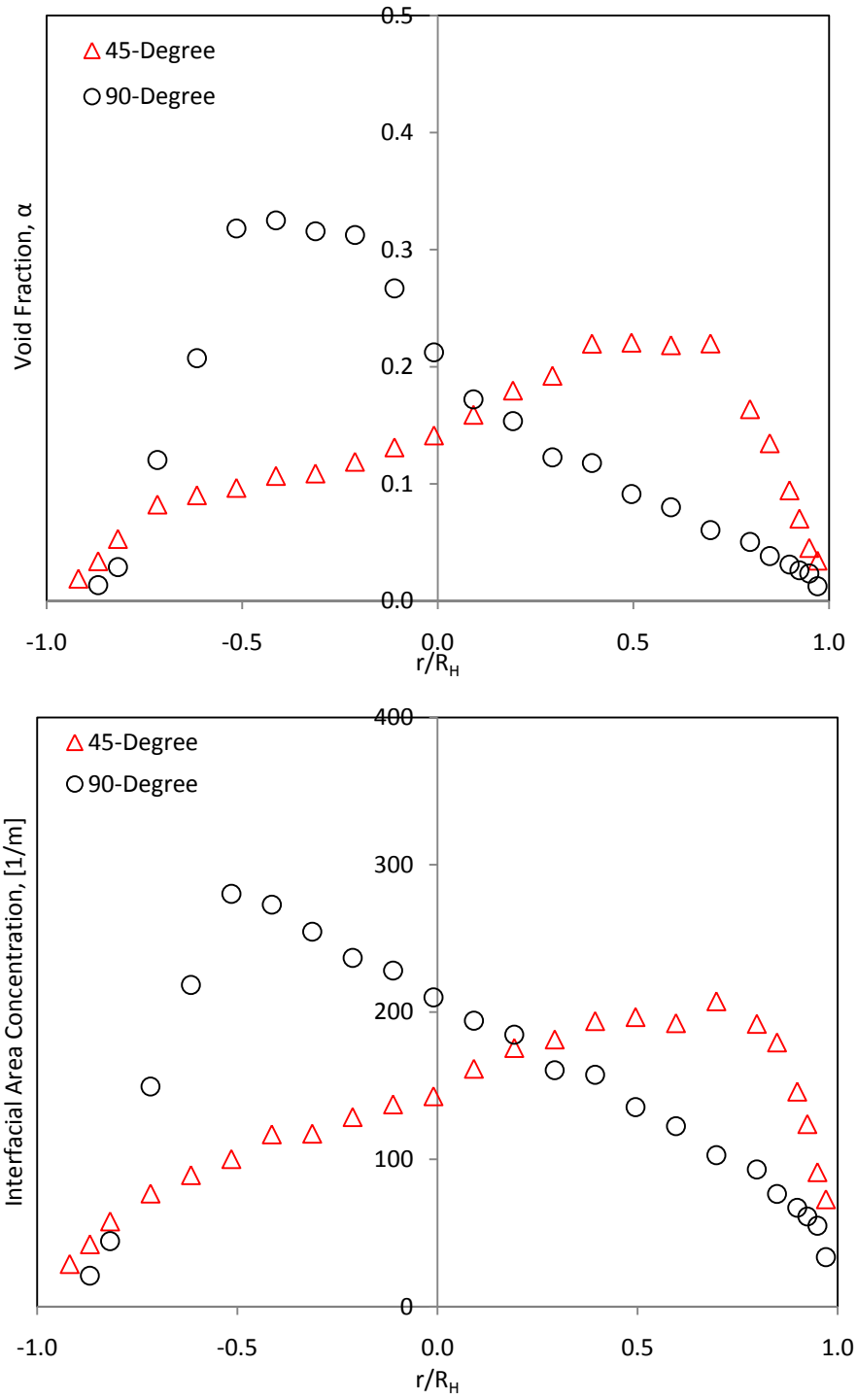

Figure **A2-12**: Comparison of local horizontal α and a_i profiles for 45-degree and 90-degree elbows at $j_{g,atm}$= 1.0 m/s; j_f=4.3 m/s

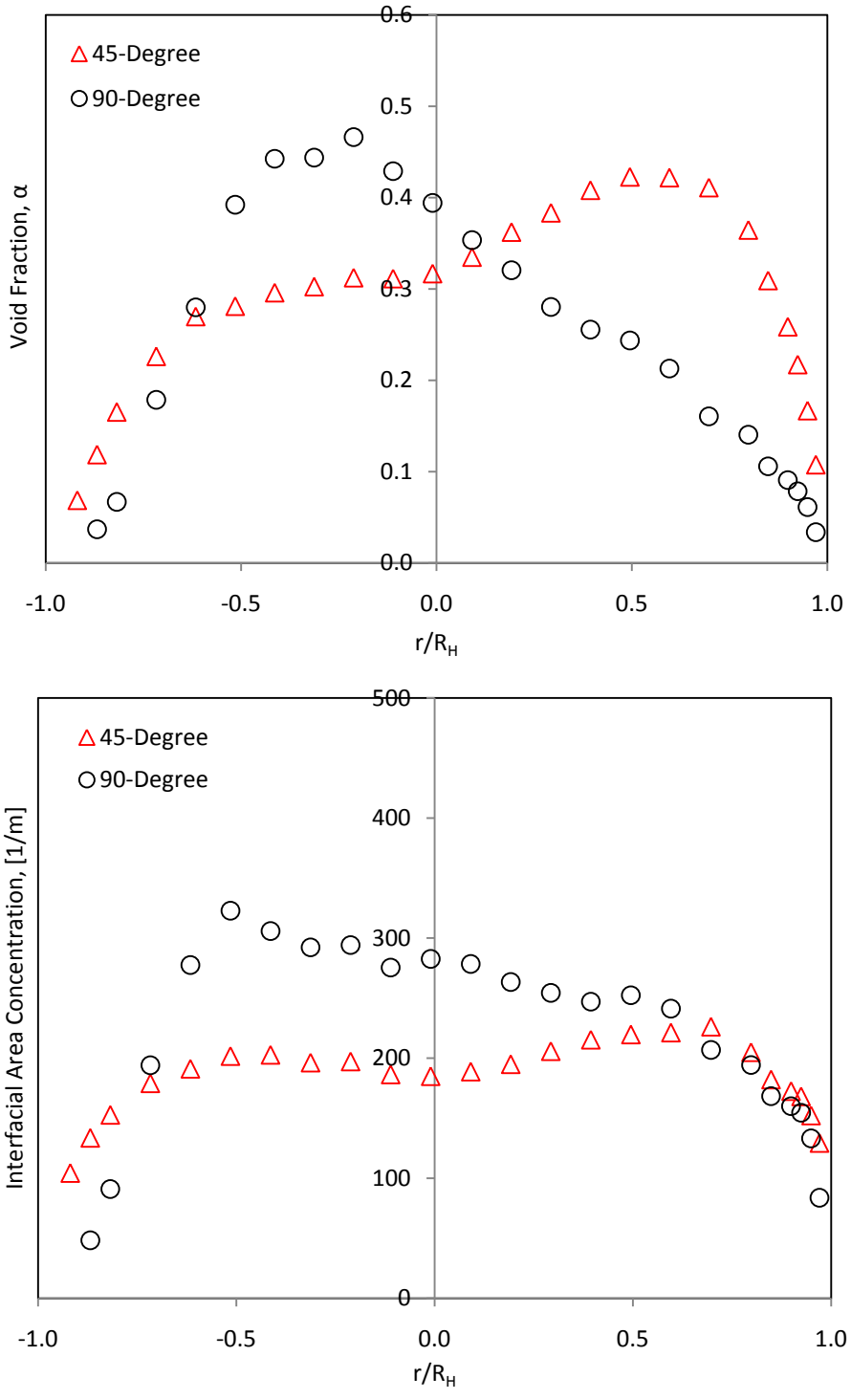

Figure **A2-13**: Comparison of local horizontal α and a_i profiles for 45-degree and 90-degree elbows at $j_{g,atm}$= 1.3 m/s; j_f=3.8 m/s

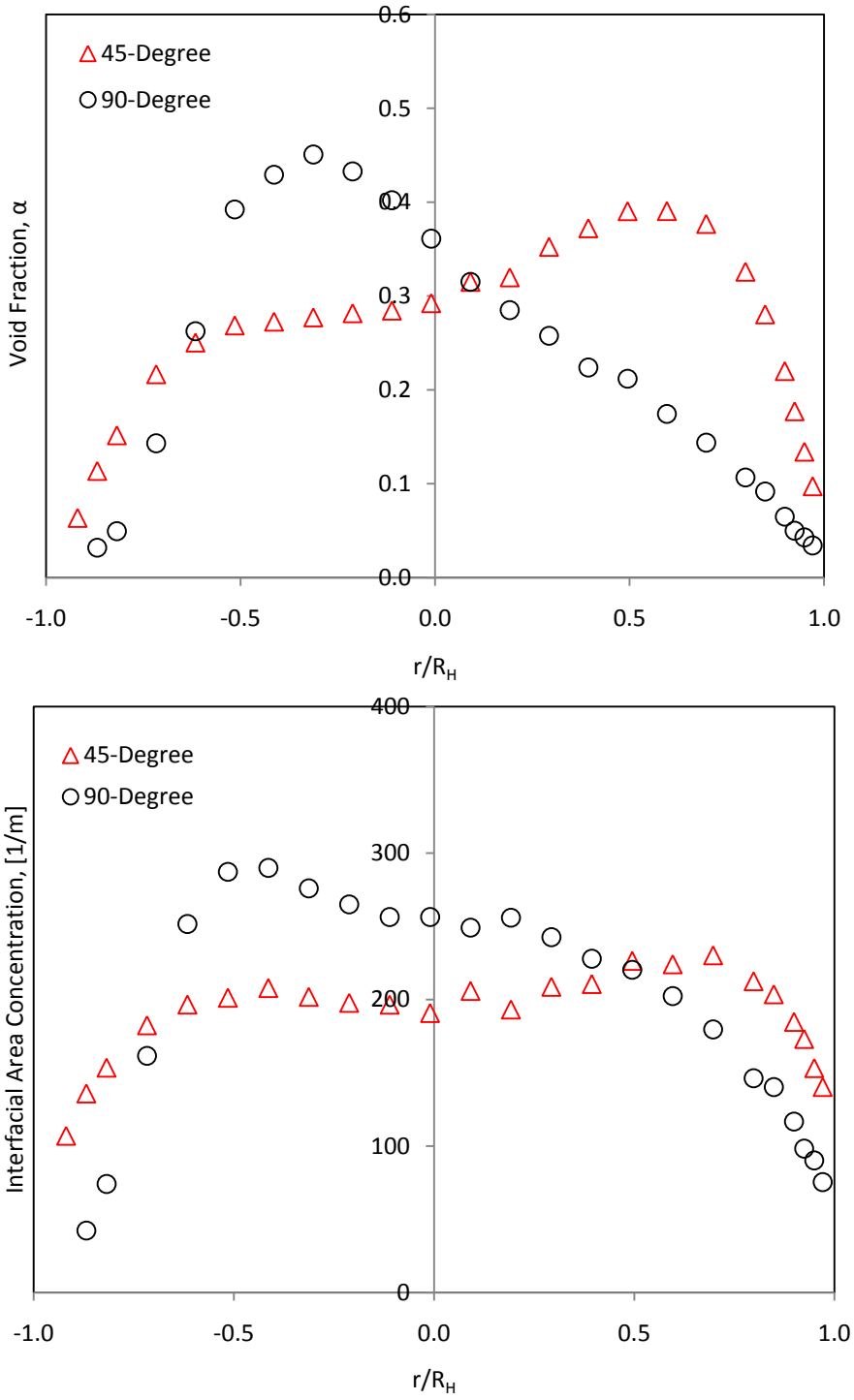

Figure **A2-14**: Comparison of local horizontal α and a_i profiles for 45-degree and 90-degree elbows at $j_{g,atm}$= 1.3 m/s; j_f=4.0 m/s

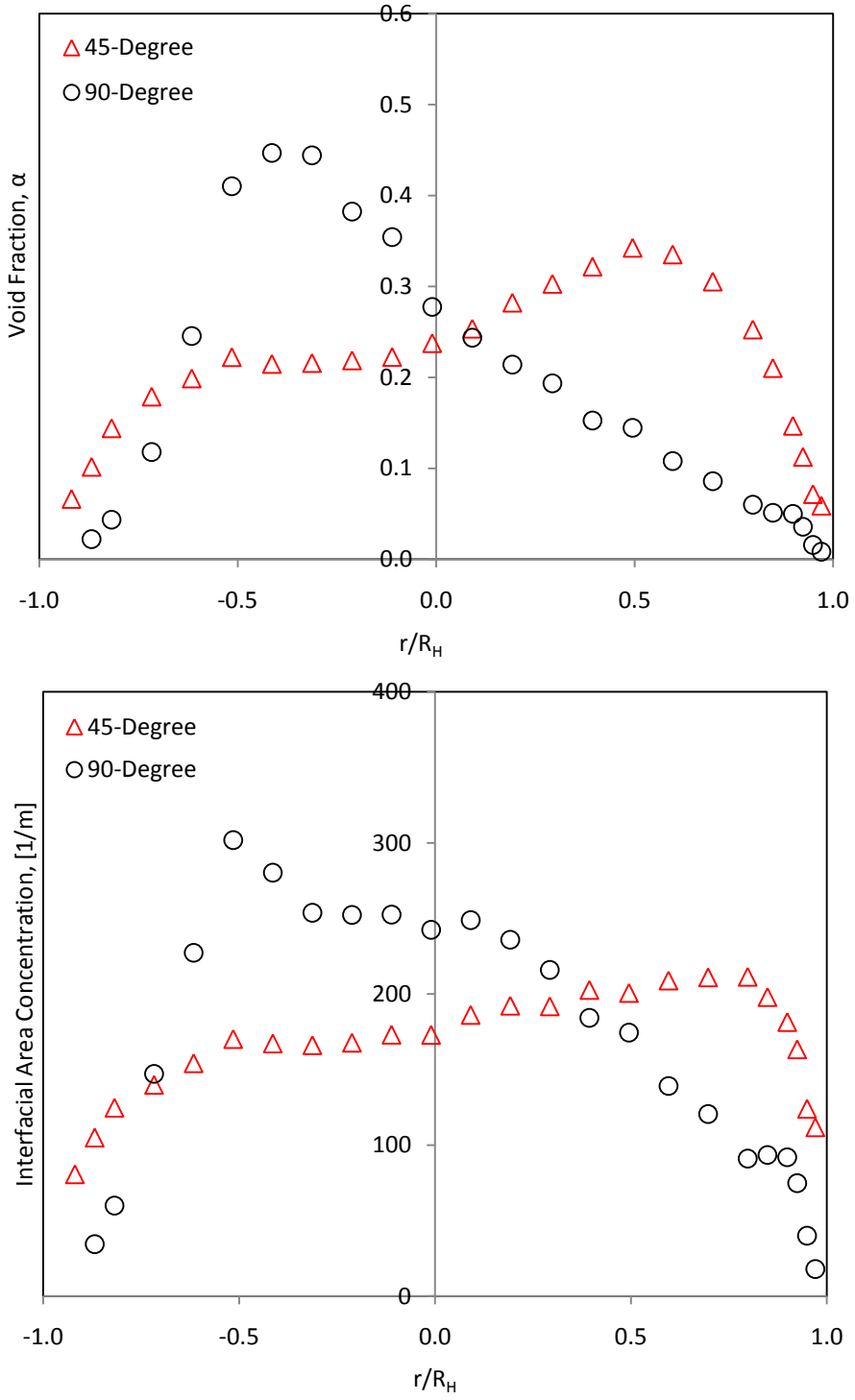

Figure **A2-15**: Comparison of local horizontal α and a_i profiles for 45-degree and 90-degree elbows at $j_{g,atm}$= 1.3 m/s; j_f=4.3 m/s

Appendix A3

Effect of Gas Flow Rate on Horizontal Profiles

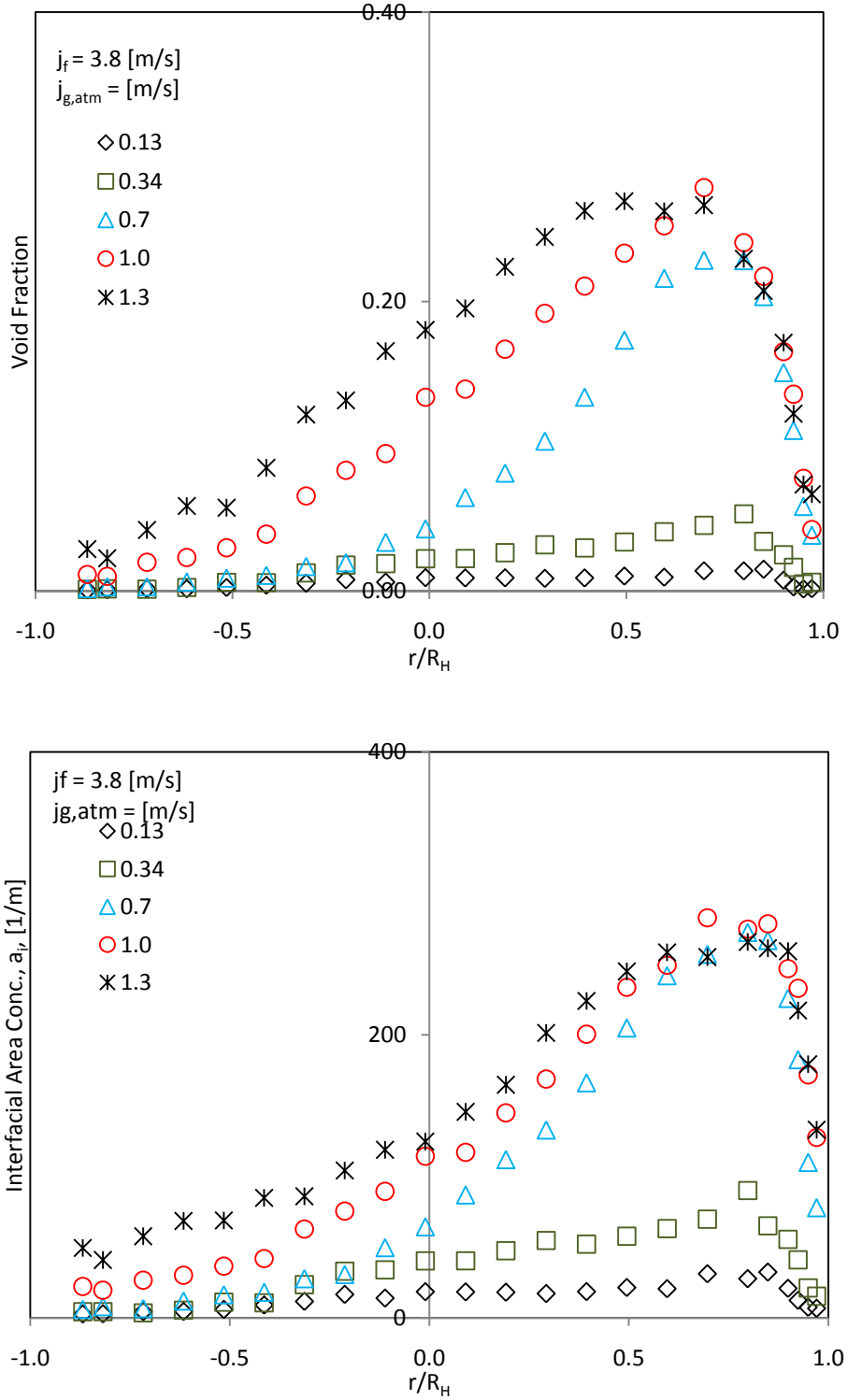

Figure **A3-1**: Effect of the increasing gas flow rate on the horizontal α and a_i profiles for 90-degree elbow at constant liquid flow rate; j_f = 3.8 m/s at L/D = 250

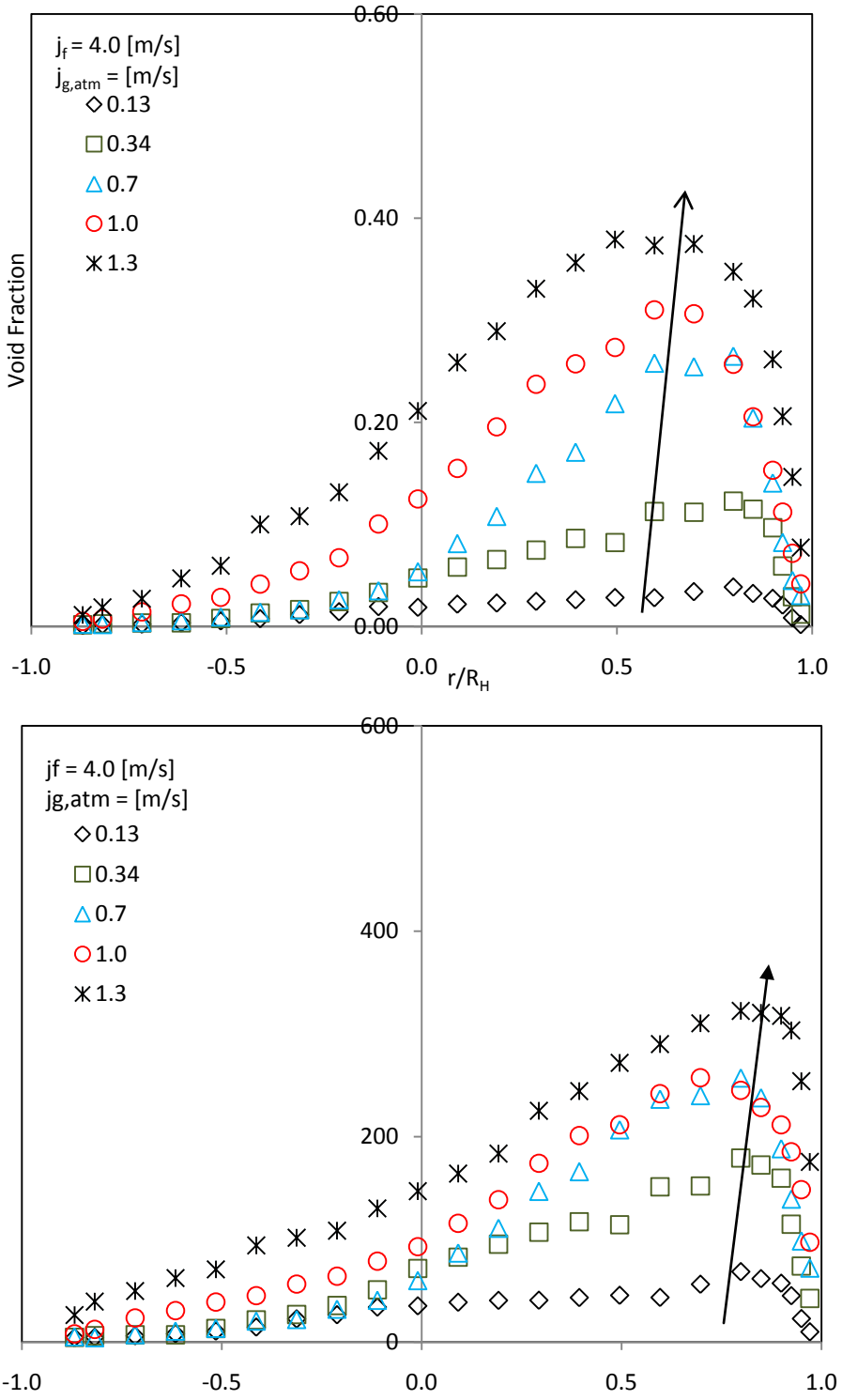

Figure **A3-2**: Effect of the increasing gas flow rate on the horizontal α and a_i profiles for 90-degree elbow at constant liquid flow rate; j_f = 4.0 m/s at L/D = 250

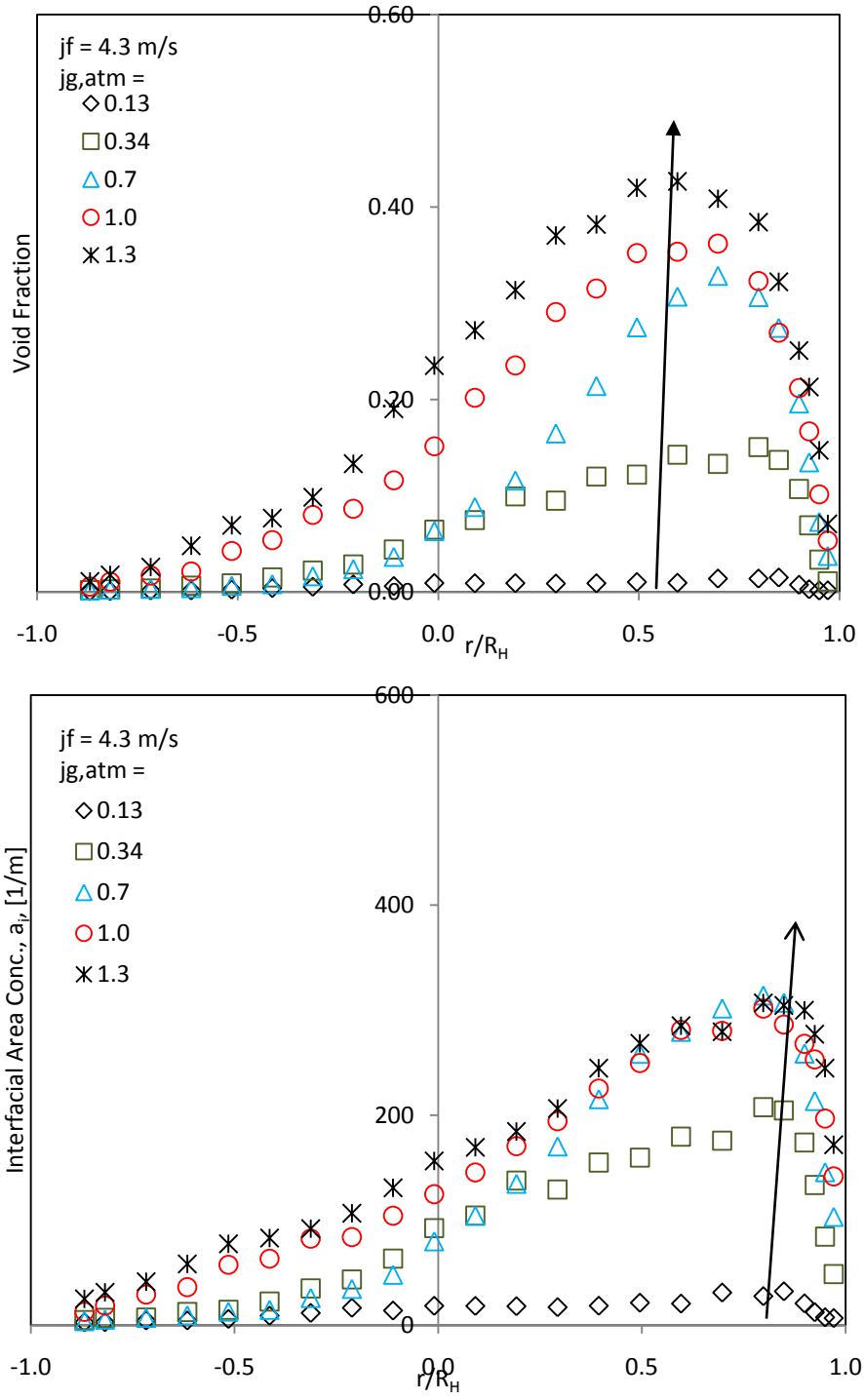

Figure **A3-3**: Effect of the increasing gas flow rate on the horizontal α and a_i profiles for 90-degree elbow at constant liquid flow rate; j_f = 4.3 m/s at L/D = 250

Appendix A4

Effect of Gas Flow Rate on Horizontal Profiles

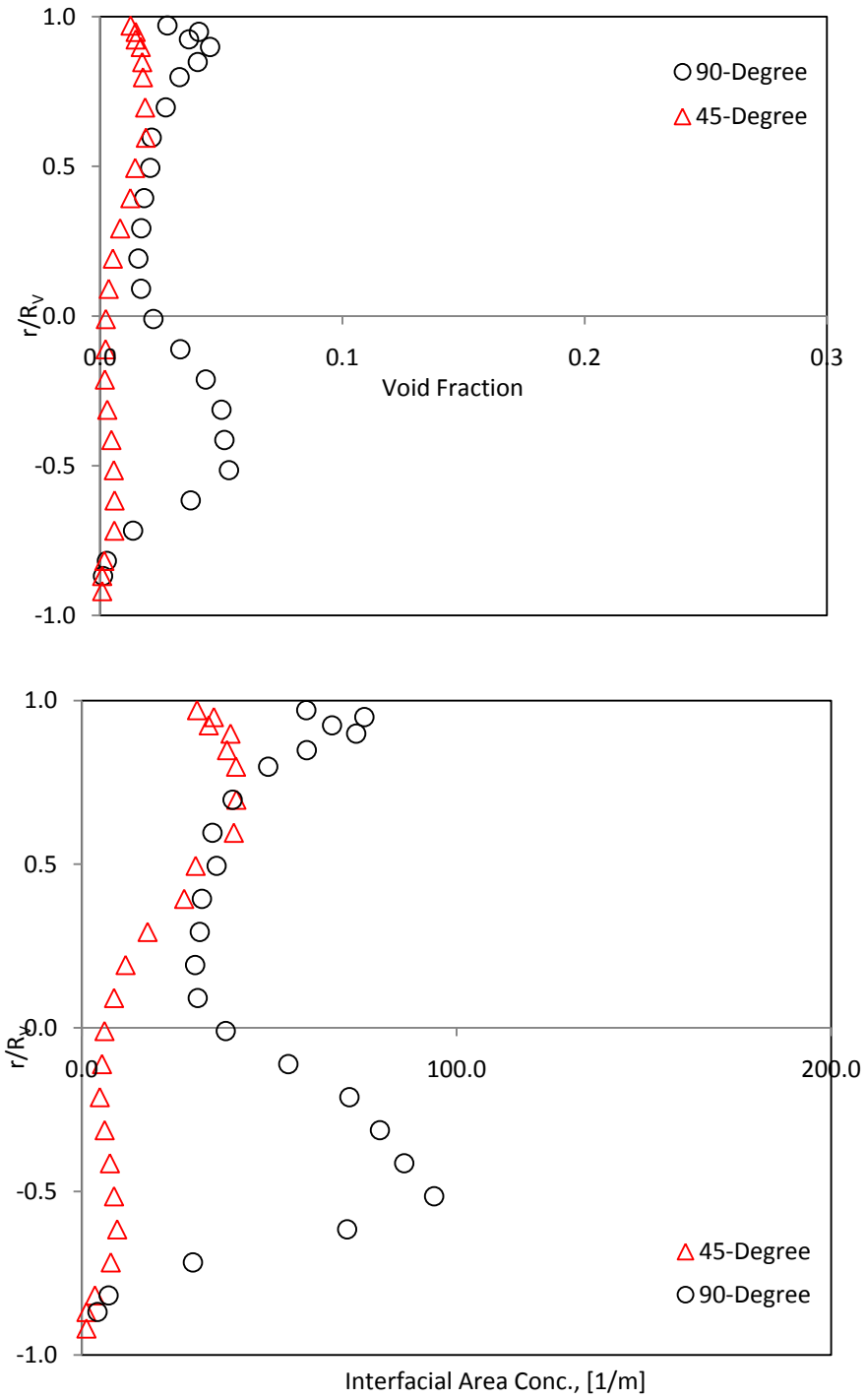

Figure **A4-1**: Comparison of local vertical α and a_i profiles for 45-degree and 90-degree elbows at $j_{g,atm}$= 0.1m/s; j_f=3.8 m/s

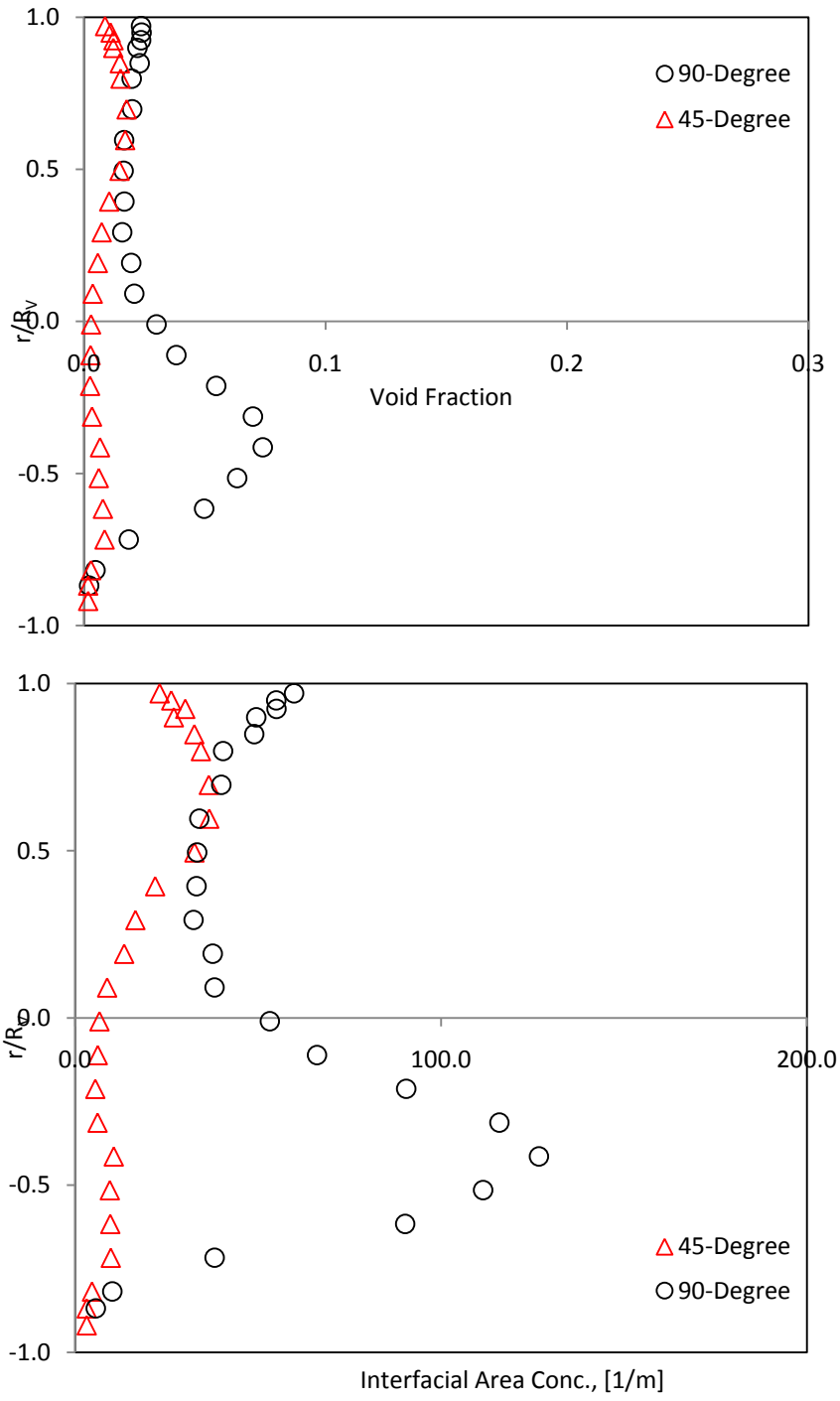

Figure **A4-2**: Comparison of local vertical α and a_i profiles for 45-degree and 90-degree elbows at $j_{g,atm}$= 0.1 m/s; j_f=4.0 m/s

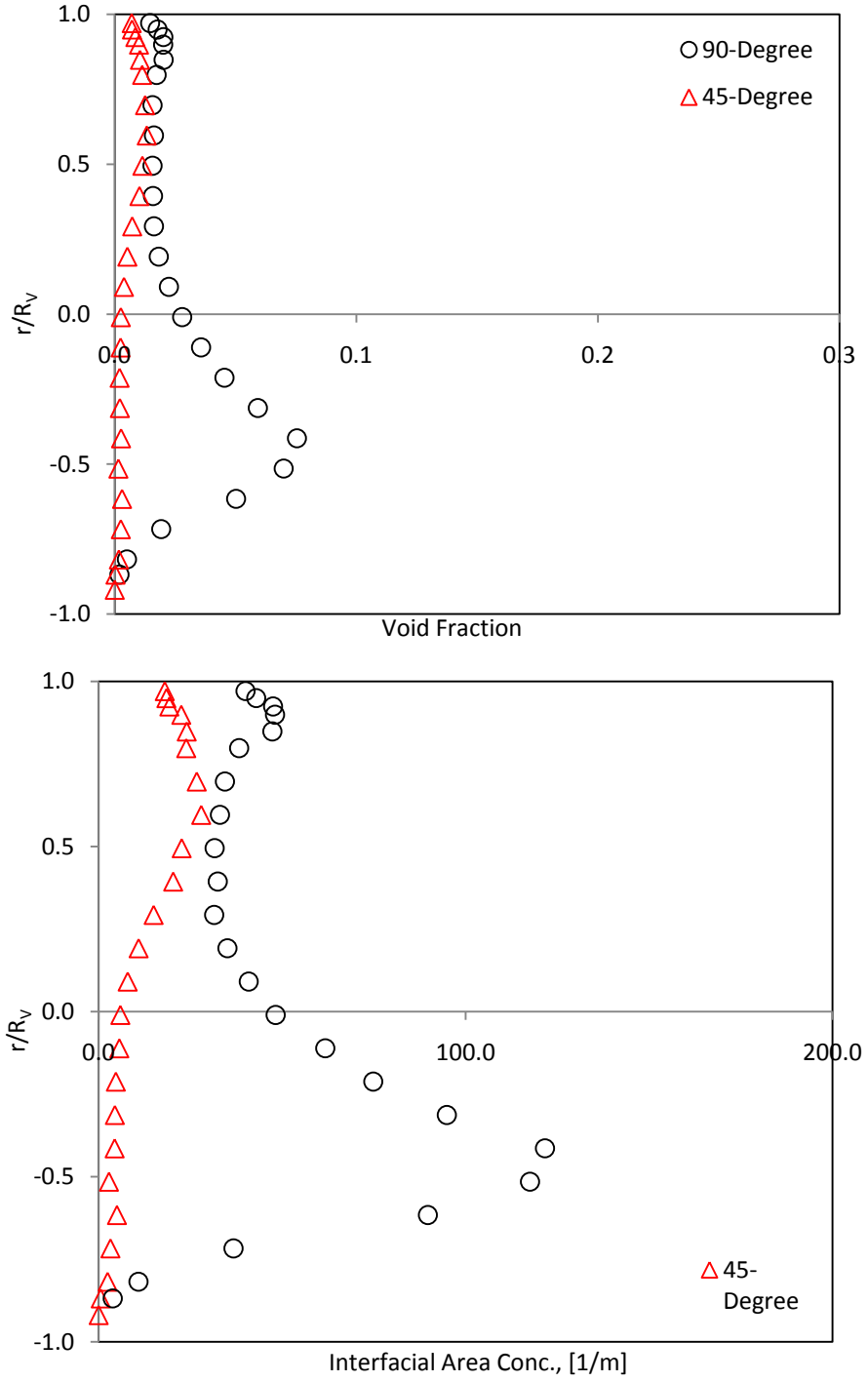

Figure **A4-3**: Comparison of local vertical α and a_i profiles for 45-degree and 90-degree elbows at $j_{g,atm}$= 0.1 m/s; j_f=4.3 m/s

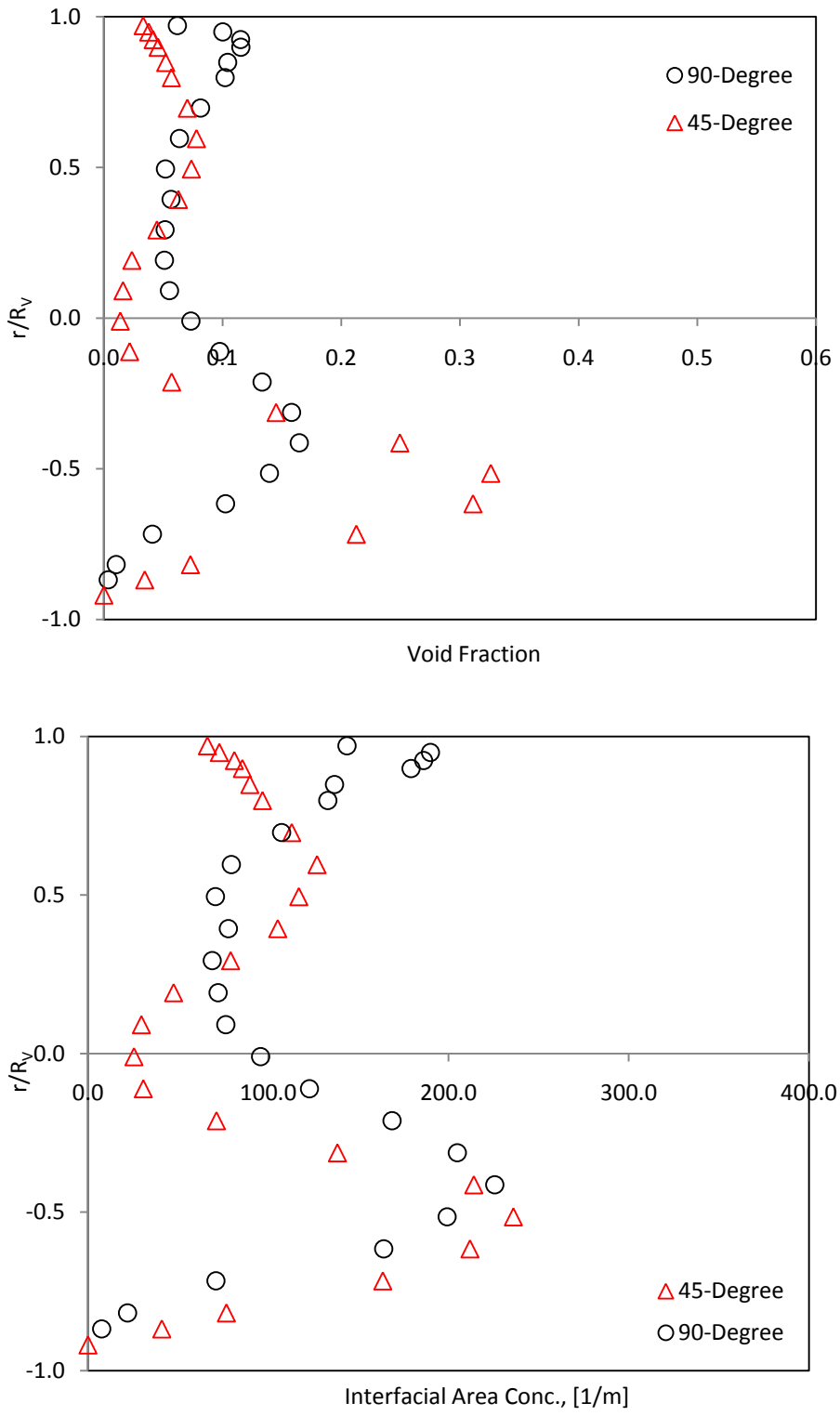

Figure **A4-4**: Comparison of local vertical α and a_i profiles for 45-degree and 90-degree elbows at $j_{g,atm}$= 0.3 m/s; j_f=3.8 m/s

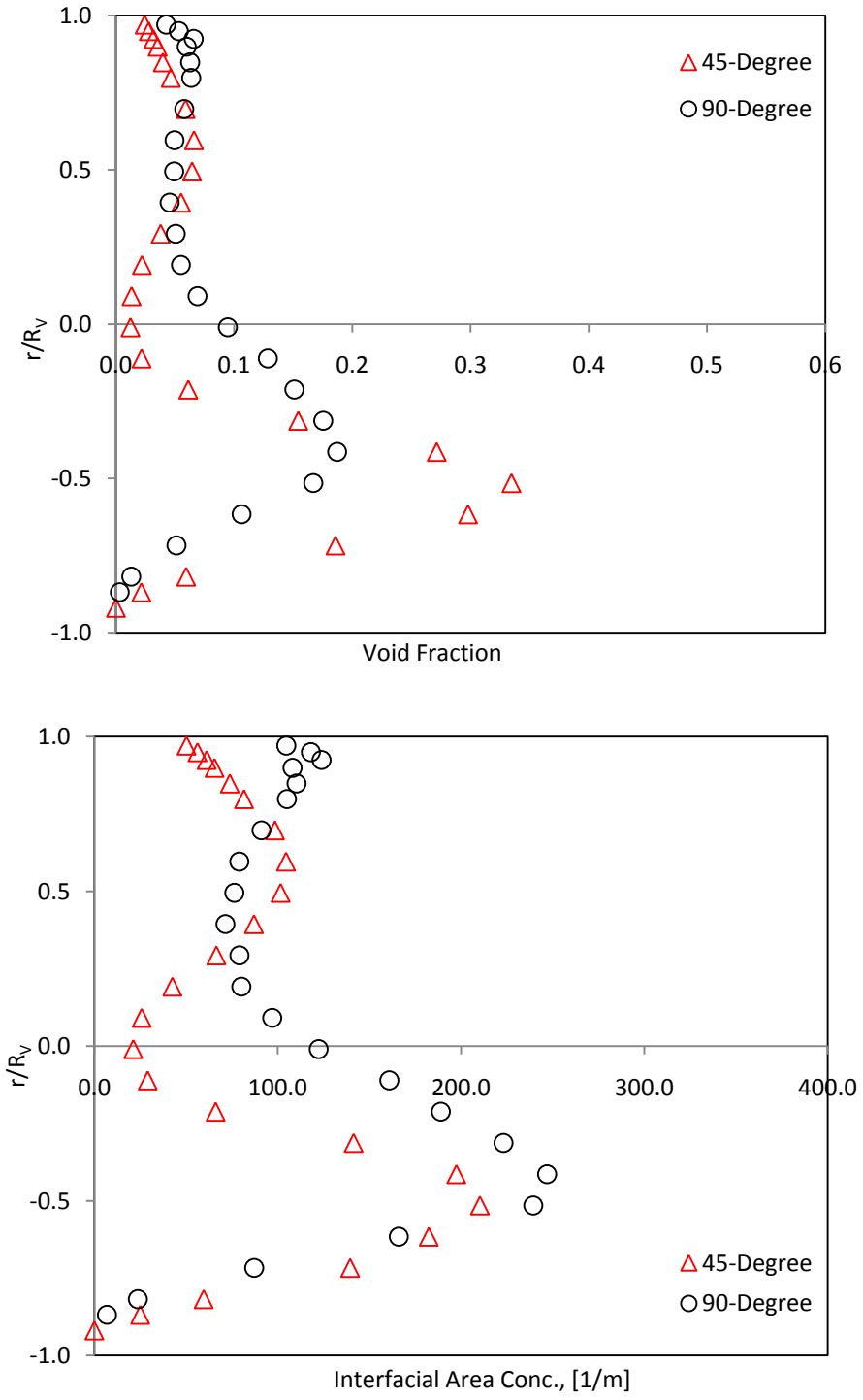

Figure **A4-5**: Comparison of local vertical α and a_i profiles for 45-degree and 90-degree elbows at $j_{g,atm}$= 0.3 m/s; j_f=4.0 m/s

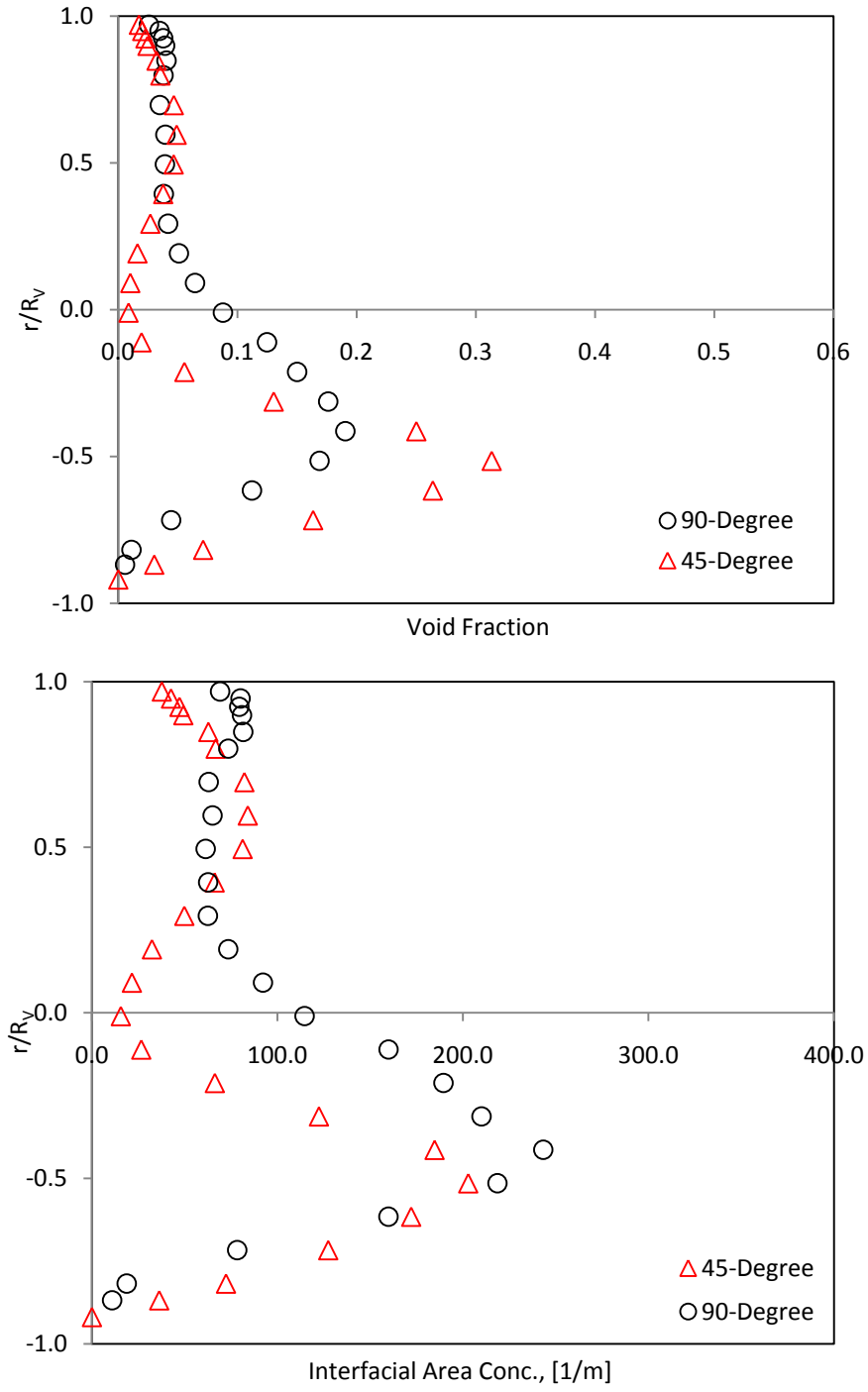

Figure **A4-6**: Comparison of local vertical α and a_i profiles for 45-degree and 90-degree elbows at $j_{g,atm}$= 0.3 m/s; j_f=4.3 m/s

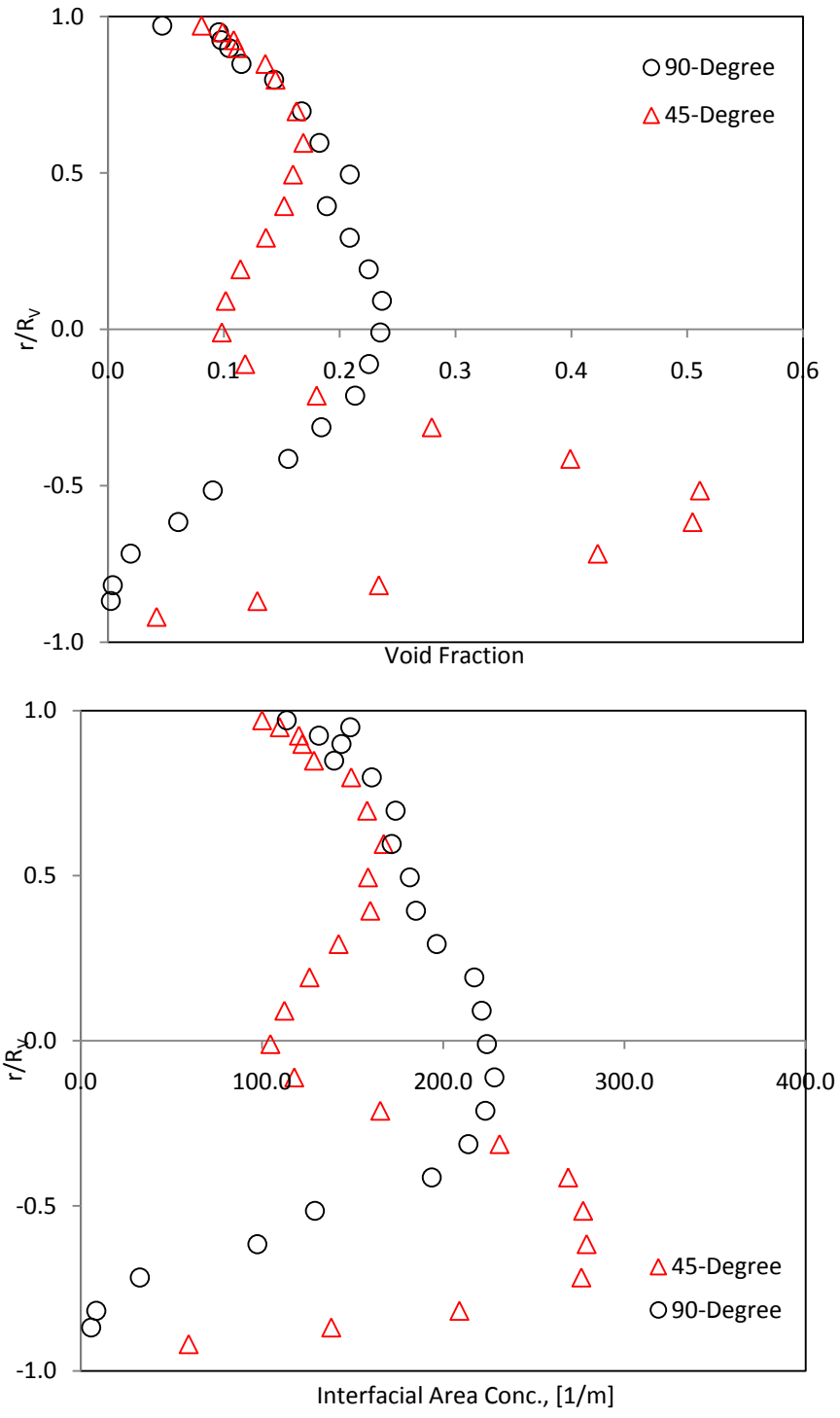

Figure **A4-7**: Comparison of local vertical α and a_i profiles for 45-degree and 90-degree elbows at $j_{g,atm}$= 0.7 m/s; j_f = 3.8 m/s

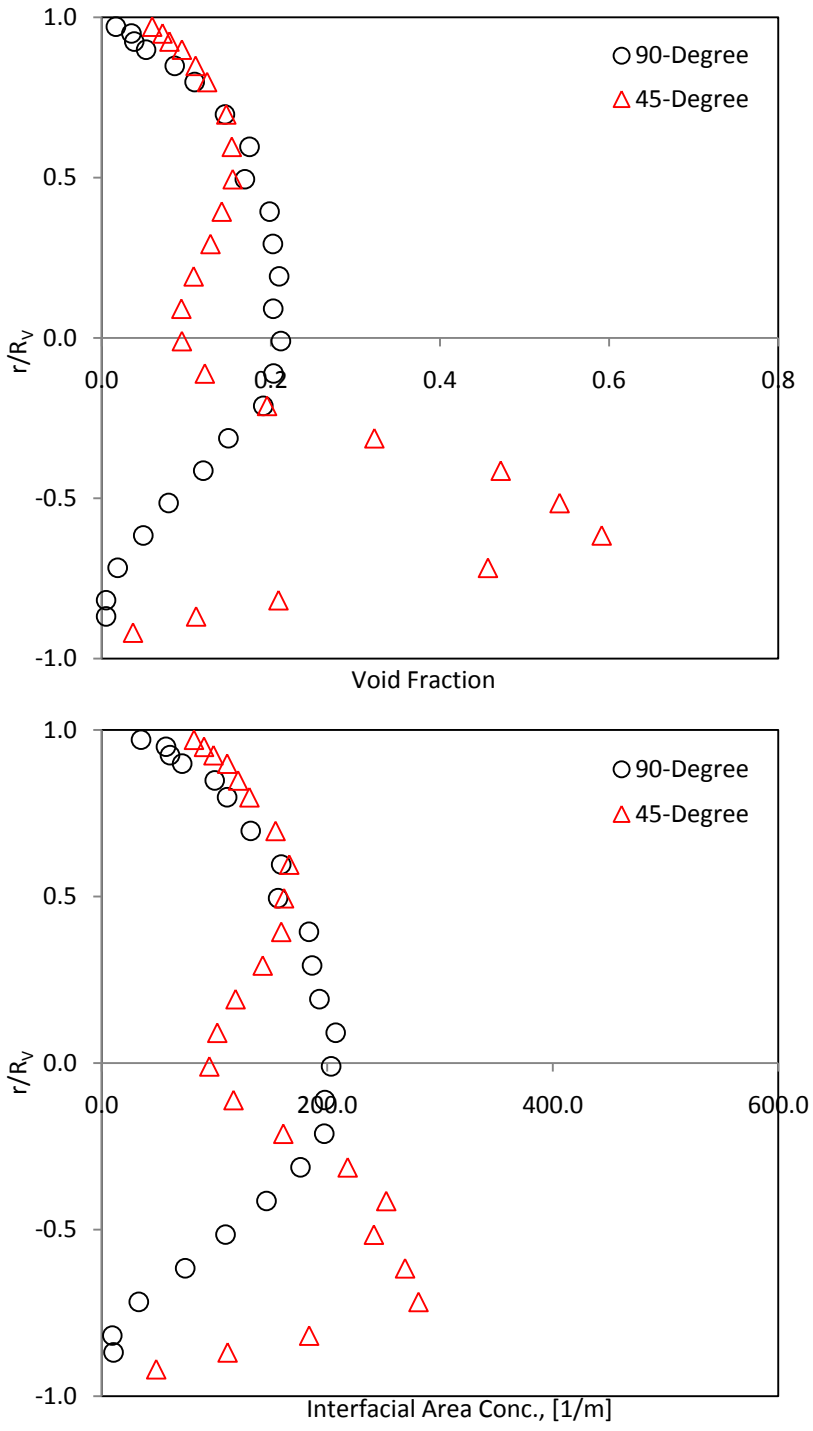

Figure **A4-8**: Comparison of local vertical α and a_i profiles for 45-degree and 90-degree elbows at $j_{g,atm}$= 0.7 m/s; j_f=4.0 m/s

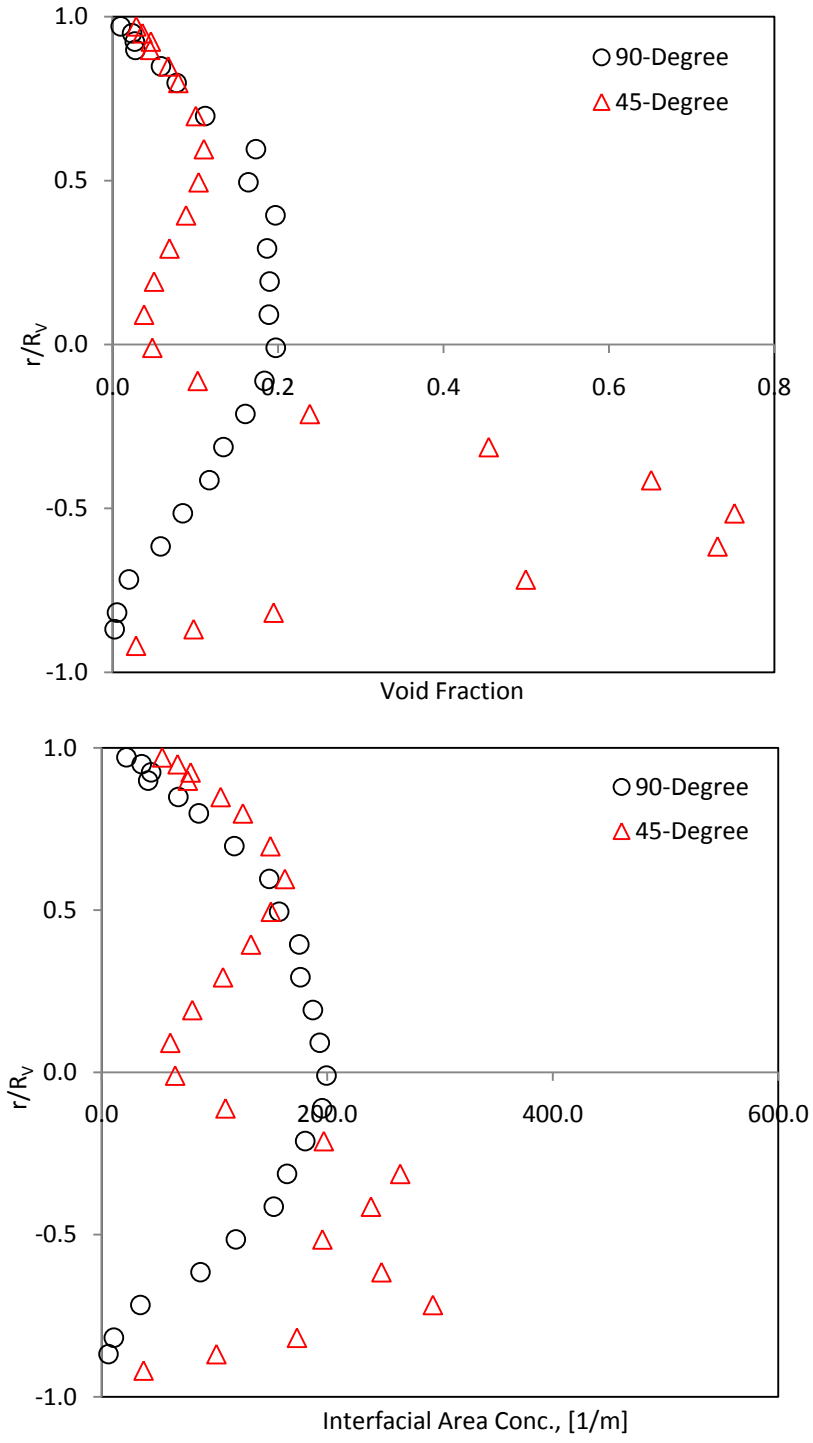

Figure **A4-9**: Comparison of local vertical α and a_i profiles for 45-degree and 90-degree elbows at $j_{g,atm}$= 0.7 m/s; j_f=4.3 m/s

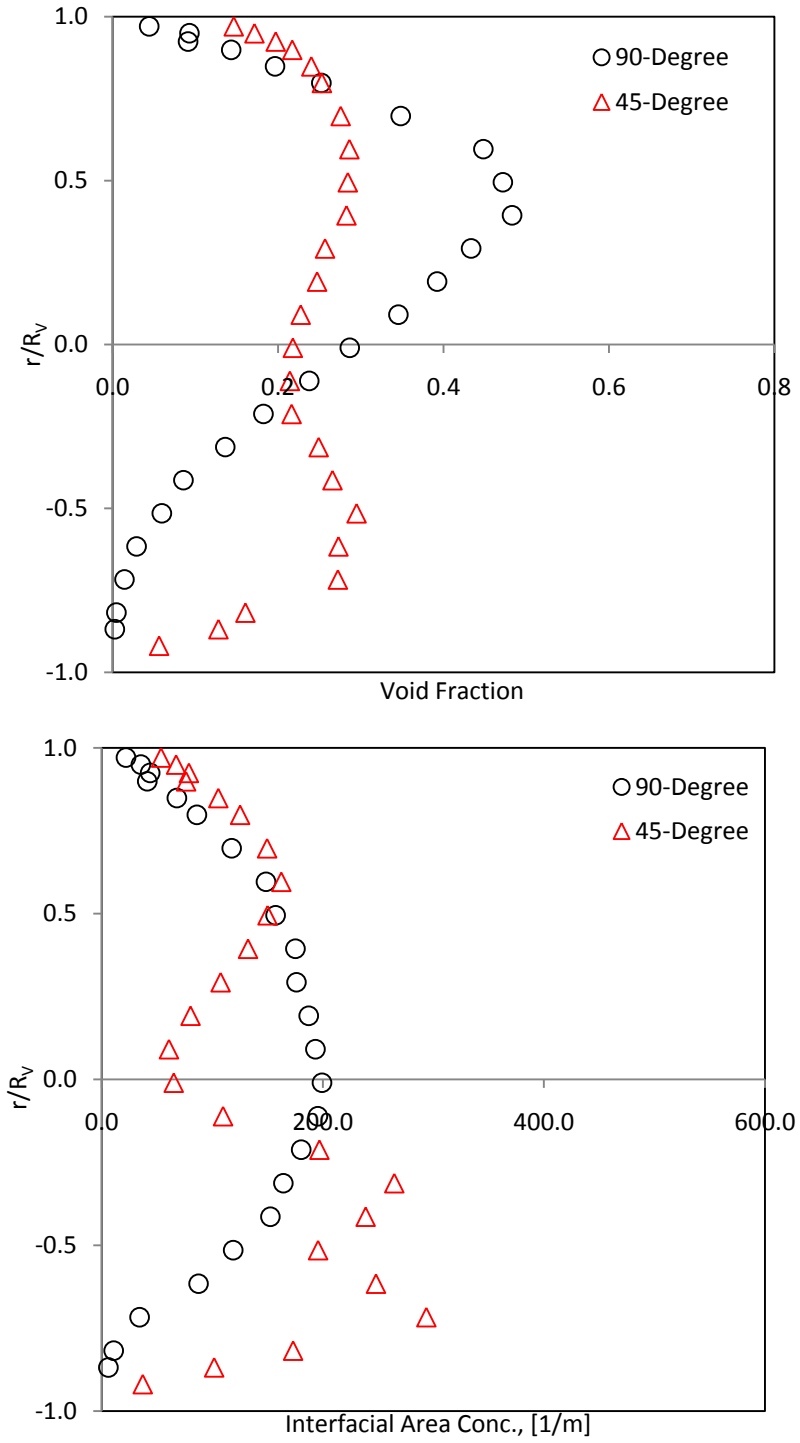

Figure **A4-10**: Comparison of local horizontal α and a_i profiles for 45-degree and 90-degree elbows at $j_{g,atm}$= 1.0 m/s; j_f=3.8 m/s

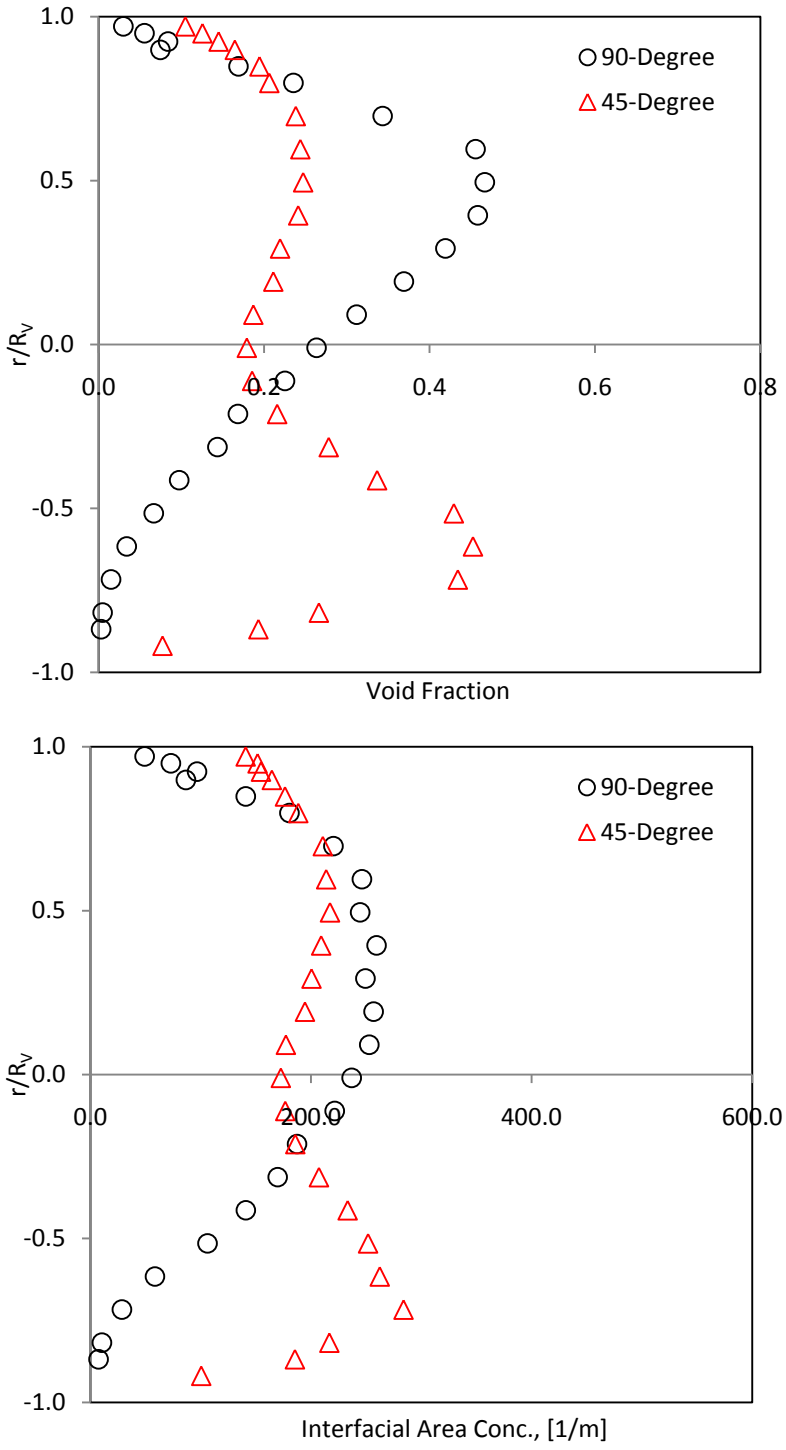

Figure **A4-11**: Comparison of local vertical α and a_i profiles for 45-degree and 90-degree elbows at $j_{g,atm}$= 1.0 m/s; j_f=4.0 m/s

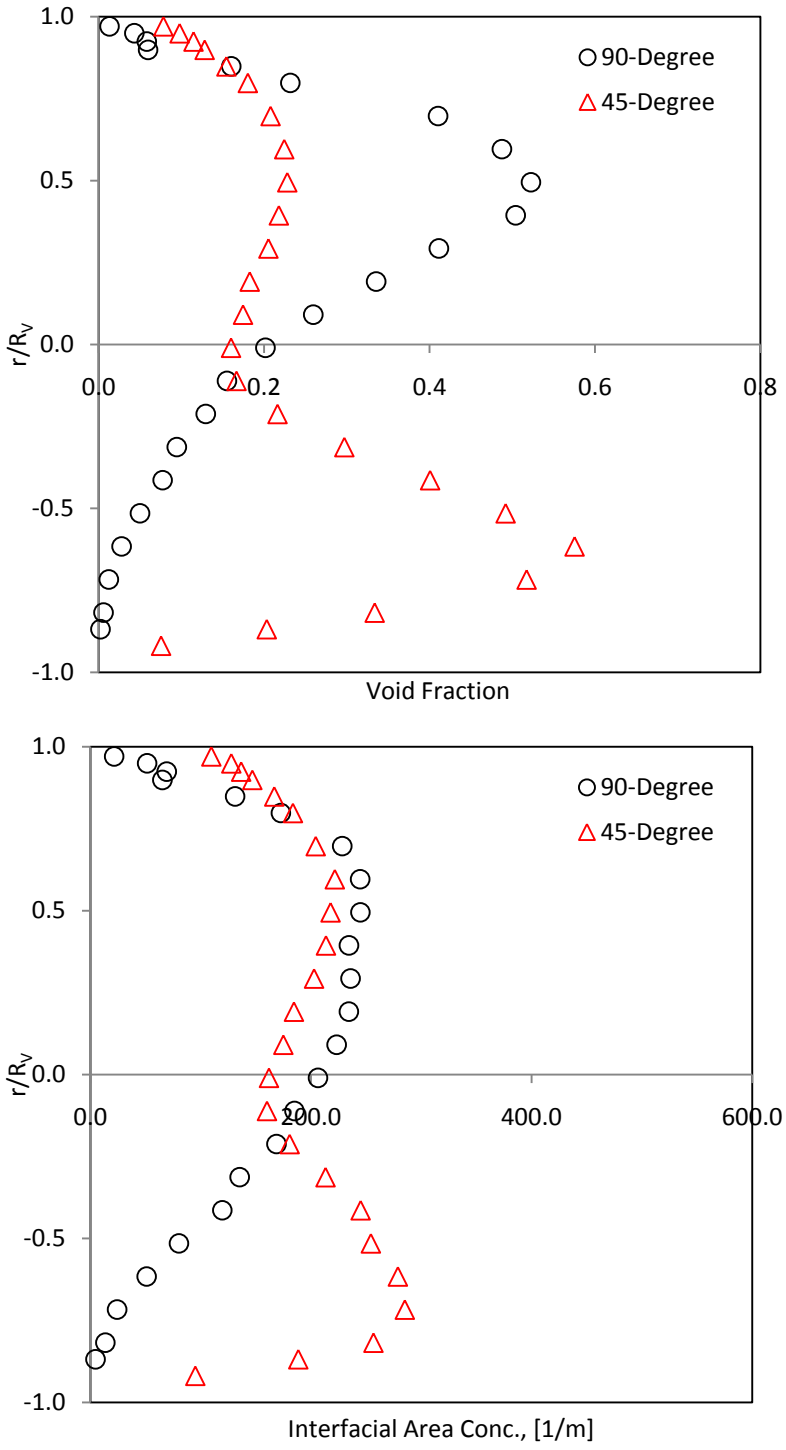

Figure **A4-12**: Comparison of local vertical α and a_i profiles for 45-degree and 90-degree elbows at $j_{g,atm}$= 1.0 m/s; j_f=4.3 m/s

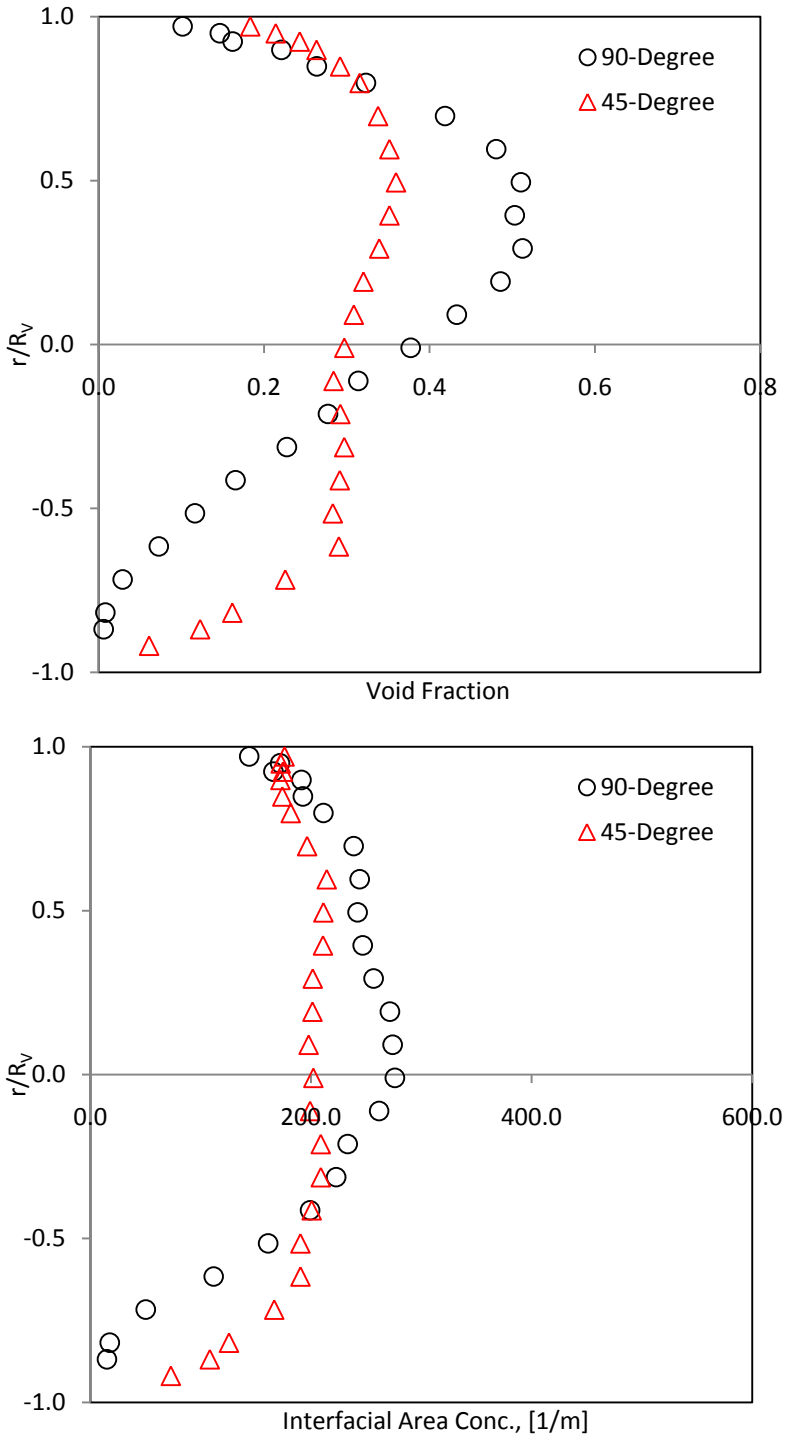

Figure **A4-13**: Comparison of local vertical α and a_i profiles for 45-degree and 90-degree elbows at $j_{g,atm}$= 1.3 m/s; j_f=3.8 m/s

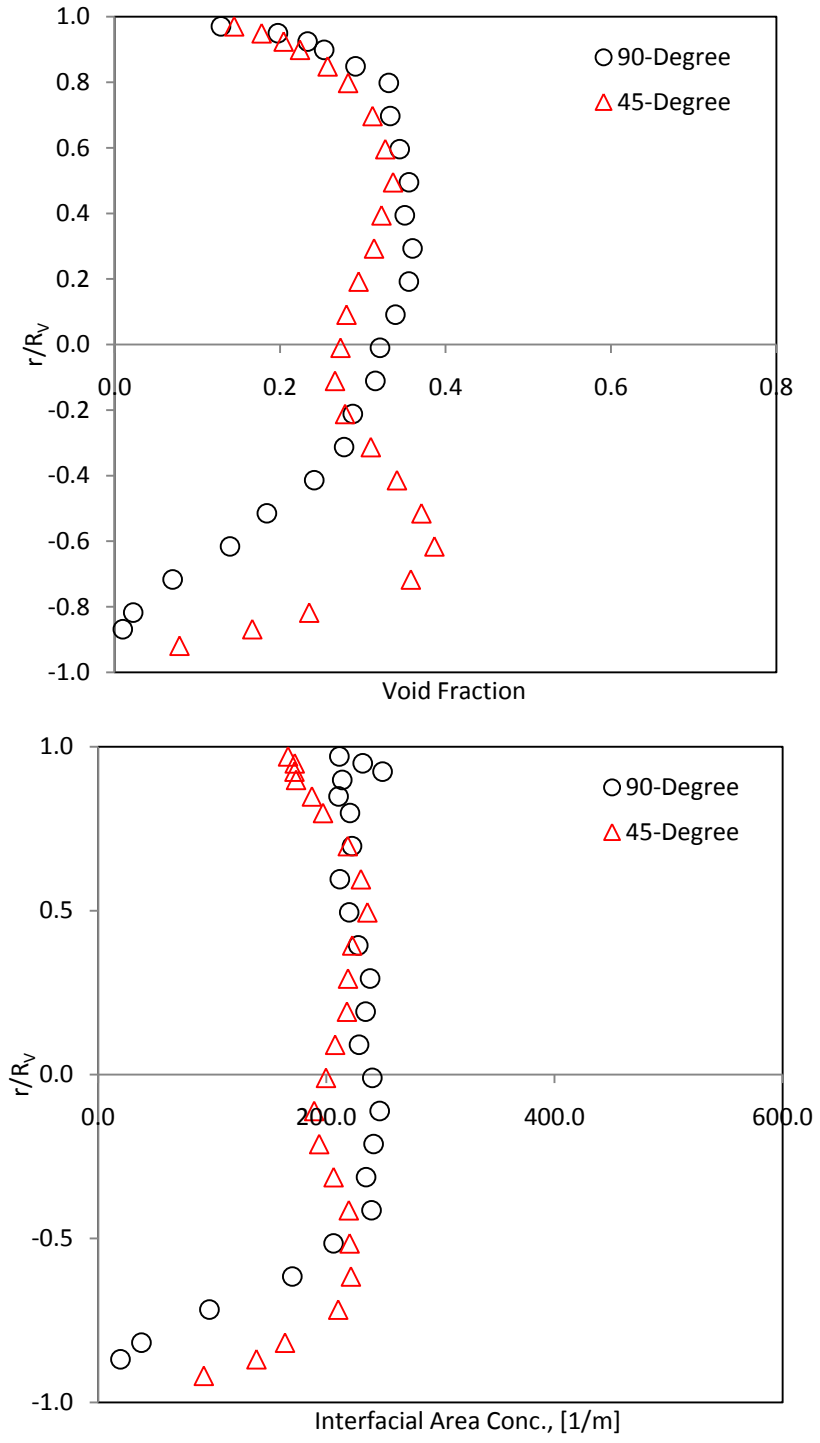

Figure **A4-14**: Comparison of local vertical α and a_i profiles for 45-degree and 90-degree elbows at $j_{g,atm}$= 1.3 m/s; j_f=4.0 m/s

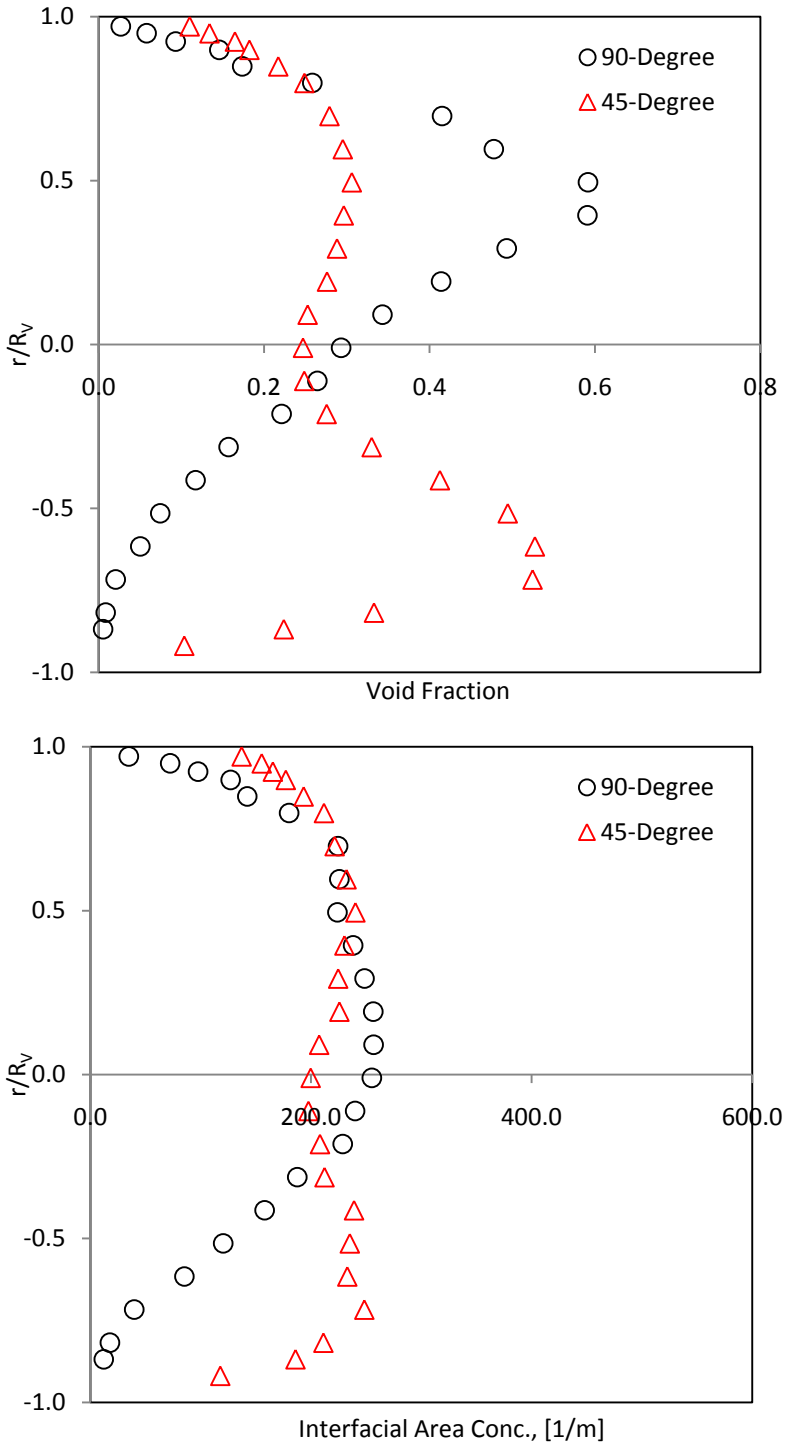

Figure **A4-15**: Comparison of local vertical α and a_i profiles for 45-degree and 90-degree elbows at $j_{g,atm}$= 1.3 m/s; j_f=4.3 m/s

Appendix A5

Axial Development of Area-Averaged Interfacial Structures

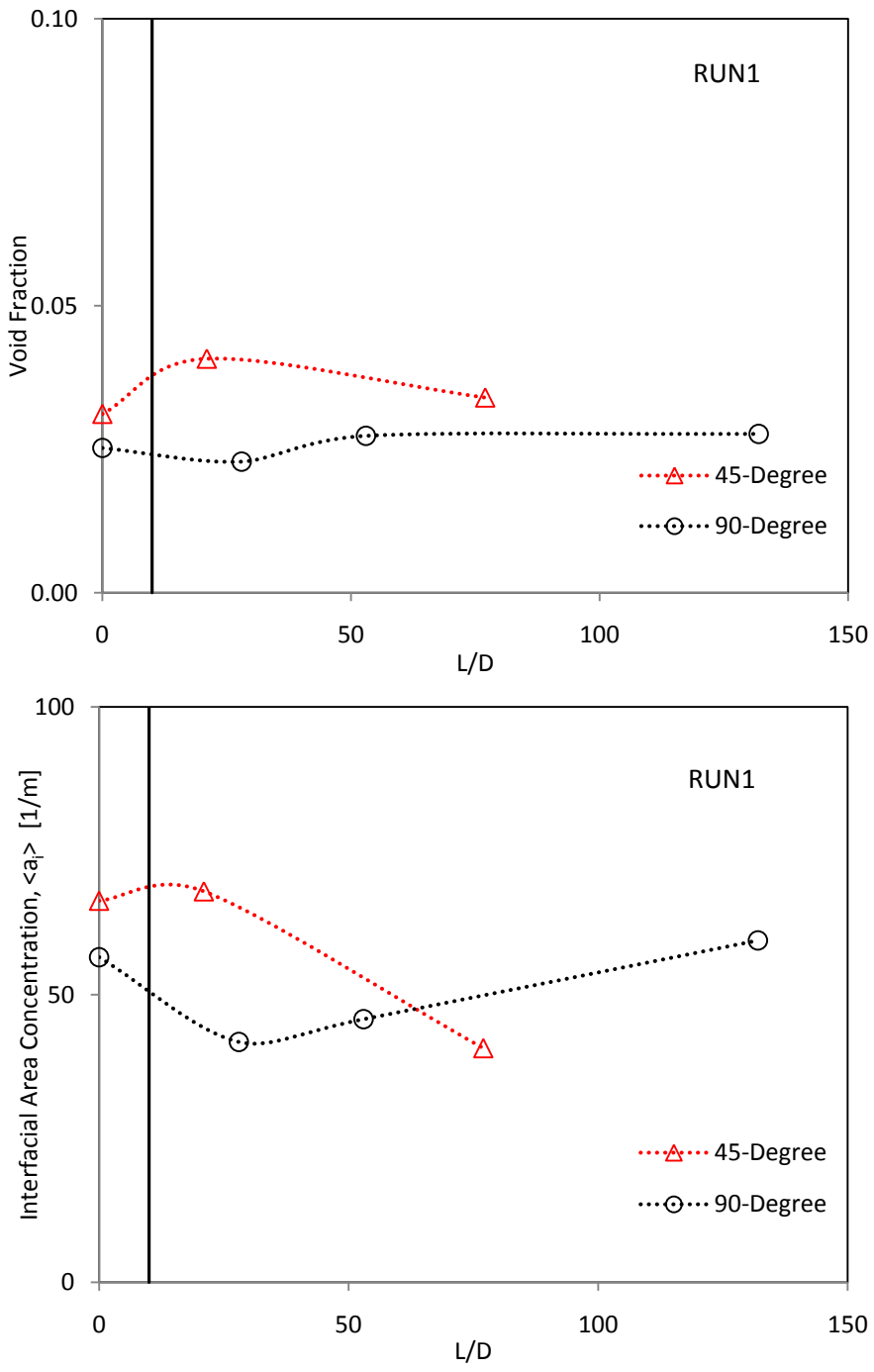

Figure **A5-1**: Comparison of the one-dimensional transport of $<\alpha>$ and $<a_i>$ across the elbows for two characteristic flow conditions with constant j_f=4.3 m/s

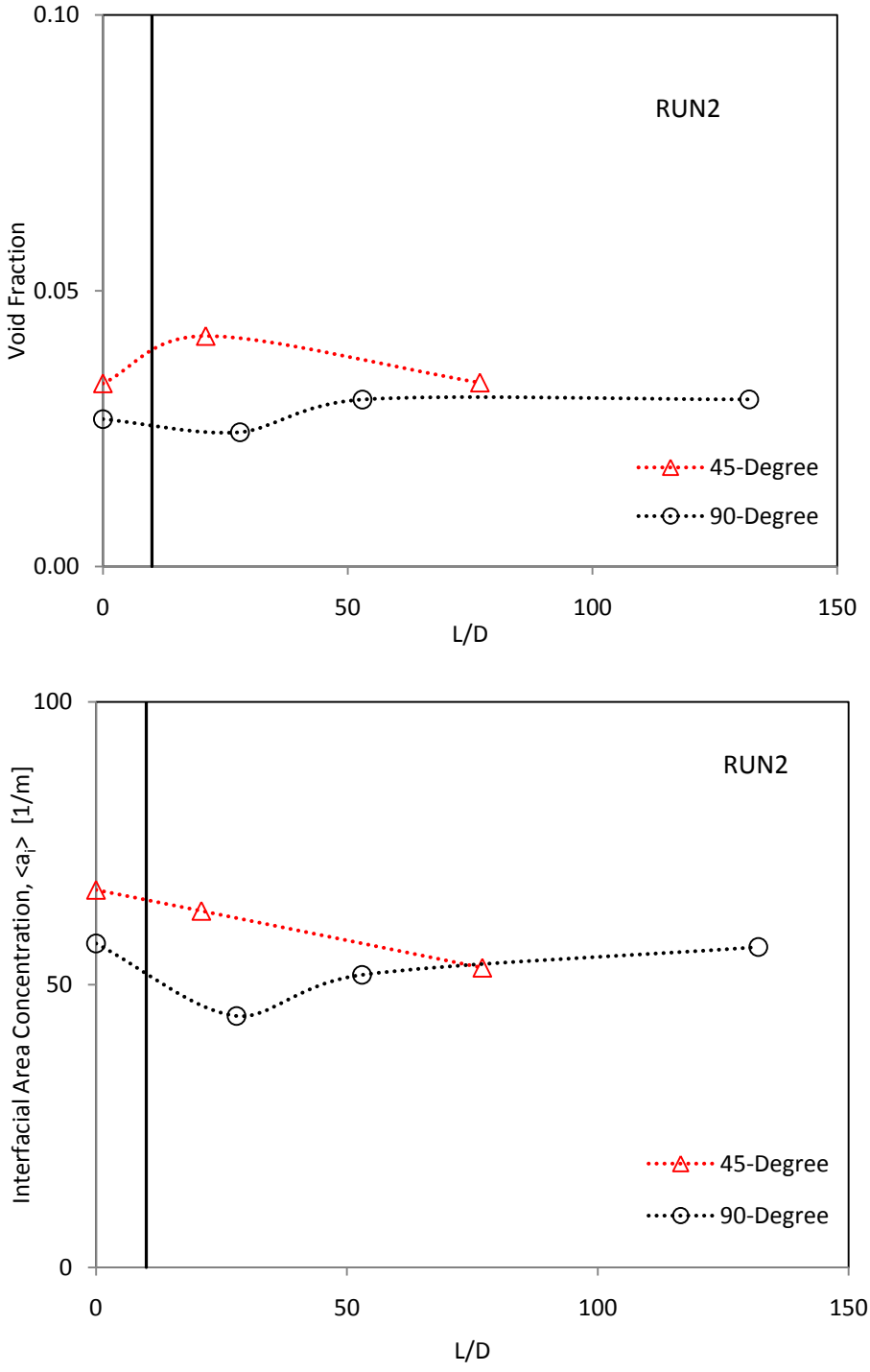

Figure **A5-2**: Comparison of the one-dimensional transport of $<\alpha>$ and $<a_i>$ across the elbows for two characteristic flow conditions with constant j_f=4.3 m/s

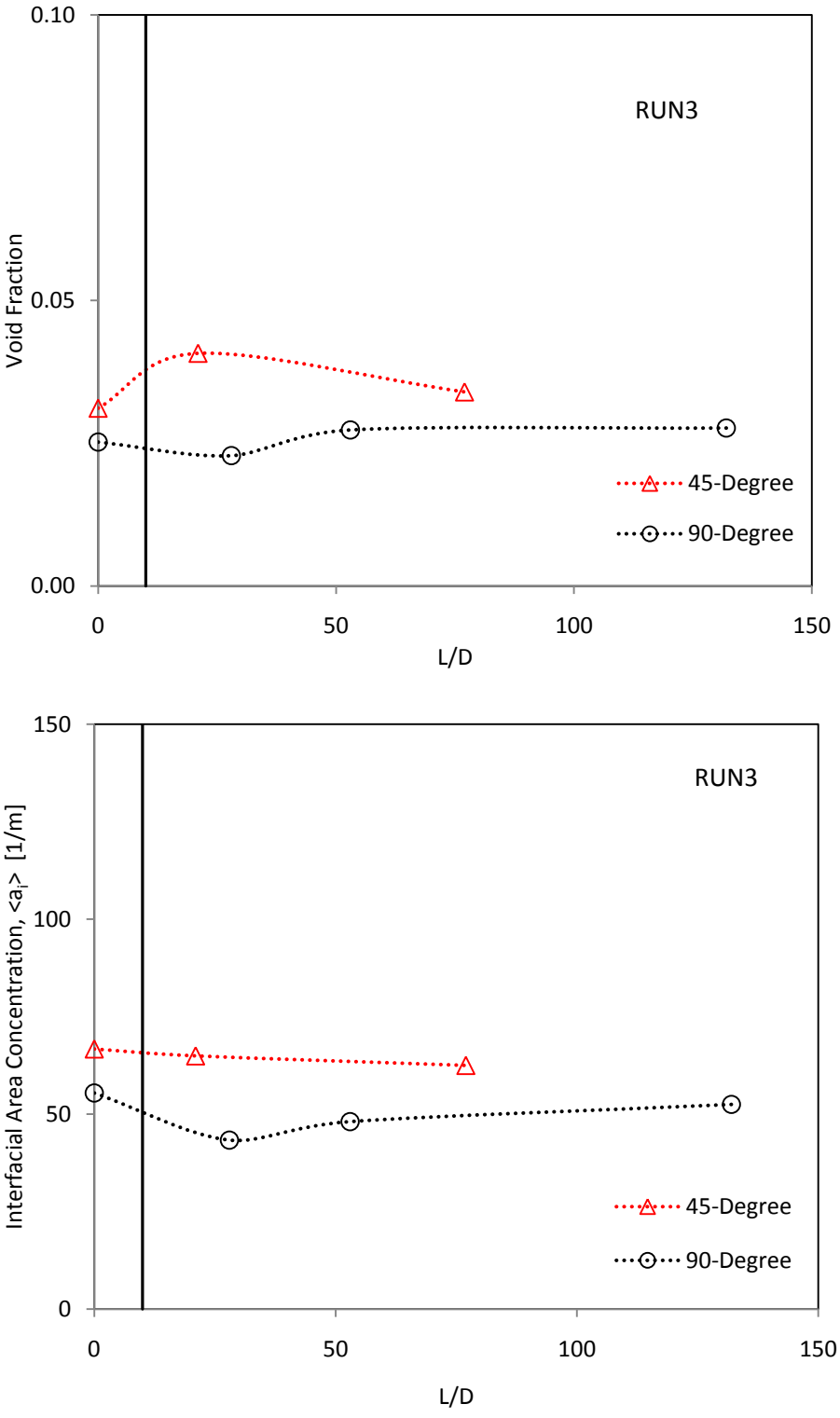

Figure **A5-3**: Comparison of the one-dimensional transport of $<\alpha>$ and $<a_i>$ across the elbows for two characteristic flow conditions with constant j_f=4.3 m/s

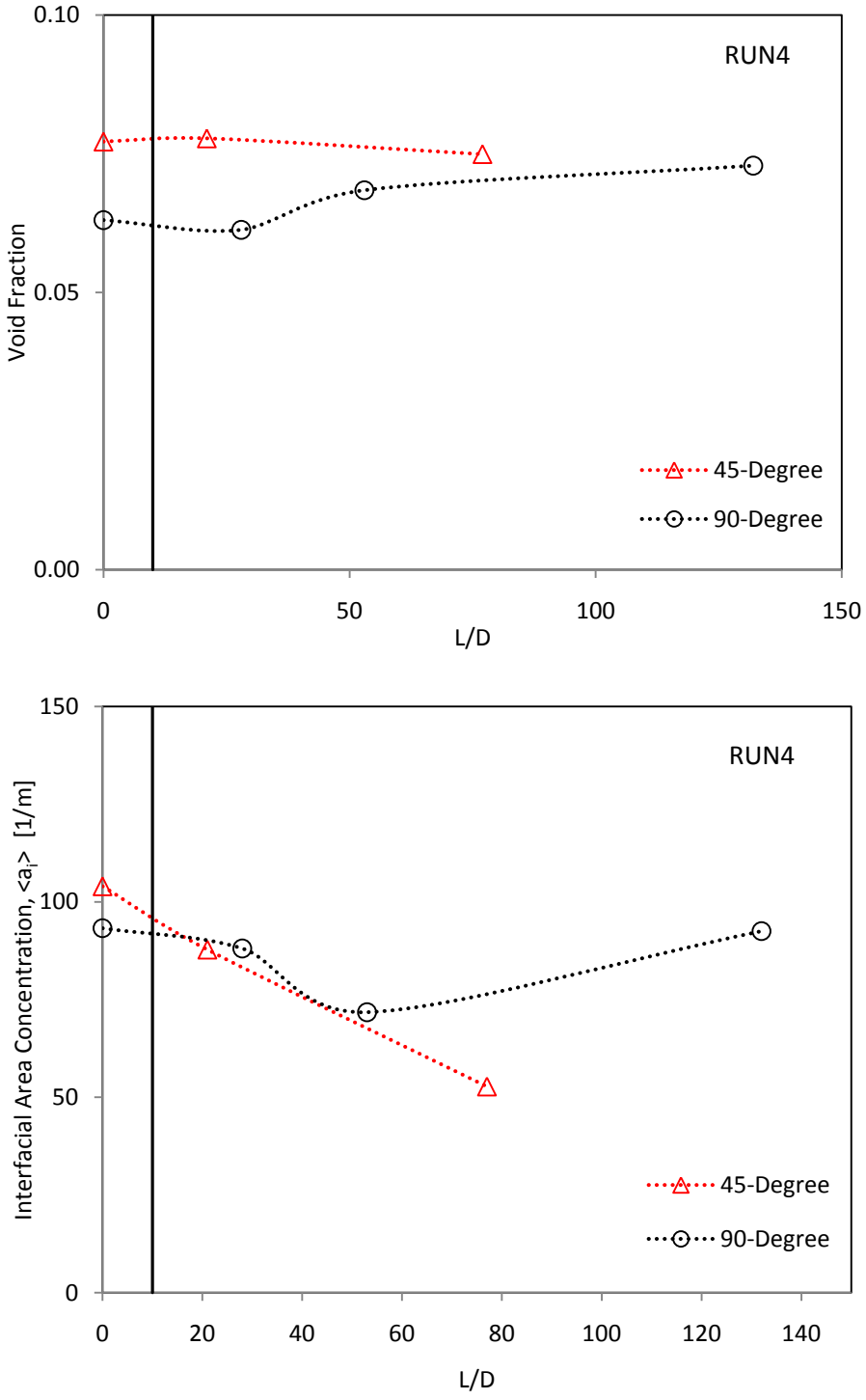

Figure **A5-4**: Comparison of the one-dimensional transport of $<\alpha>$ and $<a_i>$ across the elbows for two characteristic flow conditions with constant j_f=4.3 m/s

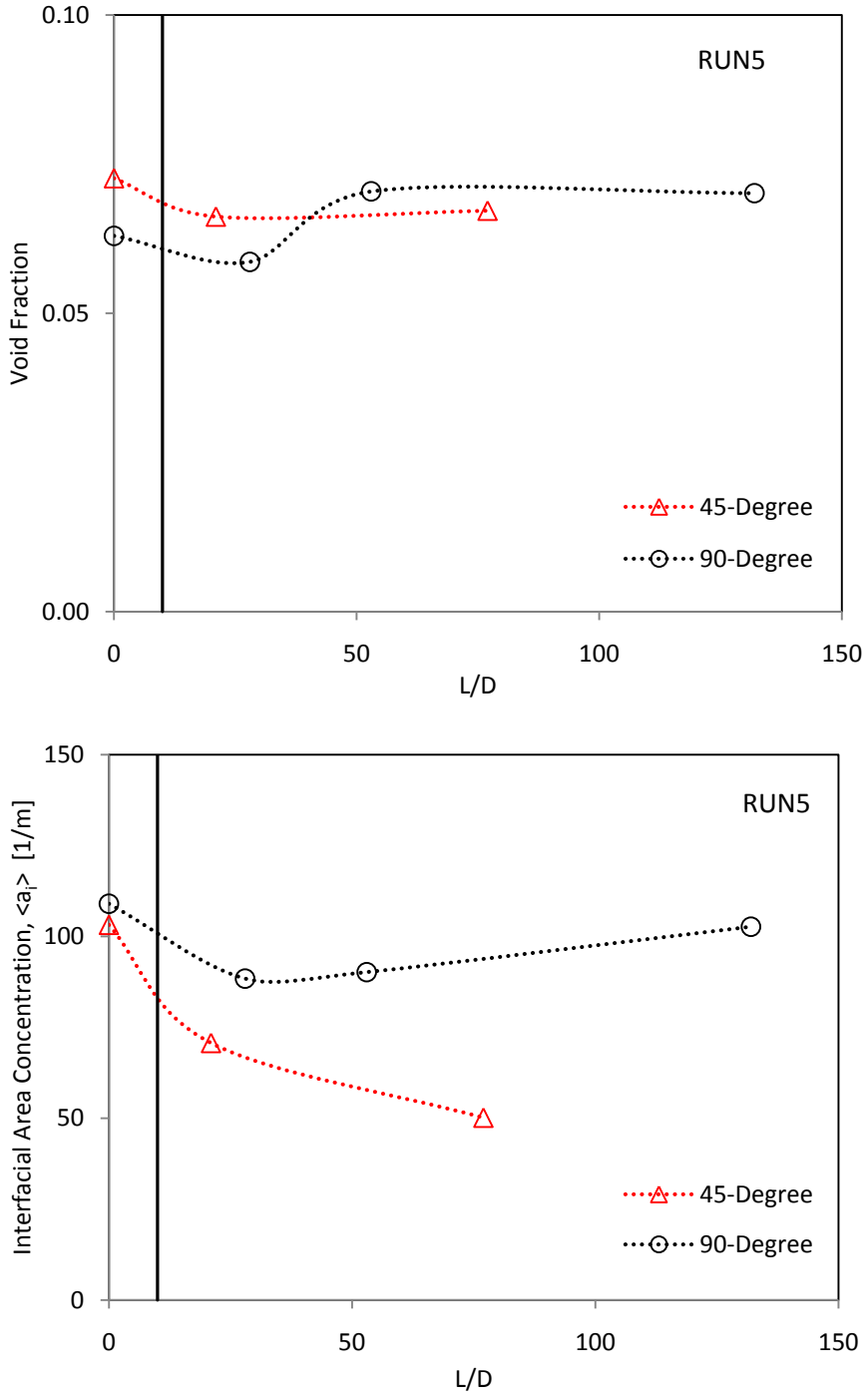

Figure **A5-5**: Comparison of the one-dimensional transport of $<\alpha>$ and $<a_i>$ across the elbows for two characteristic flow conditions with constant j_f=4.3 m/s

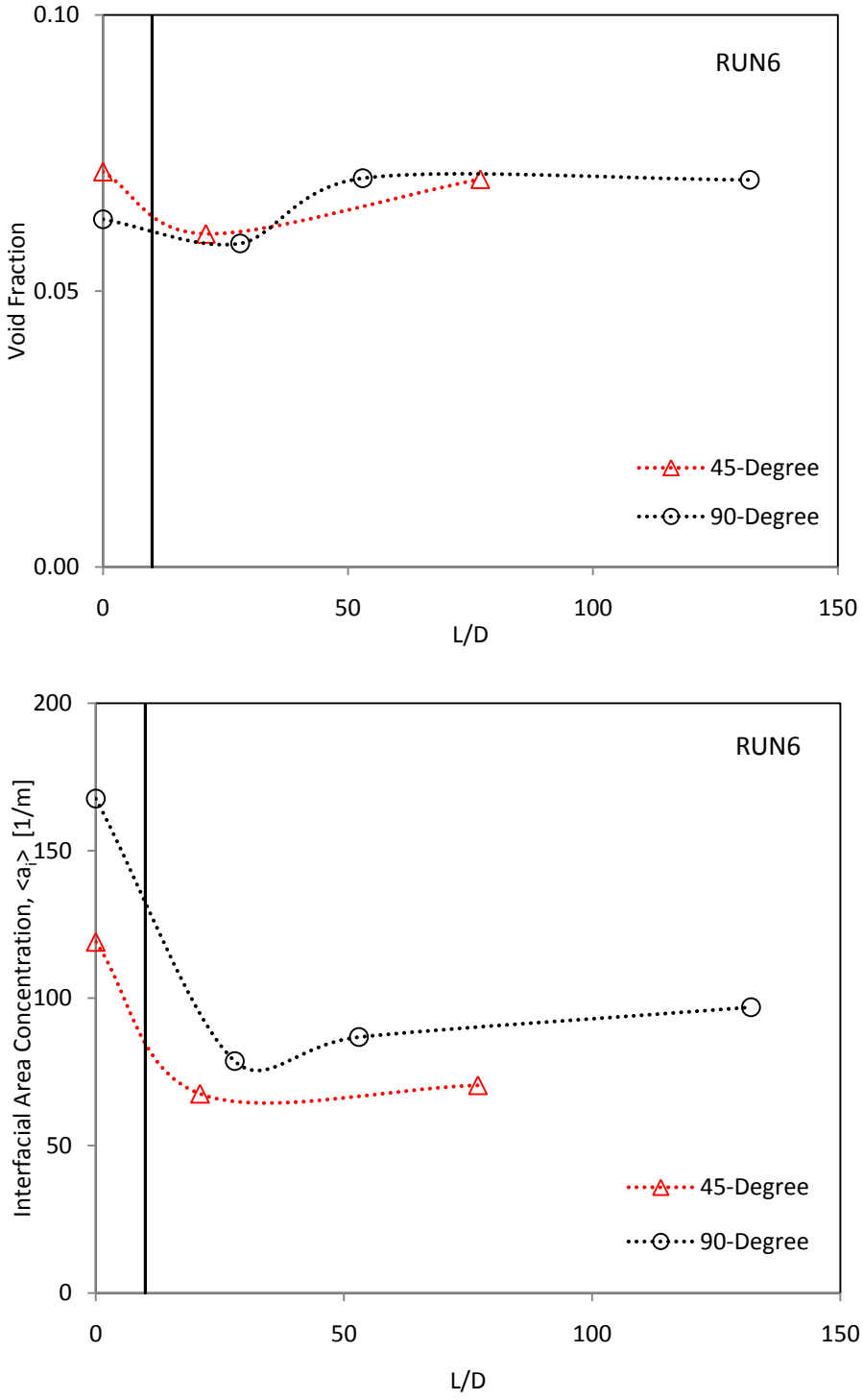

Figure **2-6**: Comparison of the one-dimensional transport of $<\alpha>$ and $<a_i>$ across the elbows for two characteristic flow conditions with constant j_f=4.3 m/s

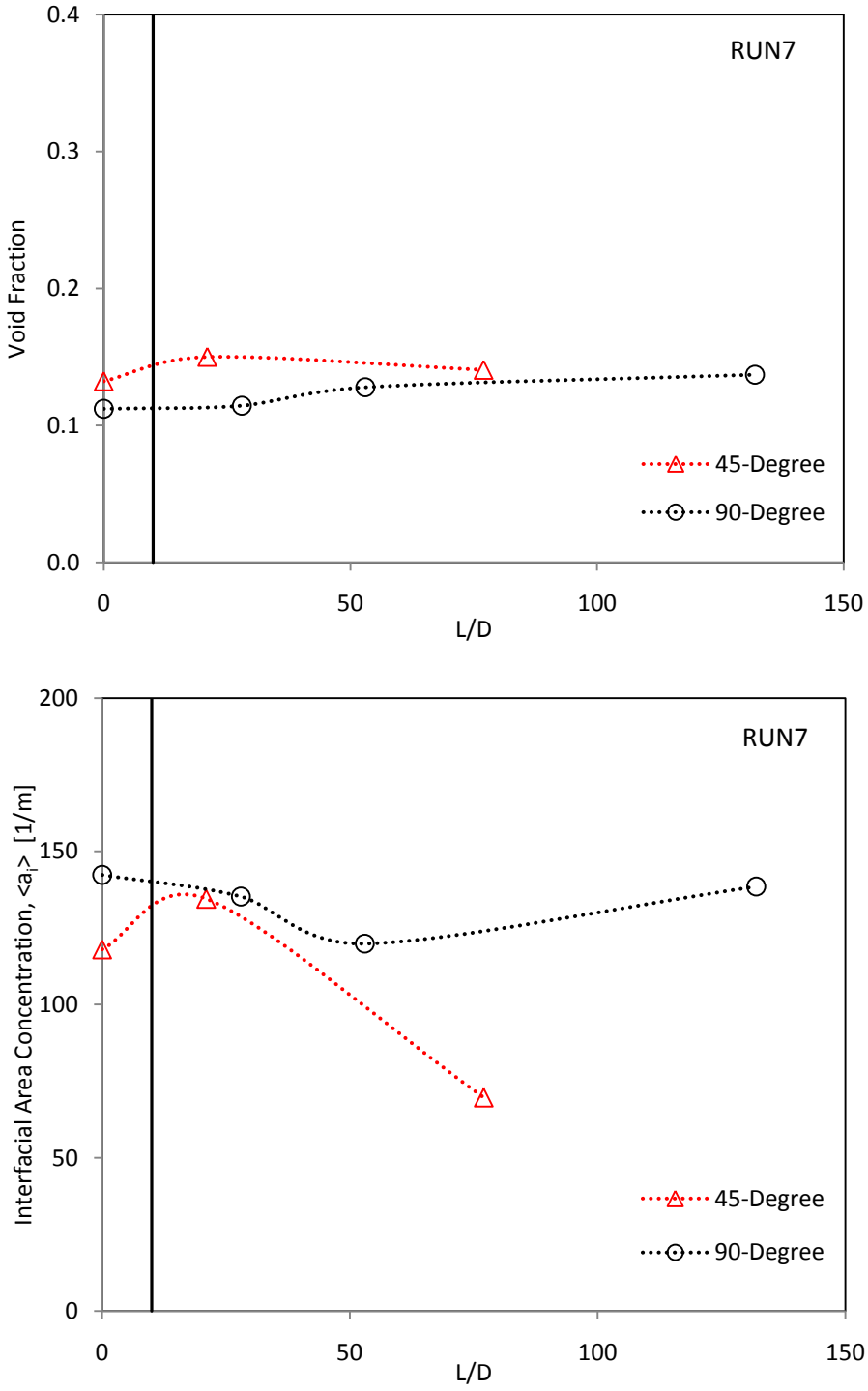

Figure **A5-7**: Comparison of the one-dimensional transport of $<\alpha>$ and $<a_i>$ across the elbows for two characteristic flow conditions with constant j_f=4.3 m/s

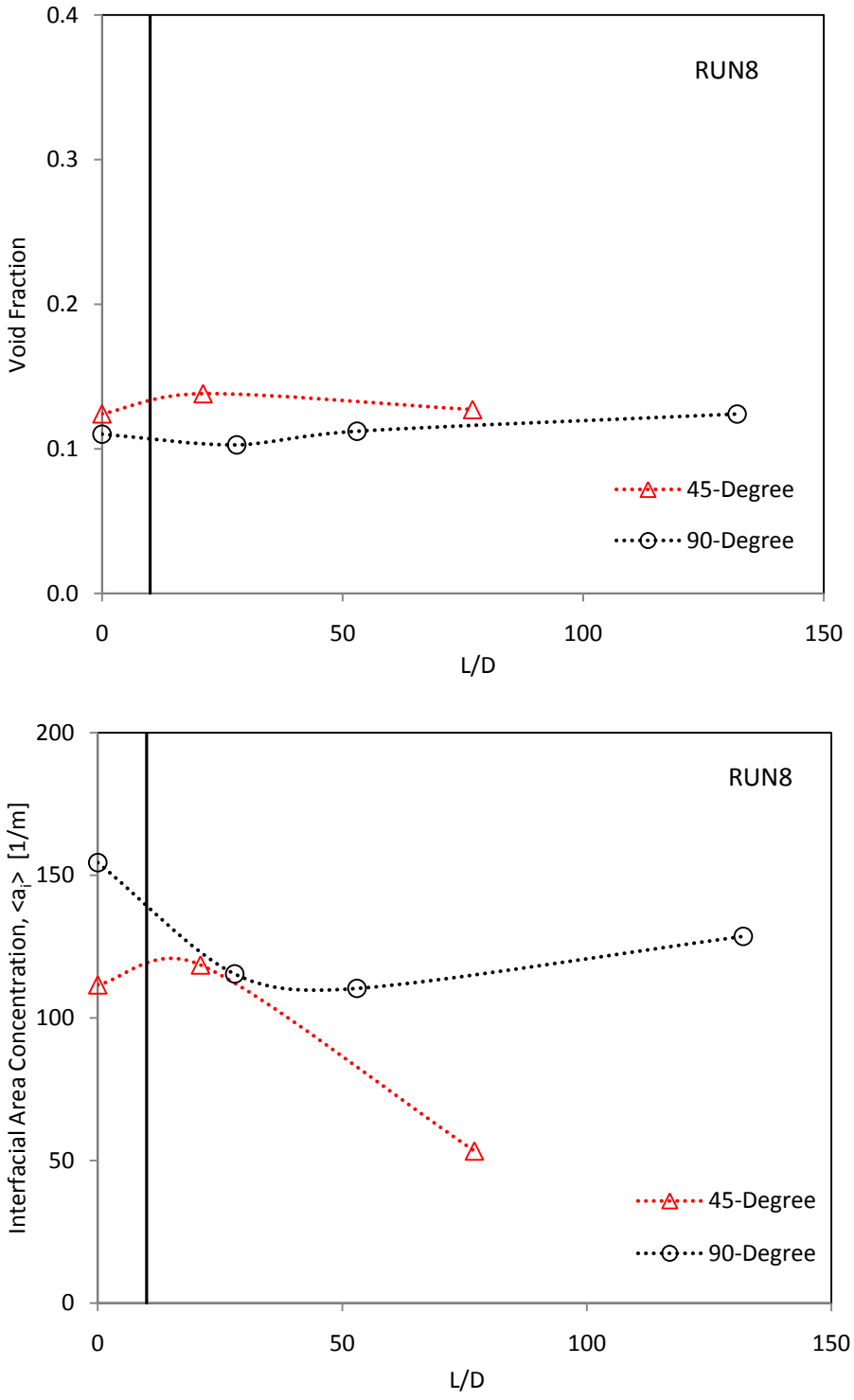

Figure **A5-8**: Comparison of the one-dimensional transport of $<\alpha>$ and $<a_i>$ across the elbows for two characteristic flow conditions with constant j_f=4.3 m/s

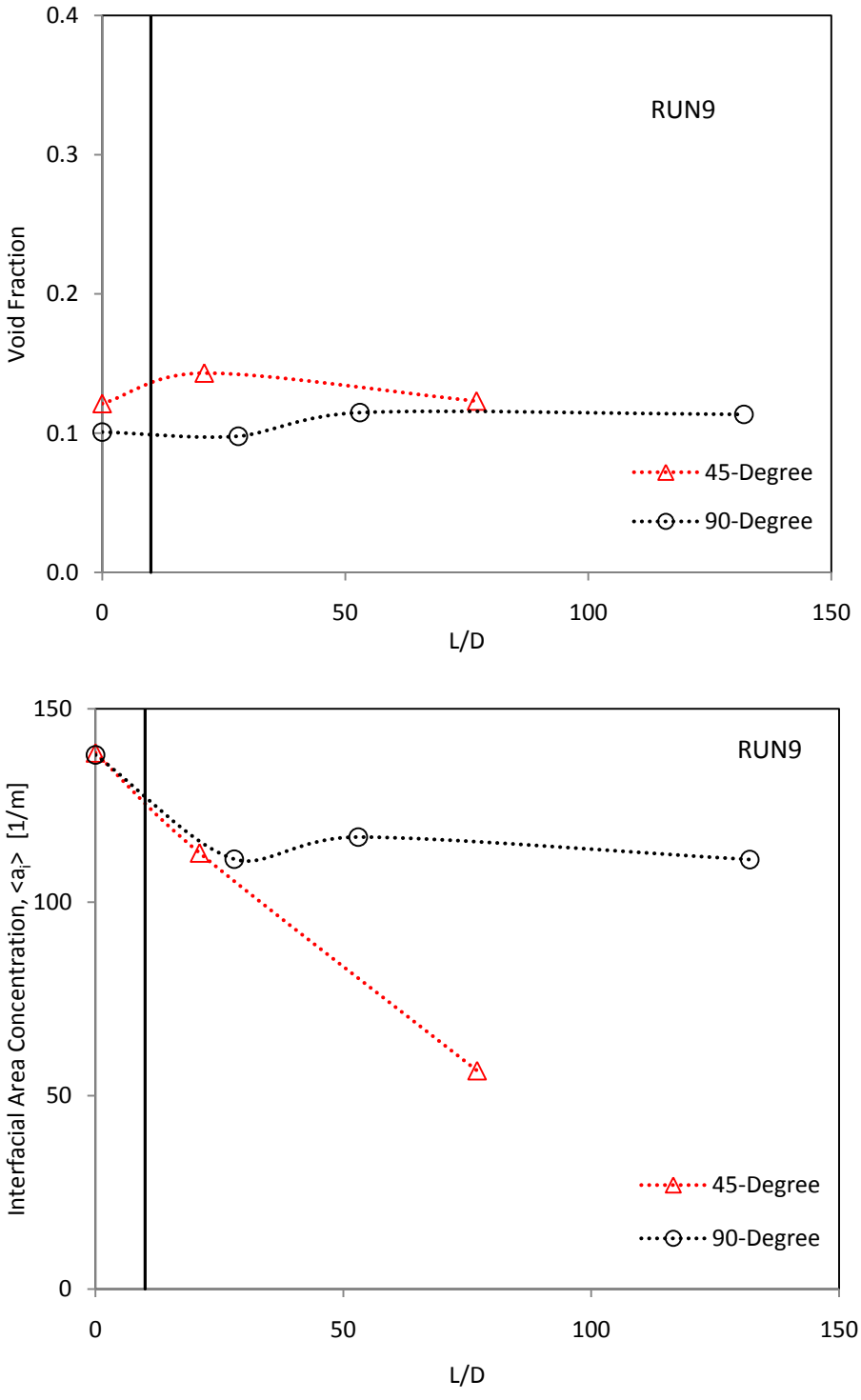

Figure **A5-9**: Comparison of the one-dimensional transport of $<\alpha>$ and $<a_i>$ across the elbows for two characteristic flow conditions with constant j_f=4.3 m/s

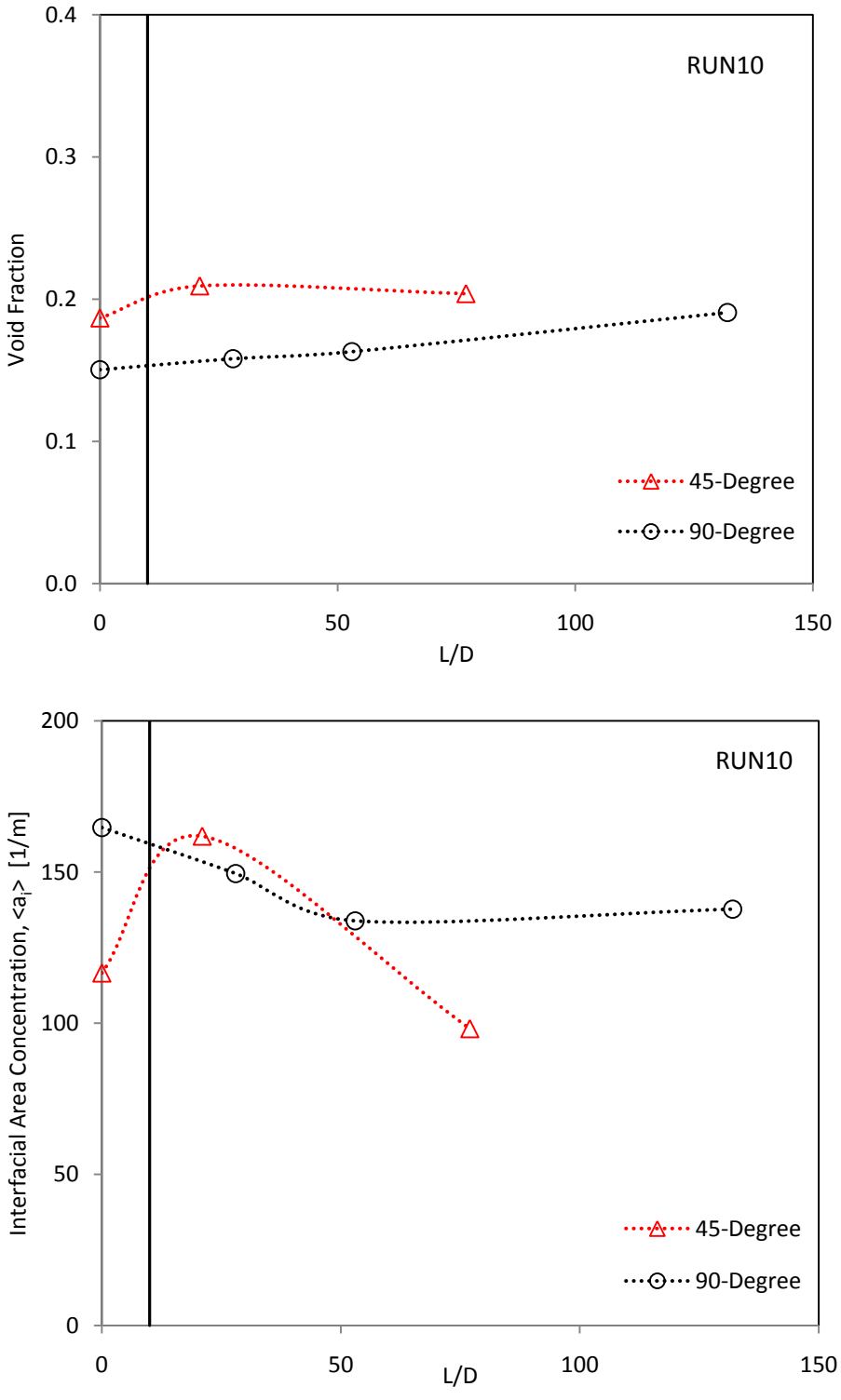

Figure **A5-10**: Comparison of the one-dimensional transport of $<\alpha>$ and $<a_i>$ across the elbows for two characteristic flow conditions with constant j_f=4.3 m/s

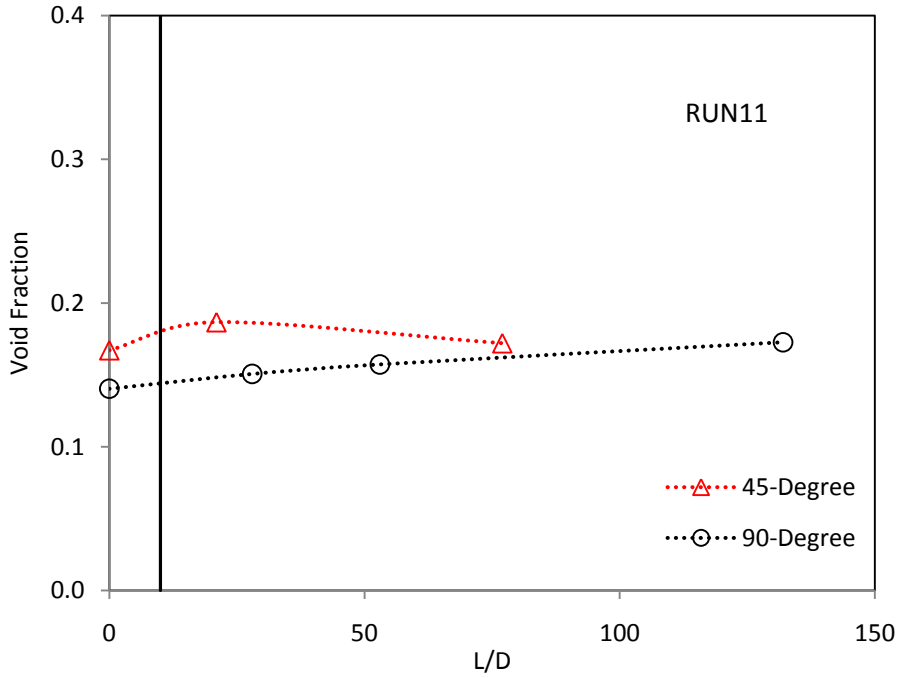

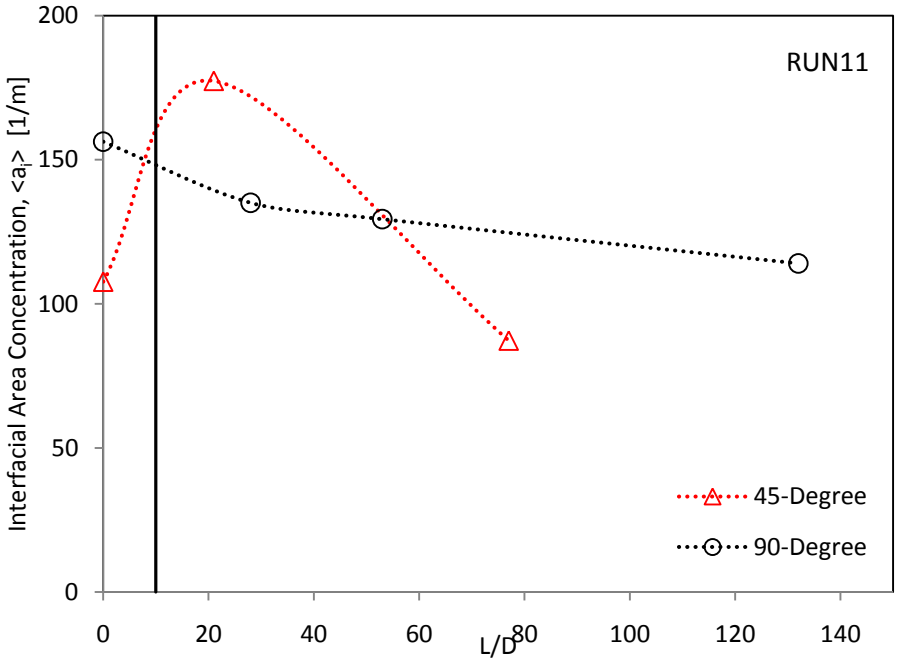

Figure **A5-11**: Comparison of the one-dimensional transport of <α> and <a_i> across the elbows for two characteristic flow conditions with constant j_f=4.3 m/s

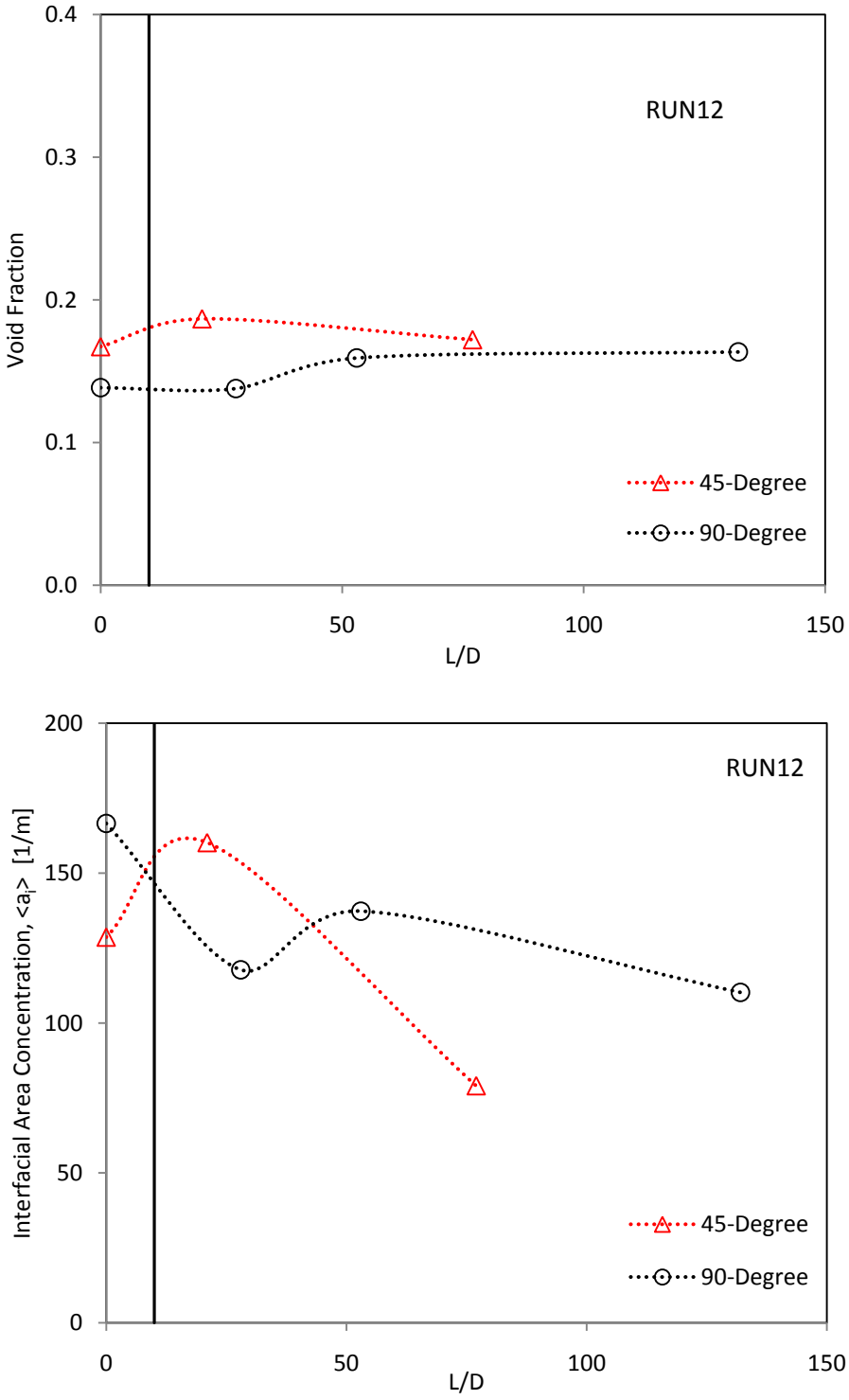

Figure **A5-12**: Comparison of the one-dimensional transport of $<\alpha>$ and $<a_i>$ across the elbows for two characteristic flow conditions with constant j_f=4.3 m/s

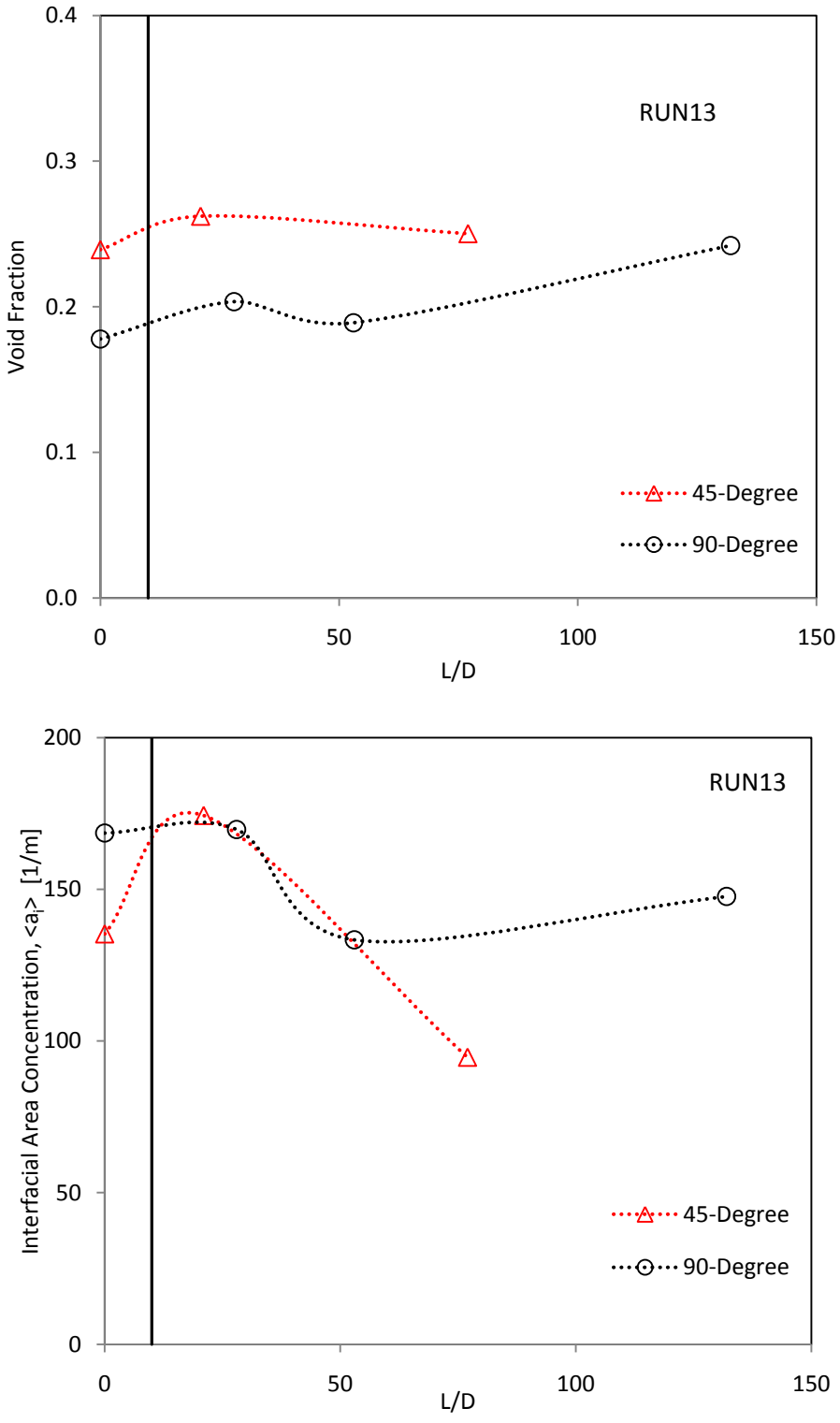

Figure **A5-13**: Comparison of the one-dimensional transport of $<\alpha>$ and $<a_i>$ across the elbows for two characteristic flow conditions with constant j_f=4.3 m/s

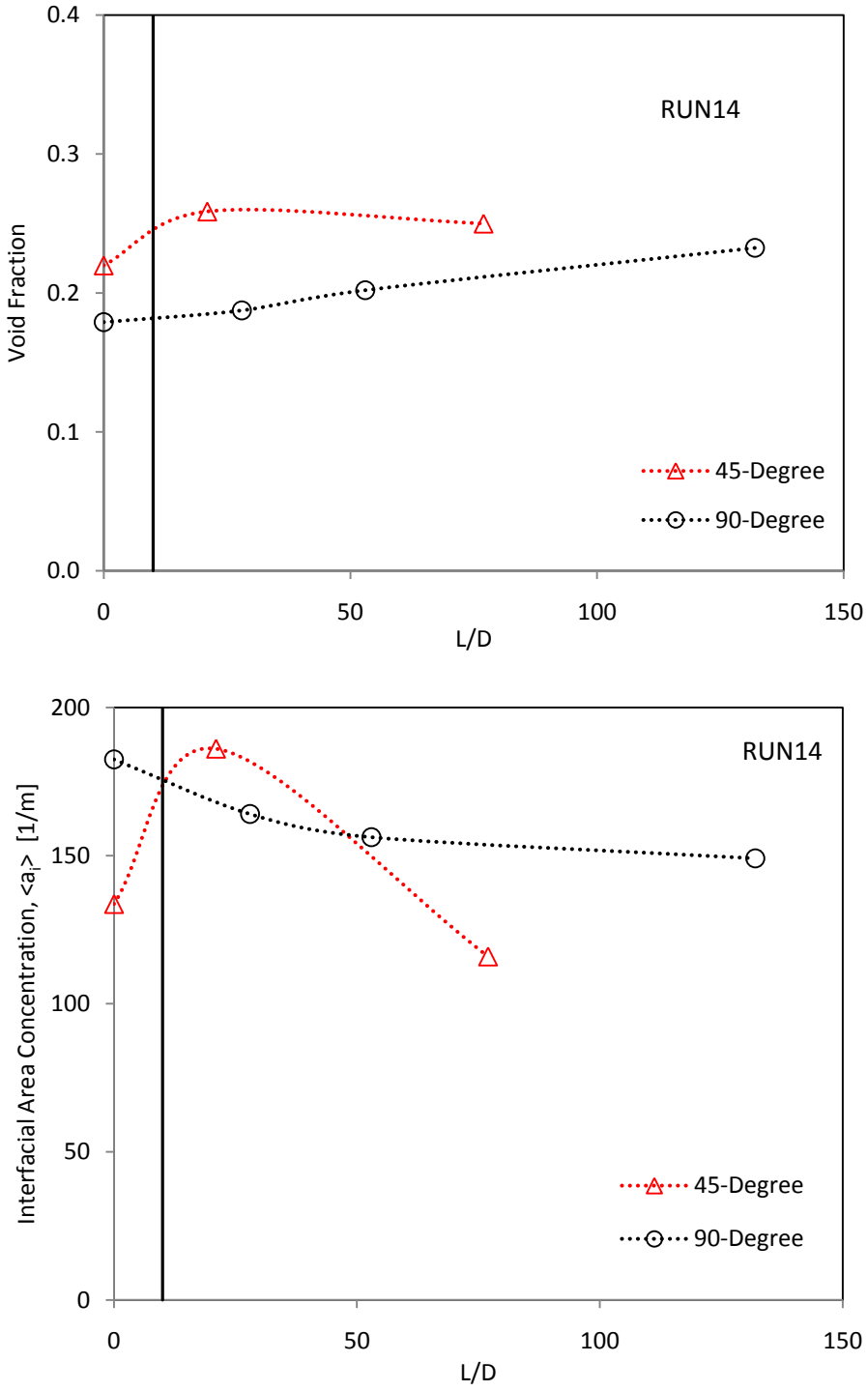

Figure **A5-14**: Comparison of the one-dimensional transport of $<\alpha>$ and $<a_i>$ across the elbows for two characteristic flow conditions with constant j_f=4.3 m/s

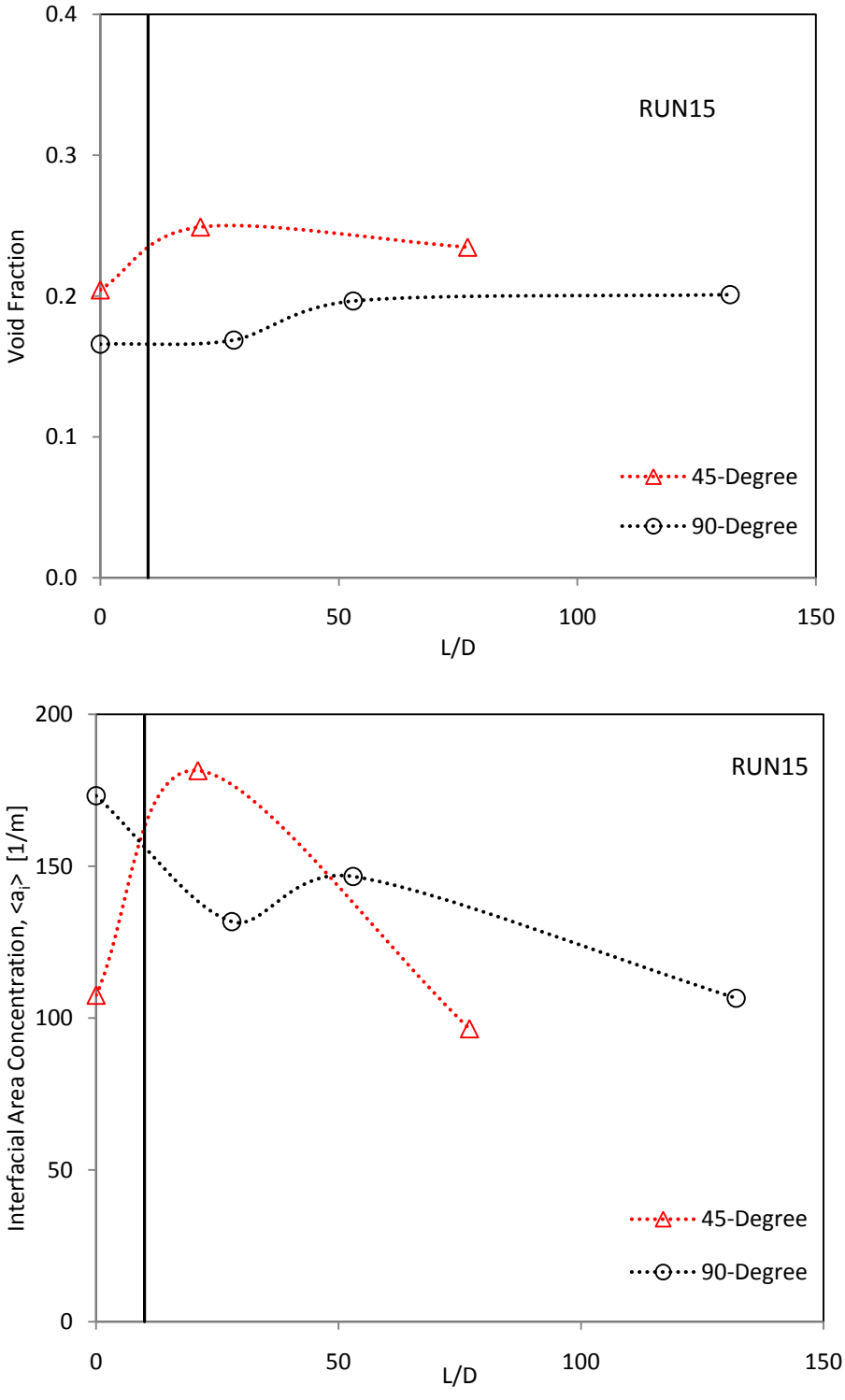

Figure **A5-15**: Comparison of the one-dimensional transport of $<\alpha>$ and $<a_i>$ across the elbows for two characteristic flow conditions with constant j_f=4.3 m/s

Appendix A6

Axial
Development of Void-Weighted Bubble Velocity

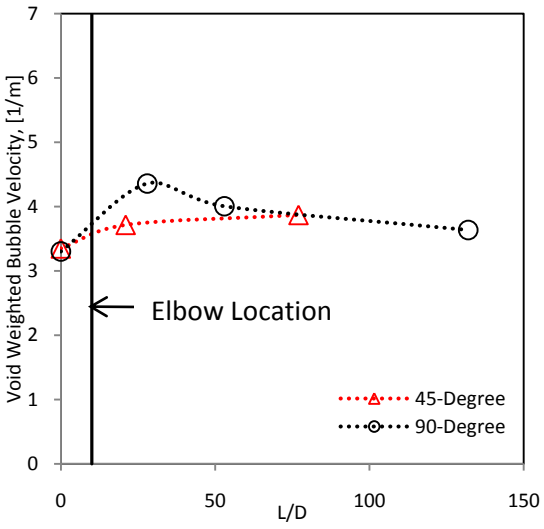

a) j_f = 3.8 m/s

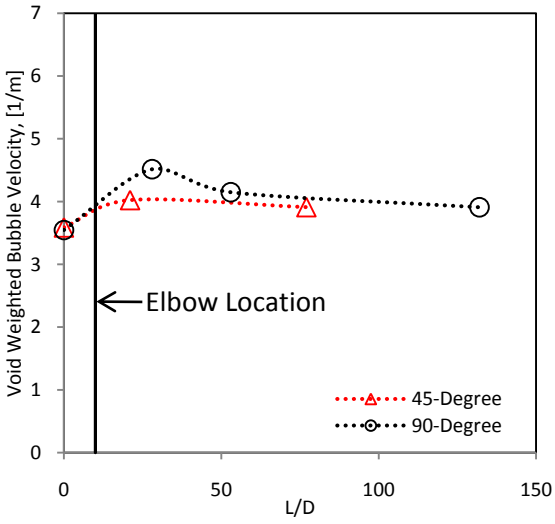

b) j_f = 4.0 m/s

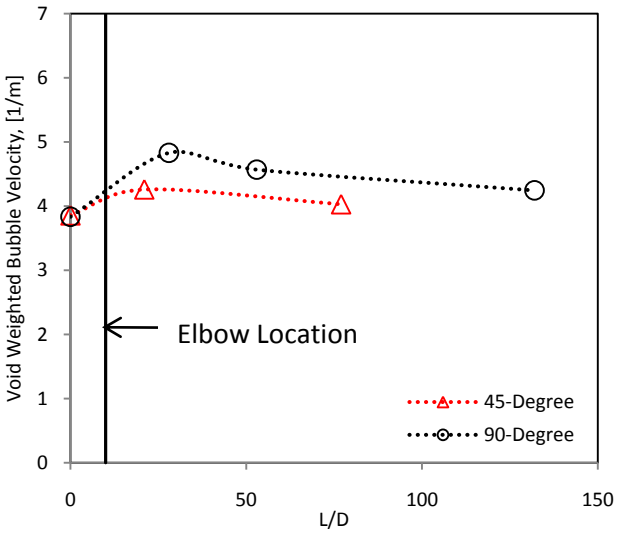

c) j_f = 4.3 m/s

Figure **A6-1**: Comparison of the axial development of one dimensional void weighted bubble velocity in three different liquid flow rates at constant gas flow rate; $j_{g,atm}$=0.1 m/s

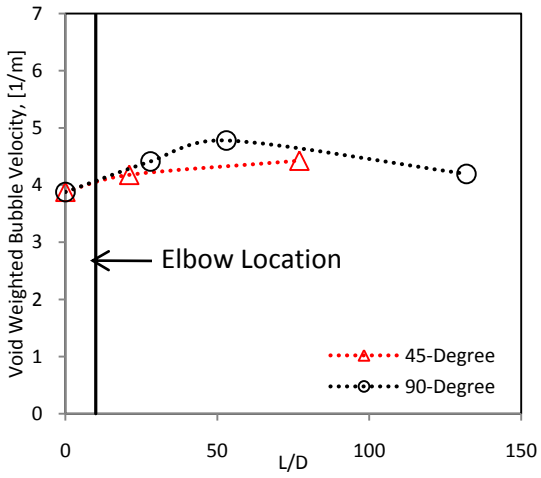

a) j_f = 3.8 m/s

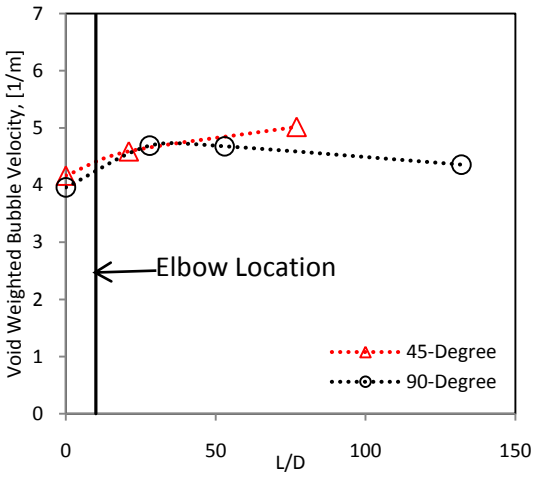

b) j_f = 4.0 m/s

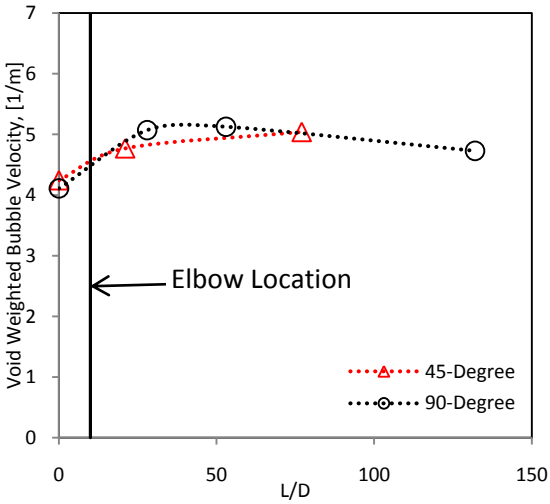

c) j_f = 4.3 m/s

Figure **A6-2**: Comparison of the axial development of one dimensional void weighted bubble velocity in three different liquid flow rates at constant gas flow rate; $j_{g,atm}$= 0.3 m/s

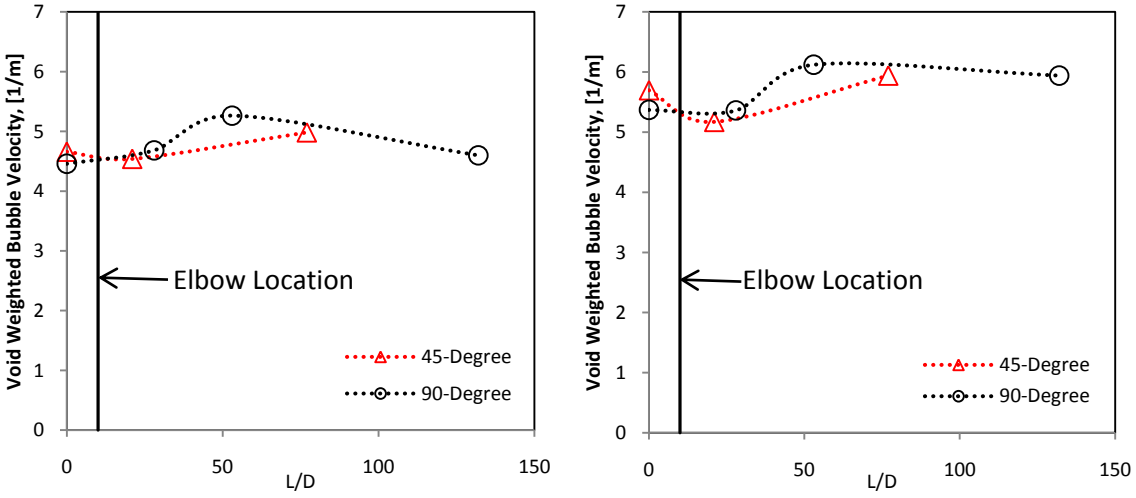

a) j_f = 3.8 m/s

b) j_f = 4.0 m/s

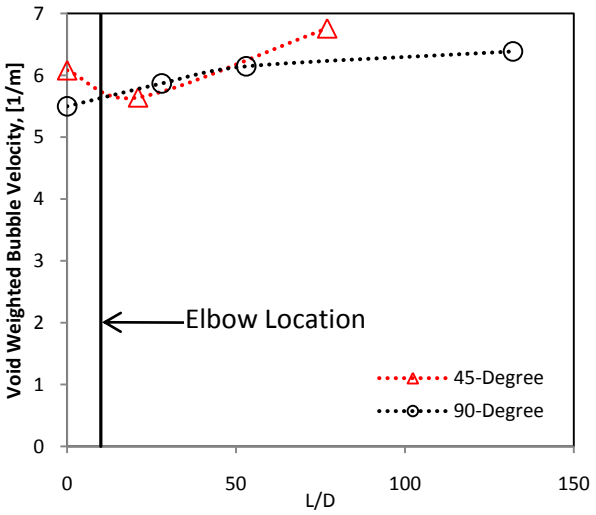

c) j_f = 4.3 m/s

Figure **A6-3**: Comparison of the axial development of one dimensional void weighted bubble velocity in three different liquid flow rates at constant gas flow rate; $j_{g,atm}$ = 0.7 m/s

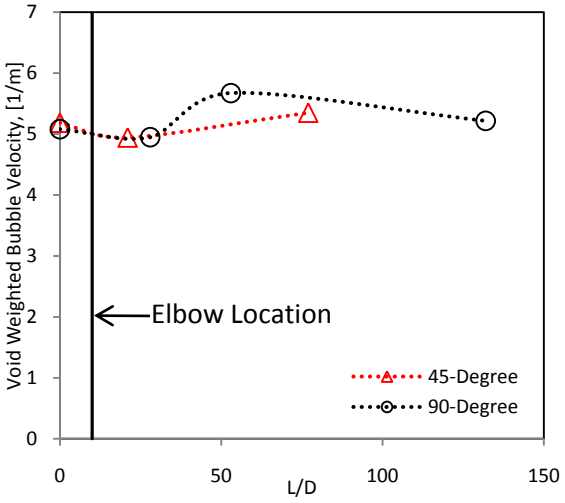

a) j_f = 3.8 m/s

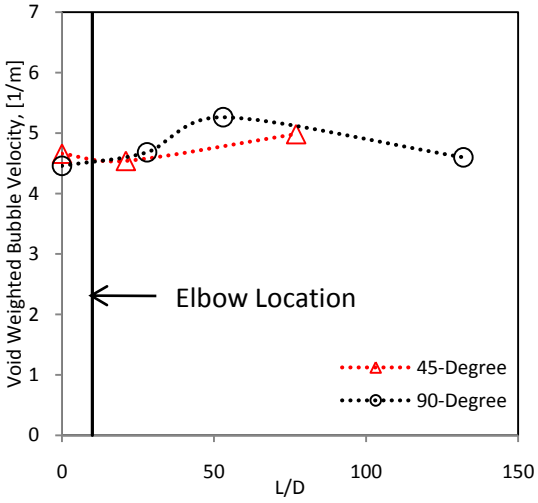

b) j_f = 4.0 m/s

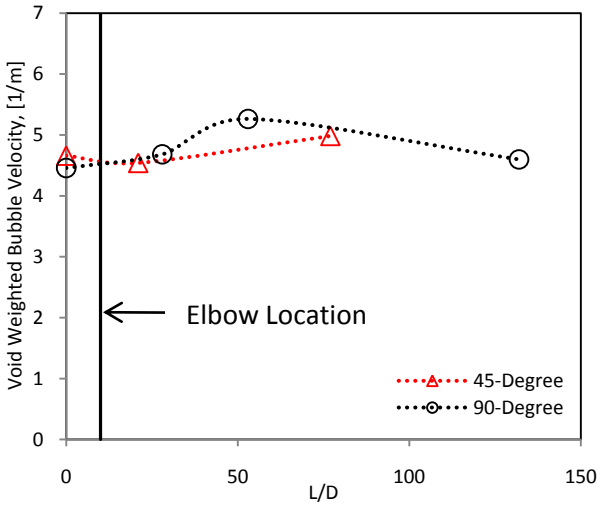

c) j_f = 4.3 m/s

Figure **A6-4**: Comparison of the axial development of one dimensional void weighted bubble velocity in for three different liquid flow rates at constant gas flow rate; $j_{g,atm}$= 1.0 m/s

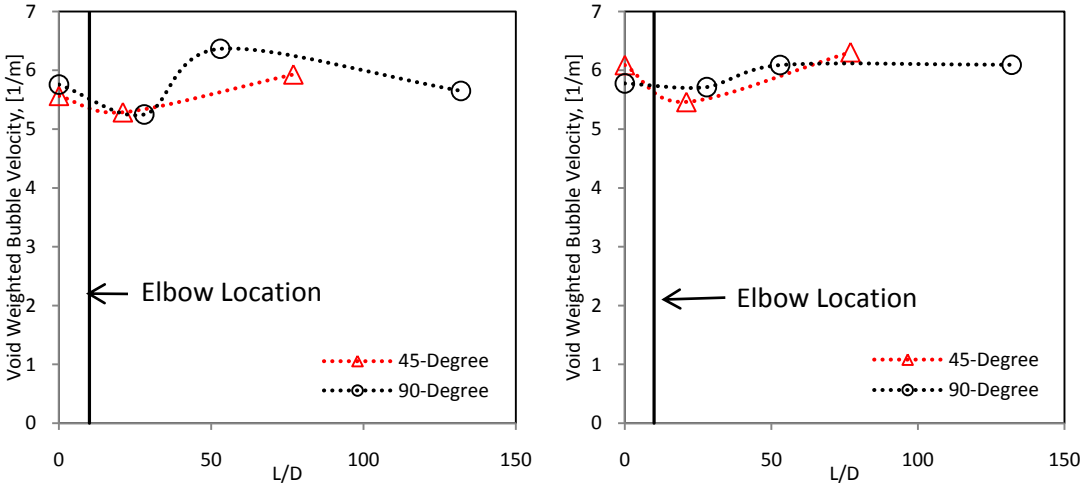

a) j_f = 3.8 m/s

b) j_f = 4.0 m/s

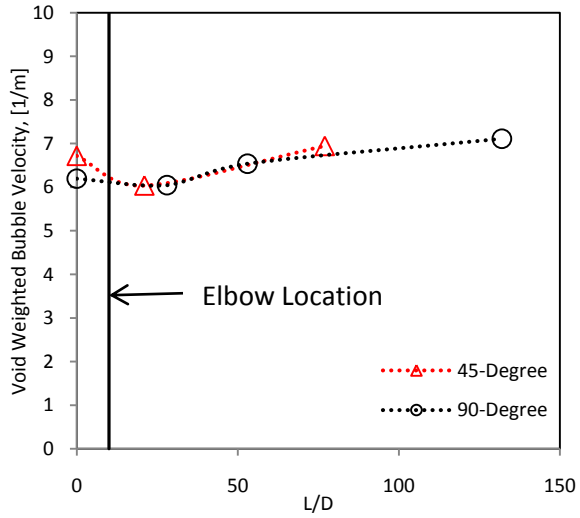

c) j_f = 4.3 m/s

Figure **A6-5**: Comparison of the axial development of one dimensional void weighted bubble velocity for three different liquid flow rates at constant gas flow rate $j_{g,atm}$= 1.3 m/s

Appendix A7

Local interfacial structures in vertical upward section in combinatorial channels

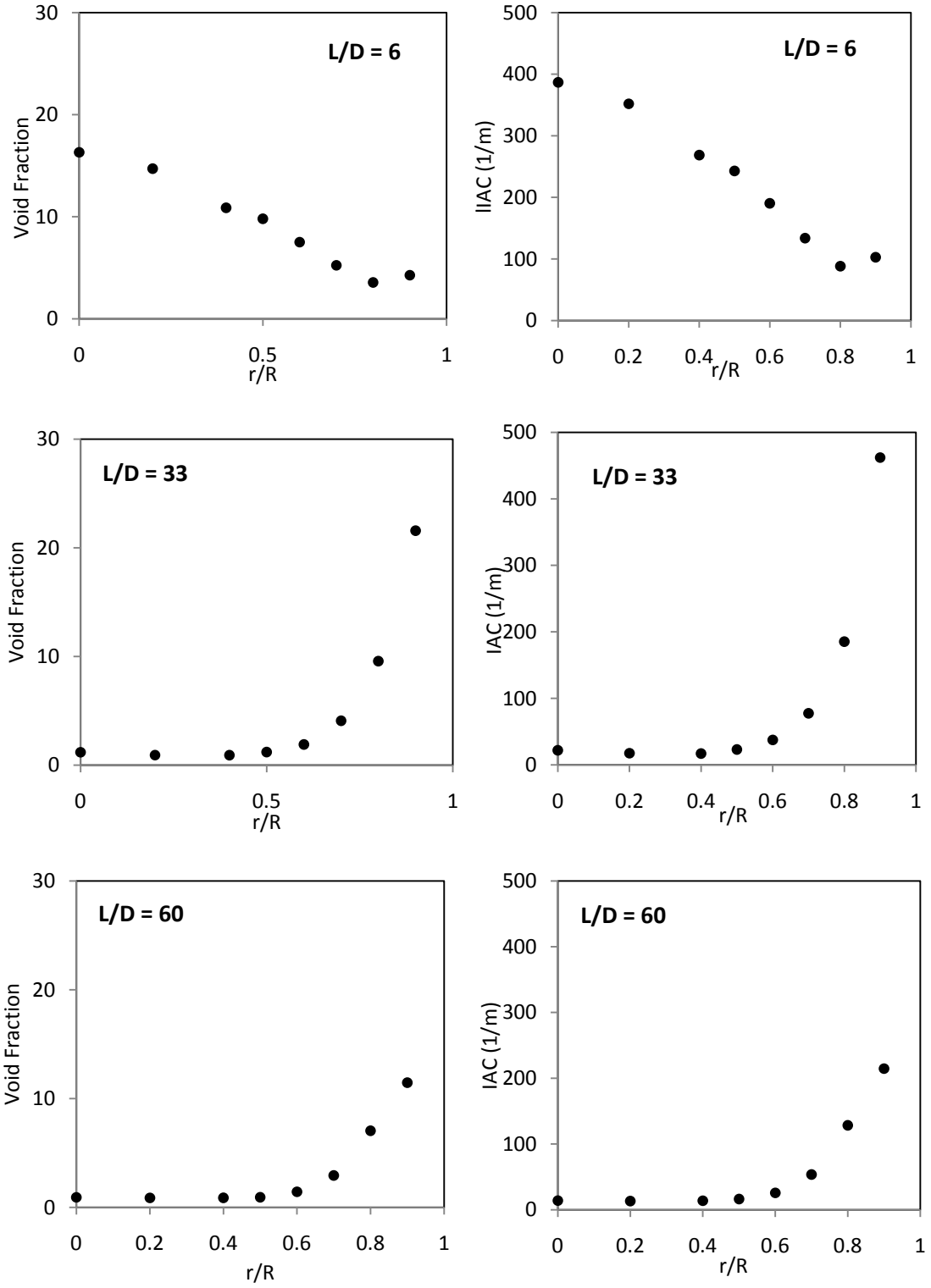

Figure **A7-1**: Local profiles of α and a_i for j_f = 2.0 m/s and $j_{g,atm}$ = 0.228 m/s along the vertical section

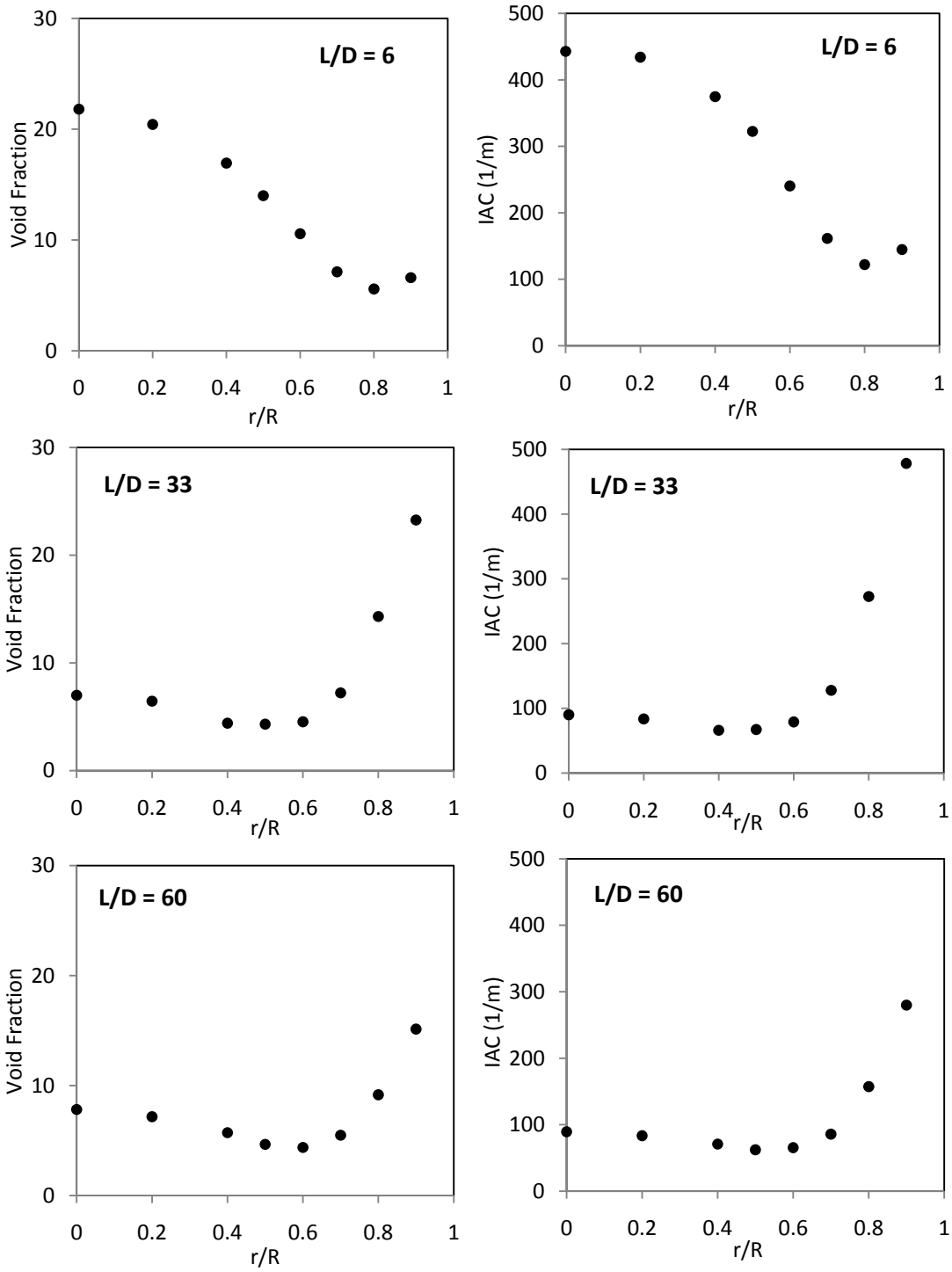

Figure **A7-2**: Local profiles of α and a_i for j_f = 2.0 m/s and $j_{g,atm}$ = 0.343 m/s along the vertical section

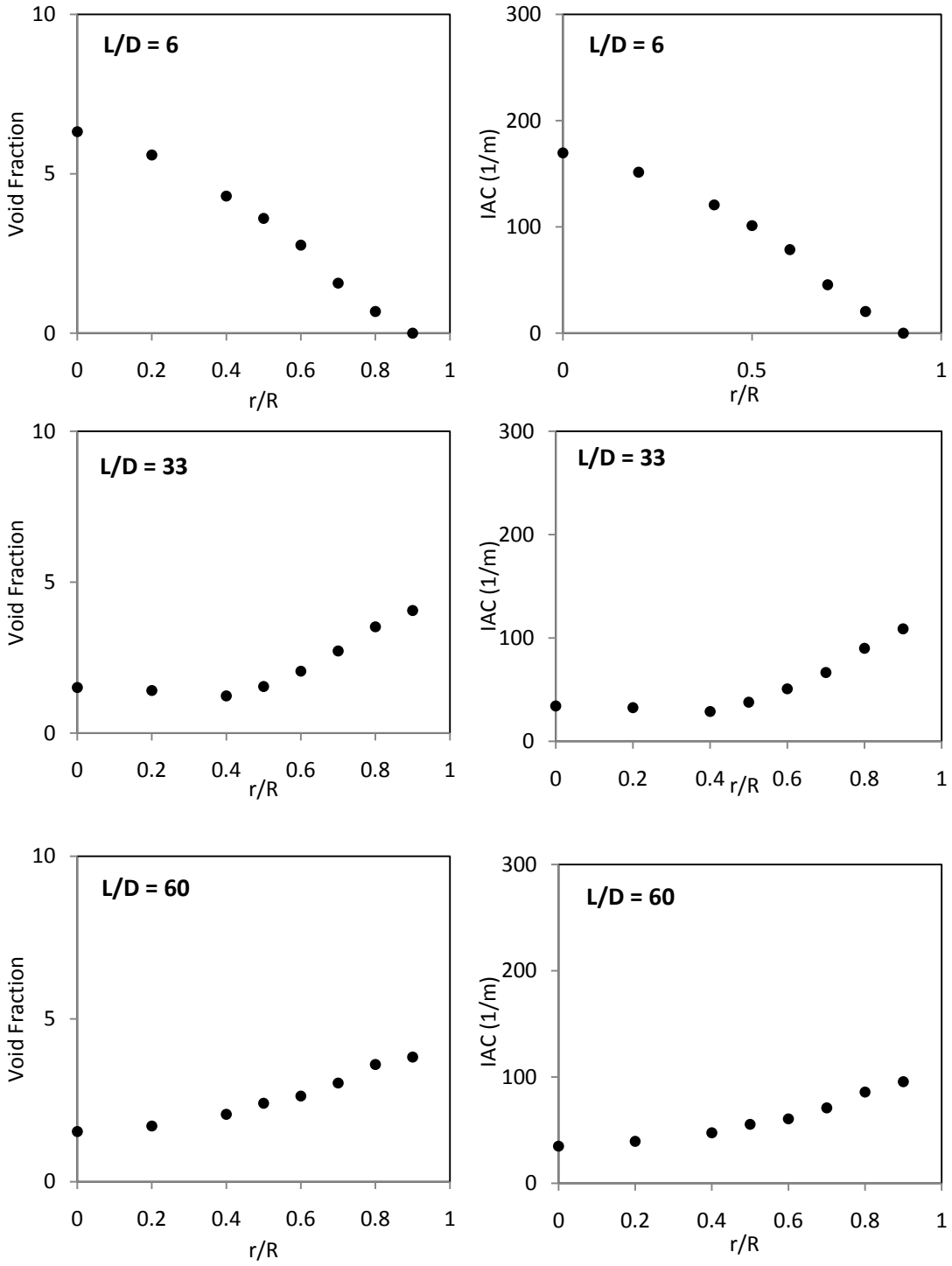

Figure **A7-3**: Local profiles of α and a_i for j_f = 3.0 m/s and $j_{g,atm}$ = 0.139 m/s along the vertical section

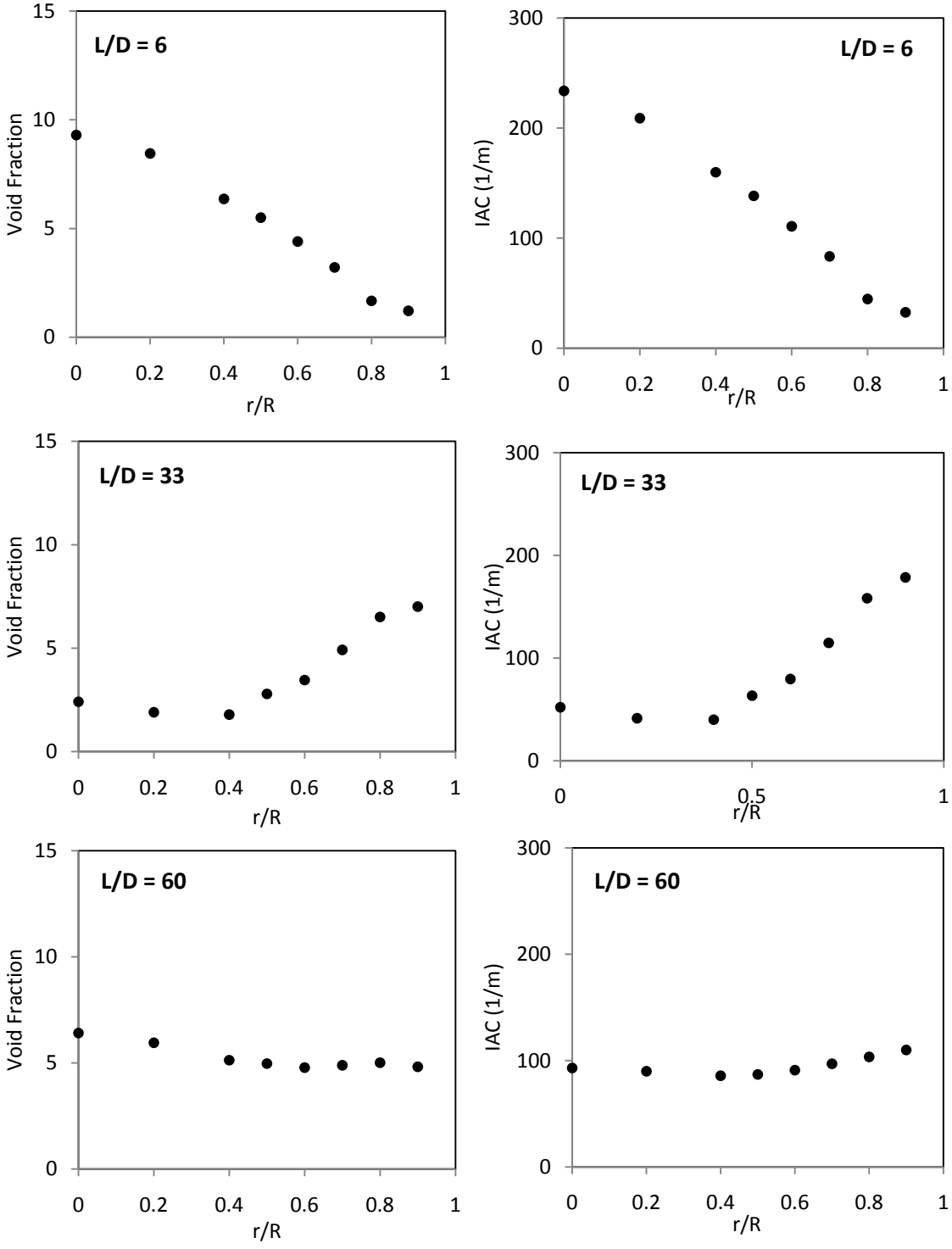

Figure **A7-4**: Local profiles of α and a_i for j_f = 3.0 m/s and $j_{g,atm}$ = 0.232 m/s along the vertical section

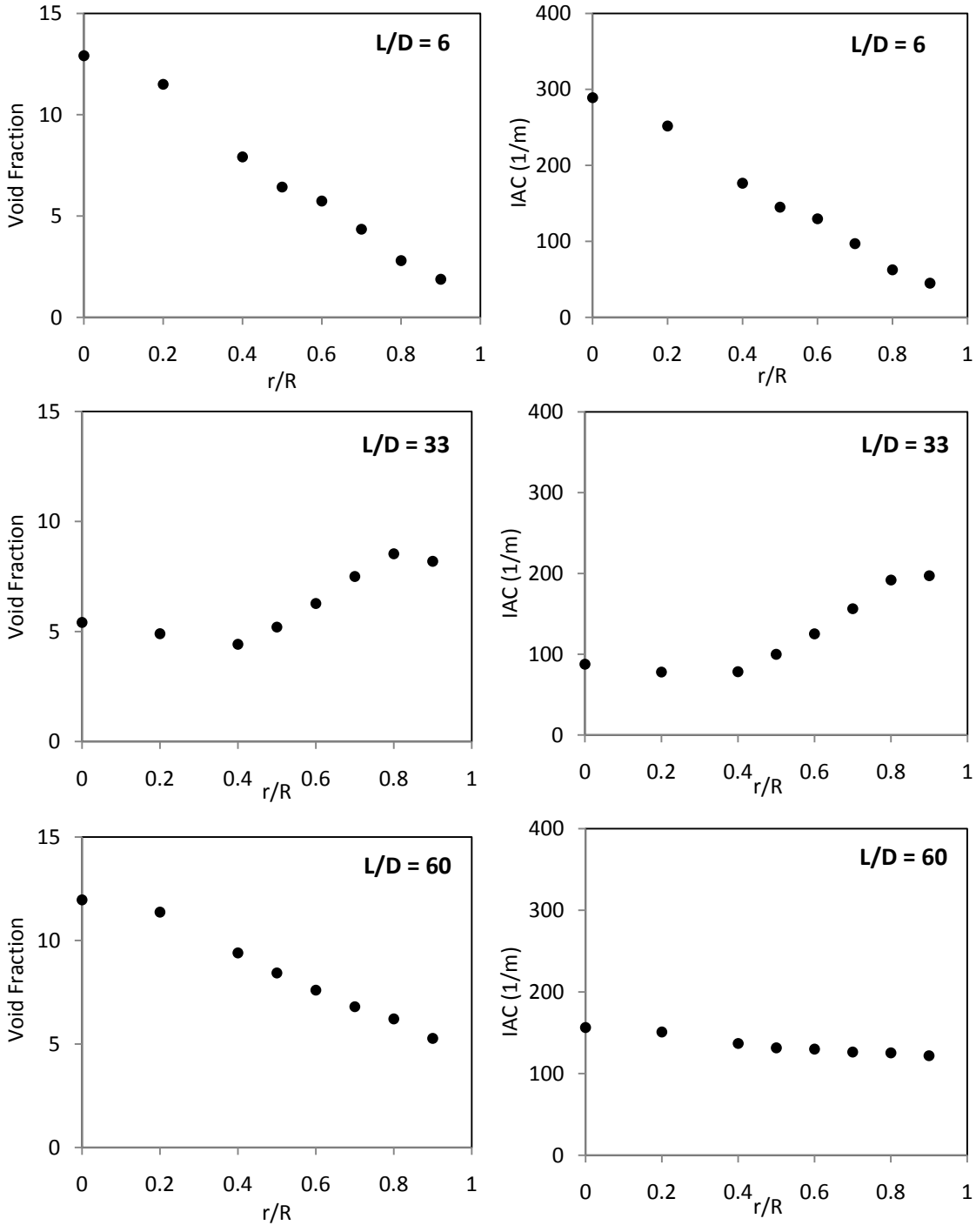

Figure **A7-5**: Local profiles of α and a_i for j_f = 3.0 m/s and $j_{g,atm}$ = 0.353 m/s along the vertical section

Appendix A8

Local interfacial structures in horizontal section in combinatorial channels

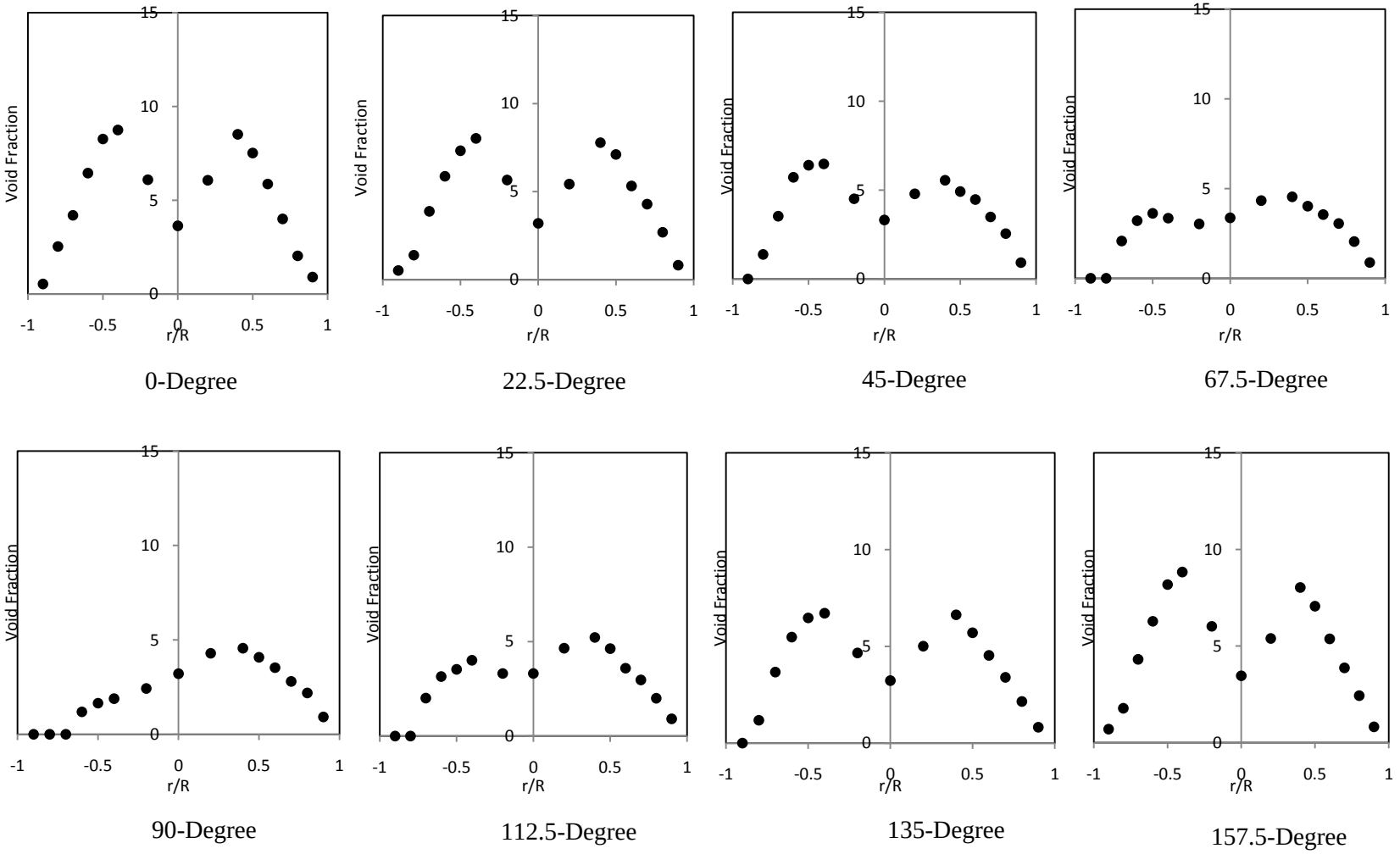

Figure **A 8-1**: Local profiles of void fraction at different angles of measurement at port P4, L/D = 3 from the 90-degree vertical elbow at Run-4; j_f = 3.0 m/s and $j_{g,atm}$ = 0.139 m/s

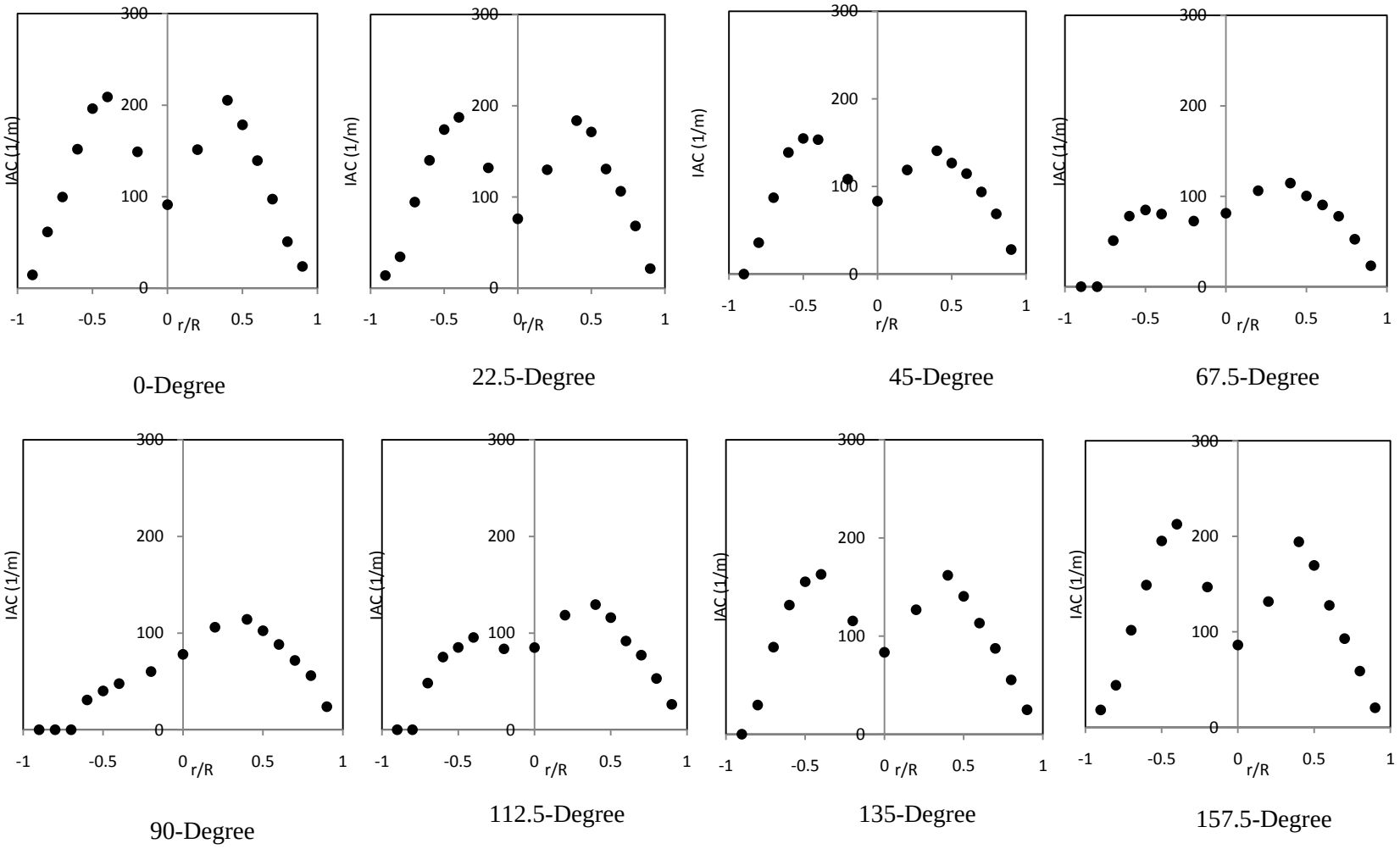

Figure **A 8-2**: Local profiles of interfacial area concentration at different angles of measurement at port P4, L/D = 3 from the 90-degree vertical elbow at Run-4; j_f = 3.0 m/s and $j_{g,atm}$ = 0.139 m/s

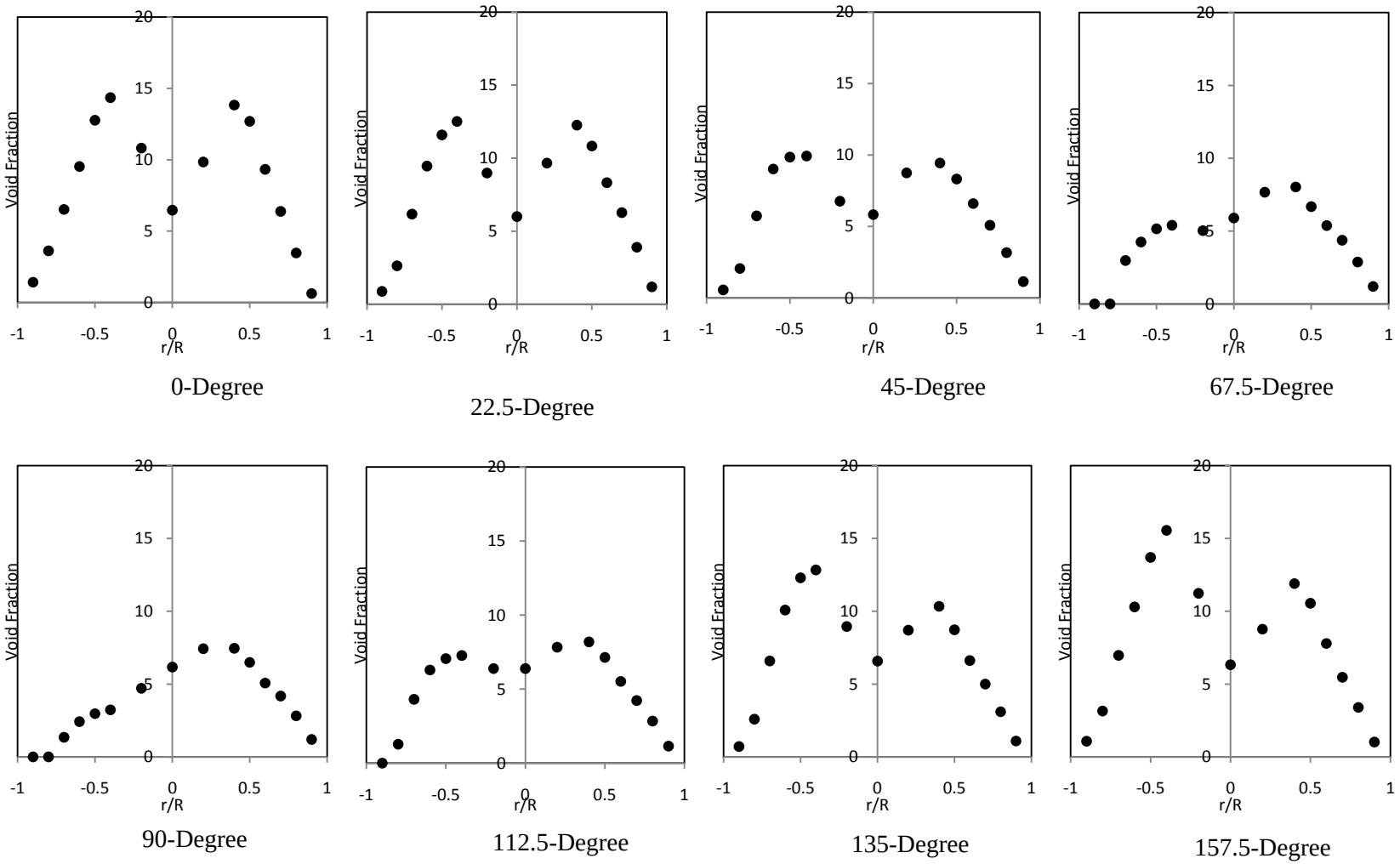

Figure **A 8-3**: Local profiles of void fraction at different angles of measurement at port P4, L/D = 3 from the 90-degree vertical elbow at Run-5; j_f = 3.0 m/s and $j_{g,atm}$ = 0.232 m/s

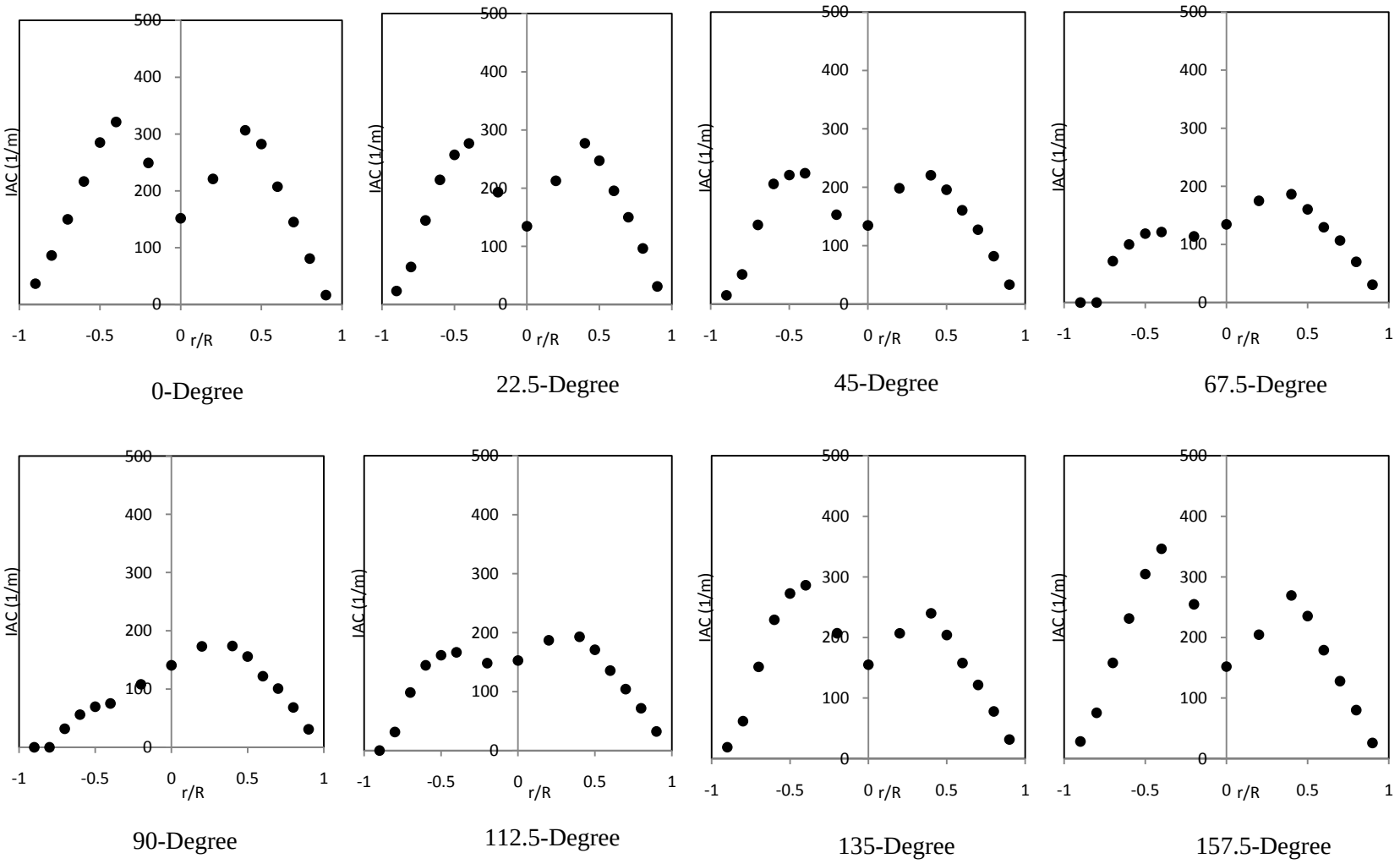

Figure **A 8-4**: Local profiles of interfacial area concentration at different angles of measurement at port P4, L/D = 3 from the 90-degree vertical elbow at Run-5; j_f = 3.0 m/s and $j_{g,atm}$ = 0.232 m/s

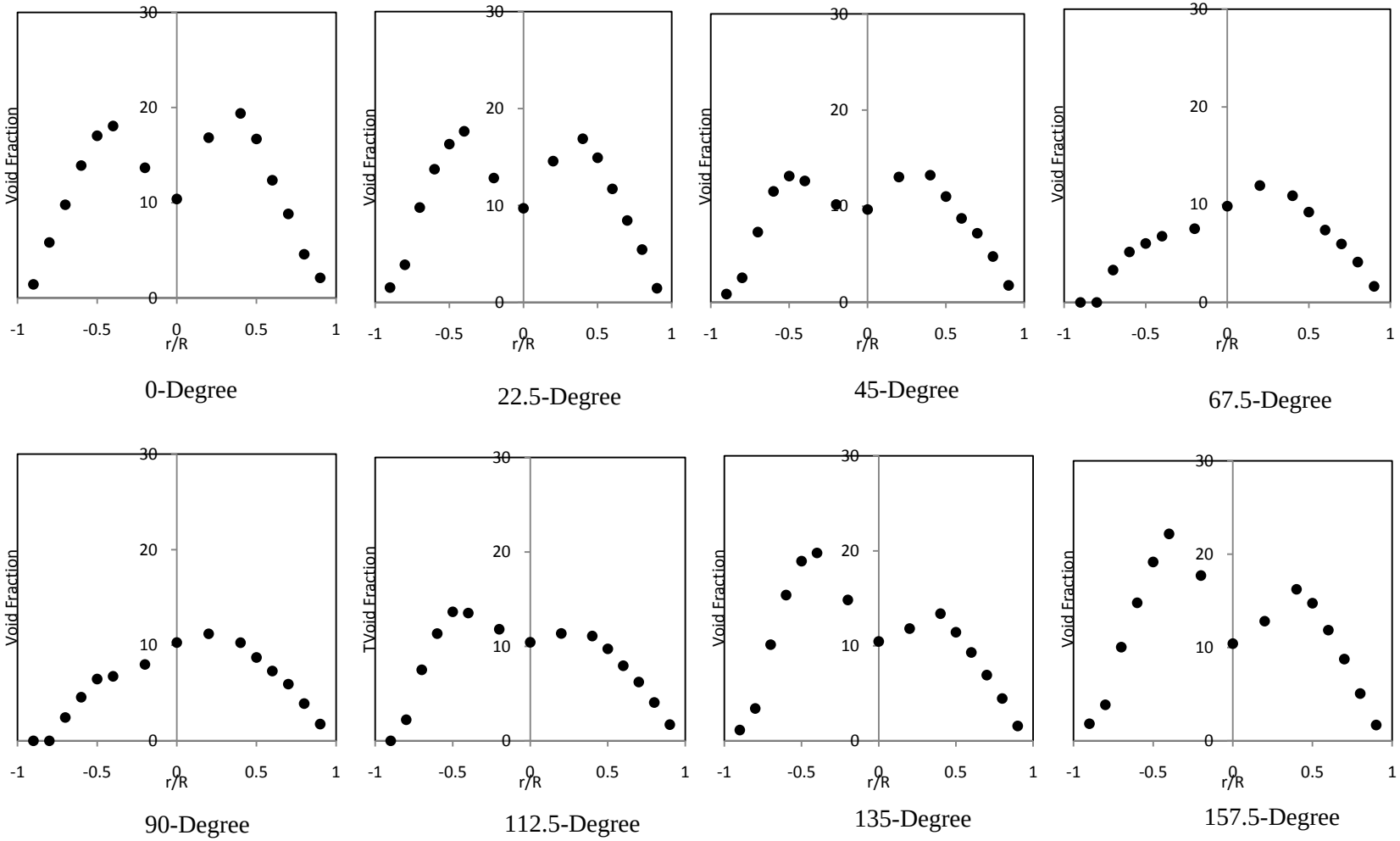

Figure **A 8-5**: Local profiles of void fraction at different angles of measurement at port P4, L/D = 3 from the 90-degree vertical elbow at Run-6; j_f = 3.0 m/s and $j_{g,atm}$ = 0.353 m/s

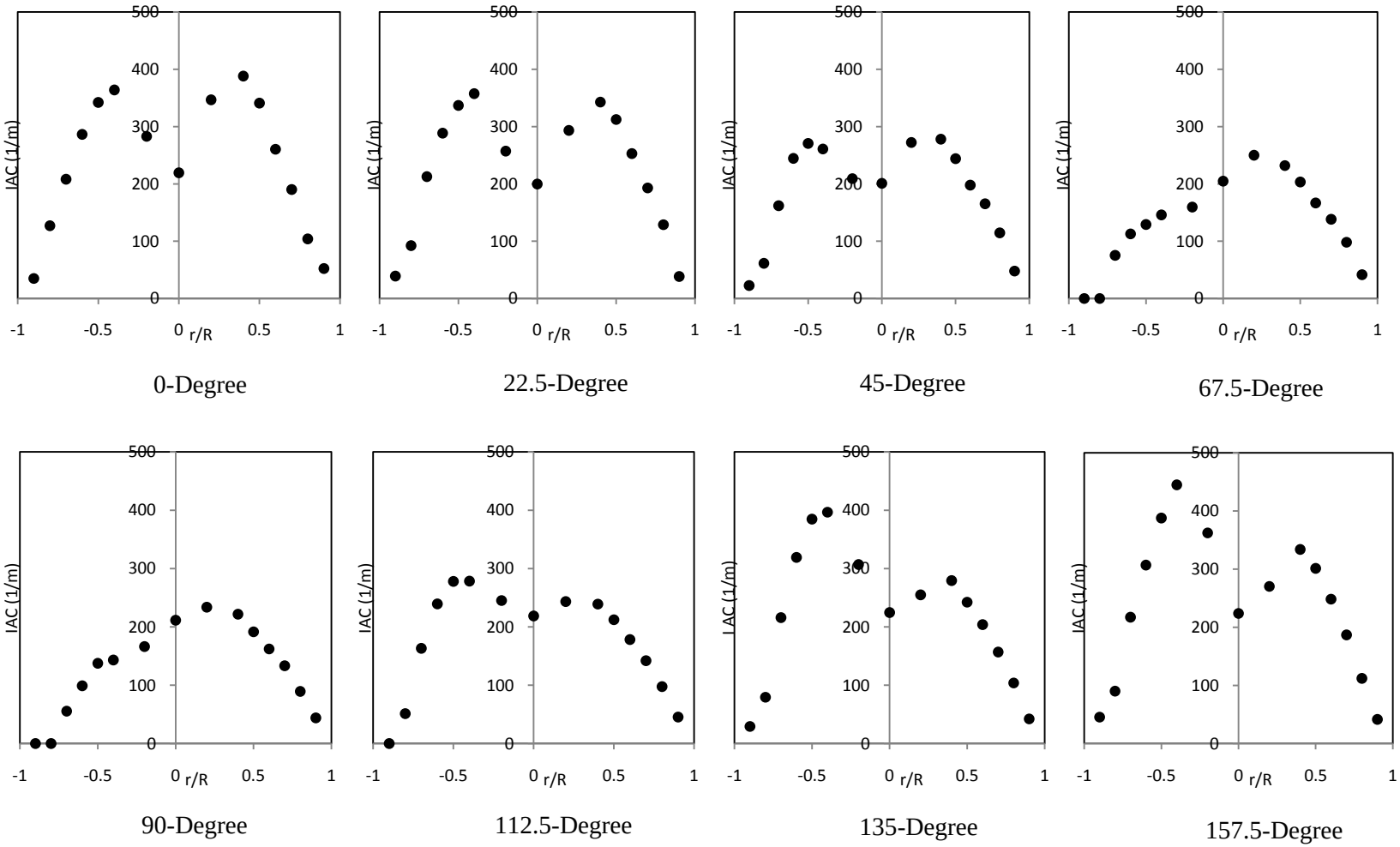

Figure **A 8-6**: Local profiles of interfacial area concentration at different angles of measurement at port P4, L/D = 3 from the 90-degree vertical elbow at Run-6; j_f = 3.0 m/s and $j_{g,atm}$ = 0.353 m/s

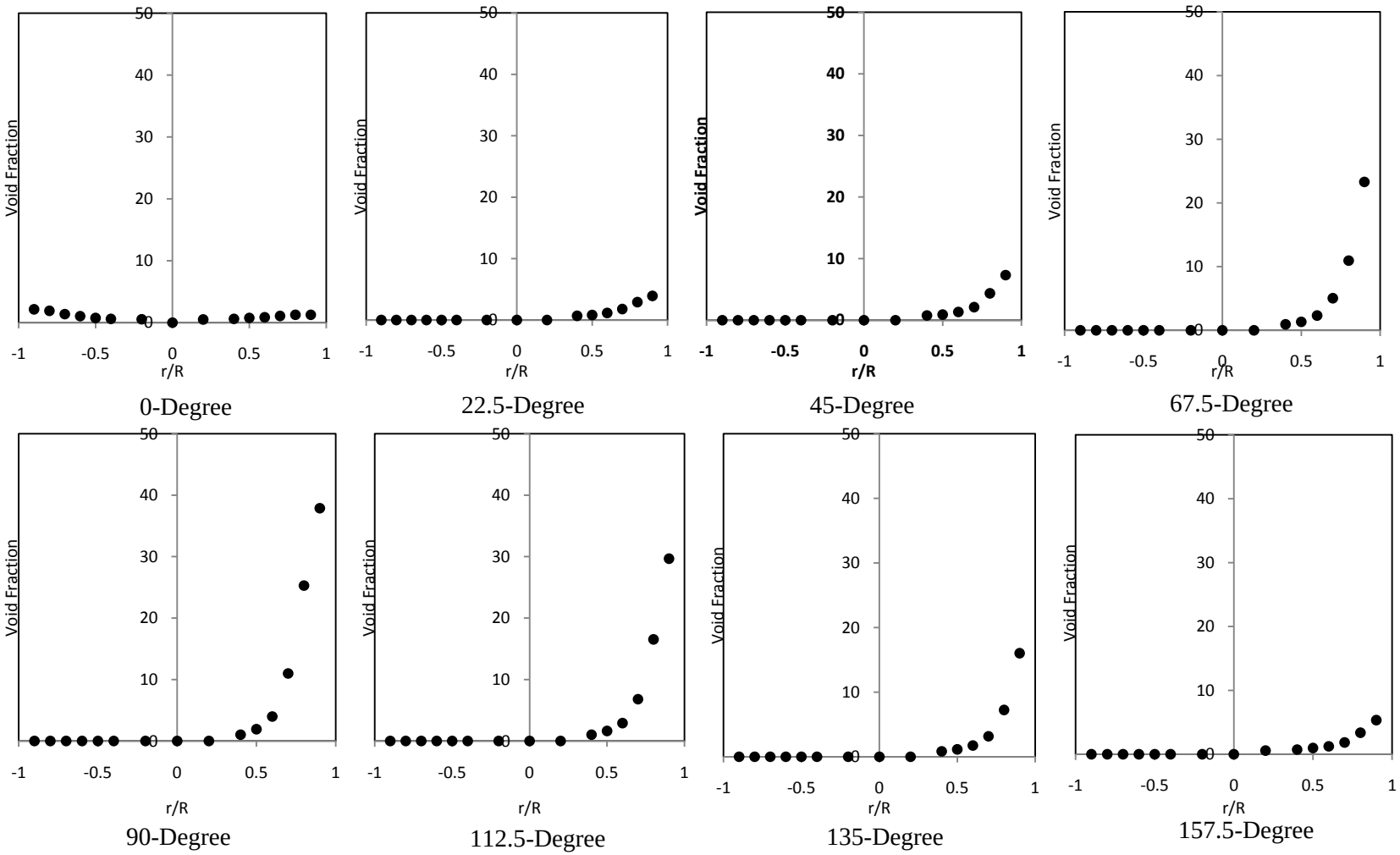

Figure **A 8-7**: Local profiles of void fraction at different angles of measurement at port P5, L/D = 30 from the 90-degree vertical elbow at Run-4; j_f = 3.0 m/s and $j_{g,atm}$ = 0.139 m/s

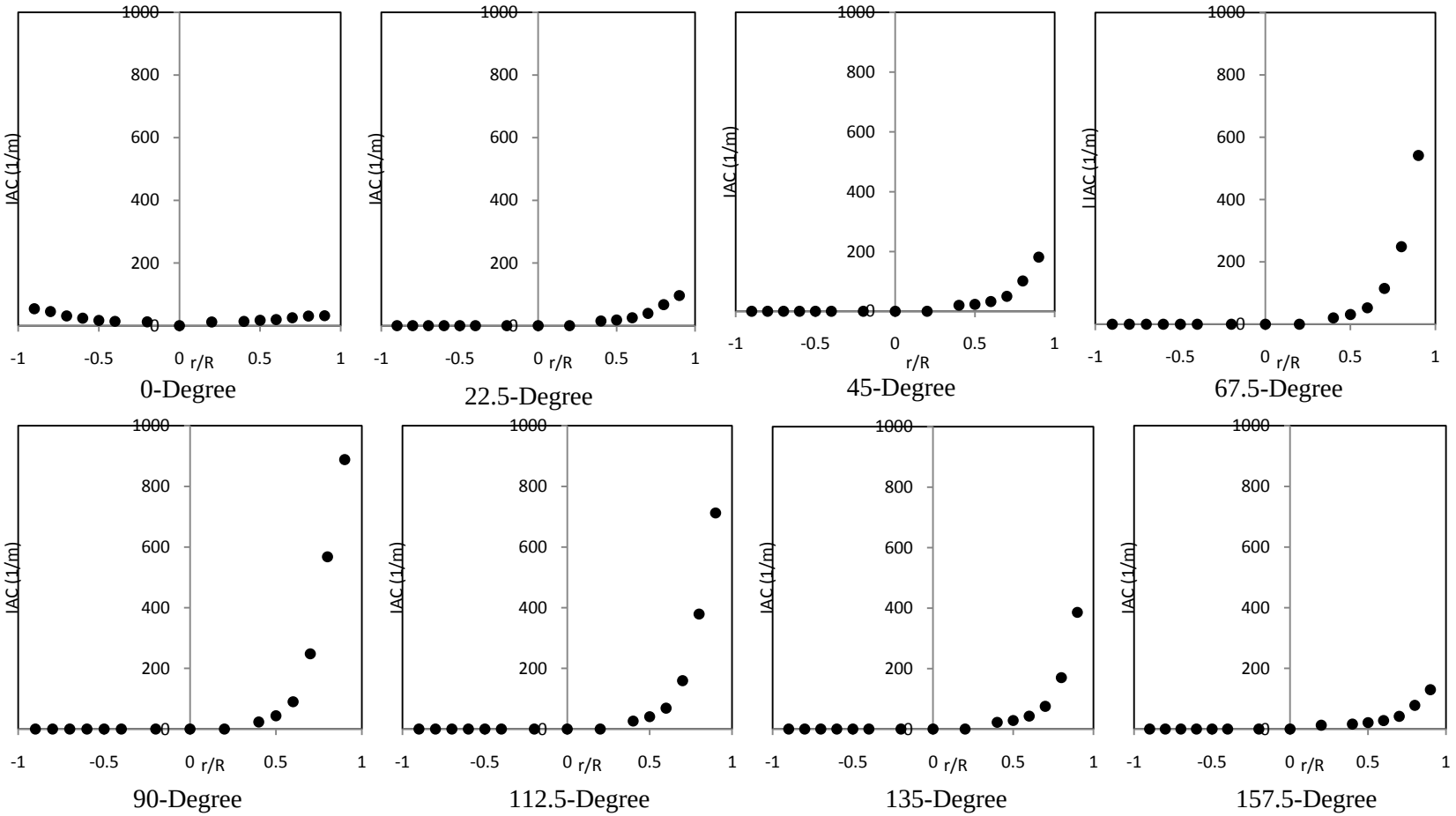

Figure **A 8-8**: Local profiles of interfacial area concentration at different angles of measurement at port P5, L/D = 30 from the 90-degree vertical elbow at Run-4; j_f = 3.0 m/s and $j_{g,atm}$ = 0.139 m/s

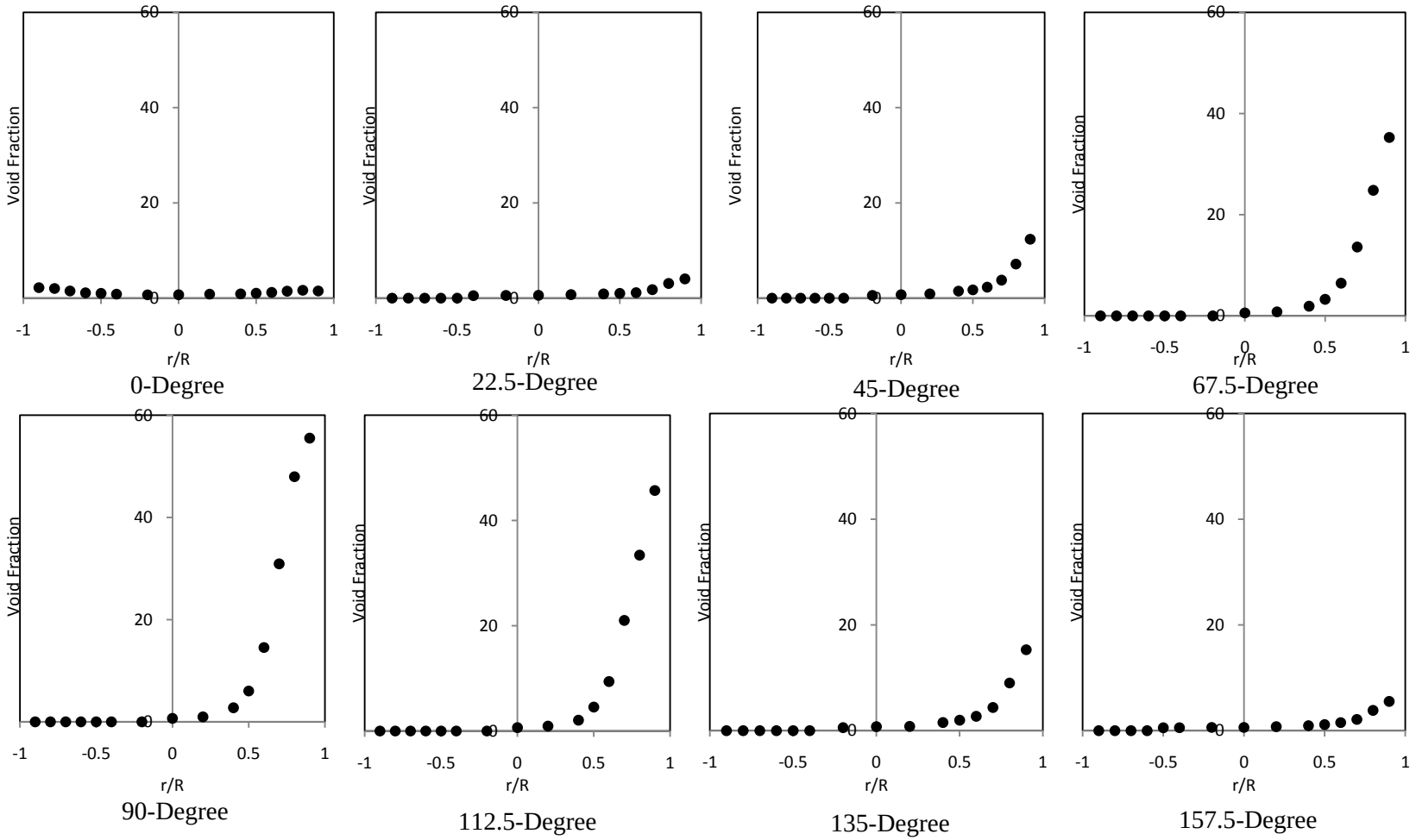

Figure **A 8-9**: Local profiles of void fraction at different angles of measurement at port P5, L/D = 30 from the 90-degree vertical elbow at Run-5; j_f = 3.0 m/s and $j_{g,atm}$ = 0.232m/s

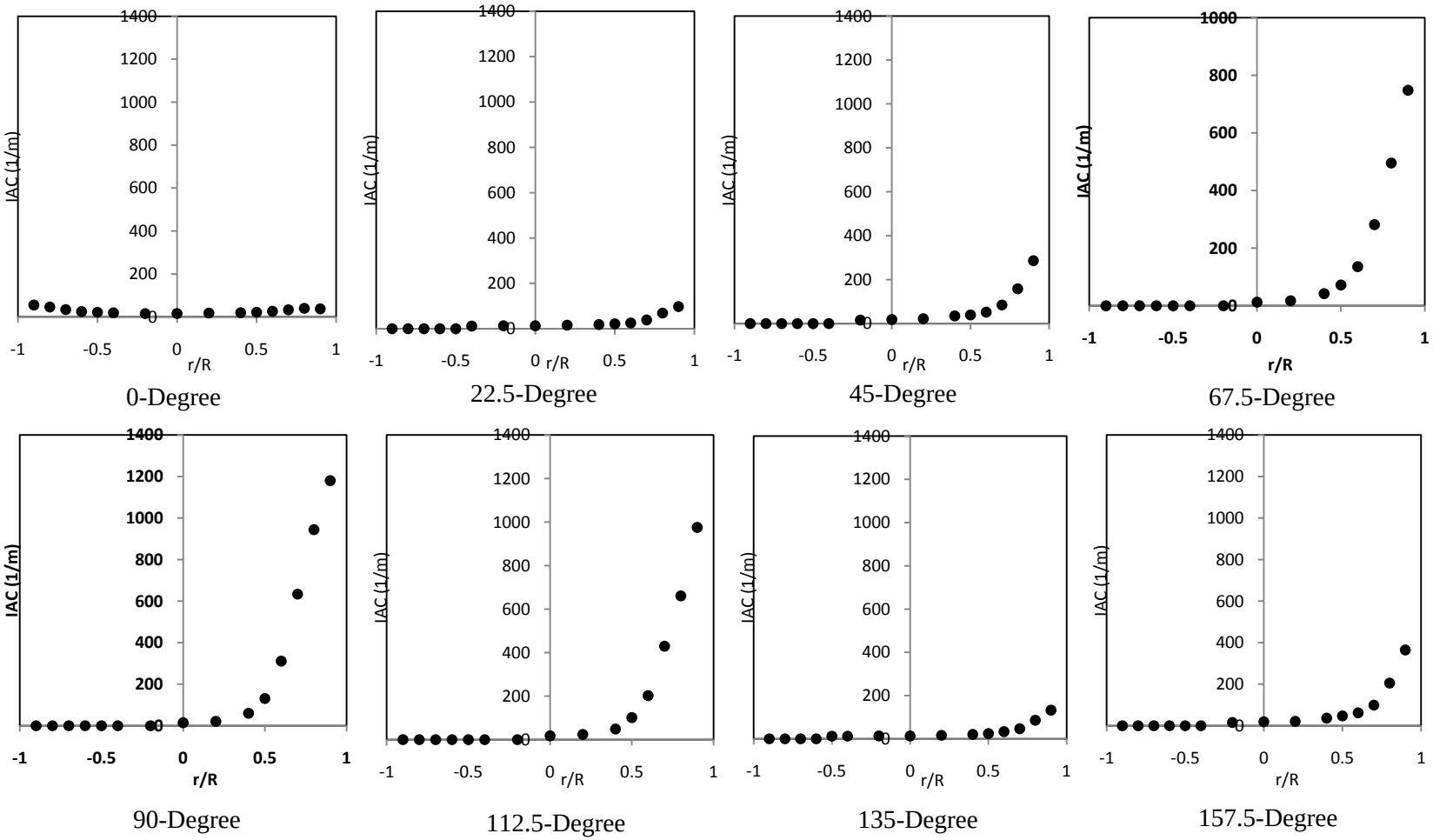

Figure **A 8-10**: Local profiles of interfacial area concentration at different angles of measurement at port P5, L/D = 30 from the 90-degree vertical elbow at Run-5; j_f = 3.0 m/s and $j_{g,atm}$ = 0.232 m/s

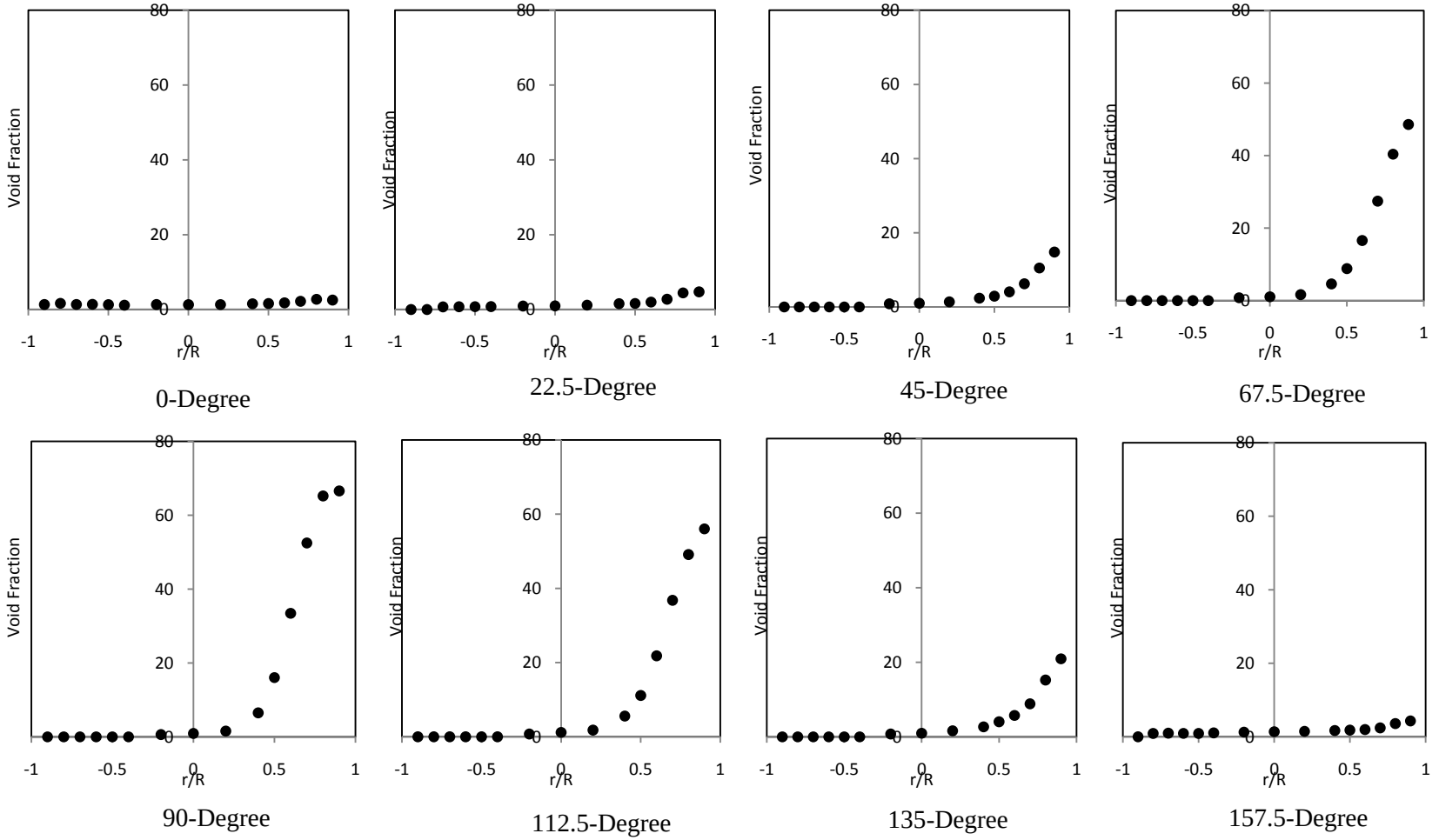

Figure **A 8-11**: Local profiles of void fraction at different angles of measurement at port P5, L/D = 30 from the 90-degree vertical elbow at Run-6; j_f = 3.0 m/s and $j_{g,atm}$ = 0.353m/s

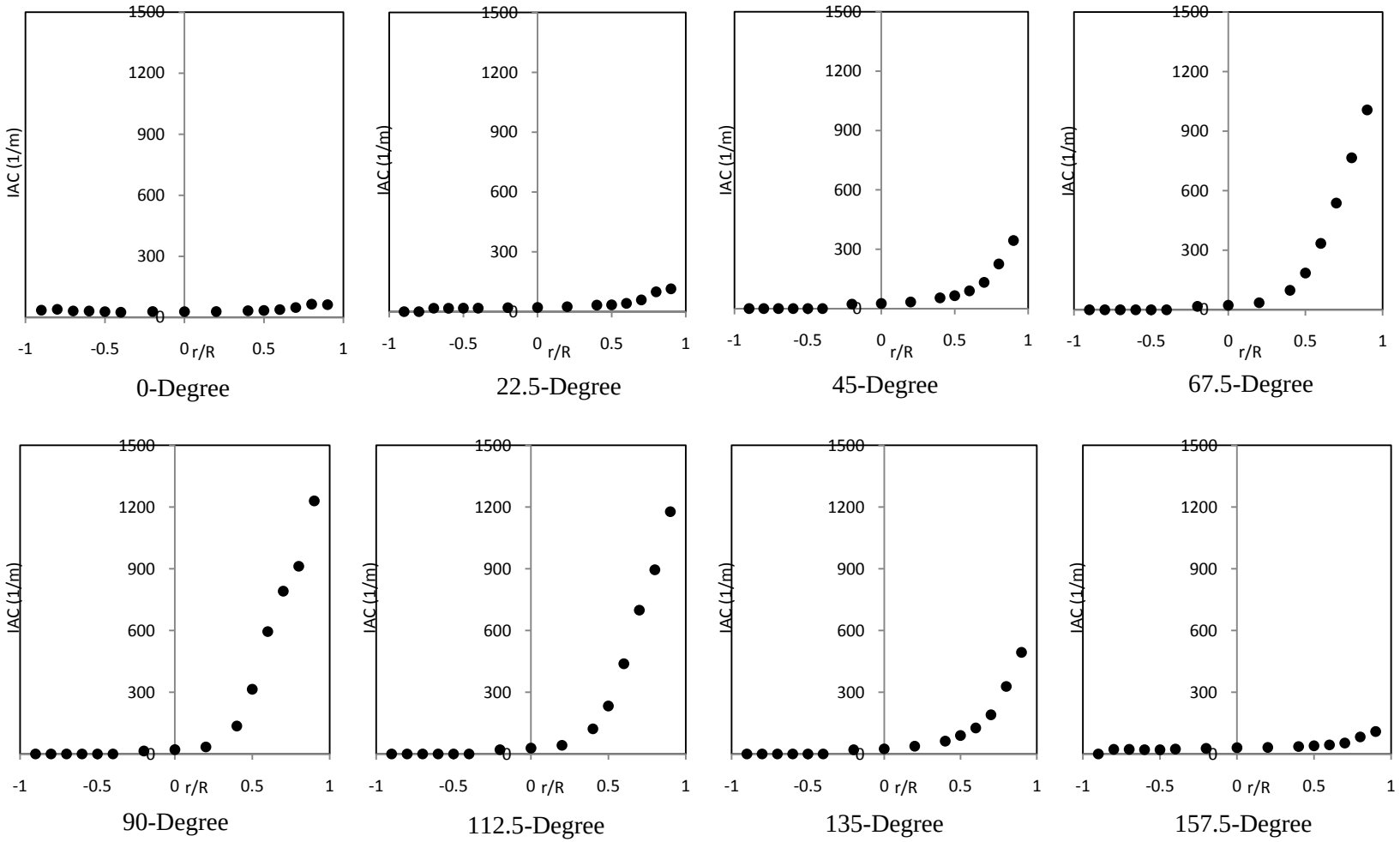

Figure **A 8-12**: Local profiles of interfacial area concentration at different angles of measurement at port P5, L/D = 30 from the 90-degree vertical elbow at Run-6; j_f = 3.0 m/s and $j_{g,atm}$ = 0.353 m/

Appendix A9

Local interfacial structures in horizontal section in combinatorial channels

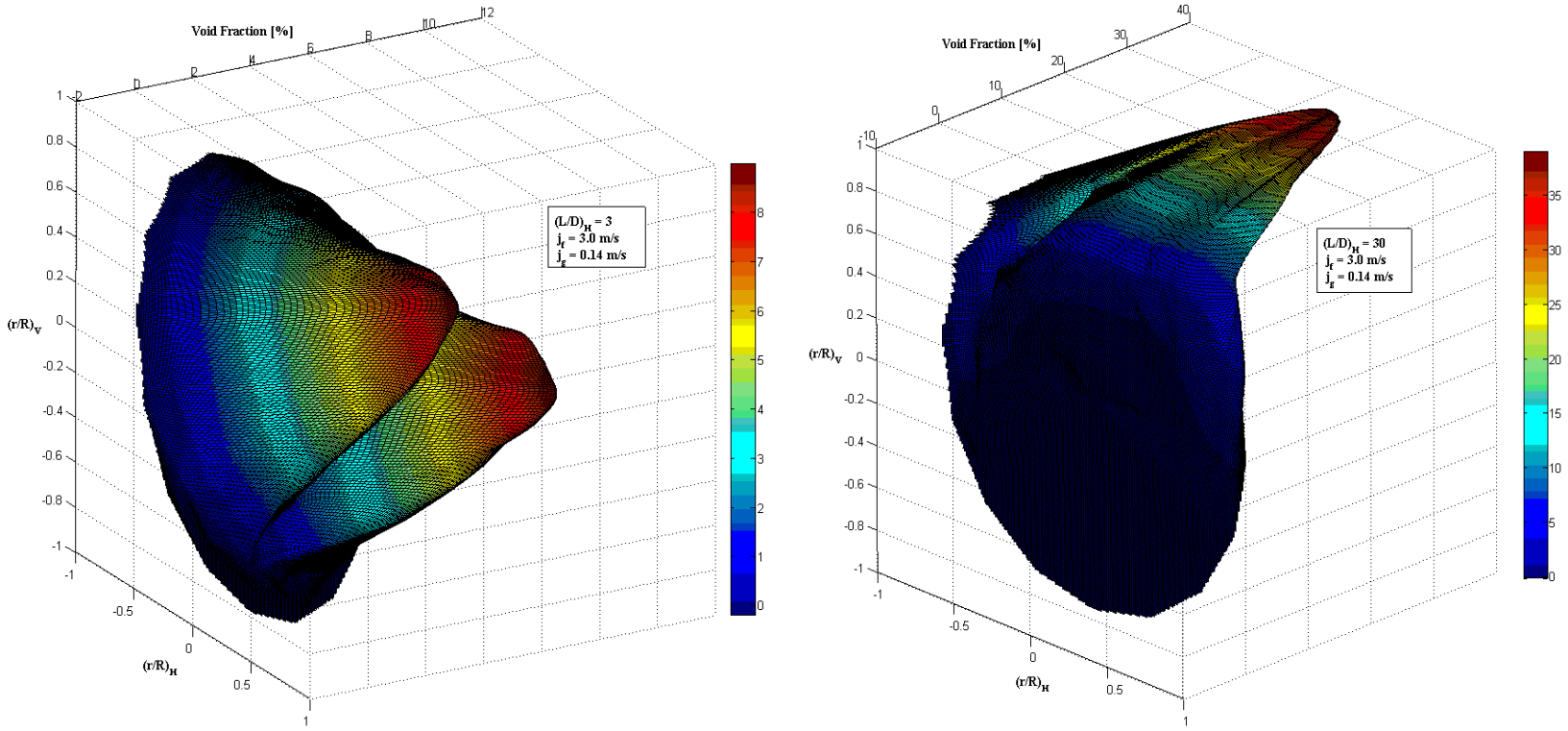

$(L/D)_H = 3$ $(L/D)_H = 30$

Figure **A 9-1**: Three-dimensional profiles of void fraction as the flow develops downstream of the 90-degree vertical elbow at Run-4, $j_f = 3.0$ m/s and $j_{g,atm} = 0.139$ m/s

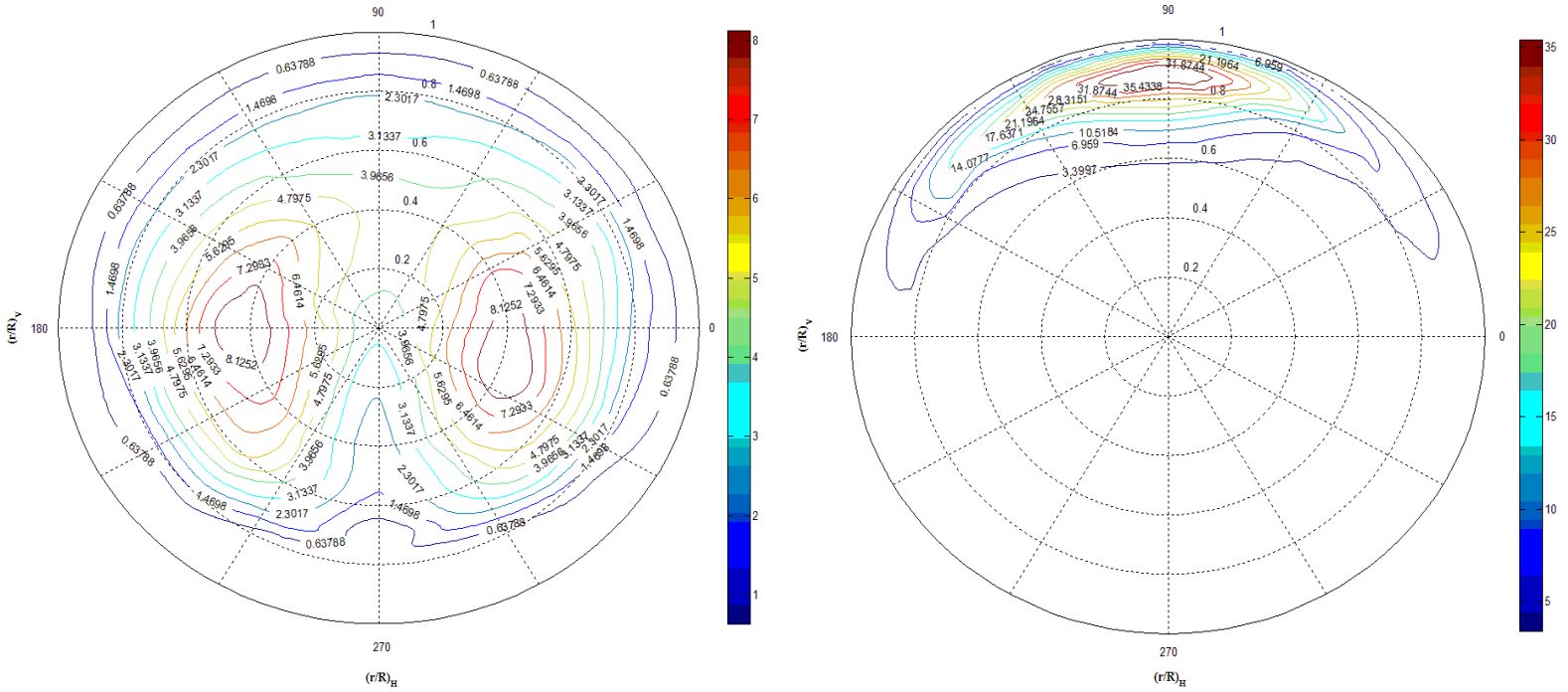

$(L/D)_H = 3$ $(L/D)_H = 30$

Figure **A 9-2**: Contour plots of local void fraction as the flow develops downstream of the 90-degree vertical elbow at Run-4, j_f = 3.0 m/s and $j_{g,atm}$ = 0.139 m/s

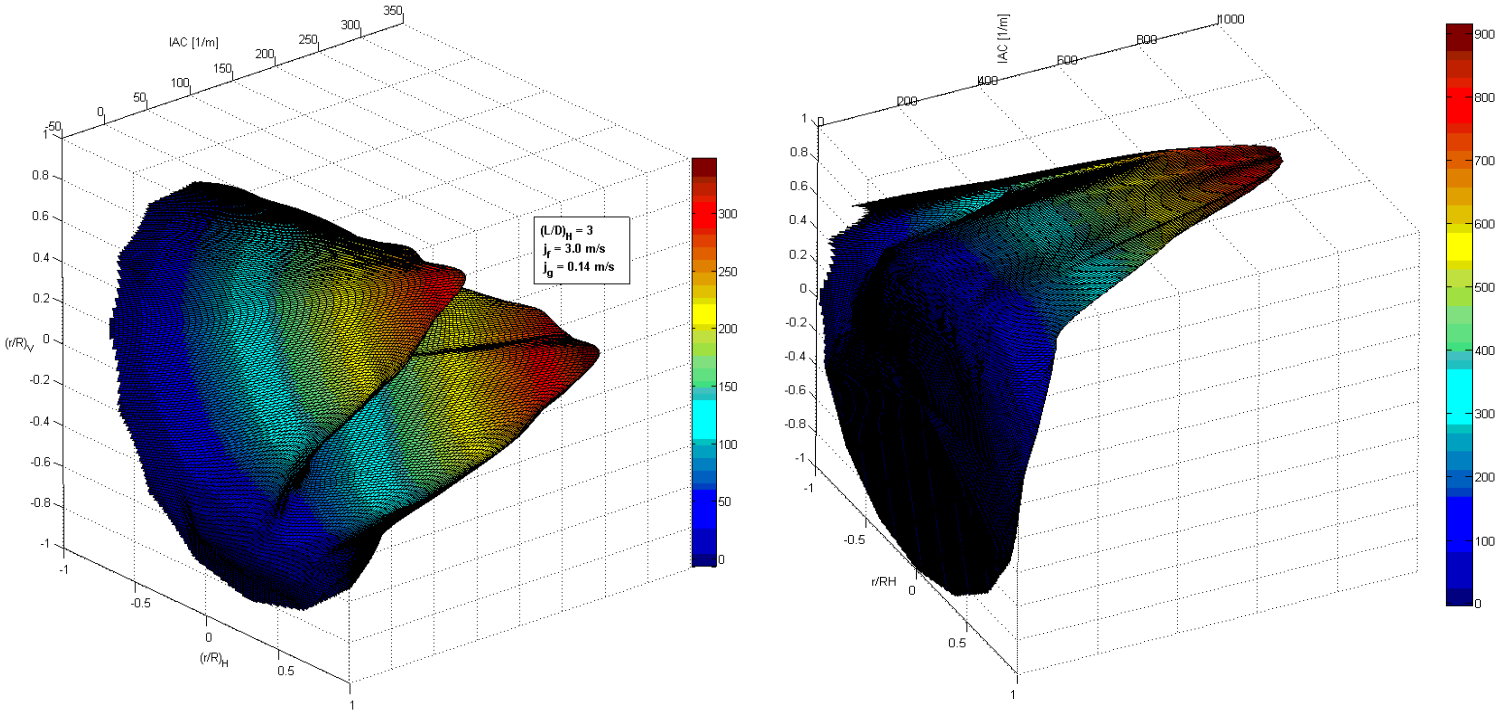

$(L/D)_H = 3$ $(L/D)_H = 30$

Figure **A 9-3**: Three-dimensional profiles of interfacial area concentration as the flow develops downstream of the 90-degree vertical elbow at Run-4, $j_f = 3.0$ m/s and $j_{g,atm} = 0.139$ m/s

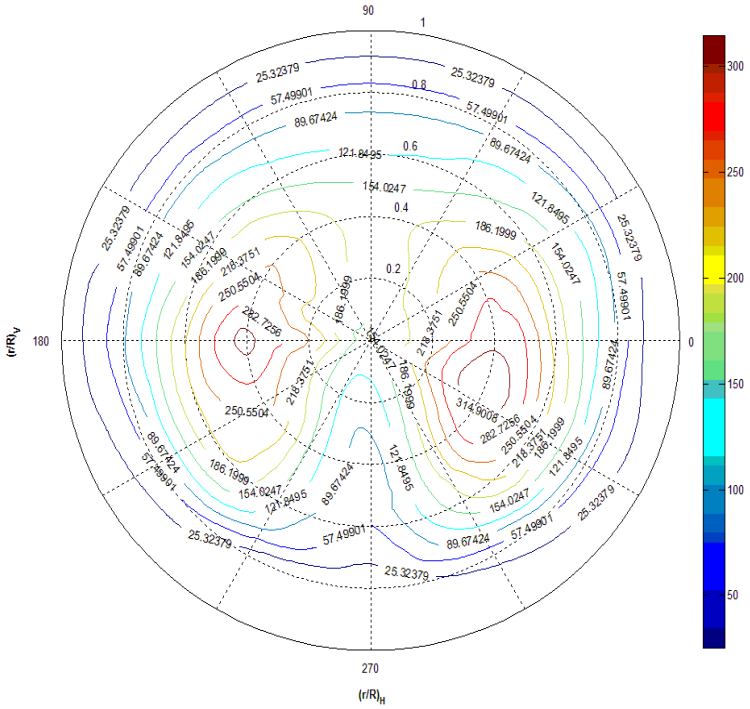

$(L/D)_H = 3$

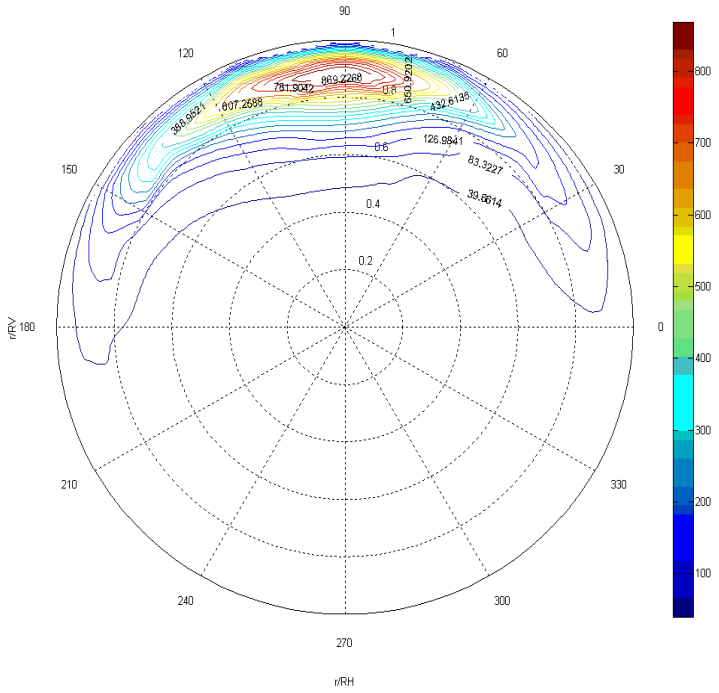

$(L/D)_H = 30$

Figure **A 9-4**: Contour plot of interfacial area concentration as the flow develops downstream of the 90-degree vertical elbow at Run-4, j_f = 3.0 m/s and $j_{g,atm}$ = 0.139 m/s

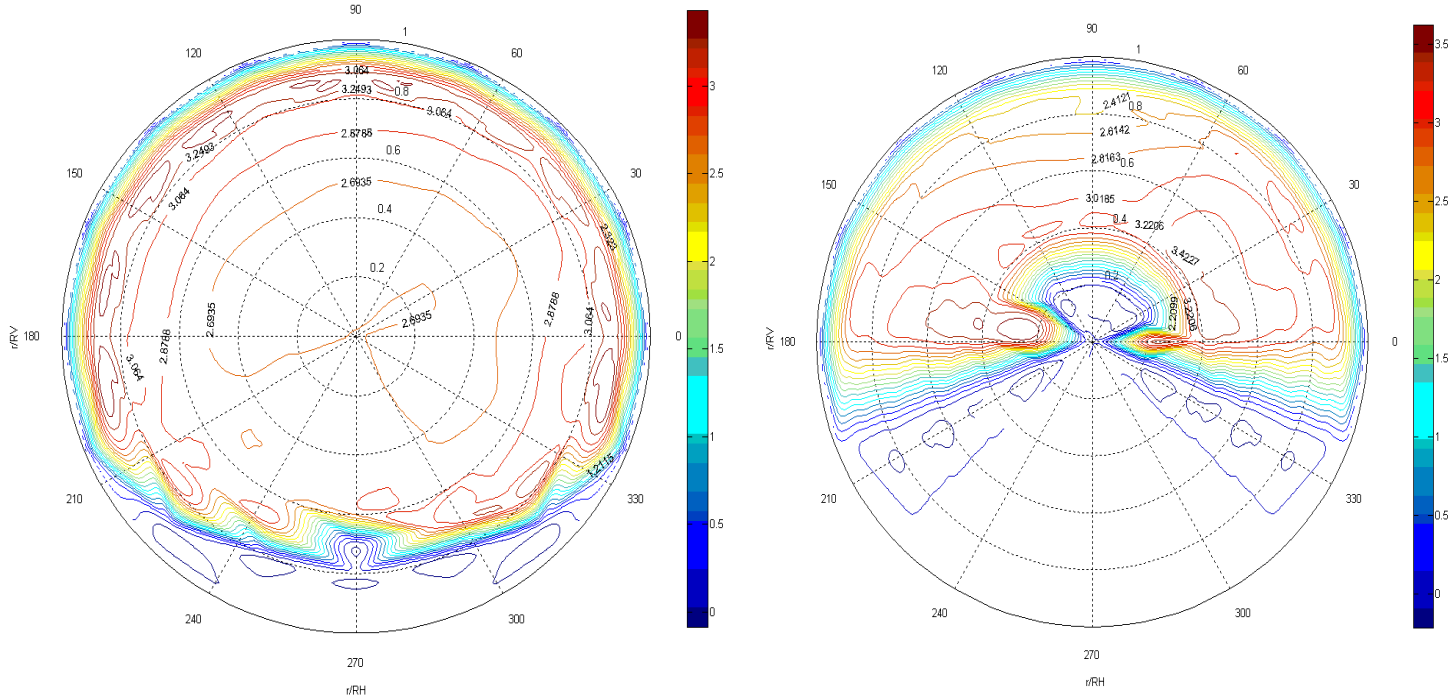

$(L/D)_H = 3$

$(L/D)_H = 30$

Figure **A 9-5**: Contour plot of bubble velocity as the flow develops downstream of the 90-degree vertical elbow at Run-4, $j_f = 3.0$ m/s and $j_{g,atm} = 0.139$ m/s

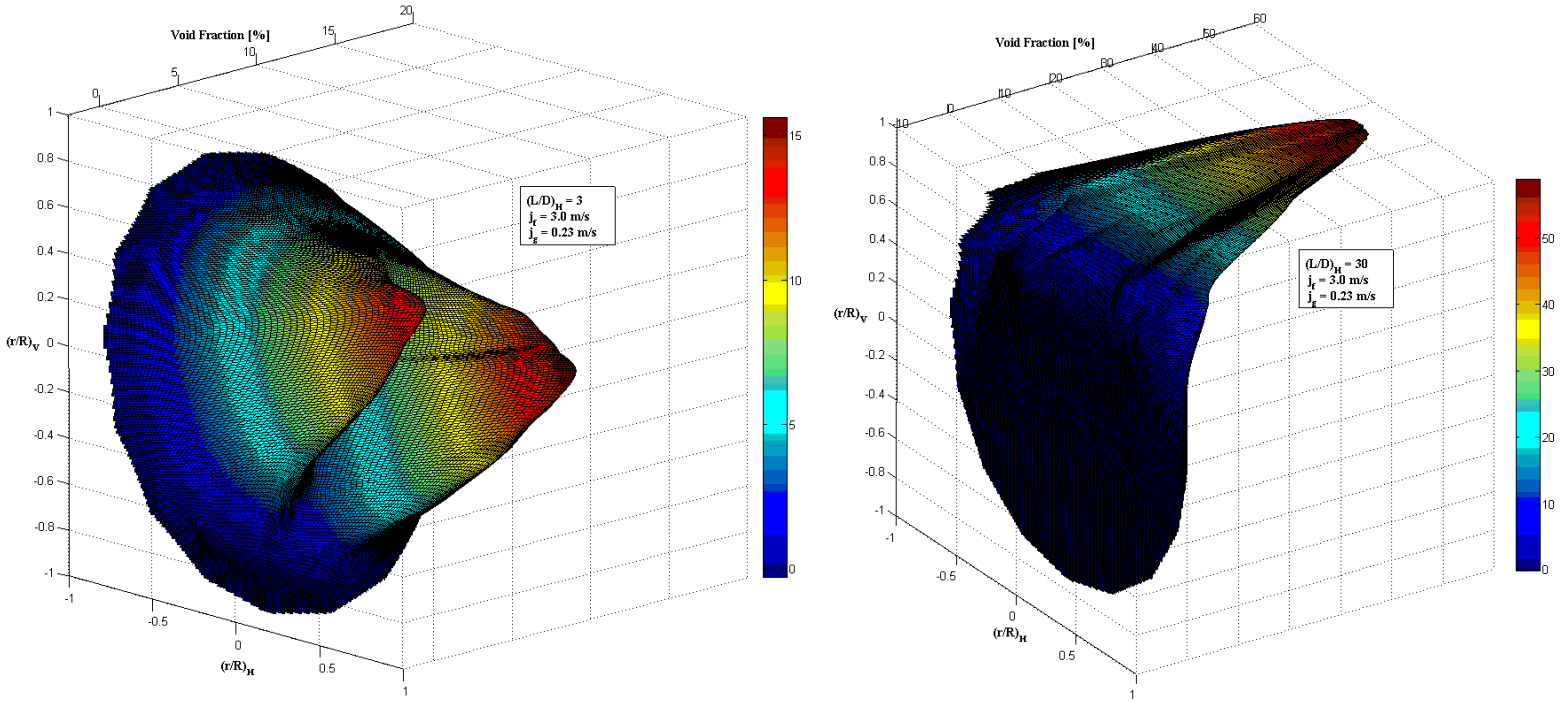

$(L/D)_H = 3$ $(L/D)_H = 30$

Figure **A 9-6**: Three-dimensional profiles of void fraction as the flow develops downstream of the 90-degree vertical elbow at Run-5, $j_f = 3.0$ m/s and $j_{g,atm} = 0.232$ m/s

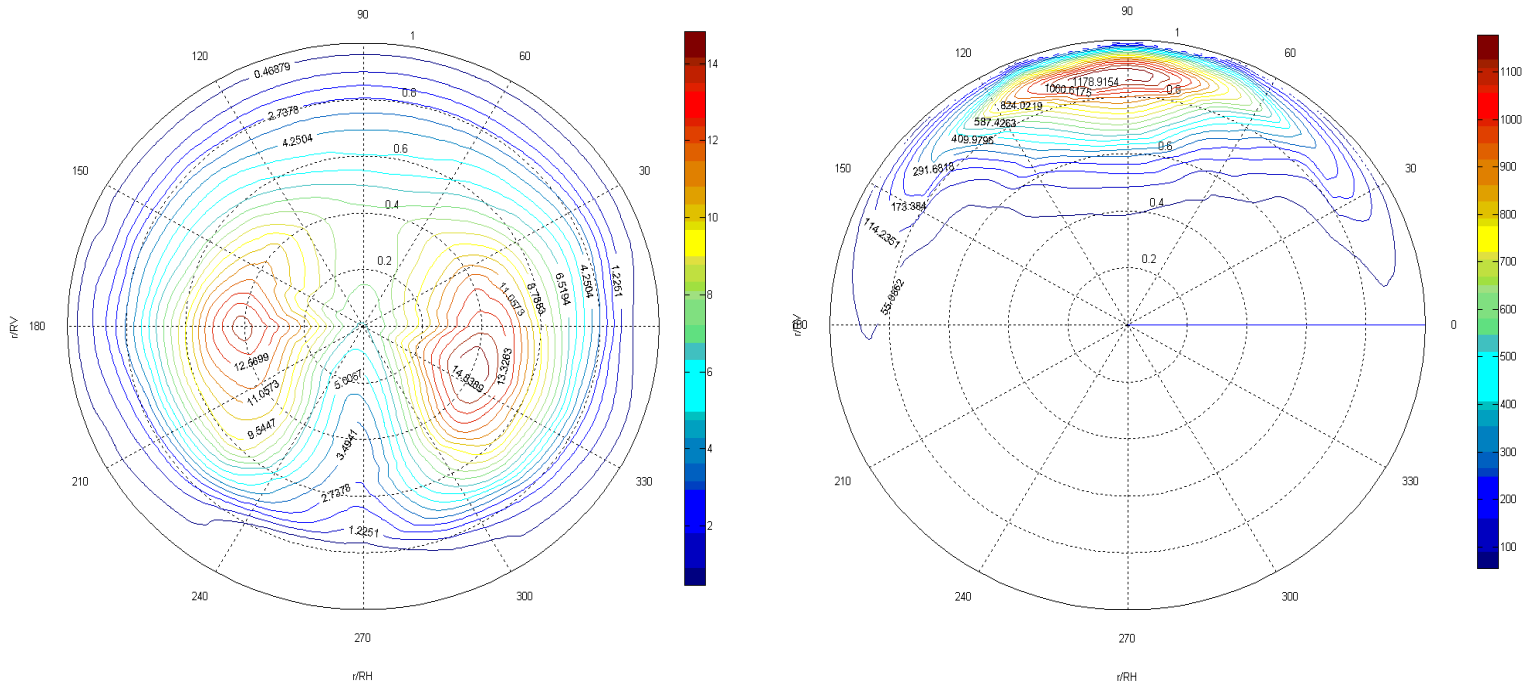

$(L/D)_H = 3$ $(L/D)_H = 30$

Figure **A 9-7**: Contour plots of the local void fraction as the flow develops downstream of the 90-degree vertical elbow at Run-5, $j_f = 3.0$ m/s and $j_{g,atm} = 0.232$ m/s

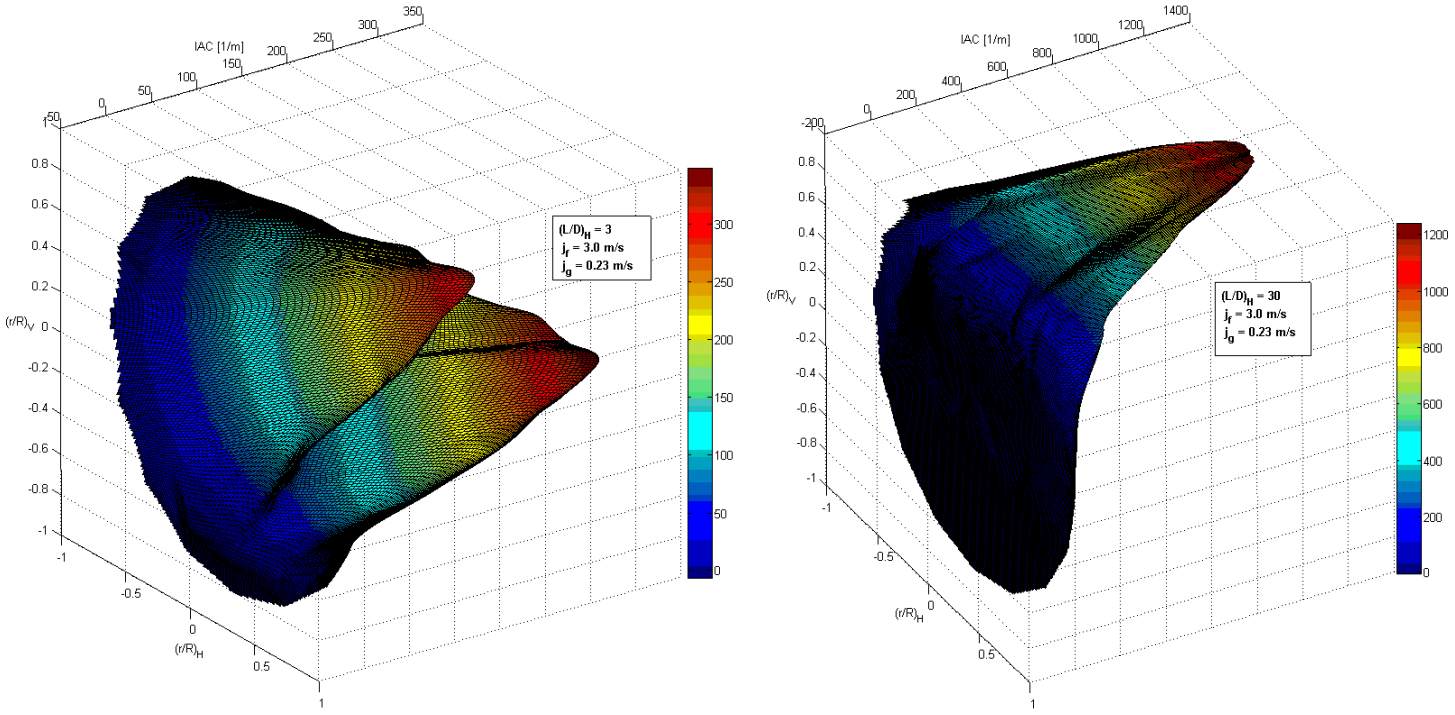

$(L/D)_H = 3$ $(L/D)_H = 30$

Figure **A 9-8**: Three-dimensional profiles of interfacial area concentration as the flow develops downstream of the 90-degree vertical elbow at Run-5, $j_f = 3.0$ m/s and $j_{g,atm} = 0.232$ m/s

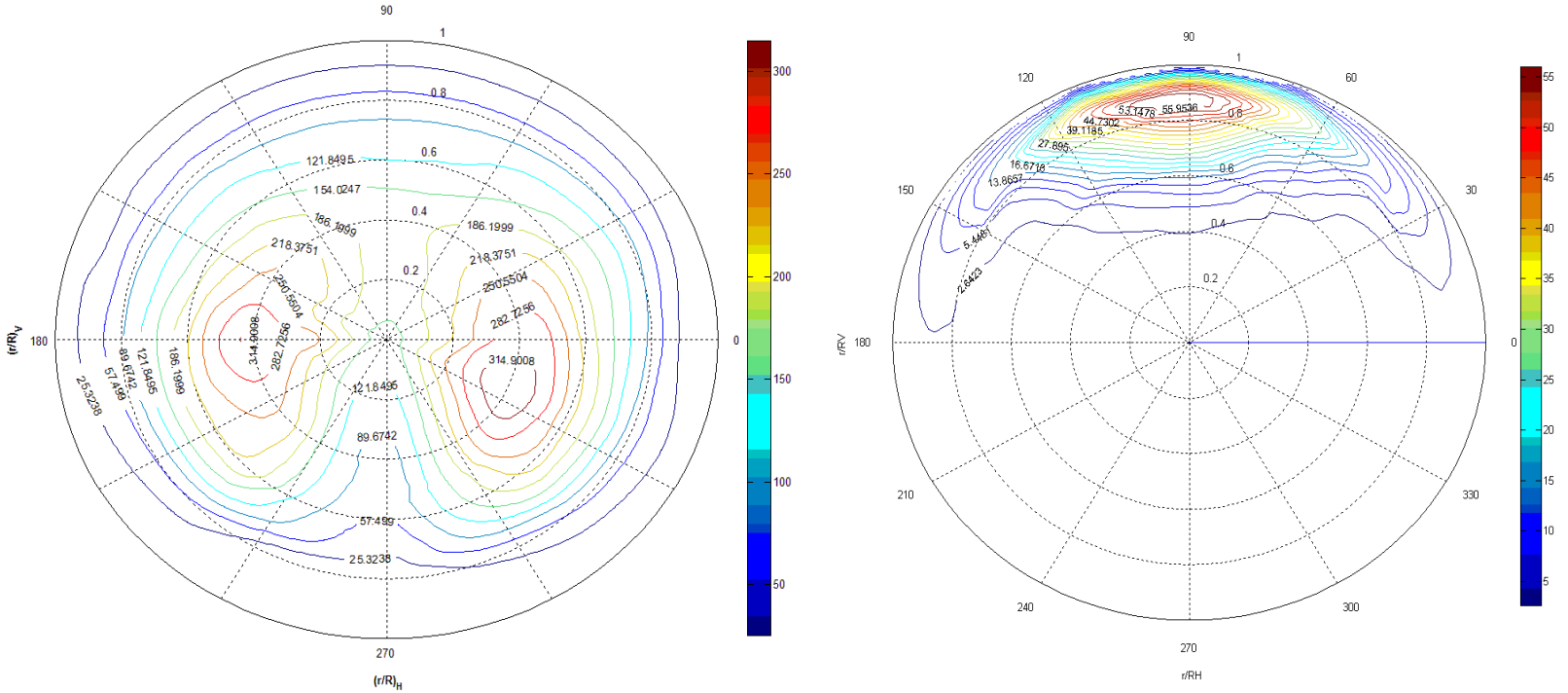

$(L/D)_H = 3$ $(L/D)_H = 30$

Figure **A 9-9**: Contour plots of interfacial area concentration as the flow develops downstream of the 90-degree vertical elbow at Run-5, j_f = 3.0 m/s and $j_{g,atm}$ = 0.232 m/s

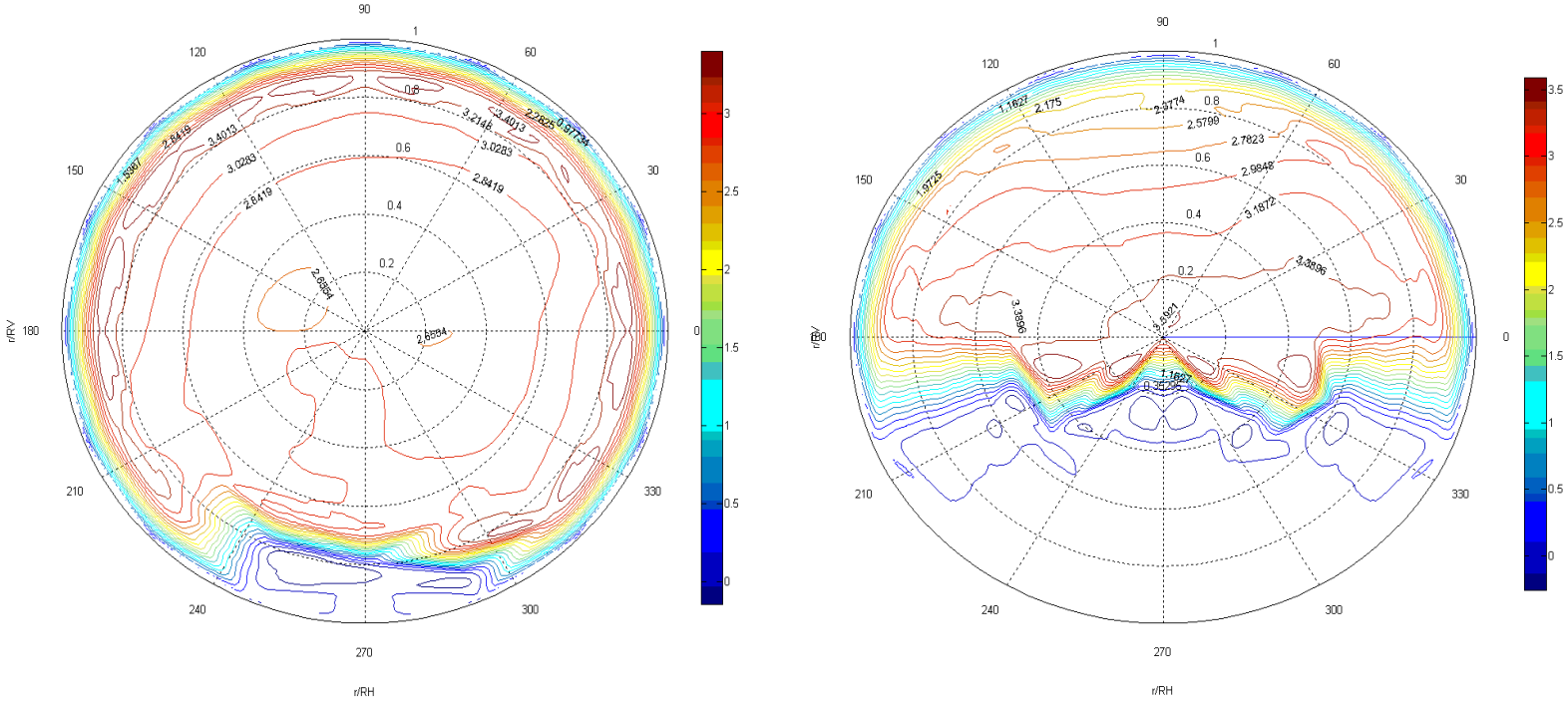

$(L/D)_H = 3$ $(L/D)_H = 30$

Figure **A 9-10**: Contour plots of local bubble velocity as the flow develops downstream of the 90-degree vertical elbow at Run-5, $j_f = 3.0$ m/s and $j_{g,atm} = 0.232$ m/s

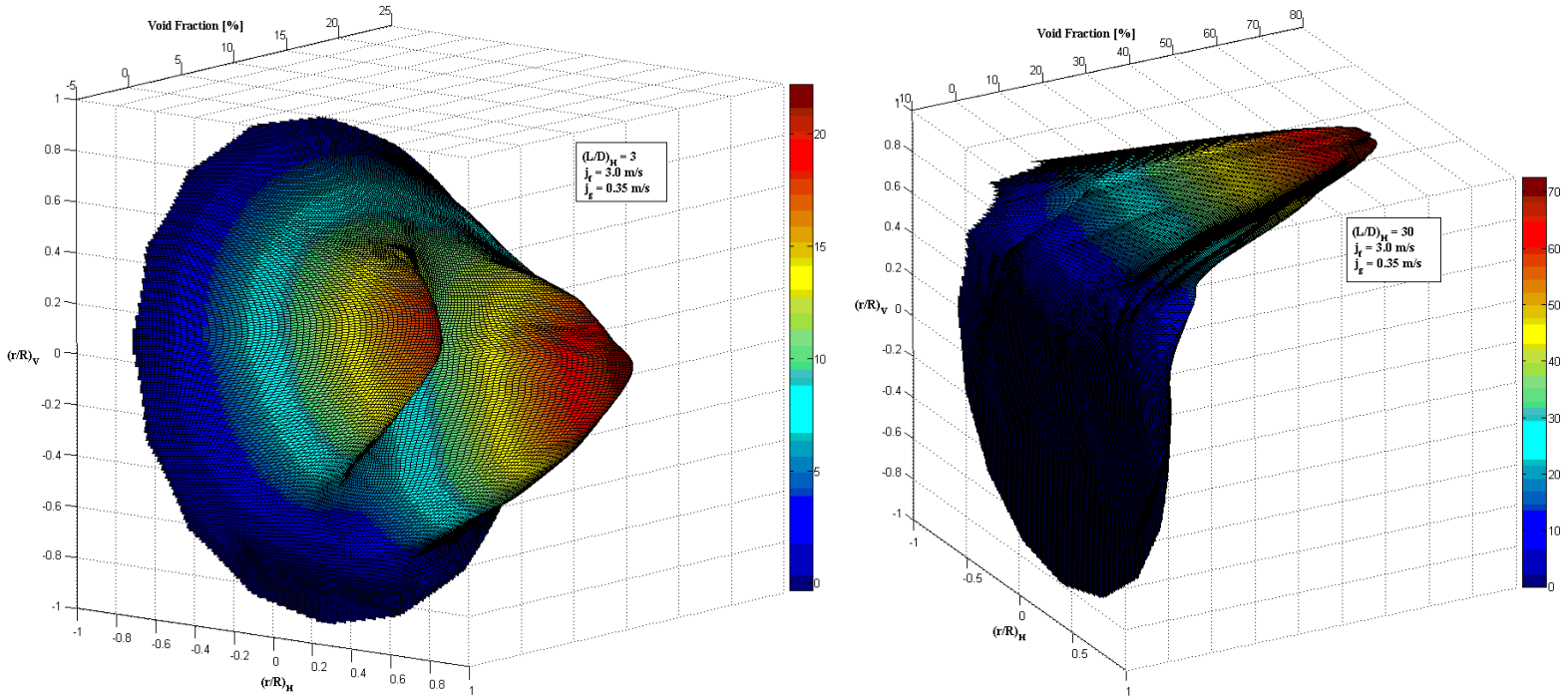

$(L/D)_H = 3$ $(L/D)_H = 30$

Figure **A 9-11**: Three-dimensional profiles of void fraction as the flow develops downstream of the 90-degree vertical elbow at Run-6, $j_f = 3.0$ m/s and $j_{g,atm} = 0.353$ m/s

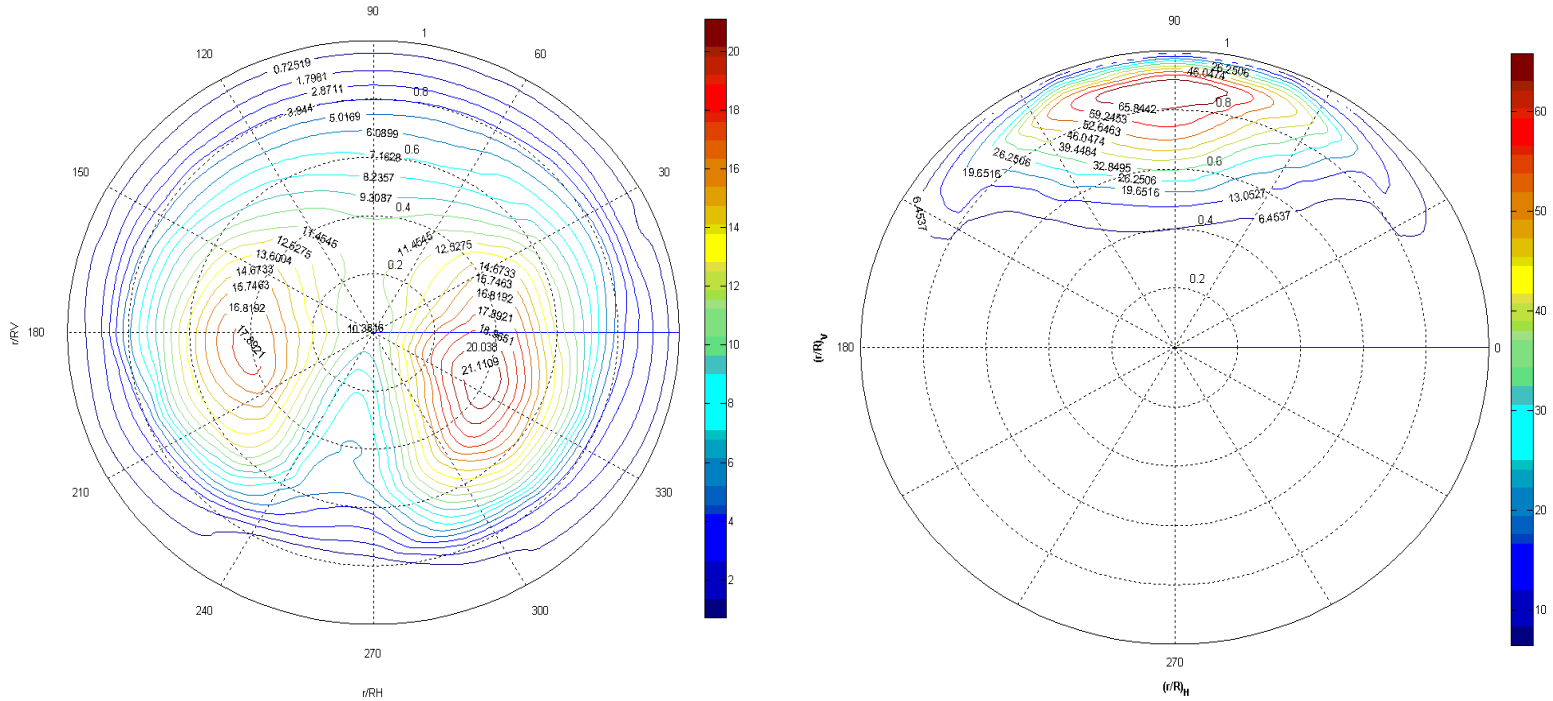

$(L/D)_H = 3$ $(L/D)_H = 30$

Figure **A 9-12**: Contour plots of the local void fraction as the flow develops downstream of the 90-degree vertical elbow at Run-6, $j_f = 3.0$ m/s and $j_{g,atm} = 0.353$ m/s

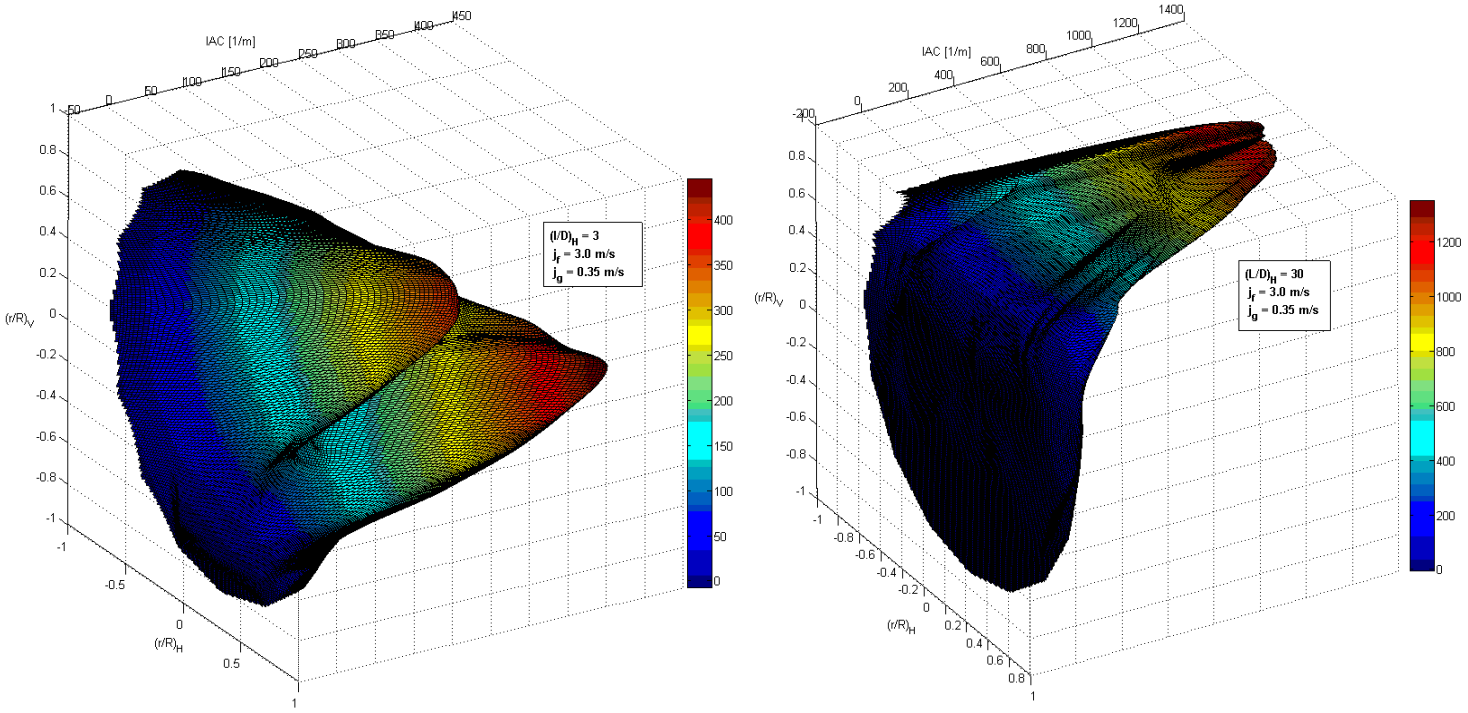

$(L/D)_H = 3$ $(L/D)_H = 30$

Figure **A 9-13**: Three-dimensional profiles of interfacial area concentration as the flow develops downstream of the 90-degree vertical elbow at Run-6, $j_f = 3.0$ m/s and $j_{g,atm} = 0.353$ m/s

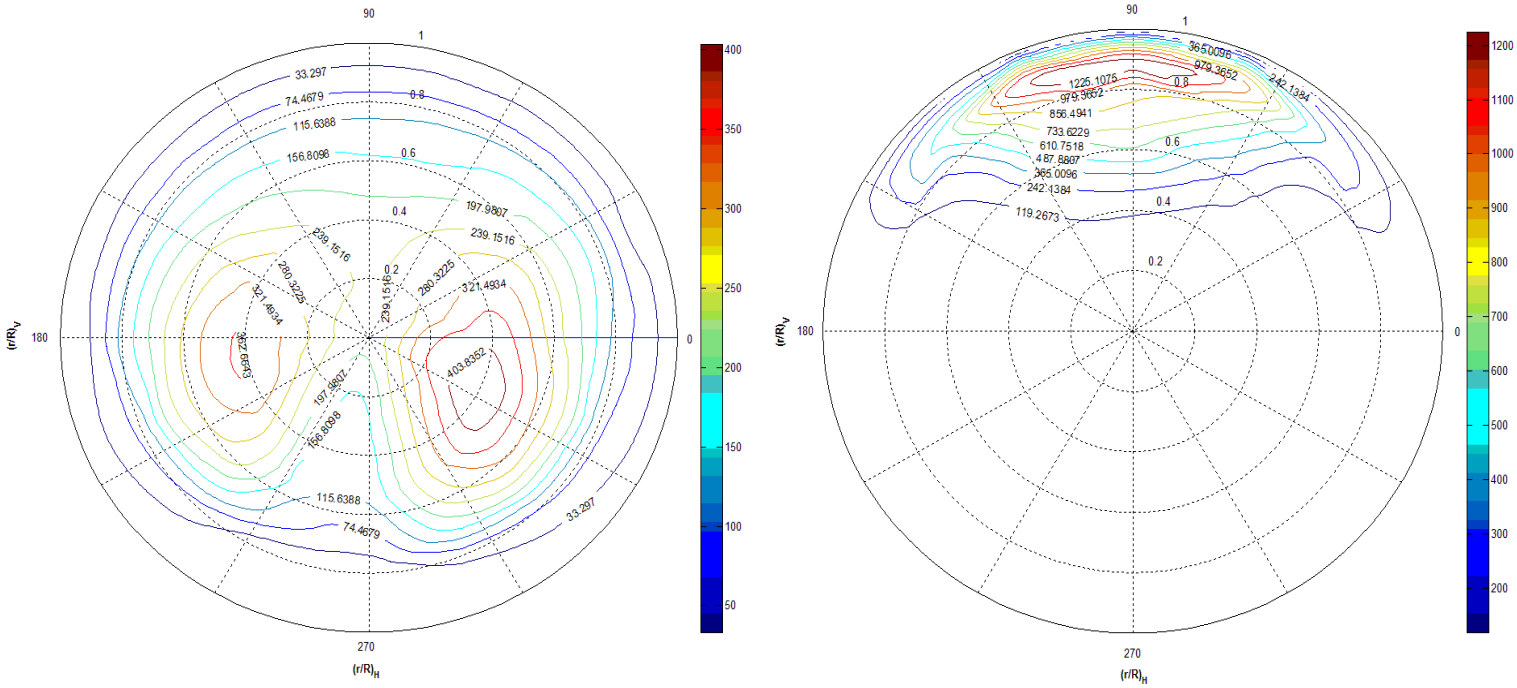

$(L/D)_H = 3$ $(L/D)_H = 30$

Figure **A 9-14**: Contour plots of local interfacial area concentration as the flow develops downstream of the 90-degree vertical elbow at Run-6, $j_f = 3.0$ m/s and $j_{g,atm} = 0.353$ m/s

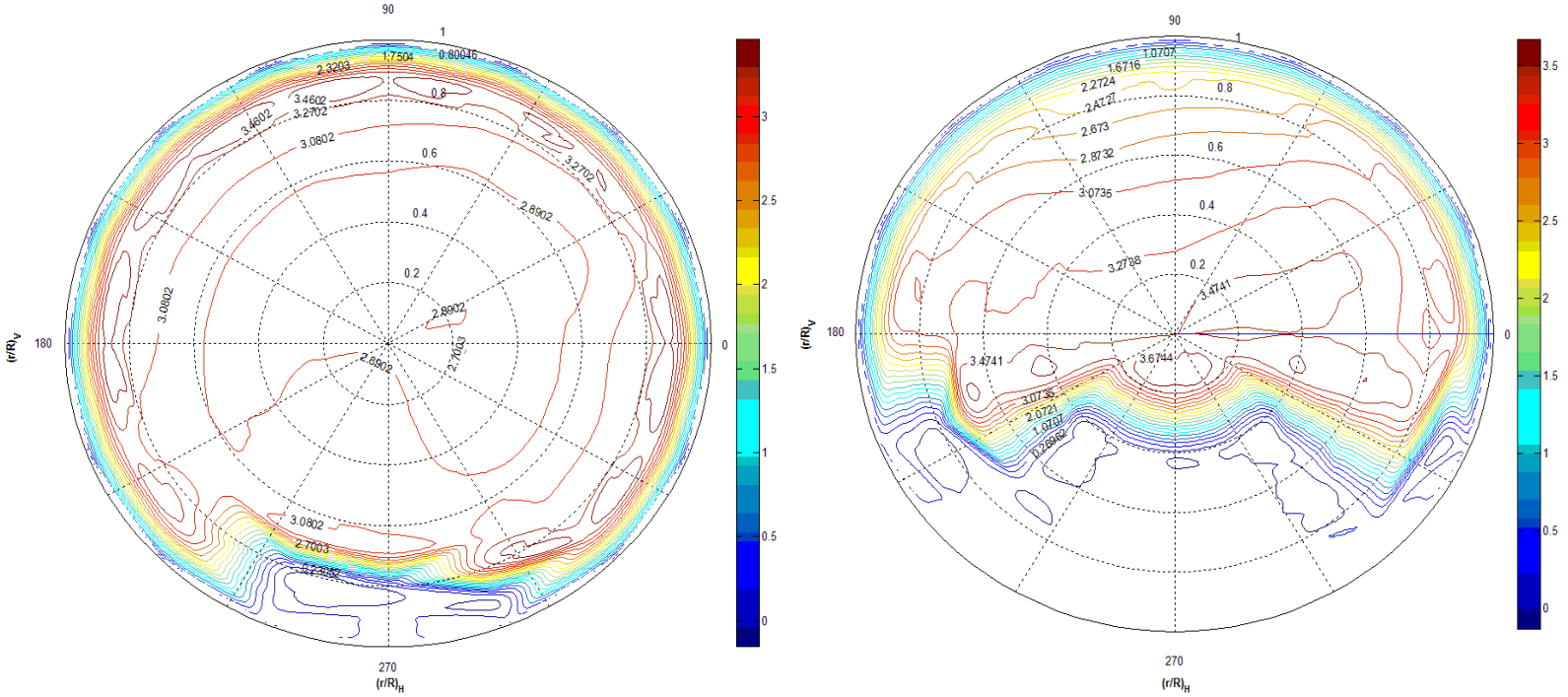

$(L/D)_H = 3$ $(L/D)_H = 30$

Figure **A 9-15**: Contour plots of local bubble velocity as the flow develops downstream of the 90-degree vertical elbow at Run-6, $j_f = 3.0$ m/s and $j_{g,atm} = 0.353$ m/s